Spring 1-1-2014

Processing, Structure and High Temperature Oxidation Properties of Polymer-Derived and Hafnium Oxide Based Ceramic Systems

Kalvis Terauds
University of Colorado Boulder, terauds@colorado.edu

Processing, Structure and High Temperature Oxidation Properties of Polymer-Derived and Hafnium Oxide Based Ceramic Systems

By:

Kalvis Terauds

B.S., Mechanical Engineering
Michigan State University, East Lansing, Michigan, 2006

M.S., Mechanical Engineering
University of Colorado, Boulder, Colorado, 2011

A Thesis Submitted to the

Faculty of the Graduate School of the

University of Colorado in partial fulfillment

of the requirement for the degree of

Doctor of Philosophy

Department of Mechanical Engineering

2014

This thesis entitled:

Processing, Structure and High Temperature Oxidation Properties of Polymer-Derived and Hafnium Oxide Based Ceramic Systems

Written by Kalvis Terauds
has been approved for the Department of Mechanical Engineering

_____
Dr. Rishi Raj
Department of Mechanical Engineering, University of Colorado, Boulder

_____
Dr. David Marshall
Teledyne Scientific Company, Thousand Oaks, California

_____
Dr. Randall Hay
Air Force Research Lab, Materials and Manufacturing Directorate, Dayton, Ohio

_____
Dr. Steven George
Department of Chemistry and Biochemistry, University of Colorado, Boulder

_____
Dr. Wei Tan
Department of Mechanical Engineering, University of Colorado, Boulder

Date_____

The final copy of this thesis has been examined by the signatories, and we find that both the content and the form meet acceptable presentation standards of scholarly work in the above mentioned discipline.

Abstract

Terauds, Kalvis (Ph.D. Mechanical Engineering)

Processing, Structure and High Temperature Oxidation Properties of Polymer-Derived and Hafnium Oxide Based Ceramic Systems

Dissertation directed by Professor Rishi Raj

Demands for hypersonic aircraft are driving the development of ultra-high temperature (UHT) structural materials. These aircraft, envisioned to sustain Mach 5+, are expected to experience continuous temperatures of 1200-1800°C on the aircraft surface and temperatures as high as 2800°C in combustion zones. Breakthroughs in the development of fiber based ceramic matrix composites (CMCs) are opening the door to a new class of high-tech UHT structures for aerospace applications. One limitation with current carbon fiber or silicon carbide fiber based CMC technology is the inherent problem of material oxidation, requiring new approaches for protective environmental barrier coatings (EBC) in extreme environments.

This thesis focuses on the development and characterization of SiCN-HfO_2 based ceramic composite EBC systems to be used as a protective layer for silicon carbide fiber based CMCs. The presented work covers three main architectures for protection:

(i) Multilayer films. This design uses a multilayered structure consisting of a UHT transition metal oxide, HfO_2, as the outer environmental barrier layer. Polymer-derived SiCN is used as a high-temperature bonding medium between the HfO_2 and the underlying SiC structural material. This multilayer composite design has been shown as an effective EBC for similar refractory ceramic structural materials

(ii) Polymer-derived HfSiCNO. Polymer-derived materials, like the SiCN bond layer mentioned above, have also been shown to be effective EBCs by themselves. This section details the doping of an SiCN precursor with Hf-O, to create an amorphous HfSiCNO material directly from the polymer route. Since it is processed as a liquid polymer, material systems of this kind have the potential for many CMC uses, ranging from the development of new fiber chemistries to new ceramic matrix materials.

(iii) Composite SiCN-HfO_2 infiltrations. The section explores infiltrating CMC "preforms" using a composite material consisting of HfO_2 particles in a polymer-derived SiCN matrix. The ceramic matrix is fabricated from the liquid polymer route enabling the infiltration of complex net shape CMC structures such as gas turbine blades.

The scope of this thesis covers processing development, material characterization, and high temperature oxidation behavior of these three SiCN-HfO_2 based systems. This work shows that the SiCN-HfO_2 composite materials react upon oxidation to form $HfSiO_4$, offering a stable EBC in streaming air and water vapor at 1600°C

Acknowledgement

This research was supported by the US AFOSR (Dr. Ali Sayir) and NASA (Dr. Anthony Calomino) under the National Hypersonic Science Center for Materials and Structures (AFOSR contract no. FA9550-09-1-0477).

Table of Contents

Table of Figures

1 Background and Introduction

1.1 Introduction

Hypersonic aircraft development is raising a new set of demands for high-tech refractory ceramic materials. These air-breathing aircraft, envisioned to sustain Mach 5+, will experience prolonged exposures to ultra-high temperatures (UHT) in a chemically reactive environment. It is expected that the aircraft must withstand temperatures of 1200-1500°C at the surface and even as high as 2800°C in the combustion chamber zones [1].

1.2 Hypersonic Materials and Structures

Prolonged temperature exposures seriously limit the amount of feasible design materials for hypersonic structures. For example, there are only around 15 materials currently known with melting temperatures above 3000°C. This includes a three elemental materials (C, W, and Re), and a few ceramic compound nitrides, borides, carbides, and one metal-oxide (ThO_2) [2]. However, it is important to note in this case that melting temperature is characterized in inert environment where the materials cannot react with their surroundings. Hypersonic application materials also must withstand ultra-high temperatures in the presence of oxidizing species such as O_2 and H_2O. Elemental carbon, for example, is stable to >3500°C in inert atmosphere but will readily burn into CO_2 or CO at temperatures >600°C in oxidizing environments [3, 4].

Hypersonic aircraft are also posing a new set of challenges for structural design. The key difference between existing UHT aerospace structures and those required for hypersonic flight is the duration of exposure. Previous designs, such as those for atmospheric re-entry, only experience UHT conditions for short periods of peak exposure whereas hypersonic aircraft may experience peak conditions continually. This imposes new demands particularly in the area of heat management.

Existing UHT technology has predominantly used insulating or ablating heat shields [5]. Insulating shields, such as those on the underside of a space shuttle, were made as a thermal conduction barrier since peak exposure time was limited. Heat builds up at the surface during peak conditions and is then is emitted as the conditions lessen. This poses a problem for sustained hypersonic flight because heat buildup is continuous and requires dynamic heat management. To keep surface temperatures at an operable level the heat must be proactively channeled away, requiring the use of thermal conductors instead of insulators. Using a strong thermal conductor would allow the heat to be captured and possibly exploited, such as pre-heating of fuel, or captured and expelled. Other protective coatings, known as ablative coatings, have been used in similar applications such as re-entry capsules. These ablative shields effectively act as a sacrificial layer which slowly burn with environmental exposure at peak conditions. The obvious drawback to a design of this kind is that they would only permit flight for a finite time (depending on thickness of the ablative layer), and they would have to be regularly reapplied to the surface of the aircraft.

These constraints require that hypersonic materials be fabricated from materials with high specific strength, thermal stability, oxidation resistance, and thermal conductivity. These materials would remain structurally stable in UHT oxidizing atmospheres and could aggressively draw heat flux from the aircraft surface, lowering the operation

temperature and permitting sustained hypersonic flight. Metals are an obvious choice for high thermal conductivity, but they have low operating temperature compared to their refractory ceramic counterparts, and they have generally poor oxidation resistance [6]. This forces the design to be based on refractory ceramics materials. The highest temperature ceramics come in the form of transition metal carbides, nitrides, borides, and oxides [7]. Other materials, such as rare-earth silicates, silicides, and beryllides, have also been considered for applications above 1650°C, however, research to date suggests they are not as strong candidates [8].

Transition metal borides are materials of interest since they have high melting temperatures, for example ZrB_2 and HfB_2 both melt around 3300°C, and they have some of the highest thermal conductivities of refractory ceramics. Transition metal diborides can exhibit metal-like thermal conductivity at temperatures in excess of 1400°C [9, 10]. The major drawback to these materials in their pure is that they show unfavorable oxidation resistance. The MB_2 materials (where M= Ti, Zr, Hf) react with environmental oxygen to form MO_2 and B_2O_3. At the temperature of interest for hypersonic applications, the B_2O_3 vaporizes and leave a porous MO_2 oxide scale which is permeable by environmental O_2 for continued oxidation [11, 12].

Transition metal carbides, such as HfC, TaC, and ZrC, are interesting for hypersonic applications because they are extremely hard and have some of the highest melting temperatures of any known material. They show similar oxidation behavior as the diborides and react with environmental oxygen to form a porous MO_2 layer, with the gaseous oxide product in this case being carbon monoxide (CO) [13]. The oxidation resistance has been shown to increase at higher temperatures (>1800°C) where the formed MO_2 layer densifies from sintering [14]. SiC is also a promising carbide material as it shows superior oxidation rates below 1600°C [15]. The key difference between the

silicon carbide and the transition metal carbides is that SiC oxidizes to create SiO_2 glass. The formed SiO_2 layer is molten and therefore creates a dense layer forcing oxygen diffusion, rather than permeation through open oxide scale porosity. SiC also offers a high melting point of 2820°C and offers high thermal conductivity and excellent mechanical properties. The major drawback to SiC is that the SiO_2 layer has lower thermal stability than $(Zr,Hf)O_2$ type oxides, and it is unsuitable as a standalone material for rapidly streaming environments as it would recess via viscous flow.

Transition metal oxides, such as ZrO_2 and HfO_2, are also promising UHT materials. Since they are already a stable oxide phase, they can be applied as a dense layer with no significant environmental reaction. The major drawback to these materials is they tend to be thermal insulators and show relatively lower thermal stability rendering them unfeasible for some of the highest temperature structural components [16]. For example, the 2800°C conditions observed in combustion chambers would exceed the melting point of almost all metal oxides. This limits their application to the aircraft surface and structural components. However, at expected surface temperatures, metal oxides have been shown to have favorable specific strengths compared to some of the higher temperature carbide or boride materials.

The final class of materials given consideration for hypersonic applications is the metal nitrides. They have high melting points, comparable with the diborides, and show good strength and thermal conductivity. Their oxidation behavior is similar to analogous carbide materials, except their gaseous oxidation products are N_2 or NO species whereas the carbides form CO. Silicon nitride, Si_3N_4, has interesting potential as it, like SiC, forms a protective SiO_2 layer upon oxidation [15, 17].

All of these refractory ceramics are of particular interest due to their low weight, high strength, and ability to survive harsh environments without degradation. The

fundamental problem with using ceramics for hypersonic structures is their inherent brittle nature. Dense ceramics experience extremely low strain to failure and small defects can propagate with minimal energy compared to metals. Advances in ceramic-matrix-composites (CMC) are now providing a viable means by which ceramic structures can be made for the harsh environments of hypersonic flight [18]. There is also serious potential for CMC applications in the field of gas turbine engines. The state-of-the-art nickel superalloy metals used in present day gas turbine engines have maximum operating temperature limits on the order of 1000-1100°C [175-176]. The melting point of these materials effectively prevents any major continued technological advancement with superalloys. It is widely accepted that the next disruptive breakthrough for turbine material technology will come from CMCs. Current CMC research is showing promise for carbon fiber or silicon carbide fiber based composites. However, both C and SiC fiber based CMC structures require new technologies in environmental barrier coatings (EBC) due to the problem of material oxidation.

1.3 Oxidation of Si-based Materials

One distinguishing feature of silicon containing materials is that they can thermally oxidize to form silica (SiO_2) which has the one of lowest oxygen transport rates of any oxide material [19]. Upon oxidation, the formed silica layer is an amorphous glass demonstrating the capacity for viscous transport. The ability of SiO_2 to flow gives Si-based materials a self-healing benefit in oxidizing environments. For example, if a crack was to develop in Si-containing material, the viscous silica would be drawn into the damage site from capillary forces, blunting the crack tip, and suppressing further crack propagation [20]. This is an extremely desirable trait especially for the refractory ceramic materials which suffer from brittle failure modes. The self-healing nature of

silica formers and low oxygen permeability make Si-containing materials favorites for CMC applications in oxidizing environments.

The mechanisms of oxidation and measured oxidation rates depend heavily on the base material and environmental conditions. Silica formers can demonstrate passive and/or active oxidation behavior depending on temperature and partial pressures of oxidizing species such as p_{O_2} or p_{H_2O}.

Passive oxidization results in the formation of a protective SiO_2 solid oxide layer. Pure Si, SiC, Si_3N_4, and SiCN all demonstrate passive oxidation in dry atmospheric oxygen levels below ~1700°C [21-24]. The oxidation rate limiting mechanism is dependent on the initial material chemistry and temperature. Elemental silicon is believed to be rate limited at low temperatures by the diffusion of diatomic oxygen through the passive silica layer giving it quadratic oxidation kinetics. At high temperatures, the kinetics area limited by ionic transport of oxygen through the SiO_2 [25]. Carbon containing Si-based materials, such as SiC and SiCN, also show quadratic growth rates, but the rate is considerably slower than those of Si. They are believed to be rate limited by the transport of outward carbon oxide species by means of CO_2/CO diffusion or gaseous bubbling. Silicon nitride also shows slower oxidation rates than Si, indicating nitrogen plays a role in oxidation kinetics. There are competing theories for the rate limiting mechanism of Si_3N_4. One noteworthy study found the presence of a Si-N-O interface phase which may be limiting the diffusion rates of inward O_2 or outward N_2, explaining the slower than Si quadratic rate behavior [26].

The aforementioned oxidation behavior of Si-containing materials are generalities and presented here merely as a simple guide. There are a considerable number of exceptions and peculiarities which exist. For example, thermal oxidation of Si is reaction rate limited at the early stages of oxidation and exhibits linear oxide growth

rates [27]. Similarly, one study has shown that the SiC crystal face orientation greatly influences the oxidation rate, suggesting that SiC too can be reaction limited in special cases [28]. Furthermore, devitrification of glassy SiO_2 can play an important role at UHT conditions which in turn influences oxygen diffusion mechanisms and can influence rate kinetics by up to a factor of 30x [29]. Impurities in the formed silica layer, of the type commonly found in laboratory furnaces, can increase oxidation rates [30]. The list goes on, but for the relevant experimental conditions presented in this thesis, the described passive oxidation behaviors of Si, SiC, and Si_3N_4 can be assumed to hold true.

Active oxidation of silica formers, on the other hand, results in the direct volatilization into gaseous species such as silicon monoxide, SiO, or silicon hydroxide, $Si(OH)_4$. The passive-active transition depends on many factors which can include temperature, partial pressure of oxidizing species, presence of a pre-existing passive SiO_2 layer, and environmental flow rates [31-34].

Table 1. Recession mechanisms of SiO_2

Environment	**SiO_2 Recession Mechanism**
Streaming H_2O	Formation of $Si(OH)_4$ *(g)*
Rapidly streaming	Viscous flow of SiO_2
Ultra-high temperature (>1800°C depending on p_{O2})	Formation of SiO *(g)*

The use of Si-based materials for hypersonic structural components requires that they have an outer EBC to prevent recession of the protective SiO_2 layer. Table 1 outlines three recession mechanisms which are relevant to hypersonic applications.

1.4 Motivation for HfO_2-SiCN Based Systems as EBC

The proposed design, and focus of this thesis, is the use of a composite EBC coating on silicon carbide using polymer-derived SiCN and hafnium oxide based material systems. An effective environmental barrier coating should demonstrate:

- Chemical and thermal resistance to the environment
- Capability to suppress or eliminate the transport of environmental products, such as oxygen, to the substrate
- Strong bonding to the substrate
- Compatible with substrate in thermal expansion mismatch
- Chemical compatibility with substrate

The proposed hypersonic design architecture is to use SiC based CMC materials for the aircraft structural components with the addition of SiCN-HfO_2 as an environmental protection layer. The HfO_2 would act as the outermost environmental barrier layer and polymer-derived SiCN would act as UHT bonding medium between HfO_2 and the SiC.

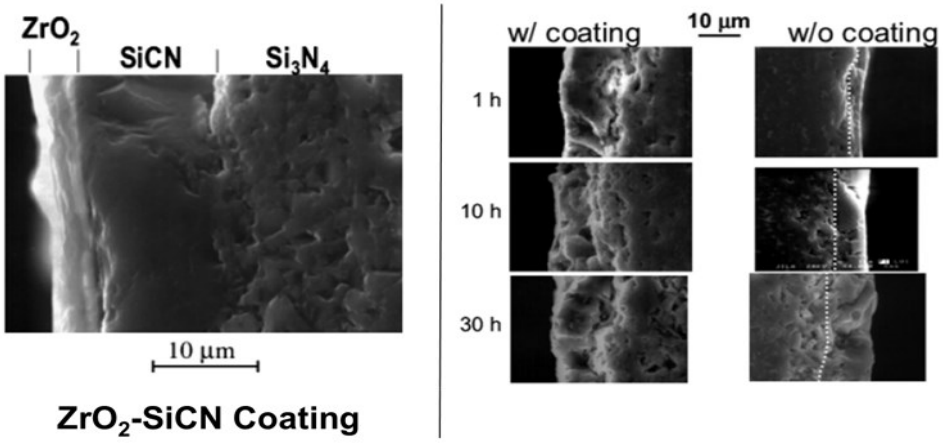

Fig. 1. Study of SiCN-ZrO_2 system as environmental barrier layer on silicon nitride [35]

Roots for this design are based off a 2007 study in which a SiCN-ZrO_2 coating was found to be an effective environmental barrier on silicon nitride (Si_3N_4) [35]. The structure of this film architecture is shown in Fig. 1 (left) where a layer of ZrO_2 is bonded to the Si_3N_4 substrate using polymer derived SiCN. The coated and uncoated Si_3N_4 fracture surfaces are given (right image) and show no appreciable oxide growth on the coated surface after 30 hours at 1350°C in air.

1.4.1 Introduction to HfO_2

HfO_2, known as hafnia or hafnium oxide, is a Group IV transition metal oxide closely related to the more well-known materials of TiO_2 (titania) and ZrO_2 (zirconia). It is selected here as the outer environmental barrier layer for its high melting temperature, chemical inertness, low vapor pressure, and phase stability. In terms of structure and chemical reactivity, HfO_2 is nearly identical to ZrO_2 and often indistinguishable from it. It has monoclinic structure at room temperature, undergoes a temperature dependent phase transition to tetragonal around 1750-1950°C, and melts at 2800°C [36].

Hafnium oxide has high enthalpy of formation of -1117 kJ/mol and is known to be extremely refractory [37]. Its effective twin material, ZrO_2, is commonly used for UHT furnace elements, insulation material, and environmental barrier coatings. HfO_2 could be interchanged for most of these applications as well but is often not due to its significantly manufacturing higher cost.

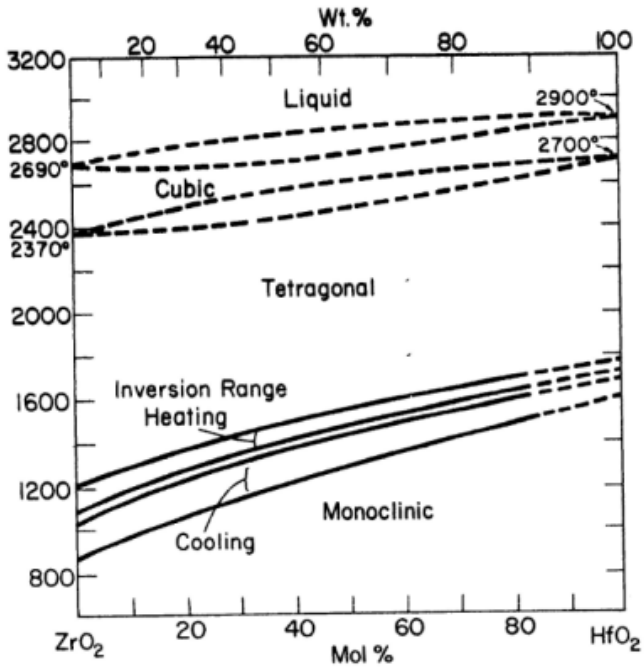

Fig. 2. Binary phase diagram of ZrO_2-HfO_2 [38]

The primary driver for the use of SiCN-HfO_2 systems, as opposed to the analogous ZrO_2 case, is the higher temperature stability of HfO_2. Fig. 2 shows a binary phase diagram of ZrO_2 and HfO_2 [38]. It can be seen that the two materials behave similarly except that all phase changes and melting temperatures are shifted upward with increasing HfO_2 content. This is particularly relevant for the monoclinic to tetragonal phase transition. There is conflicting data in literature for the exact temperatures, but is shown to occur in range 1750-1950°C for HfO_2 and around 1000°C for ZrO_2. This is important for the case of hypersonic applications where phase changes are undesirable within the operating temperature envelope. Additionally, HfO_2 has been shown to have lower oxygen diffusion and permeation rates than ZrO_2 [8, 39]. The present study uses the same basic architecture as the Si_3N_4/SiCN/ZrO_2 study reported in 2007 and focuses on discovering whether or not the same protection mechanism manifests itself at even higher temperatures for the system of SiC/SiCN/HfO_2.

1.4.2 Introduction to SiCN

SiCN, or silicon carbonitride, is part of a new family of materials known as polymer-derived ceramics (PDC) which are produced from the thermal decomposition of silicon-based organic polymer precursors [40]. The typical composition of these PDCs consist of Si, C, N, and O, approximately one third molar silicon, one third carbon, and one third nitrogen or oxygen. The composition regime of these materials is shown in Fig. 3. Compared to stoichiometric mixtures of SiO_2, Si_3N_4, and SiC, these materials are carbon rich resulting in an interspersed network of what is conventionally called “free carbon”.

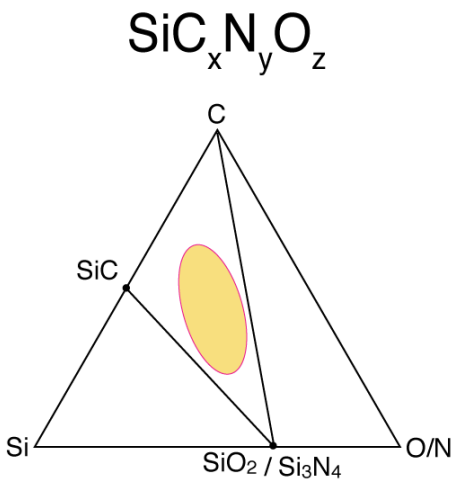

Fig. 3. Composition diagram of SiCNO ceramics [41]

PDCs are formed by controlled pyrolysis of specialized nitrogen and/or oxygen containing polymers known as polysilazanes and polysiloxanes, respectively. The polymers are prepared by thermal treatment of liquid precursors to 200-400°C where they cross-link to form a hard epoxy. Upon further heating above ~600°C, they begin to lose hydrogen and self-assemble into a pseudo-amorphous ceramic phase consisting of Si-N-O domains separated by “free carbon” in the form of disordered graphene sheets.

Small angle x-ray scattering (SAXS) reveals the domain sizes to be in the range 1-5 nm [42]. The carbon structure of PDCs, as revealed by Raman spectroscopy, show the characteristic “G” and “D” peaks of disordered sp^2 bonded carbon. This nanodomain structure is found to be thermodynamically stable, unlike traditional glasses, and has been shown to resist crystallization, creep, corrosion, and oxidation at ultra-high temperatures. [24, 40, 43-45]

It is noteworthy that the PDC nanostructure can *only* be achieved via the polymer processing route. For example, SiCO, comprised of amorphous SiO_2 domains and graphene, cannot be made by incorporating carbon in SiO_2 directly due to the lack of carbon solubility in SiO_2. It is only by the decomposition and self-assembly of these specialized polymers that the resulting nanostructure can be achieved. Since the ceramic product maintains “memory” of the polymer state in this way, the remaining nanosctructured composite offers a unique combination of properties akin to polymers and ceramics alike.

One of the primary focuses of this thesis work is to use SiCN as a bonding medium between HfO_2 and SiC. However, a number of studies in the last decade have shown PDC materials to be promising candidates for environmental barrier coatings themselves [46-47]. For static or low-streaming environments below 1500°C, SiCN and SiCO materials oxidize to form a passive layer of protective SiO_2. However, several environmental conditions prevent an SiO_2 layer from being sufficient, Table 1, where the passive layer is actively recessed thereby removing its protective ability.

It is in these recessive conditions where PDCs offer a unique alternative to traditional high temperature Si-based materials. Unlike SiC or Si_3N_4, PDCs can be readily doped with elements offering superior passive oxide layers. For example, SiAlCN has been shown to offer much higher oxidation protection than pure SiCN due to the passive

formation of Al_2O_3 in the oxide layer [48]. This effect is amplified in harsh environments where the SiO_2 is being actively recessed. As the SiO_2 is removed, the stable oxide phase (e.g. Al_2O_3, ZrO_2, HfO_2) remains behind, building a protective layer against further recession.

1.4.3 Methods of Protection for CMCs

The basic CMC design consists of single fibers (~10 μm) clustered together into fiber bundles (~1 mm) which are then woven together into a ceramic textile. The ceramic fiber weave is infiltrated further with more ceramic material known as the "matrix" material. The fibers offer the main structural benefit and the ceramic matrix ties them together into a rigid body, similar in fashion to the commonly known carbon fiber composites consisting of woven carbon fiber bundles in a polymer matrix. The composite CMC structure offers multiple approaches for protection.

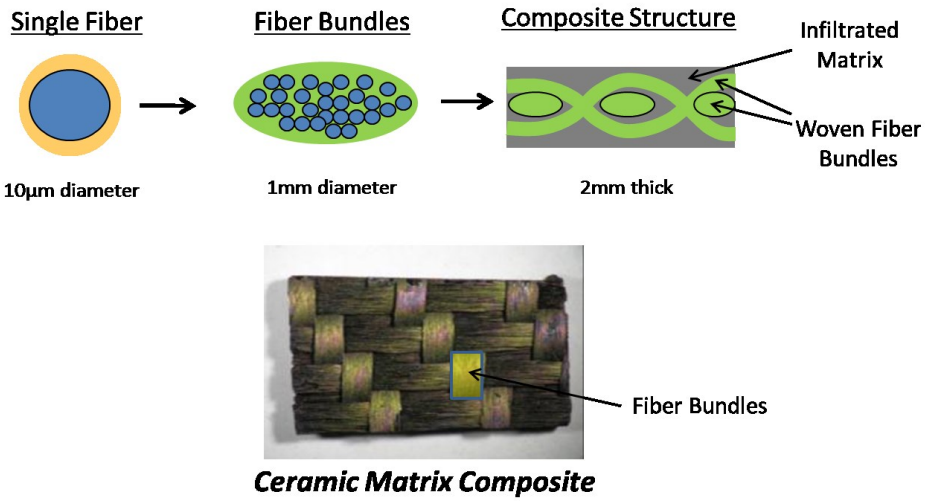

Fig. 4. SiC ceramic matrix composite structure and various pathways to protection

Fig. 4 shows some of the different approaches one might use to protect CMCs from environmental degradation. One option is to deposit protective films over the CMC itself or individual constituents thereof. This could be achieved at any level of the CMC architecture by applying conformal protective films (e.g., coating each ceramic fiber as shown in Fig. 4). A second option would be to infiltrate a protective layer around (or within) each ceramic fiber bundle. A third option is to infiltrate the whole textile with a protective matrix. Each option offers a unique level of CMC protection. All options would require that the protective medium offer good mechanical/thermal properties as the protective material would become an integral part of the CMC structural unit. It is also possible that UHT applications of CMCs, like hypersonic aircraft or gas turbine rotors, would use a combination of the various protection pathways with each level serving a unique functional purpose.

1.4.4 Goal of this Thesis

The goal of this thesis work is to understand the scientific underpinnings of using SiCN-HfO_2 based systems as a protective EBC for silicon carbide based composite structures. Results presented are for oxidation in air and streaming water vapor at 1500°C or 1600°C. This effort has been broken into three main themes, each presented here as a separate chapter, which could be used at the different levels of CMC protection.

(i) **Multilayer films –** This design uses a multilayered structure consisting of a UHT transition metal oxide, HfO_2, as the outer environmental barrier layer. Polymer-derived SiCN is used as a high-temperature bonding medium between the HfO_2 and the underlying SiC structural material. This multilayer

composite design has been shown as an effective EBC for similar refractory ceramic structural materials. The thin conformal nature of the films enables versatile designs for different levels of CMC protection.

(ii) **Polymer derived HfSiCNO –** Polymer-derived materials, like the SiCN bond layer mentioned above, have also been shown to be effective EBCs by themselves. This section details the doping of an SiCN precursor with Hf-O, to create an amorphous HfSiCNO material directly from the polymer route. Since it is processed as a liquid polymer, material systems of this kind have the potential for many CMC uses, ranging from the development of new fiber chemistries to new ceramic matrix materials. Processing, chemistry, structure, and high-temperature behavior of the polymer-derived HfSiCNO are given up to 1600°C.

(iii) **Composite SiCN-HfO_2 infiltration –** The section explores infiltrating CMC "preforms" using a composite material consisting of HfO_2 particles in a polymer-derived SiCN matrix. The ceramic matrix is fabricated from the liquid polymer route enabling the infiltration of complex net shape CMC structures such as gas turbine blades.

The scope of this thesis covers processing development, material characterization, and oxidation behavior of these three SiCN-HfO_2 based systems at temperatures up to 1600°C.

2 Multilayer HfO_2-SiCN Films on SiC

2.1 Introduction

This chapter explores the oxidation behavior of thin films consisting of polymer-derived ceramic (PDC) and hafnium oxide (HfO_2) based compounds. Films were deposited onto single crystal silicon carbide (SiC) and oxidized at 1500°C-1600°C in air. Multilayered structures consisting of PDC and HfO_2 were prepared as well as single layers consisting of Hf-doped PDC. Oxidation scale thicknesses, phase evolution, and morphology are compared to that of pure SiC.

2.2 Film Processing and Preliminary Results

Two types of films were deposited on SiC substrates using a pulsed-precursor metalorganic chemical vapor deposition (PP-MOCVD) system. A schematic of the two film architectures are shown in Fig. 5.

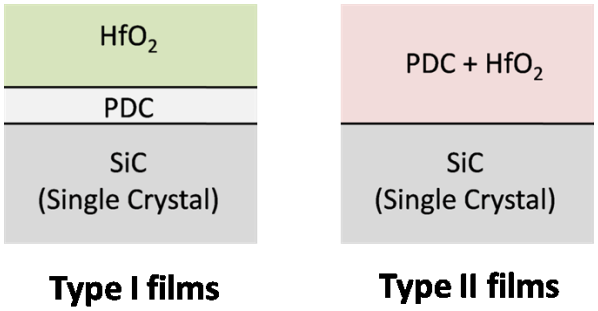

Fig. 5. The two types of films structures considered

Type I Films **-** These films are a multilayer composite structure. The outermost environmental barrier layer is HfO_2, and the substrate was single crystal silicon carbide. The intermediate bond layer between the SiC and HfO_2 is polymer-derived SiCN.

Type II Films – This film was one homogenous layer of polymer derived ceramic deposited onto single crystal silicon carbide. The polymer-derived layer was doped with Hf giving a final ceramic state of $Hf_vSi_wC_xN_yO_z$. In this case, pre-ceramic precursors for SiCN and HfO_2 were mixed in the liquid state and deposited simultaneously to yield one single amorphous ceramic layer.

The films were deposited using a combination of PP-MOCVD and spray pyrolysis techniques. PP-MOCVD involves pulsing a liquid solution into a vacuum chamber where it flashes into chemical vapor [49]. The solution typically consists of a small weight fraction metalorganic precursor dissolved into a high vapor pressure solvent. The metalorganic vapor arrives at a heated substrate surface, adsorbs, and then decomposes into a desired ceramic product. The spray pyrolysis technique involves directly spraying the ceramic precursor onto a substrate in the liquid state. The liquid precursor then undergoes pyrolytic treatment to form the desired polymer or ceramic compound. A process diagram of each deposition method is shown in Fig 6.

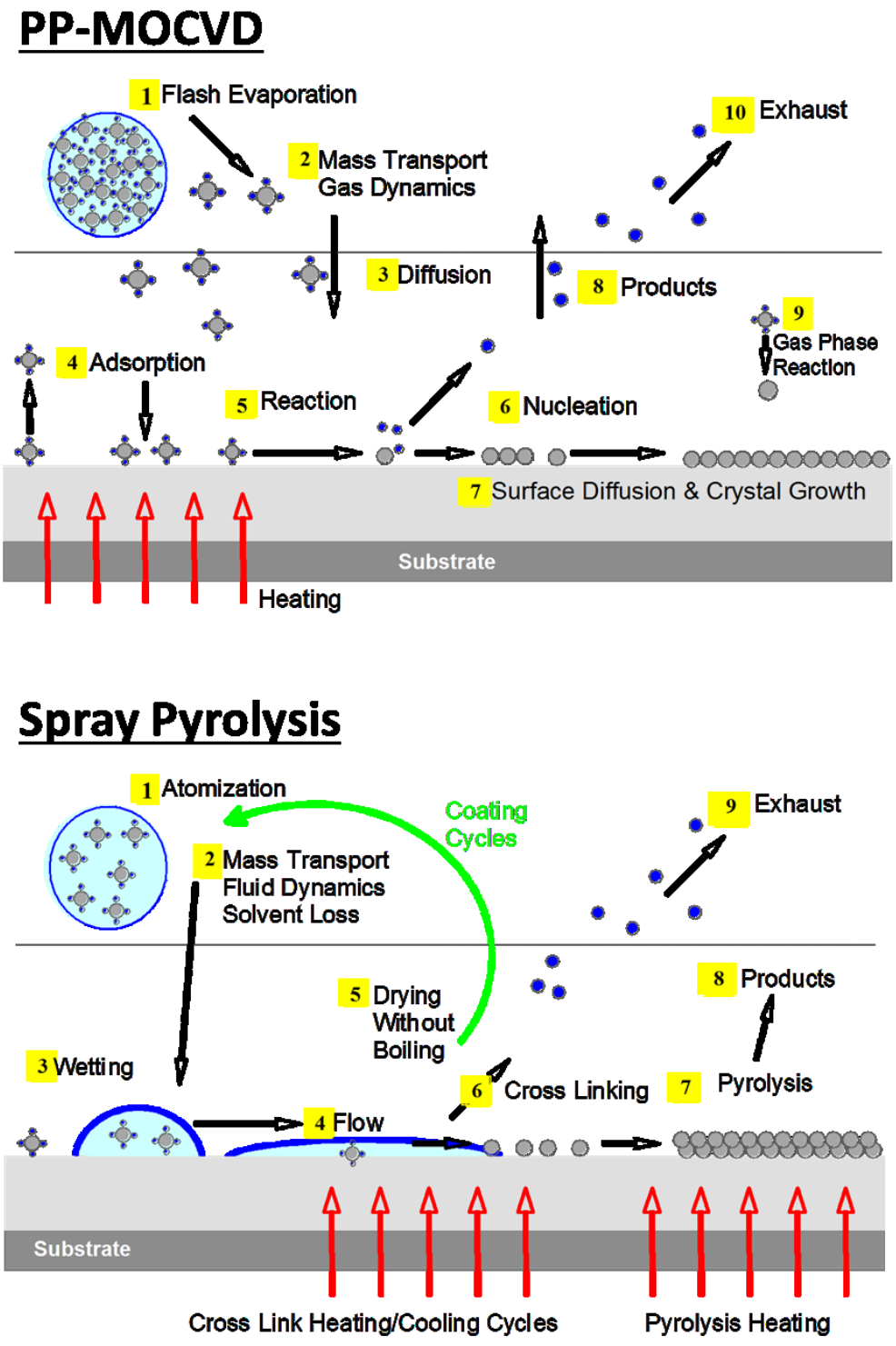

Fig. 6. Process diagrams for film deposition by PP-MOCVD (upper) and spray pyrolysis (lower)
(Image from Susan Krumdieck, University of Canterbury, New Zealand)

2.2.1 Type I Films: HfO_2-SiCN Multilayers

Type I multilayer films of SiCN and HfO_2 were sequentially deposited onto SiC. The deposition system and process technique have been described in literature for analogous SiCN-ZrO_2 films [35]. This process was adapted to SiCN-HfO_2 by using Hf *tert*-butoxide as the metal oxide source instead of Zr-isopropoxide as published [50]. Films were deposited with target thicknesses of 1 μm for each layer.

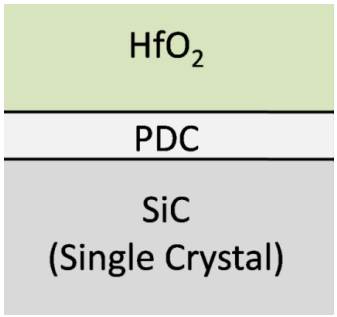

Fig. 7. Type I film architecture

The SiCN polymer derived ceramic bond coat was deposited by spray pyrolysis. Liquid silazane Ceraset® (Kion Defense Technologies), the precursor for SiCN, was dissolved at 2% wt. in thetrahydrofuran (THF). The solution was pulsed onto a warm SiC substrate held at 180°C. Each pulse was 0.39 mL in volume, and 15 pulses were delivered to obtain a ~1 micron SiCN film after pyrolysis at 1000°C.

The HfO_2 top layer was deposited in vapor phase using hafnium tert-butoxide, an Hf-based metalorganic ($Hf[OC_4H_9]_4$) [51]. The butoxide was dispersed in THF to 5% wt. and pulsed into a vacuum chamber containing the SiC substrate. The solution is passed into the chamber through an ultra-sonic nozzle (Sono-tek Corp.) which nebulizes the flow into micron sized droplets. The nebulized mist flash vaporizes upon

entering the chamber due to the high surface area to volume ratio of the droplets. The vaporized Hf alkoxide arrives at the substrate surface (held at 550°C), adsorbs, and decomposes into HfO_2. A total of 50 pulses, at 0.39 mL per pulse, were used to deposit ~1 μm HfO_2 film.

The films were oxidized in air at 1600°C in a $MoSi_2$ element box furnace (Del-Tec). Samples were sectioned for scanning electron microscope (SEM) imaging and tunneling electron microscope (TEM) imaging, and x-ray diffraction patterns were taken to observe phase evolution after oxidation.

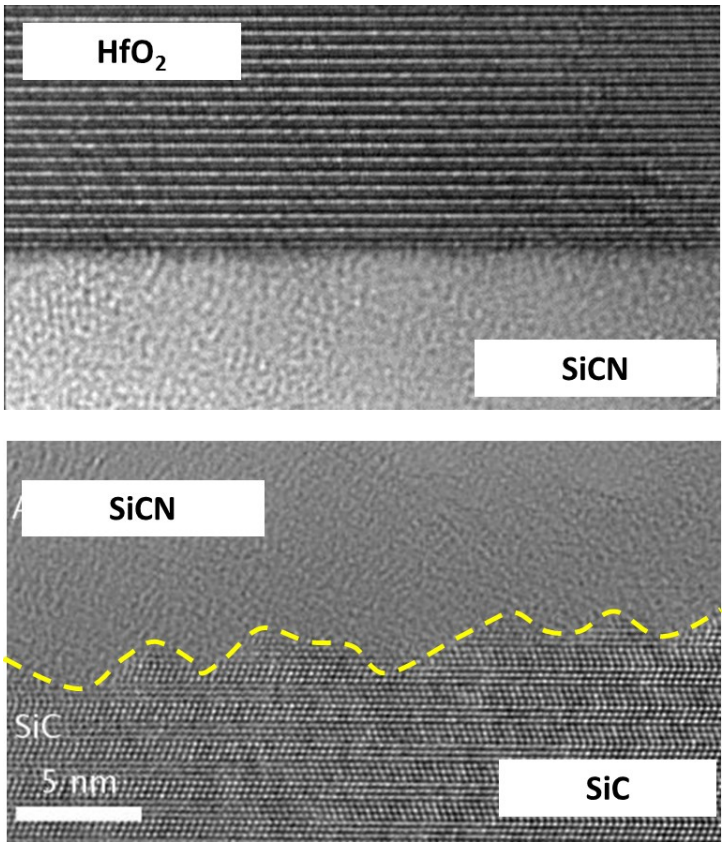

Fig. 8. High resolution TEM showing HfO_2-SiCN interface (top) and SiC-SiCN interface (bottom). *(Images from Aidan Taylor, University of Leoben, Austria)*

High resolution tunneling electron microscope (HR-TEM) images were acquired for the multilayers of HfO_2-SiCN coated on single crystal SiC, shown in Fig. 8. The upper image shows the SiCN interface with HfO_2, and the lower image shows the interface of the SiC substrate and SiCN. Note the difference in morphology between the two interfaces. The HfO_2 forms a flat interface, and there is no apparent change in crystal structure within one or two monolayers from the interface. The SiC is in the form of single crystal and nominally shows an atomically smooth surface. However, the SiC surface develops an undulating interface, with peak-valley spacing of ~5nm, when coated with SiCN. One possibility is that the SiC interface is growing by pulling Si and C content from the SiCN. The Ceraset precursor has been shown to grow Si_3N_4 and SiC upon pyrolysis when in the presence of seed crystals [52]. Another possibility is that SiC from the crystal surface is being drawn into amorphous solution with the SiCN. In either case, these TEM images confirm SiCN as being an extremely good bonding medium between both HfO_2 and SiC materials.

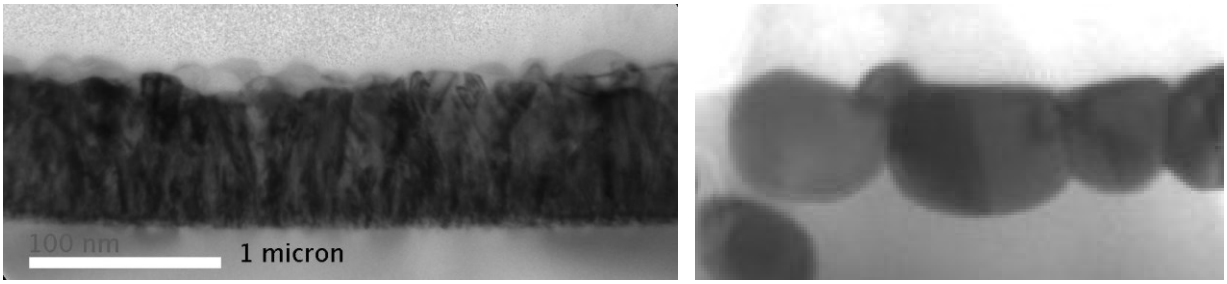

Fig. 9. TEM of HfO_2 film showing columnar growth (left) and beading after oxidation (right) *(Images from Aidan Taylor, University of Leoben, Austria)*

Fig. 9 shows TEM images of the HfO_2 top layer before and after oxidation. The as-deposited HfO_2 is ~900 nm thick and appears to have columnar growth structure before oxidation (left image). After oxidation for 1 hr at 1600°C (right image), the layer coarsens into spherical grains on the order of 0.5-1.0 μm in diameter. The TEM results

suggest the Hf-based particles are HfO_2 or $HfSiO_4$ crystals. The layer beneath the HfO_2 remained amorphous, though it was never determined if this sub layer was the deposited SiCN or was amorphous SiO_2.

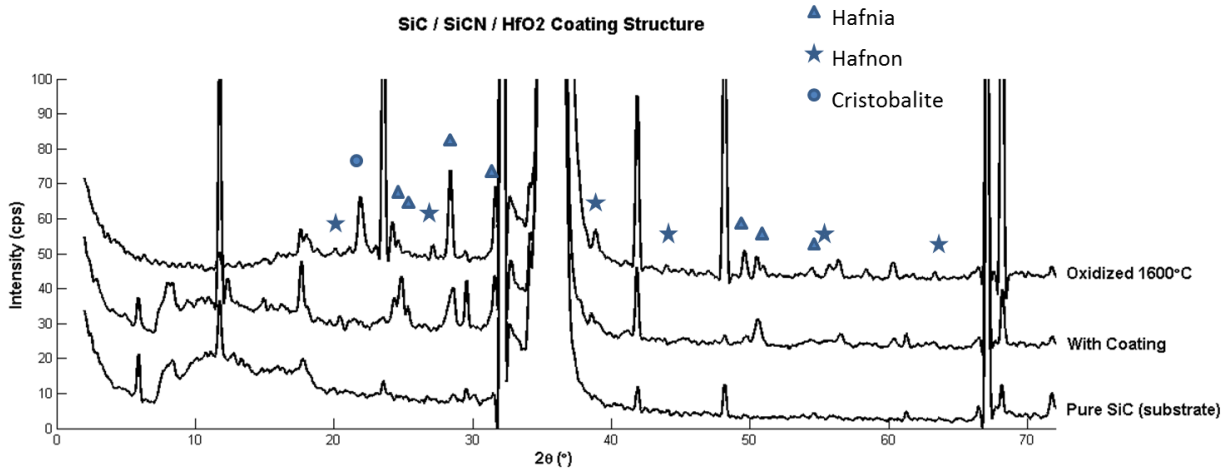

Fig. 10. X-ray diffraction patterns of Type I coating before and after oxidation at 1600°C

The Type I films were observed with x-ray diffraction before and after oxidation for 1 hour at 1600°C in air. This is shown in Fig. 10 along with the diffraction pattern of an uncoated SiC substrate for reference. These results are difficult to interpret since the thin films yield small diffraction peaks compared to those of the single crystal substrate and since there may be significant amorphous content. Crystalline hafnia is observed after deposition and the primary peaks for *m*-HfO_2 (28.36° and 31.64° [53]) become narrower and more intense after oxidation, suggesting the HfO_2 top layer is partially amorphous and/or nano-crystalline after deposition at 550°C [54]. Cristobalite (SiO_2) and hafnon ($HfSiO_4$) peaks emerge after oxidation. The formation of SiO_2 suggests the SiCN bond layer is oxidizing, which then reacts with the HfO_2 top layer to form $HfSiO_4$ [55]. Significant presence of HfO_2 suggests that only a small amount of the HfO_2 is reacting to form $HfSiO_4$.

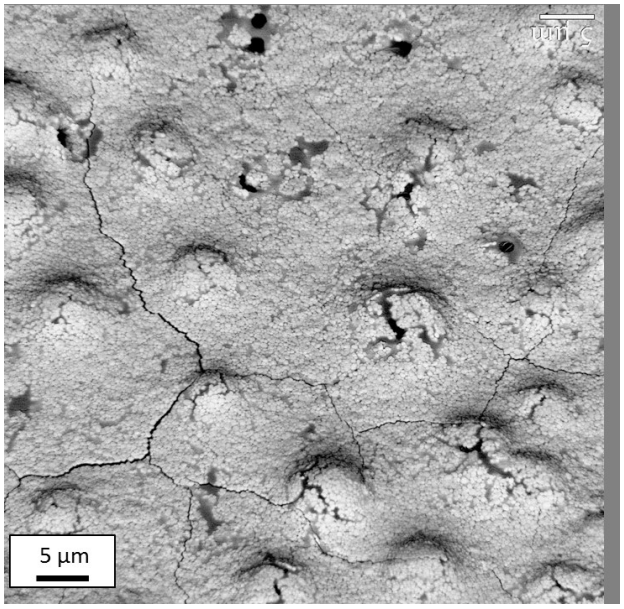

Fig. 11. SEM surface micrograph after oxidation at 1600°C for 1 hour
(Image from Dave Marshall, Teledyne Scientific Company, Thousand Oaks, CA)

Surface profiles and through thickness cross-sections were observed by SEM. The image of Fig 11 shows a top view (~45° angle of incidence) of the film surface after oxidation. The image reveals a hafnia layer consisting of micron sized spherical grains. (Hafnium has high atomic weight, 178 AMU, and therefore any Hf-based compounds appear brighter than the other materials.) Bubbles can be seen erupting through the hafnia overlayer. These were originally ascribed to possible defects in the deposited SiCN film but were subsequently understood to be carbon monoxide bubbles (CO), a gaseous byproduct from oxidizing the underlying SiCN and SiC. At longer exposure times the HfO_2 surface layer was observed to coarsen into HfO_2 and/or $HfSiO_4$ islands. Both images show evidence of cracking which is believed to occur upon cooling from the thermal expansion mismatch between SiO_2 and SiC.

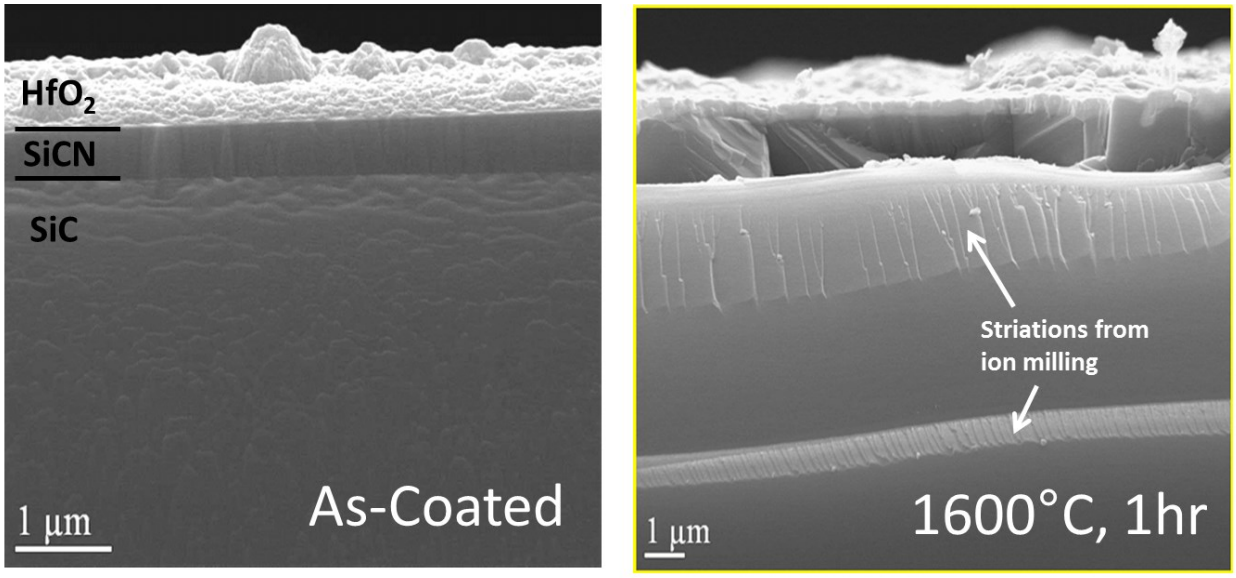

Fig. 12. Through thickness cross-sections of Type I films after deposition (left) and after oxidation for 1 hour at 1600°C (right). *(Image from Dave Marshall, Teledyne Scientific Co., Thousand Oaks, CA)*

The film cross-sections, Fig. 12, showed similar results for the hafnia top layer. The SiCN bond layer showed evidence of oxidation but were difficult to quantify because the presumed oxide layer and initial SiCN layer were of similar thickness. Inherent ambiguity in the SiCN thickness from the deposition process made this even more difficult. Furthermore, SiO_2 and SiCN also show similar SEM contrast and cannot be distinguished easily without a smooth section. These initial results drove the need for a thinner and more uniform SiCN bond layer to properly quantify oxidation.

2.2.2 Type II Films: Hf-doped SiCN and SiCO

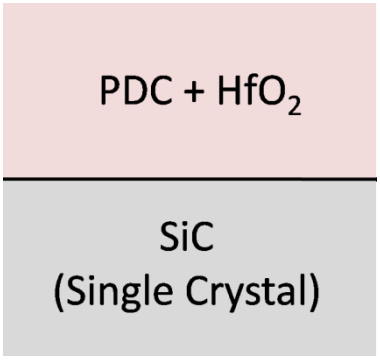

Fig. 13. Type II film architecture

The type II films were exploratory compounds of Hf-doped polymer-derived ceramics. Precursors for polymer-derived SiCO and SiCN were mixed with hafnium tert-butoxide, a common CVD and sol-gel precursor for HfO_2. The two liquid precursors were dispersed in solvent and deposited by spray pyrolysis. The deposition conditions were the same as outlined above for Type I bond layer of SiCN. The only difference being that these films included the Hf-alkoxide precursor along with the PDC precursor. The expectation was that spraying both precursors simultaneously using a single source solution would incorporate Hf into the polymer derived SiC(N or O) structure. Each solution consisted of 95% toluene and 2.5% PDC precursor (SiCO-H or SiCN-H) and 2.5% Hf *tert*-butoxide by weight.

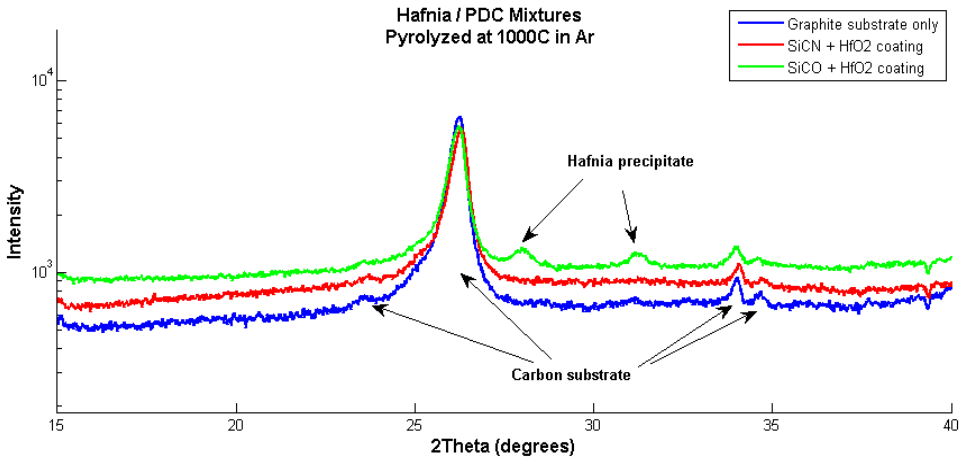

Fig. 14. Films of Hf-doped SiCN and SiCO on carbon substrates after pyrolysis

X-ray diffraction patterns of the Type II films are shown in Fig. 14 after pyrolysis at 1000°C in argon. The substrate used for these experiments was pliable carbon paper which was chosen since it would not react with the PDC materials during pyrolysis, and it was thin/porous enough to permit complete x-ray transmission. The Hf-doped SiCN sample was x-ray amorphous after pyrolysis, whereas the Hf-doped SiCO sample showed small peaks of monoclinic HfO_2. The broadness of the peaks suggests HfO_2 nano-crystals which is consistent with that observed in literature for a similar polymer derived SiCO-ZrO_2 system [56]. No carbide or nitride phases were observed in either sample.

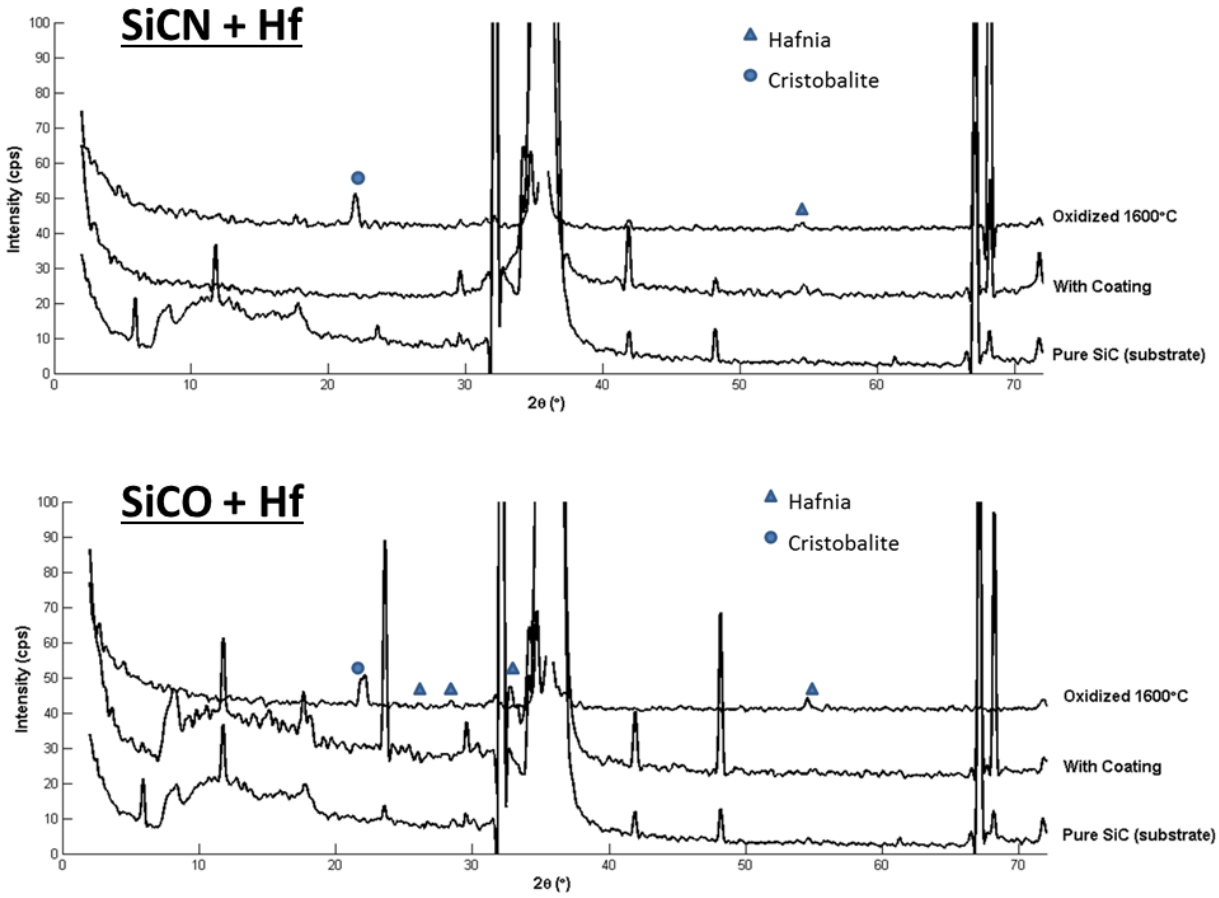

Fig. 15. X-ray diffraction spectra of Hf-doped PDC compounds: SiCN (top) and SiCO (bottom). Each data set shows the film before and after oxidation for 1 hour at 1600°C

Films composed of Hf-doped SiCO and SiCN were deposited on SiC substrates and oxidized at 1600°C in air. Their x-ray diffraction patterns, Fig. 15, show the formation of cristobalite and hafnia after oxidation. These spectra also show small diffraction peaks of *m*-HfO_2 in the pyrolyzed Hf-doped SiCO. An interesting feature of these diffraction patterns is the lack of substrate definition after oxidation. The x-ray penetration depth is expected to be on the order of 1-5 microns depending on Hf content and diffraction angle. Note that nearly all of the SiC peaks disappear in the air annealed samples. This is likely due to oxidation of the sub-surface SiC forming amorphous SiO_2 or critobalite. After oxidation, only structural features which lie above this layer are visible

by x-ray diffraction. Both Hf-doped materials show cristobalite formation after oxidation; however, it cannot be determined from XRD alone which layer the SiO_2 is coming from. Cristobalite can evolve from oxidizing the HfSiCO and HfSiCNO materials as well from oxidizing the SiC substrate.

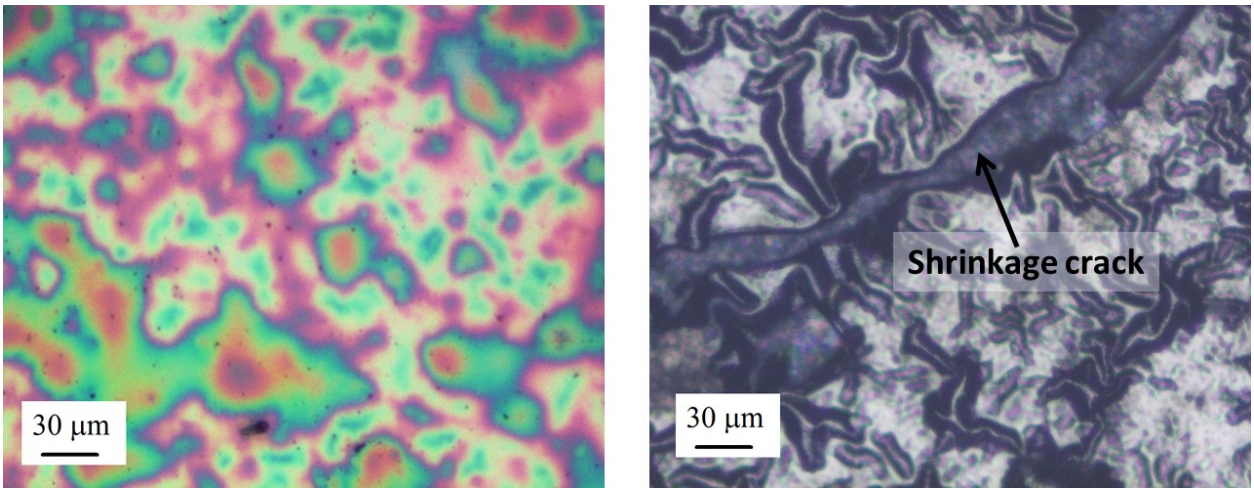

Fig. 16. Type II film as deposited (left) and after annealing at 1500°C in argon (right)

Attempts were made to anneal the films at high-temperature in inert environment prior to oxidation. The films were deposited on SiC by spray pyrolysis and annealed at 1500°C in argon. At 1500°C the films experienced a significant amount cracking from apparent volume shrinkage, shown in Fig. 16. Subsequent experiments show this to be from carbothermal reduction within the film itself. The HfSiCNO reduces to hafnium carbide (HfC) and silicon carbide (SiC) at temperatures greater than ~1450°C in low oxygen pressure.

2.3 Development of Hybrid PP-MOCVD System

The Type I and Type II thin film experiments demonstrated the need for further process development and understanding of both film types. The Type I films were difficult to characterize since the measured oxidation scale thicknesses were on the same order of magnitude as deposited film thickness. Furthermore, processing peculiarities made it difficult to obtain uniform SiCN layer using the existing PP-MOCVD system adapted for spray pyrolysis. This lead to the development of a new hybrid CVD system which could accommodate deposition of nanometer thin SiCN films with uniform coverage, as well as HfO_2 films via the existing PP-MOCVD method.

Type II films were also difficult to characterize for oxidation since both the SiC substrate and Si-based films oxidize in similar fashion. This pressed the need to understand the oxidation behavior of both the SiC substrate and HfSiCNO films independently. The film material of HfSiCNO were subsequently processed in bulk and characterized in the powder form. Powders offered a significant advantage in that they could be analyzed with a variety of techniques unsuitable for thin films. The processing, chemistry, and high-temperature behavior of HfSiCNO materials are detailed in Chapter 3.

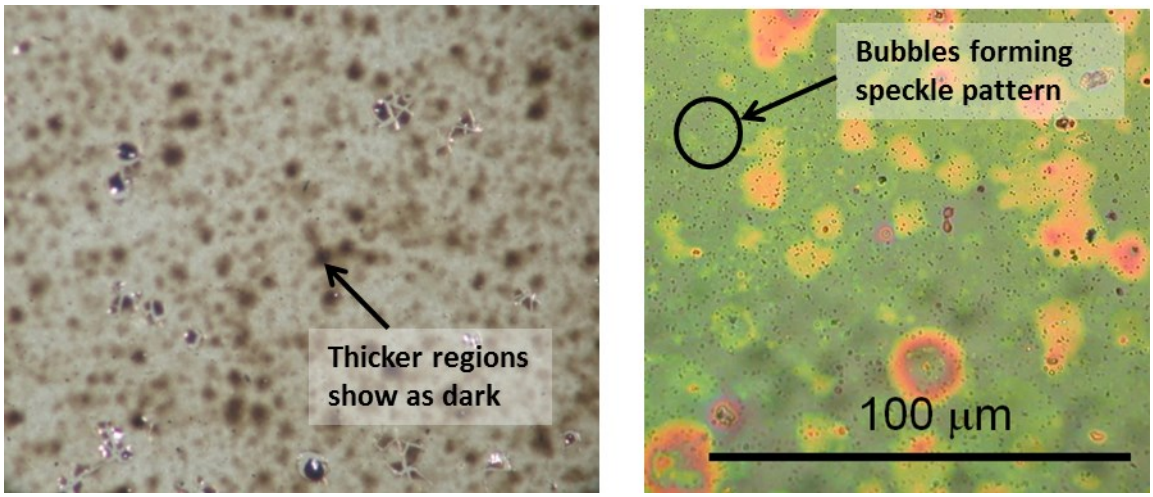

Fig. 17. Optical surface micrographs of SICN deposited on SiC by spray pyrolysis

One of the most significant problems with the spray pyrolysis setup was the lack of uniformity of the SiCN bonding layer. SiCN was deposited by spraying a solution of SiCN precursor and THF solvent on a heated SiC substrate. The liquid silazane solution wets the substrate poorly and retracts in pools, even under rapid cross-linking conditions. This pooling effect is shown in the left image of Fig. 17 where the dark regions represent a thicker film than the brighter areas. This is a somewhat surprising result as the solution has a relatively low surface tension of 26 mN/m^2 [57]. The high energy surface of the SiC crystal would seem to favor wetting by the solution. This behavior is likely due to a thin native oxide layer on the SiC substrate. Attempts were made to soak the substrate in hydrofluoric acid (HF) prior to deposition to etch any surface layer of any native SiO_2. However, the silazane showed the same wetting behavior of SiC before and after HF etching. The wetting could be enhanced for future experiments using some form of silazane coupling agent to increase the favorability of the SiC surface [58]. One further problem with the SiCN deposition was that spraying directly onto the hot substrate causes boiling of the solvent leaving micron or sub-

micron sized bubbles trapped in the polymer film. This is seen as a speckle-like pattern in the right image of Fig. 17.

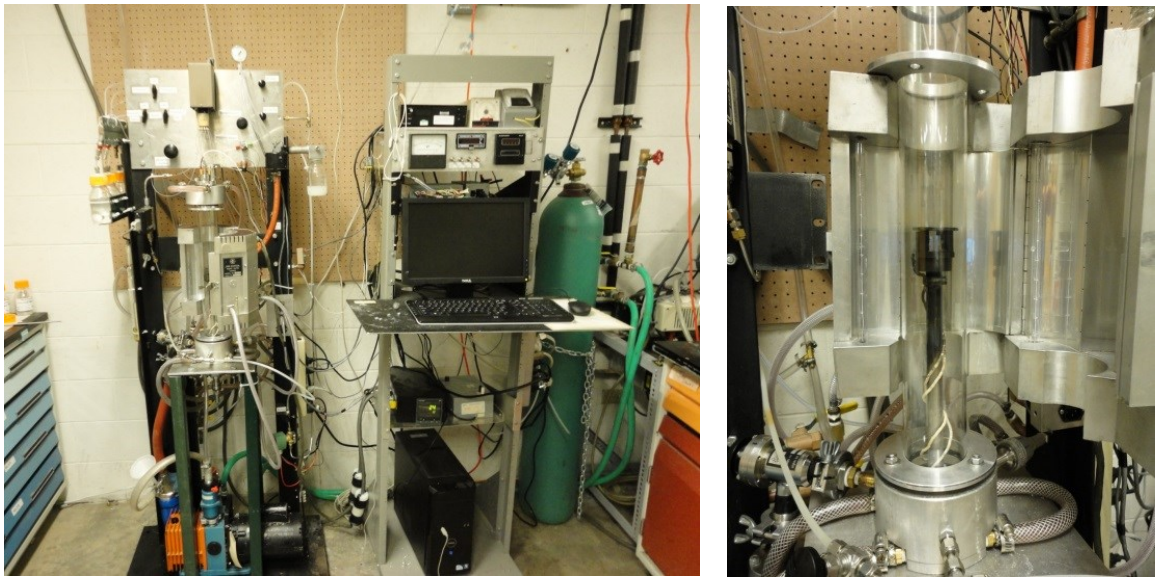

Fig. 18. Hybrid PP-MOCVD system

A new CVD system was built to permit a more controlled deposition of polymer-derived materials. Flexibility for deposition conditions were the chief design constraint. The machine was built to accommodate traditional vapor phase deposition as well as a variety of controlled spray pyrolysis conditions. A summary of the primary system variables are:

Radiant heating – allows for broad temperature control from 25°C – 900°C covering the range necessary for in-situ vapor deposition, polymer cross-linking, and ceramic pyrolysis. The radiant design also enables rapid heating and cooling cycles.

Mobile stage – the substrate has variable position within the hot zone column. This is mostly relevant for spray pyrolysis where the spray distance determines the surface flux

and droplet distribution. This parameter can also be tuned to control the degree of solvent remaining in the droplet upon arrival at the substrate surface.

Variable pressure – can be controlled using vacuum pump and digital argon leak valve.

Ultrasonic nozzle – nebulizes the precursor solution and permits flash vaporization for pulsed precursor MOCVD processes. The system can inject solution into the reaction chamber as a spray jet or as a nebulized mist.

Other variables which can be controlled are the volume and number of pulse injections, precursor concentration, deposition environment, and injection rates.

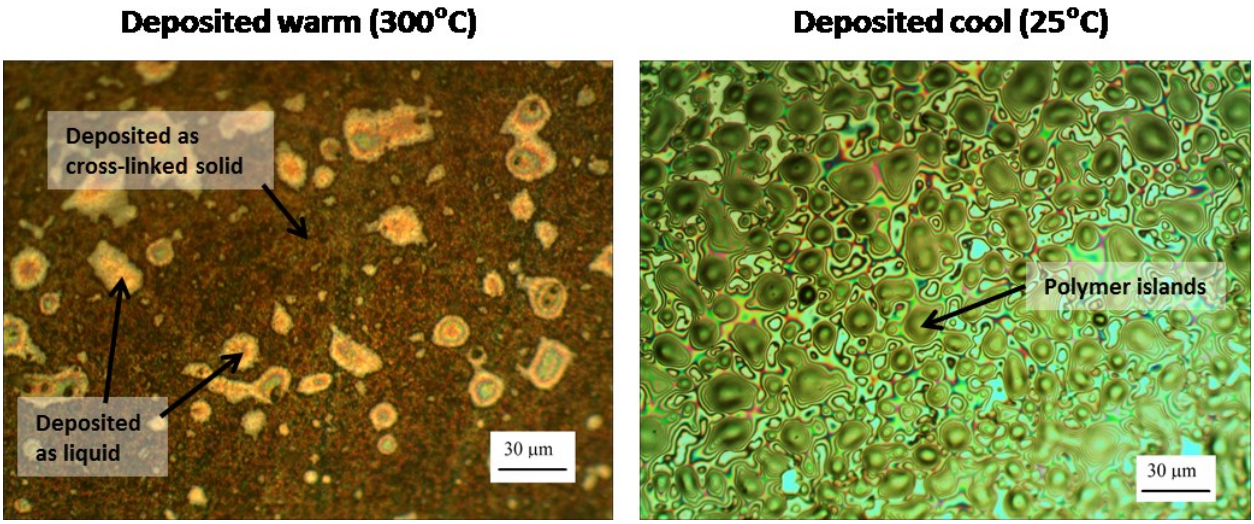

Fig. 19. Effects of substrate temperature on polymer deposition by spray pyrolysis

A number of deposition conditions were tried in an attempt to overcome the poor surface wetting of the SiC substrate. The two primary options were to deposit onto a warm substrate where the liquid precursor would cross-link immediately, or deposit onto a cool substrate and then raise the chamber to cross-linking temperature. Each technique showed fundamental problems. When deposited warm, much of the nebulized solution would polymerize before arriving at the substrate surface, shown in

Fig. 19 (left). Depositing on the cool substrate would result in islanding of the precursor due to a poor wettability, Fig. 19 (right). Neither scenario worked well when using the nebulized mist from the ultrasonic nozzle. However, without the nozzle the deposition was non-uniform as demonstrated with prior films.

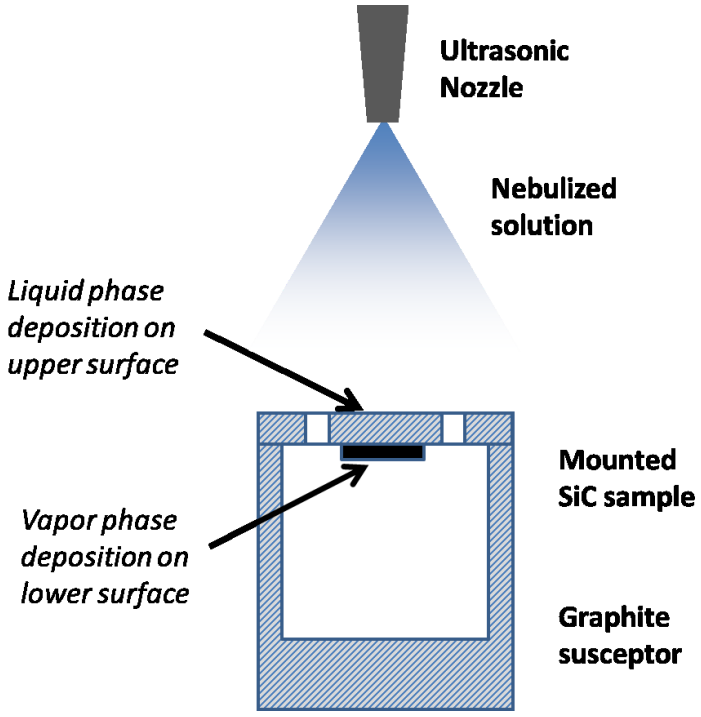

Fig. 20. Process schematic for vapor phase deposition of SiCN

A significant breakthrough was revealed when it was discovered that the Ceraset precursor could be deposited in the vapor phase, previously not thought possible. The Ceraset precursor has a relatively high molecular weight with a viscosity of 50-200 cps @ 25°C [59]. When the substrate was pre-heated to 300°C, the majority of the Ceraset precursor would cross-link prior to arriving at the surface. This technique proved nearly impossible to achieve dense SiCN films. However, optical micrographs showed the additional presence of an ultra-thin SiCN layer beneath the cross-linked particles. This thin layer was the result of vapor phase deposition of small weight silazane molecules.

The silazane has some polydispersity as purchased. The majority of the precursor volume (heavy molecules) will not vaporize, but a small fraction of the lowest weight molecules will vaporize. This can be seen by an early degree of boiling when the precursor is submitted to a vacuum. These small molecular weight silazanes were exploited by mounting the SiC substrate upside down in the reaction chamber as shown schematically in Fig. 20. In this way, only the vapor phase silazane arrives at the SiC surface. The Ceraset precursor was found to adsorb and cross-link on the SiC surface in the range 250-350°C.

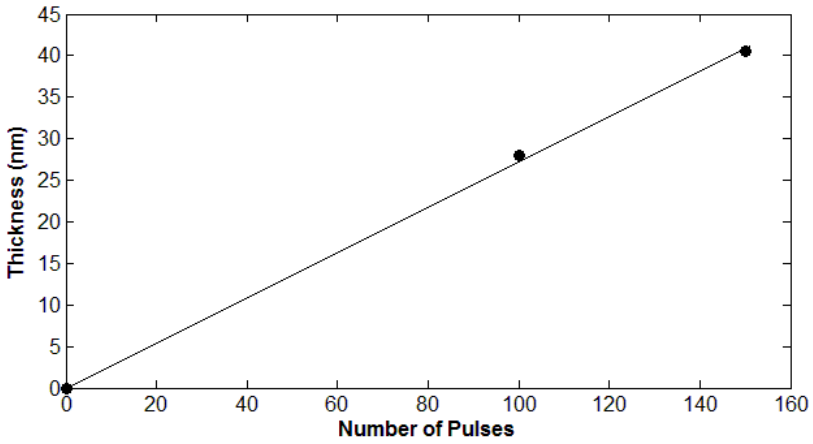

Fig. 21. Thickness of SiCN layer as a function of pulse number

SiCN films were deposited for analysis using the vapor phase technique. The reaction chamber was pre-saturated with 30 pulses of pure THF solvent at ambient pressure. Raising the THF vapor pressure to saturation and depositing at atmospheric pressure were both used to prevent the solvent from flash vaporizing when injected as a nebulized precursor solution. Solvent content in the nebulized droplets allows the low weight silazane molecules to escape before the droplets thermally cross-link. A dilute solution of 1% Ceraset in THF was found to result in essentially 1 monolayer of polymer per pulse. Deposition conditions were 66 μL per pulse with the substrate at held at 300°C in argon at ambient pressure. The film thickness after pyrolysis at 1000°C was

quantified using x-ray reflectivity (XRR) technique [60]. The XRR results for film thickness vs precursor pulses are shown in Fig. 21. The film chemistry, necessary for XRR analysis, were taken from bulk powder data and assumed to be $Si_{0.35}C_{0.29}N_{0.32}O_{0.03}$.

2.4 Oxidation of monolithic SiCN/HfO_2 multilayers

Type I multilayer films were deposited by vapor phase for both SiCN and HfO_2 layers. These films were deposited in 4 successive cycles of SiCN and HfO_2 on a SiC substrate. The underlying idea for this layered deposition is that it would create multiple SiCN-HfO_2 interfaces. A previous study had shown the existence of ~5 nm boundary layer interface in HfO_2-SiCN nano-composites which is believed to be a strong diffusion barrier [61]. A schematic of this film structure and their SEM cross-section after deposition are shown in Fig. 22. One observation was that the SiCN layer was considerably thinner than the expected deposition target of 50 nm. The principal reason for this is unknown. It is possible that the SICN is reacting with HfO_2 during deposition, though no reactions were observable by XRD or Raman. It is also possible that SiCN-H nucleates less effectively on HfO_2. All CVD growth studies of SiCN were performed on SiC or Si single crystal substrates. However, some layering is clearly evident which suggests that SiCN can be nucleated on HfO_2, but the growth rate on HfO_2 was never quantified specifically. Similar behavior has been observed with nanometer scale films of polymer-derived SiCO and SiCN on certain metal substrates [62]. These films show a critical thickness, on the order of 10-100 nanometers depending on material systems, for there to be any SiC(N,O) films remaining after pyrolysis. If the thickness is below this critical value, the film reacts with the substrate during pyrolysis and is effectively consumed.

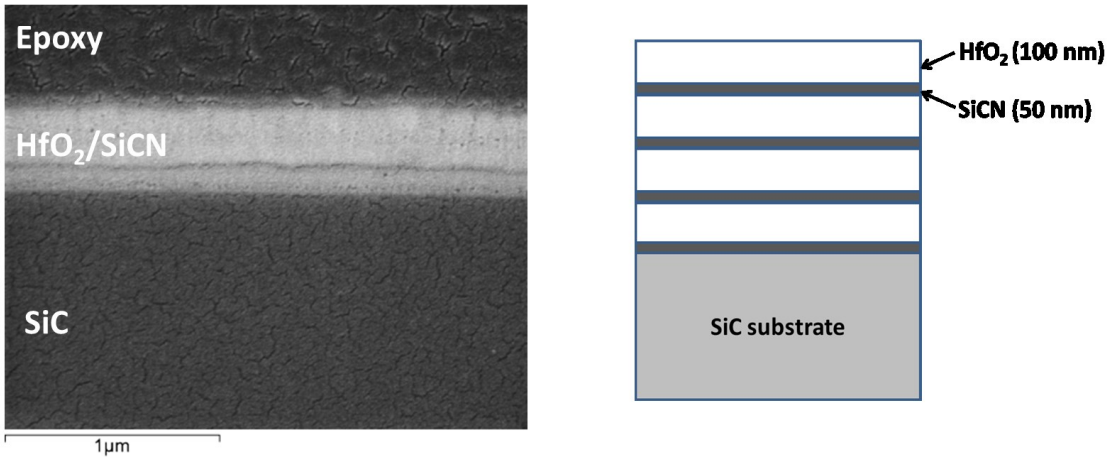

Fig. 22. Multilayer design to maximize SiCN-HfO_2 interfaces

The multilayer films were oxidized at 1500°C and 1600°C in a $MoSi_2$ element box furnace in ambient air. Fig. 23 shows example SEM cross-sections for 3 combinations of time and temperature. The left images are the coated surface of the SiC substrate and right are the uncoated surface. The epoxy shown at the top of every image is potting material used to permit quality ion milled sections.

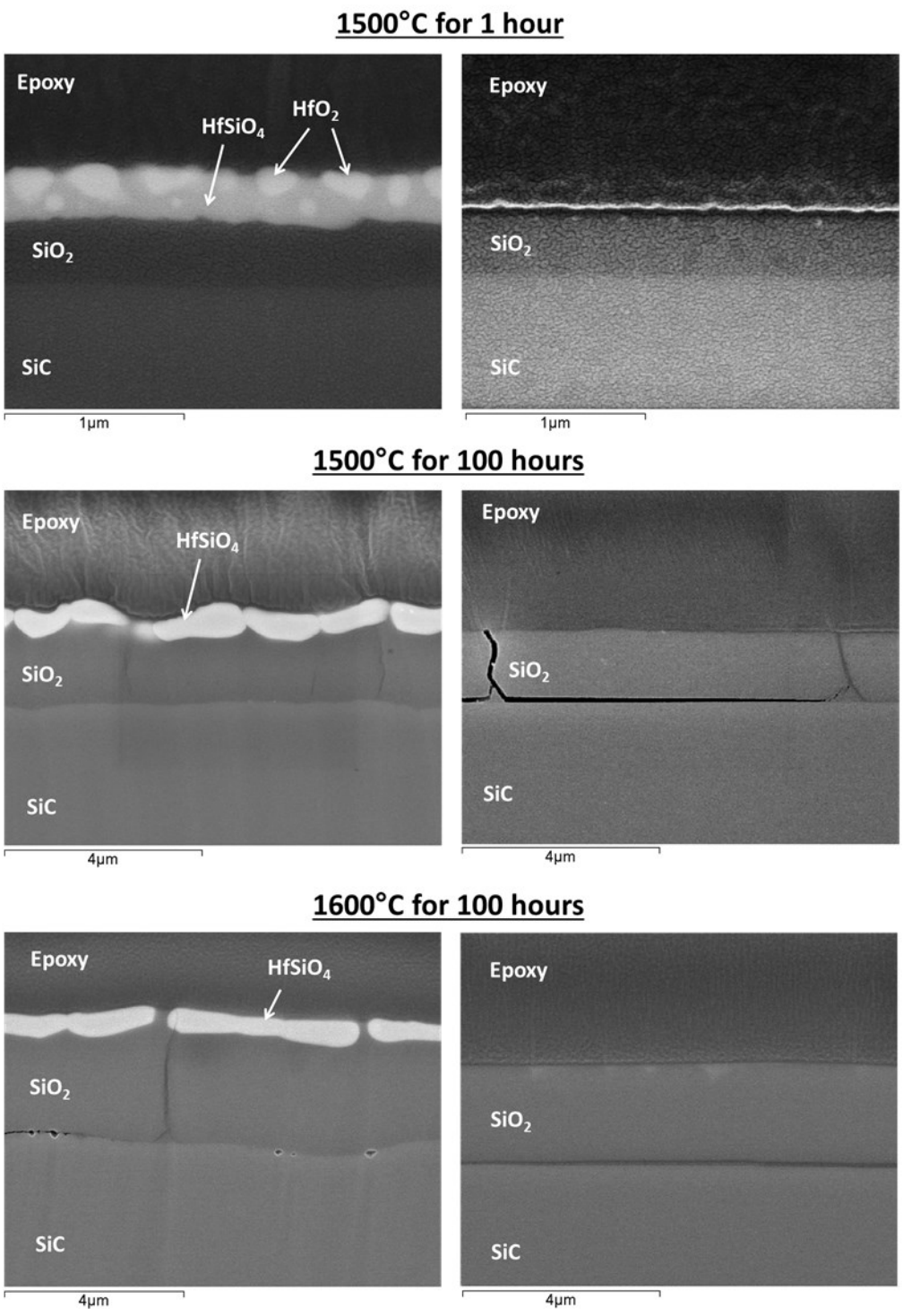

Fig. 23. Oxidation scale cross-sections; coated surface (left) and uncoated (right)

The coated case of 1500°C for 1 hour (top right) shows an interesting result regarding the HfO_2 + SiO_2 reaction. Approximately ½ of the initial HfO_2 content is shown to have reacted with freshly formed SiO_2 to result in $HfSiO_4$. At all extended times, the HfO_2 layer was completely reacted with silica to form hafnium silicate. Note that the initial deposition was a layered cake structure of SiCN and HfO_2. This architecture shortens the diffusion distance for $HfSiO_4$ formation since intermediate layers of SiCN would oxidize to SiO_2 prior to any substrate oxidation.

In all cases the oxidation scale thicknesses underneath the Hf-based film appear similar in magnitude to the uncoated SiC crystal. The oxidation in both cases shows quadratic rate dependency with time suggesting diffusion as the rate limiting mechanism. These similar oxidation rates suggest the inward oxygen diffusion through HfO_2 and $HfSiO_4$ is greater than or equal to the outward CO diffusion rate in SiO_2, otherwise the coated samples would show reduced rates. The oxidation of bare SiC and SiCN under these conditions is expected to be rate limited by CO through SiO_2.

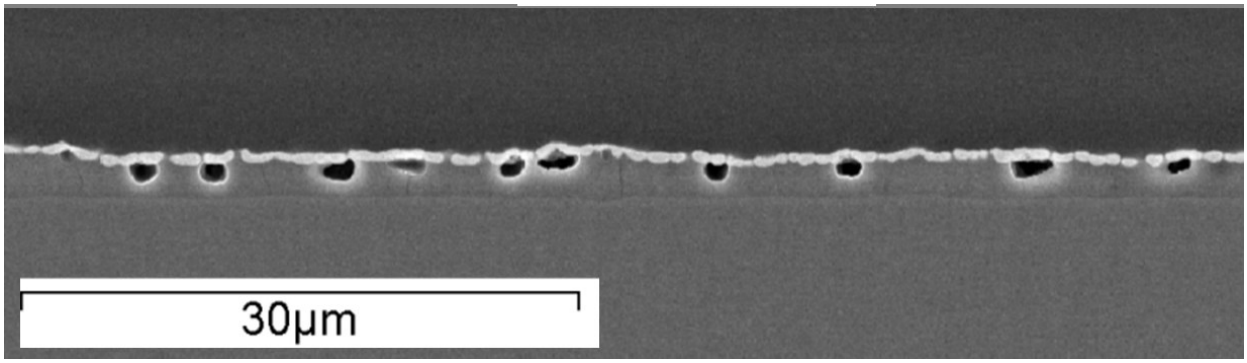

Fig. 24. Carbon monoxide bubbles trapped in oxide scale (1500°C, 100hrs)

An interesting observation with these coated samples is the capture of bubbles beneath the outer HfO_2/$HfSiO_4$ layer as shown in Fig. 24. These bubbles are credited to gaseous CO which forms from oxidizing SiCN and SiC. It is rare to see these bubbles

in the oxidation of uncoated SiC. The majority of sources in literature have not observed CO bubbling during the oxidation of SiC [63-66], though a few exceptions do exist [67]. Unexpectedly, the top HfO_2 layer prevents the bubbles from escaping and allows them to grow to large sizes on the order of a few microns readily observable by SEM. It is expected that these bubbles exist during SiC oxidation as well, but, since they can escape freely, their presence is missed by post-oxidation SEM imaging. (In a different experiment, bubbles were observed in the oxidation scale of pure SiC fibers bundles which are believe possible only due to a furnace power failure. The rapid quench of sample temperature froze the silica scale before the bubbles had opportunity to burst. Other experiments for SiC oxidation used a controlled thermal ramp down and CO bubbles were not observed.)

Careful inspection shows that these bubbles nucleate at the SiO_2-SiC interface and rise through the silica overgrowth, ultimately becoming trapped by the $HfSiO_4$ layer, as shown in Fig. 25. The existence of these bubbles at the interface also confirms the outward diffusion of CO as the apparent rate limiting mechanism for oxidation. The buildup of CO pressure (in solution at the interface) eventually overcomes the nucleation barrier and CO bubbles form. If CO diffusion was not rate limiting, then it would be expected to simply diffuse through the passive silica scale.

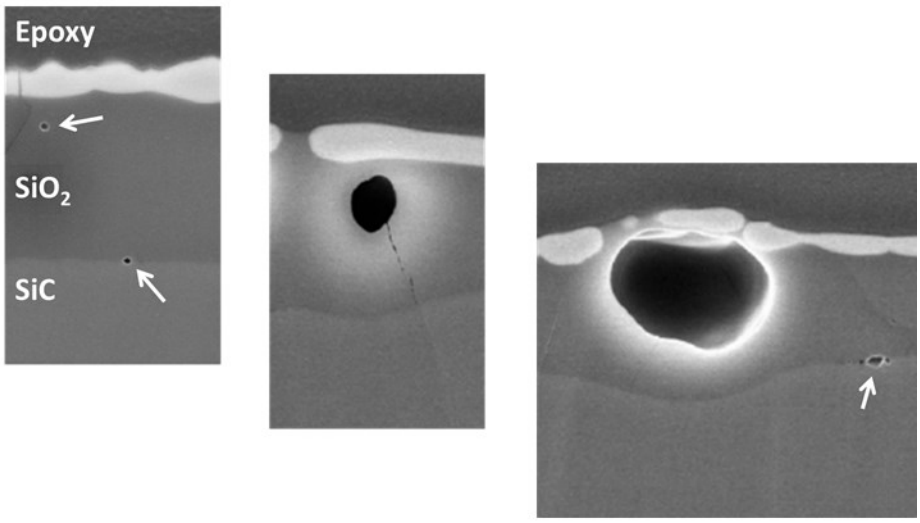

Fig. 25. Carbon monoxide bubble evolution during oxidation

In the initial stages of oxidation where the SiCN is oxidizing to SiO_2, it is at least possible that some of the bubbles are from N_2 or at least contain N_2 in addition to CO. The formation of N_2 bubbles would depend on the diffusion rate of nitrogen though SiO_2 which was neither quantified nor found in literature. However, it is fairly certain that after the SiCN layer oxides all subsequent bubbles are CO based. Evidence for this is can be seen at the SiC-SiO_2 interface which shows freshly nucleated bubbles in the absence of any nitrogen content.

Note the eroded area beneath the interface CO bubbles. This was a consistent observation and is attributed to the active decomposition of SiC into silicon monoxide (SiO) and CO. This type of active oxidation can only occur when a fresh surface of SiC is exposed at the testing temperature. Experimentally this is rarely observed because the SiC always forms a passive oxide layer during thermal ramping. Therefore, this kind of active oxidation is only seen when a bubble has nucleated at the SiO_2-SiC interface, exposing a fresh SiC surface. In this experimental case, active oxidation would occur only by volatilizing the outer silica scale by the reaction $2SiO_2$ to $2SiO + O_2$. It may be

possible to confirm this active SiC oxidation by heating to 1600°C in inert atmosphere and then switching to oxygen atmosphere after reaching temperature.

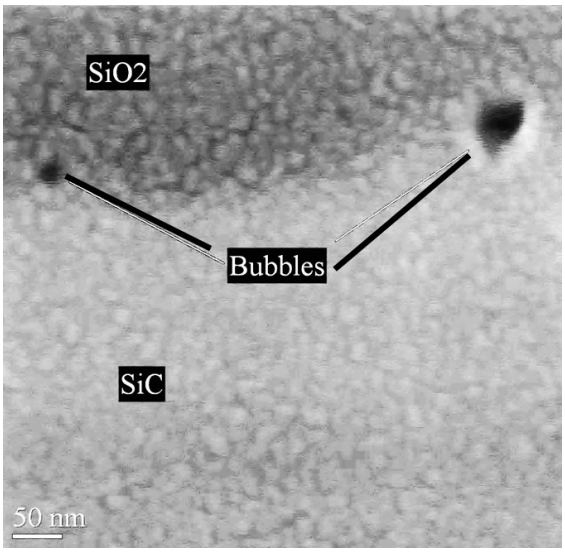

Fig. 26. Nucleation of CO at the SiO_2/SiC interface. The minimum CO bubble size observed at the interface is ~20 nm

The smallest observed CO bubble by means of SEM was about 20 nm and is shown in Fig. 26. The 10-20 nm granular pattern which veils the image is from a thin sputtering of gold on the sample to prevent surface charging under the electron beam. The smallest observed bubble size is an important parameter as it defines the maximum limit for critical nucleation size. A greater nucleation barrier results in higher interfacial pressure of CO.

A final experiment with the Type I multilayer coatings were made to quantify whether or not the HfO_2 overlayer prevented active oxidation of SiO_2 to SiO. The degree of this active oxidation at 1600°C is unknown. Active SiO oxidation would occur at the exposed surface and would recess the SiO_2 layer. In a regime where both passive and active oxidation are present, one would expect the oxide growth to behave mostly

parabolic at low times and then plateau off as the oxide growth rate decays to equal to active oxidation rate [68-70]. The oxide thickness would achieve a constant steady state value once the passive scale growth rate is equal to the active volatilization rate. A small amount active oxidation would result in a thick steady state oxide scale, and a rapid oxidation would result in a thin scale. This concept is detailed in Ch.4 for streaming water vapor experiments where heavy amounts of active recession are present by the formation of volatile $Si(OH)_4$.

No steady state film thickness was experimentally observed at 1600°C in air. From this it can be concluded the active oxidation of SiO_2 is slight (if at all) which would require extremely long oxidation times to achieve a steady state scale thickness. An alternate approach to quantifying relative recession in low volatilizing conditions would be to have side-by-side measurements of coated vs uncoated SiC. Though the absolute values for active oxidation rates would remain unknown, the relative rates between coated and uncoated materials could be determined.

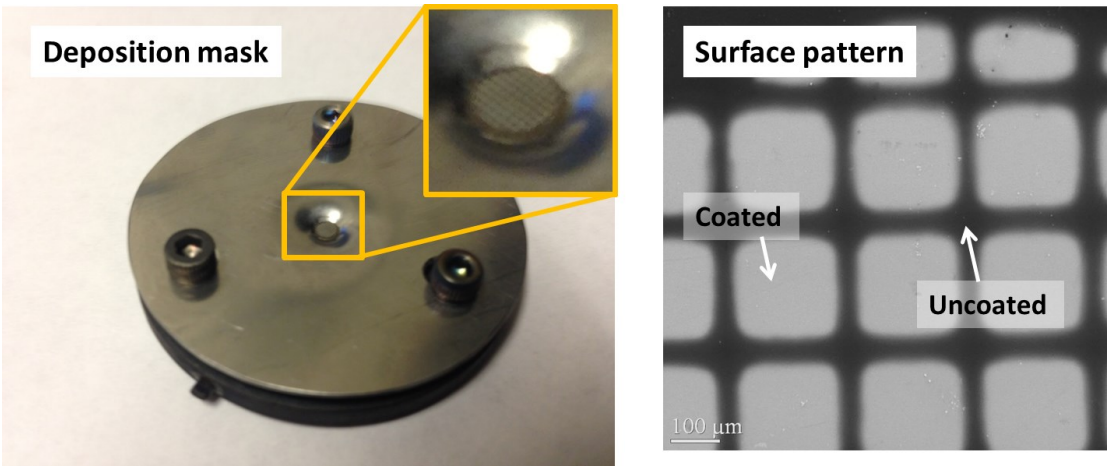

Fig. 27. Masked deposition of SiCN-HfO_2 on SiC

Samples were made to quantify relative SiO_2 recession by creating side-by-side surfaces of coated vs uncoated SiC. This would maintain a constant reference plane for both conditions. The samples were prepared by using a molybdenum TEM grid as a deposition mask for vapor deposited SiCN and HfO_2. The masking setup and resulting film pattern are shown in Fig. 27. No measurable difference of SiO_2 scale thickness was observed on the masked crystal regions after oxidation. It can be concluded from this that (I) there is no significant active oxidation of SiO_2 at 1600°C in air, or (II) if active oxidation is present, then the HfO_2 layer does not inhibit it.

2.5 Chapter summary and conclusions

The oxidation behavior of micron thick films of polymer-derived ceramic (SiCN and SiCO) and hafnium oxide (HfO_2) based system was measured. Two types of architectures were deposited and characterized for high-temperature oxidation behavior.

Type I films consisted of SiCN and HfO_2 monolithic layers deposited sequentially on SiC. Films were oxidized at 1600°C in air resulting in a coarsening of the HfO_2 top layer into spherical $Hf_{1-x}Si_xO_2$ crystals. High resolution TEM showed amorphous SiCN to act as an extremely effective bonding medium between SiC and HfO_2. However, non-uniformity of the SiCN bond layer resulted in ambiguous oxidation results. A new deposition system was designed to accommodate deposition of ultra-thin conformal SiCN films. New SiCN bond layers were deposited in the vapor phase by exploiting the polydispersity of the liquid Ceraset precursor.

Type II films included Hf content directly into the polymer-derived materials SiCO and SiCN by doping them with a hafnium alkoxide in the liquid precursor state. These films were shown to form cristobalite and hafnia after oxidation at 1600°C. Quantitative analysis of Type II film oxidation behavior was difficult due to the similarities between substrate and film oxidation products. Separate experiments were designed to characterize the Hf-doped material in bulk. This is the subject content of the following chapter.

Multilayer films of Type I design were deposited using sequential layers of SiCN and HfO_2. This design was created to maximize the number of layering interfaces as a possible means to prevent oxygen diffusion and coarsening of the outer HfO_2 layer upon oxidation. These films were oxidized for various times at 1500°C and 1600°C air and compared to the oxidation of SiC. Oxidation scale growths were found to be roughly equivalent for SiC and HfO_2-SiCN coated systems.

The formation of hafnium silicate, $HfSiO_4$, was an interesting result and could potentially be utilized for high temperature oxidizing conditions. Though it appears to diffuse oxygen, it is a much more stable phase than SiO_2 at temperatures below 1750°C [71] and, since it is crystalline, it would not flow like amorphous silica in streaming conditions. Thicker HfO_2 layers could be used in this manner as a SiO_2 chemical sink which would react silica into the more stable UHT phase of $HfSiO_4$.

The oxidation experiments also revealed a significant presence of CO bubbles which nucleate at the oxidation front and rise through the viscous SiO_2 scale becoming trapped below the $HfSiO_4$ layer. The bubbles confirm that oxidation of SiC and SiCN materials is likely rate controlled by CO diffusion through the SiO_2 oxide scale. These bubbles are a drawback to a system of this design since they damage the film upon bursting through the HfO_2 layer. However, if a structure could be engineered to allow

the release of CO bubble in a controlled fashion, the coating structure could show strong high temperature performance in streaming environments. The outermost layer $HfSiO_4$ is stable to 1750°C, and underlying SiO_2 acts as a strong diffusion barrier to oxidizing species [72-74].

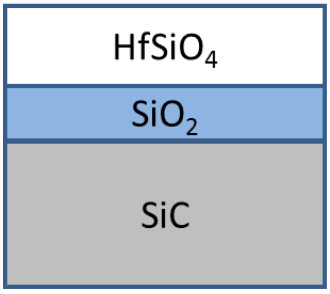

Layer	Benefit	Drawback
$HfSiO_4$	Crystalline and stable to 1750°C in air	Diffuses environmental oxygen and traps outgassing CO bubbles
SiO_2	Strong diffusion barrier	Recesses in streaming evironment from viscous flow and active oxidation
SiC	Excellent UHT mechanical and thermal properties	Oxidizes to form viscous SiO_2 and CO bubbles

Fig. 28. Multilayer structure after oxidation with tabulated summary of the positives and negatives for each layer

In summary, it is widely accepted that next generation UHT structures will be made from ceramic composite materials which can utilize the benefit of one material and mitigate the drawbacks of another. The multilayer film results presented here seem to reinforce this basic concept. Fig. 28 shows the resulting films structure after oxidation in air and gives a summary of the high temperature properties for each layer.

3 Polymer-Derived HfSiCNO

3.1 Introduction

This chapter details the processing and properties of an amorphous HfSiCNO material derived from the polymer route. A theoretical basis for doping SiCNO with transition metals, including Hf, is given from the standpoint of bond enthalpies. The processing, chemistry, and structure of these materials are traced during the liquid, polymer, and ceramics states. Ultra-high temperature properties of HfSiCNO are reported for inert and oxidizing environments.

3.2 Literature Review of Doped SiCNO

Substituting silicon by transition metals in polymer-derived ceramics (PDCs) holds the potential for a new class of polymer-derived ceramics for ultrahigh-temperature structural applications. It is postulated that Hf, like Si, forms mixed-bond tetrahedra with C, O, and N. The difference in the enthalpy of Hf-based and Si-centered tetrahedra is calculated using single-bond energies, reinforcing the feasibility of substituting Si with Hf or with Zr atoms. Such polymer-based HfSiCNO compounds made directly from liquid organics, by a simple manufacturing process, may also be relevant to nanoscale dielectrics with low leakage electric charge in microelectronics applications [75].

When considering the manipulation of ceramic chemistry PDCs offer several unique advantages over traditional materials. They can be derived from single source precursors which can be designed to have a variety of compositions. The final ceramic product is a direct reflection of the polymeric precursor chemistry and structure. The ability to create a broad variety of polymer precursors therefore allows for many amorphous ceramic combinations. PDCs also offer an advantage in that they are processed at relatively low temperatures when compared to similar UHT refractory ceramics. In addition to single source precursors, PDCs have been fabricated by mixing multiple precursors to selectively include impurities. Most works of this kind involve mixing a polysilazane or polysiloxane with some other liquid compound which includes a designed impurity. This method offers a simple route to incorporating various atypical elements into the PDC structure.

To date, only a small number of studies have been completed on altering polymer precursors for impurity design of PDCs. One of the most notable and well published deviations from traditional SiCO and SiCN chemistries is the introduction of boron [76-79]. SiCB(N,O) materials of this kind have shown many improved properties over SiC(N,O) including an thermal stability up to 2000°C [80]. A few studies have created PDCs with magnetic properties by introducing Fe. This has been done by pre-ceramic mixing as well as direct incorporation of Fe into the polymer backbone [81-83]. Doping with impurities has also shown potential for tunable luminescence bands. Zhang et al. introduced $Eu(NO_3)_3$ into the polymeric precursor for SiCO and were able to produce Eu^{3+} emission within the doped SiCO glass [84]. Other studies have shown the introduction of Al, Ti, Zr, and Hf can be used to enhance selected properties of SiC(N,O) PDCs [85-88].

Most existing research of metalorganics has been on sol-gels, pi-complex polymers, and macromolecules. The majority of these decompose readily at lower temperatures and are unsuitable for polymer derived ceramic structures. For example, Hf-O-C polymers decompose to HfC and HfO_2 at relatively low temperatures (600°C) some even exhibit this behavior as low as 250°C [89, 90]. Polymers with higher thermal stability have been made by means of modification of polycarbosilanes and siloxanes. Very little research to date has involved the chemical modification of silazanes with transition metals. (However, it worth mentioning that in many cases this low-temperature decomposition could be advantageous for the forming net shape binary carbides and oxides. These low-temperature polymers offer much processing flexibility with the major drawback being significant volume shrinkage during the polymer to ceramic conversion.)

Some of the earliest work on organic-inorganic polymer systems for ceramics was the modification of high purity SiC (Nicalon) fibers. Nicalon fibers are made by the controlled thermal pyrolysis of polycarbosilanes [91]. These carbosilane polymers consist of a silicon-carbon backbone typically with hydrogen or hydrocarbon side groups [92]. Upon pyrolysis in inert atmosphere, the side groups react with one another and volatilize to leave silicon and carbon in the form of ceramic SiC.

One of the earliest and most notable developments in the chemical modification of silicon based polymers was the synthesis of Si-Ti-C-O fibers, commonly known as Tyranno [93-95]. These Ti doped ceramic fibers were processed by chemically modifying a polycarbosilane precursor, used for SiC fibers [96], with Ti-alkoxide a popular sol-gel and CVD precursor for TiO_2 [97,98]. The fibers showed an increase in thermal stability with a modulus and UTS which was equal to or greater than the undoped SiC fibers [99]. Their max tensile strength was found to occur at 1300°C

compared to 1200°C for SiC, both of which are consistent with the onset of crystallization. This phenomenon was attributed to the bonding of excess carbon to titanium or an increase in overall bond strength of the fiber constituent elements by the inclusion of Ti. Two studies within the last decade regarding Ti modified polycarbosilanes showed both Ti-C and Ti-O bonds after pyrolysis at temperatures >1000°C. The lack of crystallization seems to suggest a similar PDC model where free-carbon is dispersed amongst amorphous nanodomains of M-(N,O). Raman spectra show D and G peaks of free sp^2 carbon these systems.

Studies by X-ray absorption near edge structure (XANES) and extended X-ray absorption fine structure (EXAFS) reveal unique behavior of the alkoxide modified polymers which is inconsistent with the thermal decomposition of alkoxides alone. XANES of Ti-modified siloxane shows a peak triplet indicative of octahedral coordination whereas tetrahedral coordination (as in the alkoxide precursor) shows a single peak [100]. However, the triplets observed in the modified polymer are also inconsistent with that of TiO_2. The experimenters speculate it is the result of a combination of triplets corresponding to various Ti coordination. Similar findings have been published for Zr modified polymers which show an x-ray absorption resemblance to 7 or 8 fold coordination without actually matching either of them. These materials were found to remain amorphous. The possible formation of Si-O-Ti bonds was also suggested after EXAFS analysis which showed an octahedral triplet resembling amorphous titania [101].

Beginning in the early nineties, this concept was extended to Al-O, Y-O and Zr-O modified SiC fibers employing the same polymer-alkoxide processing technique[101-109]. After modifying PCS with Zr alkoxide, NMR shows the formation of Si-O bonds

and a decrease in Si-H bonds after annealing at 300°C. The Zr-Si-C-O was mostly amorphous after pyrolysis at 1000°C with evidence of ZrO_2 precipitates.

Several studies for SiC(N,O) systems have shown mixed Si-(C,N,O) bonding using various techniques. Very little literature exists on the mixed bonding behavior of dopants in SiC(N,O) particularly in the ceramic state. Boron has been one of the most common dopants of SiCO. It has been shown that B-O and B-N bonding and increases the thermal stability and mechanical properties of PDCs.

Another popular method of creating doped PDC has been by means of the sol-gel processing route. Some early reports of organically modified polymers via sol-gel method arose in the 1980's. In 1997, metal alkoxides (M = Ta, Ti, Al) were found to modify poly(dimethyl-siloxane) at 70°C by sol-gel route showing M-O-Si bonds [110]. Upon further heat treatment at 150°C the M-O-Si FTIR absorbance peak [917cm^{-1}] became much more pronounced indicating a considerable amount of bridging bonds were formed between the polymer and alkoxide even at this low temperature. In 2000, another sol-gel process was used to form siloxane-vandate gel with V to Si ratio of 0.12. The polymer was processed at room temperature and showed Si-O-V bonding by NMR, FTIR, and Raman[111]. A recent study examined the adsorption of Hf-butoxide onto hydrogen terminated Si and found the formation of Si-O-Hf(O-t$Bu)_2$-O-Si bridging bonds at temperatures as low as 60°C [112]. In 2003, Nb and Ta doped siloxanes were both shown to form Si-O-M bonds at low temperature by means of FTIR and NMR [113]. Very recently Zr and Hf alkoxides were used to modify siloxane and both were found to form Si-O-(Hf,Zr) bonds [114-116]. Similar work has been done on doping siloxanes with rare earth metals all of which showed absorption bands corresponding to M-O-Si (M= Nd^{3+}, Sm^{3+}, Dy^{3+}, Er^{3+}, Tm^{3+}) [117].

Of the works that exist, all but a select few involved the doping of silanes (-Si-C-) and siloxanes (-Si-O-). The focus of the present work is on silazanes (-Si-N-). One other study to date has investigated the reactions of Hf-alkoxide modified silazane which suggested the formation of Si-O-Hf and Hf-N bonds upon thermal cross-linking of the polymer [118]. It is worth noting that these polymer decomposition reactions at any temperature regime are heavily dependent on the initial polymer structure and dopants being used. Some Hf containing polymers have been shown to reduce to HfC at temperatures as low as 250°C whereas others remain as disordered up to 1000°C. One work on the decomposition of polyaluminasilanzes showed the existence of mixed Al-N and Al-C bonding at low temperatures (70-80°) by the reaction of silazane with trimethylaluminum [119, 120].

In summary, polymers containing M-C bonds are typically unstable and decompose at low temperature. Many metalorganic polymers form pi-complexes which are currently unsuitable for PDCs. The fact that SiCNO polymer derived materials do not crystallize upon annealing up to 1300°C can be traced back to their polymer structure. The polymer backbone consists on Si-N or Si-O units with hydrocarbon branches. Si forms strong covalent bonds with O, C, and N which remain stable at pyrolysis temperatures. Upon thermal treatment >600°C, the C-H bond break leaving dangling carbon bonds where carbon is firmly anchored to Si. This leads to a pseudo amorphous structure of Si(N,O) domains with “free” carbon phase which shows mixed sp^2 and sp^3 character. It is not unreasonable to suggest that metal atoms could substitute for Si in the network just described. Many transition metals have similar bond strengths with O, N, C and could potentially be substituted for Si in the amorphous ceramic network. Simple bond energy calculations will show that this M->Si atomic substitution could be energetically favorable. Very little experimental evidence for this type of substitution has been done to date.

3.3 Theoretical basis for Doping SiCN with Hf-O

3.3.1 Enthalpy of atomic substitution for Si-centered tetrahedra

The unique ceramic structure of PDCs can be traced directly to their precursor structure. All of the PDC precursors have certain bonding schemes, which are dissimilar than most polymers, allowing a controlled decomposition into the amorphous nanodomain structure. Fig. 29 shows two example structures of polymer precursors for amorphous SiCO and SiCN ceramic materials. The SiCO precursor shown (left) is a cross-linked set of D3 Si-O ring molecules. The SiCN precursor (right) is linear polymer with a -[Si-N]- backbone. In both cases hydrocarbons are anchored to the molecular backbone through strong Si-C bonds.

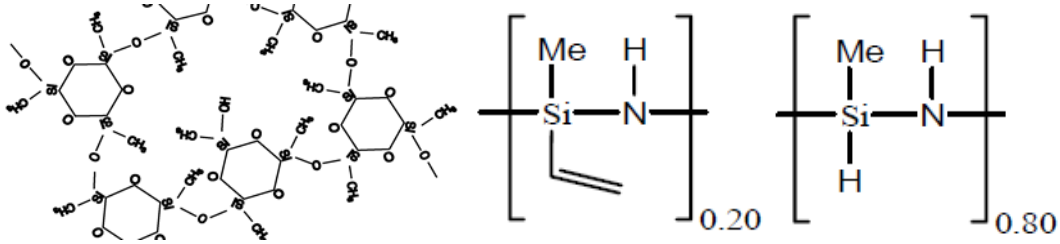

Fig. 29. Example structures of a siloxane and a polysilazane, precursors for nanostructured SiCO and SiCN ceramics

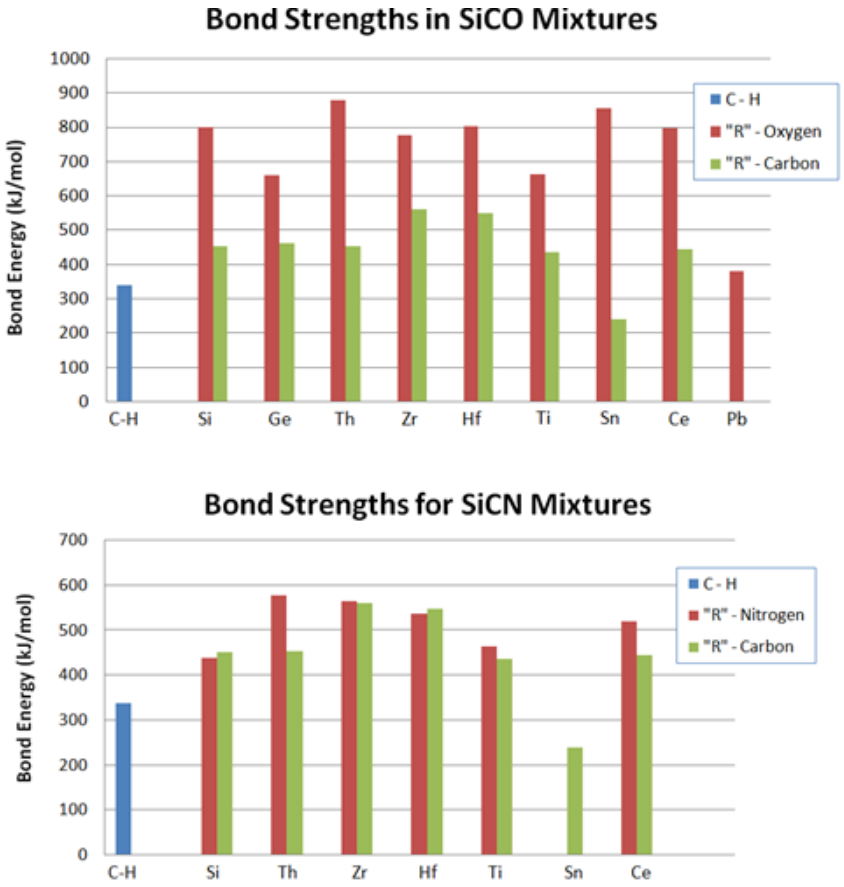

Fig. 30. Diatomic molecule bond energies for various transition metals with C, N, and O. The C-H bond energy reference is shown in blue

A variety of bonding schemes can be observed between the two polymers. An examination of both precursors shows a few commonalities which are key to the thermal breakdown of these molecules into nanostructured SiC(N,O) ceramics. Figure 30 illustrates this point. Shown are a variety of diatomic bond strengths M-O, M-C, and M-N, where 'M' are various transition metals, compared to the bond strength of C-H (highlighted in blue). Note that the bond strengths for Si-(C,N,O) are considerably greater than that of C-H. In the polymer structures shown above, the ring and linear backbones consist entirely of Si-O and S-N repeating units. Similar molecules known as carbosilanes are used as preceramic precursors for silicon carbide and consist of Si-

C backbones. Upon thermal pyrolysis, the weaker C-H bonds cleave while the strong backbone remains intact. Carbon, joined to Si through hydrocarbon sidegroups, also remains anchored while hydrogen/hydrocarbons thermally evolve. This anchored carbon forms dangling C- bonds which link together to form stochastic networks of disordered sp^2 carbon.

It should be noted that the diatomic bond energies shown here are rough approximations of a ceramic state bond and are only used as a preliminary screening tool. The energy of each bond will vary with atomic coordination. The diatomic energies given above are all for a coordination of 1. A careful analysis of select transition metals has shown these diatomic molecule values to be relatively accurate, and they also properly highlight trends of interest.

For nanostructured PDC decomposition, the basic impurity atom should form:

1) A strong carbon bond
2) Strong oxygen and/or nitrogen bond
3) Weak bond with hydrogen
4) Equivalent valency of Si (though not required)

Since the SiC(N,O) materials are amorphous, there are very accommodating of impurity atoms of various valency. The figure above only shows bond energies for substitution atoms which commonly show a valency of four. This comparison serves as a guide to which atoms may or may not be substituted for silicon into the amorphous SiC(N,O) structure.

Another important property of SiCN and SiCO materials which is often overlooked is the energy difference between Si-based crystalline and amorphous states. For example, amorphous SiO_2 remains metastable at high temperatures. Strictly speaking the crystalline forms of SiO_2 are energetically preferred but there is very little driving force

for crystallization. A difference of -10 kJ/mol between amorphous and crystalline (quartz) states is very small compared to equivalent systems such as HfO_2 which show ~100 kJ/mol. This is not to say impurities cannot be incorporated into the amorphous matrix if they have favorable energies for crystallization. This point simply tells that if the impurity content is high enough it would likely crystallize into the preferable phase.

However, it should be noted that the enthalpy of crystallization of silica is an extreme example. Materials like SiCN, with no Si-O content, still are amorphous after processing at very high temperatures (<1450°C). This phenomenon is quite remarkable and the underlying reason is not fully understood. In 2007, the enthalpy of formation of polymer-derived SiCO was measured by high-temperature oxidative drop-solution calorimetry[43]. The energies of formation for amorphous SiCO were found to be negative compared to compositions of their crystalline equivalents (composed of SiO_2, SiC, and graphite). This study showed that the thermal stability of SiCO materials was not only kinetic, like amorphous silica, but that it is thermodynamically stable as well. The exact reason for this remains unknown, but the prevailing theory is due to favorable energetics of the domain walls. The nanodomains of SiCNO have been shown to have size on the order of ~2 nanometers. At these nanoscale sizes, surface area effects such as interfaces energies can play a dominant role in bulk material behavior.

Analogous studies for SiCNO and SiCN were done in 2008 which yielded similar results [121,122]. Not surprisingly the SiCN materials showed a more positive enthalpy of formation compared to their crystalline equivalent composition. This is due to the relatively high energetics of crystallizing Si_3N_4 compared to the low energy associated with crystallizing SiO_2. Some of the SiCN samples showed slightly positive or close to zero enthalpies of formation over their crystalline equivalents. However, since only enthalpy is considered in this study, it is likely the amorphous SiCN is still

thermodynamically stable due to effects of favorable entropy. The entropy should be significantly lower in crystalline SiCN particularly at high temperature.

From Fig. 30 it can be seen that many substitution atoms appear to be at least feasible as dopants for SiCN and SiCO ceramic systems. Zr, Th, Hf, Ce, and Ti all show similar O, N, C bond strengths as compared with those of Si. This suggests they could be substituted in both SiCN and SiCO. Cerium appears favorable as a dopant for SiCO but not SiCN since it shows favorable oxide strengths and a weak nitride. The bond energies also suggest that materials like tin (Sn) and lead (Pb) would not be favorable for atomic substitution because of their weak carbon bonds.

The energy levels of Fig. 30 serve as a basis for a more complete analysis of doped SiC(N,O). The previous example is quick and easy, and the literatures for diatomic gas molecule energies are abundant. However, a complete analysis requires that the energies be derived from the amorphous ceramic state with proper atomic coordination. This was achieved by calculating the amorphous state bond energy of various carbide, oxide, and nitride compounds from enthalpy of formation values and a simple bond counting method. Total enthalpies for 'M' centered tetrahedra were compared to that of Si centered tetrahedra.

Substitution atoms of Hf, Zr, Ti, V, Al, Nb, and Ta were chosen based on the simple selection rules outlined above. The mathematical framework is described below using the example of doping SiCN with Hf. The calculations for single M-(C,N,O) bonds in the amorphous state were carried out in the following way, using HfO_2 as an example.

To find to the absolute bond energy associated with amorphous HfO_2, the desired chemical reaction is

$$Hf(g) + 2O(g) \rightarrow HfO_2(melt) + \Delta H_{HfO_2}^{melt} \quad (1)$$

In this reaction $\Delta H_{HfO_2}^{melt}$ represents the total enthalpy to form amorphous HfO_2 from solitary (gas phase) Hf and O atoms. This is obtained by starting with the enthalpy of formation, ΔH_{HfO_2}, of crystalline hafnia. Handbook values of this use standard states of Hf metal and diatomic oxygen O_2.

$$Hf(s) + O_2(g) \rightarrow HfO_2(cr) + \Delta H_{HfO_2} \quad (2)$$

The diatomic O_2 can be reduced to atomic oxygen with the dissociation energy, ΔH_{O_2}, for one oxygen molecule,

$$O_2(g) \rightarrow 2O(g) + \Delta H_{O_2} \quad (3)$$

Similarly, Hf metal can be reduced to the atomic Hf by the enthalpy of atomization, ΔH_{Hf}, of metallic Hf,

$$Hf(s) \rightarrow Hf(g) + \Delta H_{Hf} \quad (4)$$

The relationship between amorphous and crystalline states is obtained with the heat of melting of HfO_2,

$$HfO_2(crystal) \rightarrow HfO_2(melt) + \Delta H_m \quad (5)$$

Substituting (3), (4), and (5) into (2) gives,

$$Hf(g) + \Delta H_{Hf} + 2O(g) + \Delta H_{O_2} \rightarrow HfO_2(melt) + \Delta H_m + \Delta H_{HfO_2} \quad (6)$$

and after grouping like terms,

$$Hf(g) + 2O(g) \rightarrow HfO_2(melt) + \Delta H_m + \Delta H_{HfO_2} - \Delta H_{Hf} - \Delta H_{O_2} \quad (7)$$

Equating (1) and (7) it can be seen that the total cohesive energy of one amorphous HfO_2 unit is equal to,

$$\Delta H_{HfO_2}^{melt} = \Delta H_m + \Delta H_{HfO_2} - \Delta H_{Hf} - \Delta H_{O_2} \quad (8)$$

Substituting in the various enthalpy values gives [123],

$$\Delta H_{HfO_2}^{melt} = 96 - 1117 - 618 - 497 = -2136\ kJ/mol \quad (9)$$

The total cohesive bond energy was reduced to the singular bond energy values by dividing the total energy with the total number of bonds for one structural unit of HfO_2. The total number of bonds was completed by a simple bond counting mechanism. Examples of how the total number of bonds was obtained are given in Fig. 31. The respective carbide, nitride, and oxide phases were analyzed for each substitution metal selected. Each M-(C,N,O) bond that is shared between two structural units counts as ½ bond and any fully contained in a unit count as 1 bond. The total number of bonds per structural unit of HfO_2 is four. Dividing the total cohesive energy by the number of bonds gives the effective energy for one chemical Hf-O bond in the amorphous state. Results for the various oxide bond strength values were compared to existing literature and found to be extremely consistent.[124]. The values calculated shown in Table 2 are lower than those reported in [124] but this difference is entirely attributed the fact that they are observing crystalline states whereas here we consider the amorphous (melt) state.

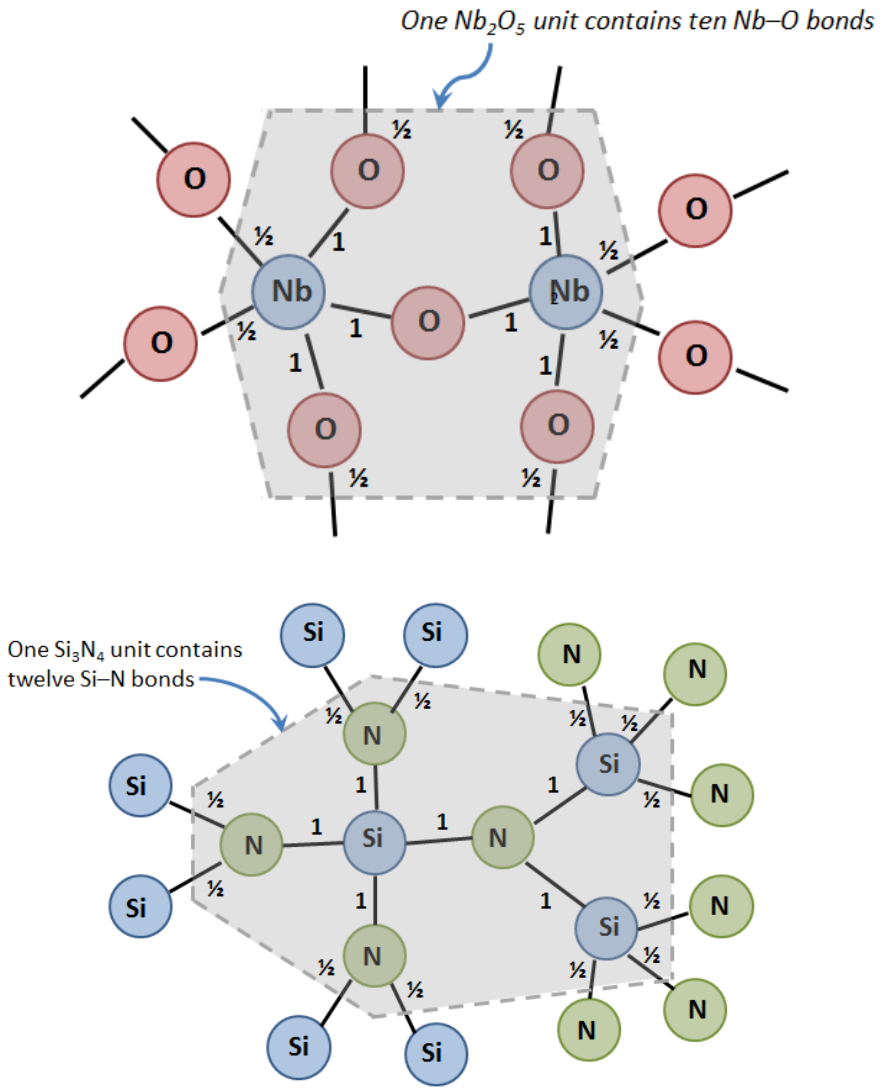

Fig. 31. Structural unit representation of Nb_2O_5 (upper) and Si_3N_4 (lower)

Note the metal dopants analyzed here can adopt various other valence states. For example, Vanadium and tantalum can be +3, +4, or +5. The valency issue was handled for substitution of 4 by normalizing the total cohesive energy to reflect a valency of 4. This also enabled the use of thermochemical data from crystals like Nb_2O_5. Furthermore, this permits the inclusion of atoms like Al which exclusively show a valency not equal to 4.

Table 2. Comparison of bond energy values from literature vs. presented method

	Zr-O	Si-O	Hf-O
Literature values	-555	-465	-559
This calculation	-529	-461	-534

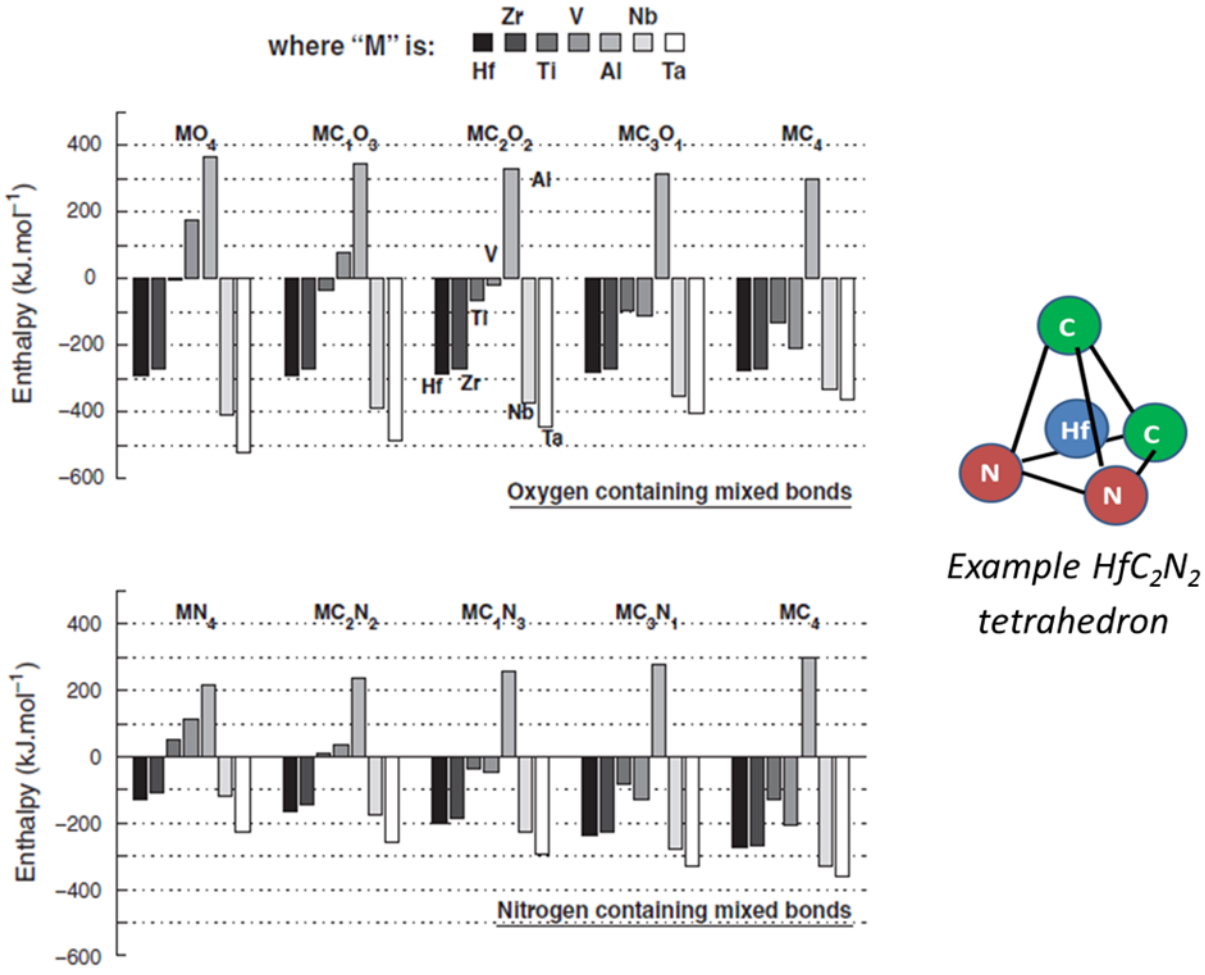

Fig. 32. The change in the enthalpy of mixed bond tetrahedra when Si is replaced by one of the other transition metals, M

The change in the bond energies when Si is replaced by Hf, Zr, Ti, Ta, Nb, or Al, calculated by the procedure outlined above is presented in Fig. 32. The zero enthalpy value represents the total bonding energy in one Si-centered tetrahedra. For example,

the change in enthalpy, plotted along the y-axis, when a Si tetrahedra of the type SiO_3C_1 is replaced by HfO_3C_1 is given by:

$$\Delta H = \left(\Delta H_{Hf-C} - \Delta H_{Si-C} \right) + 3\left(\Delta H_{Hf-O} - \Delta H_{Si-O} \right) \quad (10)$$

Negative values of ΔH suggest that substitution of Si by one of other elements is exothermic and therefore energetically favorable. Inspection of Fig. 32 leads to three groupings of doping elements: (i) Hf and Zr are favored to form mixed bonds relative to Si. However, mixed bonds with O have a lower energy than those with N, suggesting a lower activity of Hf in the presence of O. (ii) Surprisingly, Nb and Ta also form favorable mixed bonds. However, these results are tempered by the assumption of quadrivalent coordination as these elements prefer to form trivalent and pentavalent bonds with O and N. The calculation of bond energies in the present exercise has been prorated to a coordination of 4, which can cause error. (iii) The third group consists of Ti, V, and Al. These elements form weaker bonds than Si, and therefore, are more likely to be "network modifiers" rather than "network formers," with the result that they would be expected to degrade the creep properties of the amorphous networks at high temperatures. Indeed, SiAlCO materials densify readily in the 1200°C–1500°C range, whereas SiCO materials do not, [125] pointing toward low creep viscosity of the Al-modified materials.

3.3.2 Estimation of the Heat of Melting

Limited data was available in the literature for the heat of melting of the various compounds considered. In cases where no sources could be found, an approximation was made based of materials of a similar structural class (ex. HfO_2 and ZrO_2). The heat of melting is a thermodynamic quantity defining the change in enthalpy of a material as

it changes state from solid to liquid. To calculate this in situations where no published data was present, we have used the approximation that the heat of melting divided by the melting temperature, for a given class of materials, would remain unchanged.

$$\Delta G_{melt} = \Delta H_{melt} - T\Delta S_{melt} \quad (11)$$

At the phase transition (melting temperature) equilibrium will be held between the solid and liquid phases. That is, if $T = T_M$, then $\Delta G_{melt} = 0$, giving

$$\Delta S_{melt} = \frac{\Delta H_{melt}}{T_M} \quad (12)$$

This shows that the entropy gain from melting is equal to the enthalpy loss divided by the temperature at which the material melts. The entropy gain from melting is mostly configurational, and therefore it should be approximately equal for materials of a similar class. Values for heat of melting are plotting against the melting temperature of compounds for which data are available, Fig 33. While the slopes (entropy of melting) are different for the various classes of materials, they are reasonably constant for any one class. Each structural class has the same configurational entropy gain to overcome the enthalpy loss of melting.

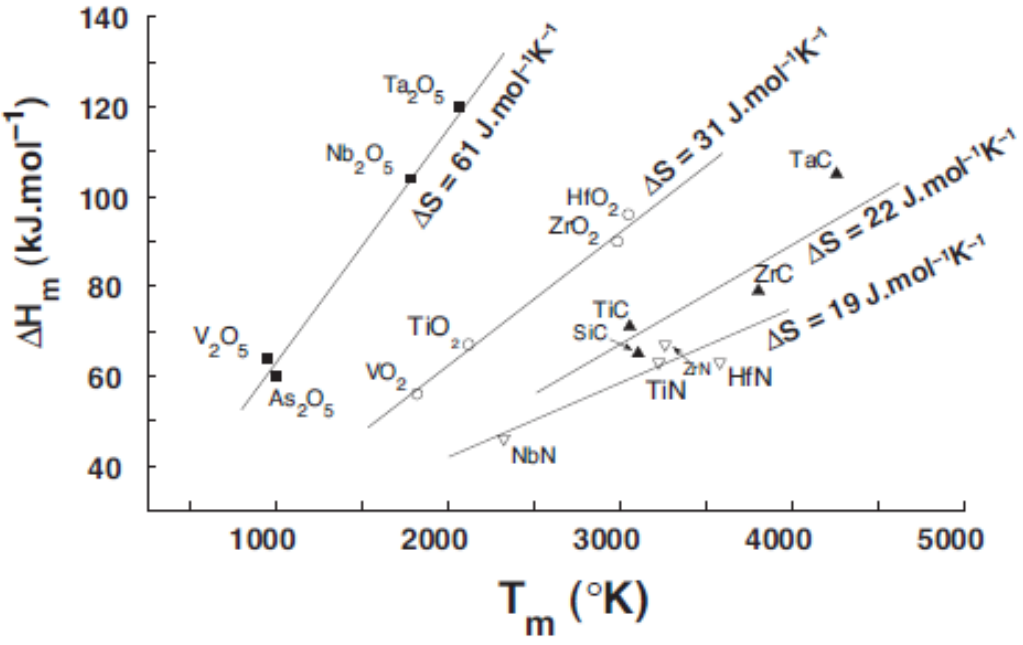

Fig. 33. Estimation of the heat of melting of compounds from the data of related materials

Note that the temperature is absolute scale, and each trend line should pass through the origin. The assumption appears to hold true. A compound with MO_2 structure and a melting temperature of 2500°K would have a heat of melting of approximately 75 kJ.mol^{-1} based on the established trend line.

3.3.3 Entropy Considerations

The analysis to this point has only considered the effect of enthalpy on doped PDC materials. The change in system entropy, which would be extremely difficult (and speculative) to calculate theoretically, has been ignored in a quantitative sense but can still be considered qualitatively. The first thing to note about entropy is that the mixed state will always be more favorable than the pure SiC(N,O) cases. An illustration of this

is in Fig 34 which shows the change in configurational entropy, ΔS, with substitution concentration. The mixture always shows favorable entropy and achieves a maximum when the Si :R ratio is equal to 1, where “R” is an arbitrary substitution element for Si..

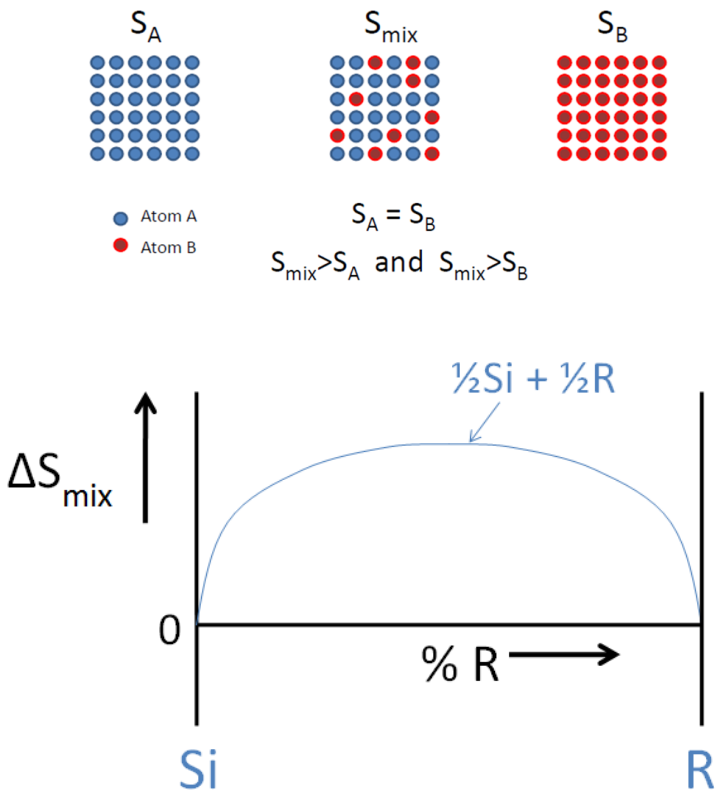

Fig. 34. Trend in configurational entropy from atomic substitution

This is an idealized state of mixing between two crystals; however, the same remains true for amorphous SiCN. Substituting Si with various transition metals would increase the amount of configurational entropy and thereby lower the total Gibbs free energy of the system.

It should also be noted in Fig 34 that the slope of the entropy approaches infinity at the endpoints. It can be concluded that a small amount of impurity will offer a large gain in entropy while having negligible enthalpy effect. This suggests some of the negative or

neutral enthalpy changes calculated above, such as VC_1O_3 and TiC_2N_2, will still have a desirable free energy at lower concentrations of the substitution atoms. This effect is shown in Fig 35 where the two cases illustrate the difference between positive and negative enthalpy on the overall free energy of the system.

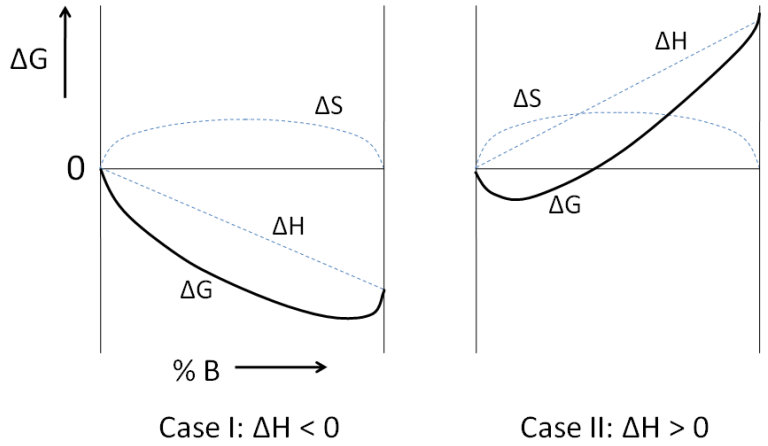

Fig. 35. Effect of substituting Si with atom of favorable enthalpy (left) and unfavorable enthalpy (right) on the total free enrgy of mixing

In short, it is expected that doping SiCN with various metal atoms would increase the configurational entropy and therefore will encourage atomic substitution more than the enthalpy calculations alone. The limit to these remain unknown but it is reasonable to expect that small levels of doping will for M-SiCNO will be energetically favorable over undoped SiCNO.

3.4 Processing, Chemistry, and Structure of Polymer Derived HfSiCNO

3.4.1 Experimental Methods

The HfSiCNO powder was prepared by mixing liquid precursors of Ceraset® (KiON Defense Technologies Inc., Huntington Valley, PA), a commercially available polysilazane, and hafnium tert-butoxide (Multivalent, Ltd., Suffolk, U.K.). The Hf-alkoxide precursor was 99.99% pure with the exception of 0.2% Zr impurity. (Hafnium and zirconium ceramic compounds are found together in natural ore deposits and show near identical chemical reactivity. As such, Hf and Zr are almost impossible to separate in an economically feasible way, and commercial Hf-based materials always come with some Zr content.) The liquid precursors were mixed in an argon glove box containing less than 1 ppm O_2 and H_2O. The two precursors, which are miscible in one another, mix and react with slight effervescence at room temperature. The mixture creates an optically transparent homogeneous solution showing no evidence of phase separation. The effervescence of the solution is clear evidence of some degree of liquid state reaction between the two precursors. The reaction appears exothermic as the solution containing test tube showed some added warmth after mixing. Details of these reactions are presented later in this section. The mixture was stirred for 2–5 min until the solution became quiescent.

The liquid was then cross-linked into a rigid polymer at 300°C under flowing argon for 4 hours in a quartz tube furnace. Pure Ceraset polysilazane cross-links rapidly into a solid body upon reaching temperature of ~115°C. It is worth noting that the Hf-alkoxide has a low melting point, 90°C [126], and therefore the mixture shows considerable weight loss during the thermal ramp to cross-linking temperature. The boiling off of alkoxide during cross-linking is presumably the reason why HfSiCNO-H polymer results

in an epoxy ‘foam’ rather than a mostly dense polymer body as with un-doped SiCN-H, Fig. 36.

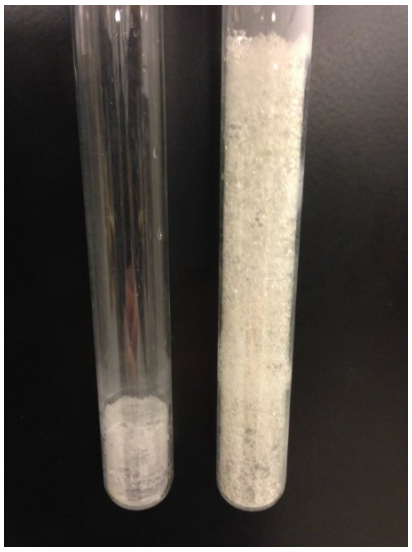

Fig. 36. Cross-linked polysilazane (left) and alkoxide modified silazane (right). Note the significant macro-scale porosity in the alkoxide modified silazane.

The cross-linked resin was crushed into coarse powder using mortar and pestle, and milled in a high-energy ball mill for 20 min. This powder was then pyrolyzed at 1000°C in an alumina tube furnace for 2 hrs under flowing argon. Silicon carbonitride samples, without hafnia, were prepared for benchmarking; they were made with the same cross-linking and pyrolysis procedure, using only the polysilazane precursor.

The chemical constitution of the pyrolyzed powders was analyzed in the following way. The carbon, oxygen, and nitrogen weight fractions were measured using a LECO C-200 Carbon Analyzer and a LECO TC-600 Oxygen–Nitrogen analyzer (Leco Corporation, St. Joseph, MI). Silicon and hafnium concentrations were measured using quantitative Energy Dispersive X-ray Spectroscopy (EDS) in a Scanning Electron Microscope (FEI XLFEG, manufactured by FEI, Hillsboro, Oregon). The SEM was equipped with an

Oxford Inca System manufactured by Oxford Instruments, Abingdon, UK. The EDS was calibrated using SiO_2, HfO_2, SiC, and Si_3N_4 standards.

Table 3. Chemical composition table with error bars

Sample Compositions $Hf_vSi_wC_xN_yO_z$ (v + w + x + y + z = 1)							Standard Deviation Error Bars (+/-)				
Sample	v	w	x	y	Z	Hf:Si ratio	v	w	x	y	z
S00	0.000	0.348	0.294	0.325	0.033	0.000	0.000	0.048	0.005	0.012	0.001
S08	0.027	0.341	0.189	0.348	0.094	0.080	0.002	0.024	0.003	0.013	0.003
S15	0.050	0.330	0.143	0.261	0.216	0.152	0.004	0.032	0.002	0.010	0.006
S22	0.070	0.311	0.117	0.201	0.302	0.224	0.005	0.024	0.002	0.008	0.009

The compositions of the four powder samples, denoted as S00, S08, S15, and S22 are given in Table 3. The nomenclature refers to the Hf/Si molar ratio, for example, in the case of S15, this ratio is equal to 0.15, and so on. The trace amount of oxygen in the pure nominally pure SiCN ceramic is due to a small amount of eurea functionalization which allows the precursor to be handled in air. Previous experiments using the same Cerast precursor show similar amounts of oxygen in the final ceramic[127].

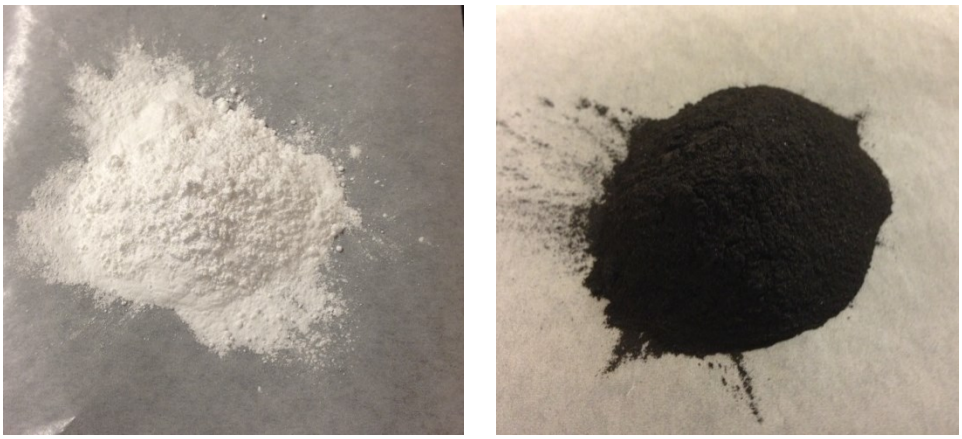

Fig. 37. S08 composition powder before (left) and after (right) pyrolysis at 1000°C

The density of the four ceramic compositions are given in the appendix Table A1. S00 and S08 densities were measured directly, and S15 and S22 sample densities were extrapolated from similar compositions. Details of the density measurements are given in Appendix A. Upon pyrolysis, the polymers convert from a white powder to dark brown, Fig 37. Significant mass loss and volume shrinkage accompany the polymer to ceramic conversion. The mass loss of pure SiCN is 25% which corresponds to a volumetric shrinkage of 63% assuming densities of 1.12 and 2.24g.cm-1 for the polymer and ceramic states, respectively. Exact shrinkage from the Hf-O doped polymers is unknown; nevertheless it is expect to be on the same order as pure SiCN.

Raman spectra were collected on a Micro-Raman spectrometer (Horiba Jobin Yvon, Japan). The spectra were recorded at room temperature in ambient atmosphere. For excitation at 532 nm, an Ar^+ laser was used with a focused laser spot size of ~5 micron. High Hf-containing samples were measured with a 633-nm laser because the shorter wavelength of 532 nm produced significant luminescence.

The FTIR were collected on a Nicolet 4700 FTIR with ~2mm diamond window (Thermo Fisher Scientific, Waltham, MA, USA). Spectra were collected at three stages: (i) liquid precursors after mixing at ambient temperature, (ii) mixed precursors after thermal cross-linking at 300^{o}C, and (iii) after thermal pyrolysis at 1000^{o}C. The polymer and ceramic state spectra were collected on pressed powder compacts. Powders used for FTIR collection were refined by high-energy ball milling to increase the measureable surface area.

Small angle and wide angle X-ray diffraction spectra were made on SAXSess High-Flux Small-Angle X-ray Scattering System from Anton Paar GmBH, Graz, Austria. The wide-angle X-ray diffraction experiments were carried out with CuKα radiation using a 40mV acceleration voltage and 50mA current. Each sample used a beam exposure time of 15

minutes. X-ray spectra were taken on thin powder films adhered a Si substrate. Powders were dispersed in acetone and dripped onto a thin Si wafer which is x-ray transparent within the measured 2θ diffraction angles.

3.4.2 Pyrolytic behavior

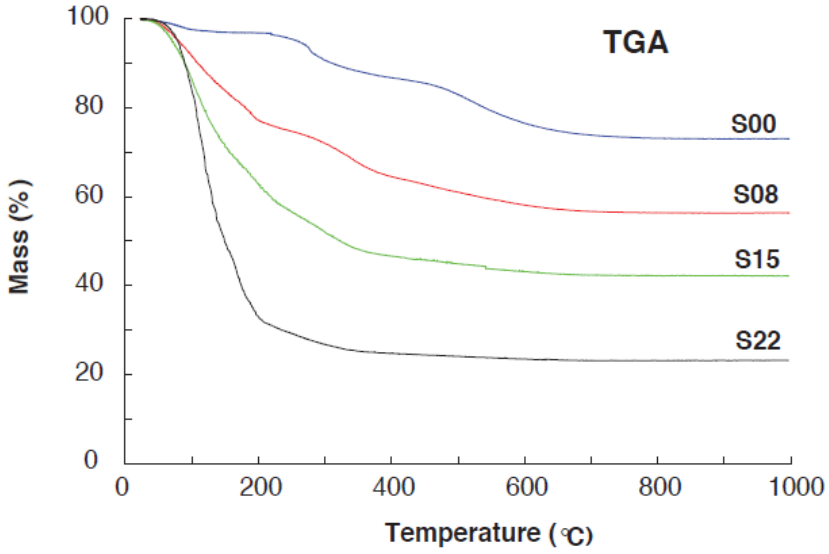

Fig. 38. Weight loss from liquid precursor to ceramic state for different compositions

Thermogravimetric analysis (TGA) data were collected on a STA 499 F3 Jupiter ® (Netzsch-Geratebau GmbH, Selb, Germany). The liquid precursors were heated from ambient to 1000°C in the TGA. The sample chamber is typically purged of air by vacuuming and backfilling with ultra-high purity argon. However, since vacuuming the chamber would have boiled the liquid precursor(s), the chamber was flushed with argon for 20 minutes instead. This inevitably results in some oxygen contamination (measurable via mass spectrometer).

The TGA data for each of the four compositions, starting from liquid precursors up to 1000°C are shown in Fig. 38. The Hf modified samples show dramatic weight loss from ambient temperature to ~200°C, due to the vaporization of Hf-alkoxide. Mass loss appears to cease at ~700°C for all samples indicating complete conversion to the ceramic phase. The vapor loss of the alkoxide implies that a considerable fraction of the alkoxide does not react with the silazane. On the other hand the incorporation of Hf into the compounds would imply that the alkoxide retained in the liquid mixture had chemically reacted with the silazane below the alkoxide boiling temperature of 90°C.

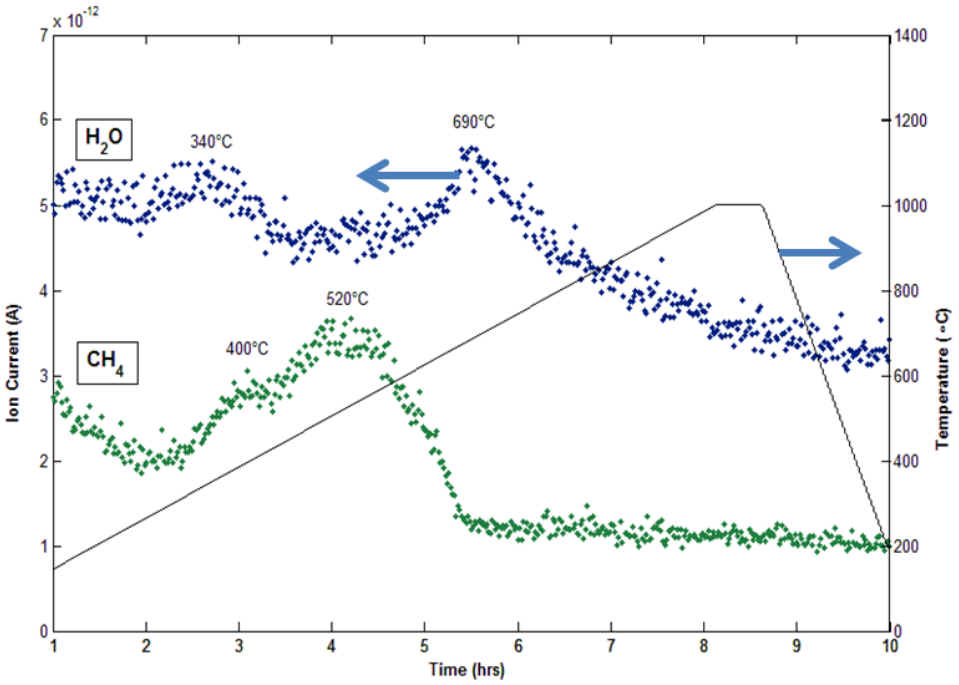

Fig. 39. Off gassing of water vapor (H_2O) and methane (CH_4) species during pyrolysis of S08 sample

Off-gassing species were traced via mass spectrometer during pyrolysis. The two most evident decomposition byproducts were water vapor and methane, Fig. 39. The water vapor is released significantly at 340°C from polymer cross-linking and 690°C during the

ceramic conversion. Methane evolution, from the loss of polymer -CH_3 groups, is evident in the range 350°C-600°C. This temperature range shows a continuous transition from polymer-like to ceramic-like material behavior.

3.4.3 The HfSiCNO-H Liquid State

The mixtures of Hf-alkoxide and silazane were originally prepared with the intent of creating 25%, 50%, and 75% wt. HfO_2 in SiCN. The ceramic yield of HfO_2 was derived theoretically from the initial and final molecular weights transitioning from the alkoxide precursor to HfO_2. The calculated ceramic yield of the alkoxide, $Hf_1(O_1C_4H_9)_4$, after conversion to HfO_2 is 44.7%. The ceramic yield of SiCN, assumed to be 72% wt., was taken from literature data for the Ceraset precursor pyrolyzed in argon. Mixtures were prepared as given in Table 4. However, due the volatilization of alkoxide the ceramic yield of HfO_2 was significantly lower than anticipated.

Table 4. Precursor mixtures of Hf-alkoxide and Ceraset (polysilazane)

Liquid State			**Ceramic State (after pyrolysis at 1000°C)**		
Sample Designation	Mixing Ratio (wt. %)		Intended HfO_2 wt. %	Actual HfO_2 wt. %	Hf:Si Ratio
	Hf-alkoxide	Ceraset			
S00	0.00	100.00	0	0.00	0
S08	34.94	65.06	25	24.65	0.08
S15	61.70	38.30	50	38.94	0.15
S22	82.86	17.14	75	48.65	0.22

The liquid state reactions were characterized by Fourier Transform Infrared Spectroscopy (FTIR). Spectra were collected from wavenumbers 400-4000 cm^{-1} on liquid mixtures. Note the sample nomenclature – S00, S08, S15, S22 – used for the

liquid state is the resulting Hf:Si ratio of the final ceramic state. The hydrogen content of the polymers, difficult to measure experimentally, was not determined and therefore the full chemistry in the liquid state is unknown. It is fair to expect that the solid polymer state and ceramic state have similar Hf:Si ratio chemistry. On the other hand, the liquid state given here will inevitably have a much higher Hf:Si ratio due to the free alkoxide content which volatilizes upon thermal cross-linking.

Fig. 40 shows the FTIR for three liquid state HfSiCNO-H samples in the mid-IR and near-IR regimes. Pure precursors of polysilazane (Ceraset®) and Hf-butoxide are shown for reference. Most of the visible peaks are found in one of the precursors, but not both, and therefore a positive rendering of reactions is obtained if (i) the mixed compositions show peaks that are present neither in pure silazane or in pure hafnium butoxide, and (ii) the peaks present in S00 are absent in S08, S15 and S22.

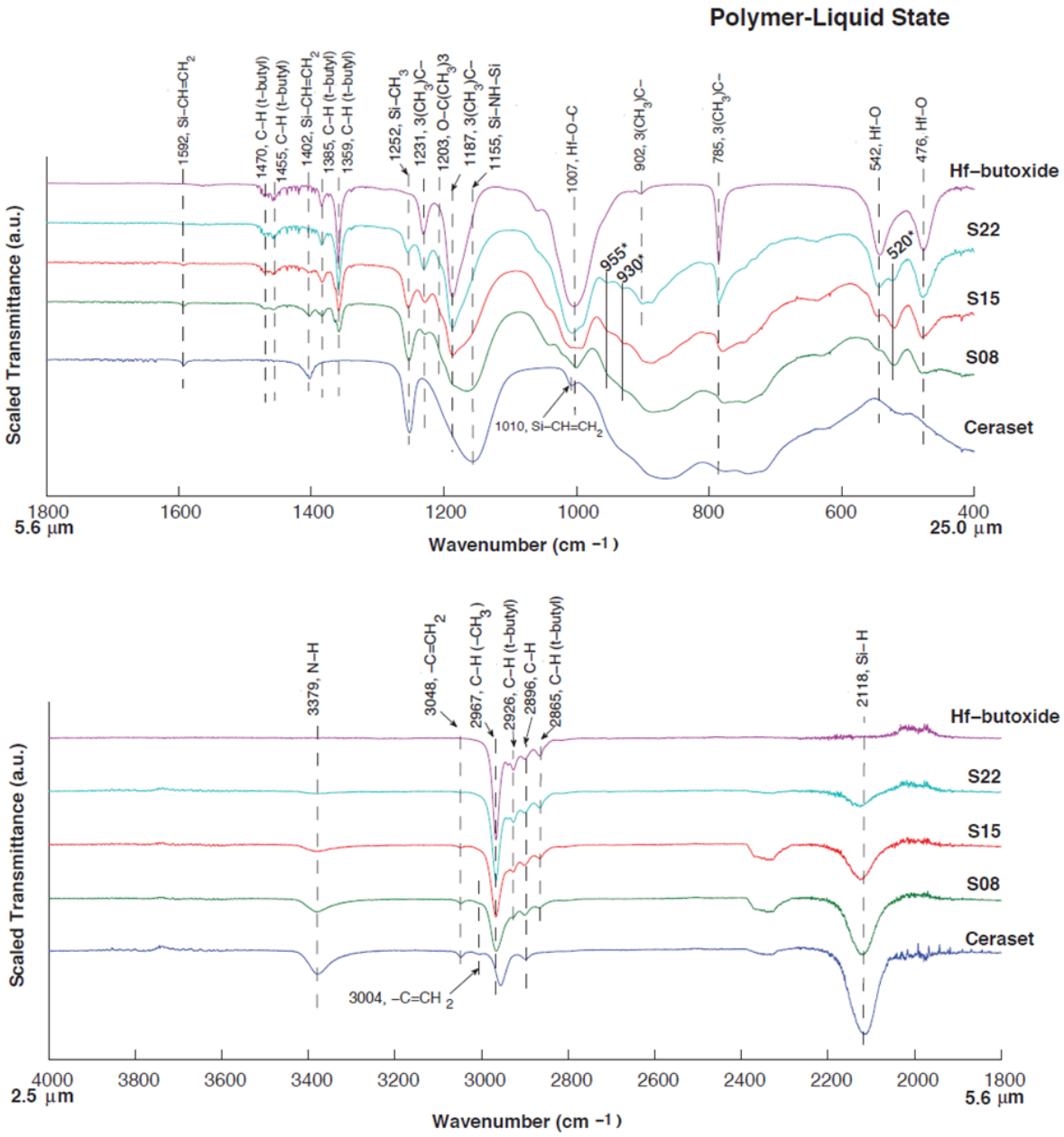

Fig. 40. Mid-IR (top) and near-IR (bottom) spectra of liquid precursors in their pure and mixed states

When combined, most liquid state absorption peaks follow rule-of-mixtures (ROM) behavior in regards to their respective peak height. A peak following ROM would suggest no reaction has taken place for that respective chemical bond. However, it is

known from solution effervescence that some spontaneous reaction is taking place upon mixing in the liquid state. A quantitative analysis of absorption peaks suggests the N-H bond is being consumed slightly faster than predicted by ROM. The N-H absorption peak (3379 cm^{-1}) does not disappear entirely, but does appear to decrease faster the ROM would suggest, Fig. 41, identifying N-H as a potential reaction site for the alkoxide.

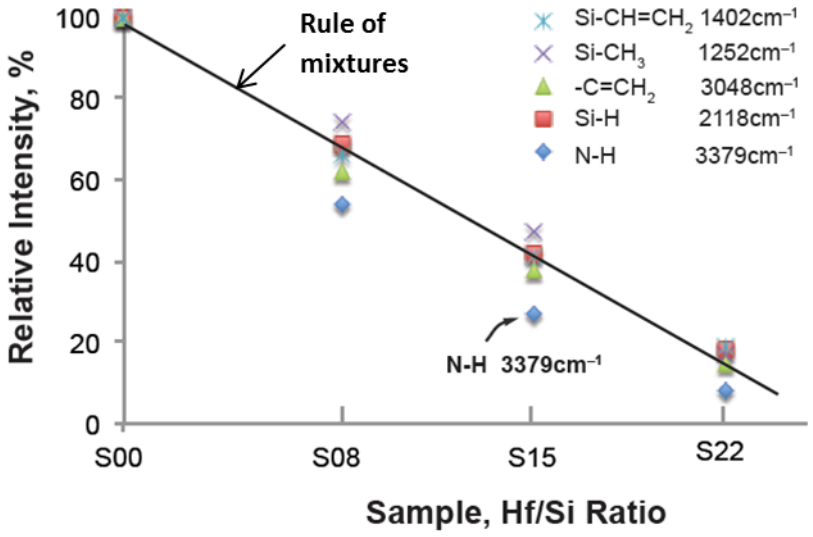

Fig. 41. Plot of the relative intensity of absorption peaks for mixed precursors. The N-H peak is consistently lower than ROM behavior.

One related observation in the liquid FTIR spectra, shown in Fig. 40 (top), is the presence of a new peak at 520 cm^{-1} which is not present either in liquid silazane or in hafnium alkoxide. It is assigned here to the Hf-N stretch where the central hafnium atom is coordinated to 4 nitrogen atoms which has been reported in literature at 527cm^{-1} [128]. Furthermore, a first order simple harmonic oscillator model, discussed in Appendix B, is in good agreement with this value.

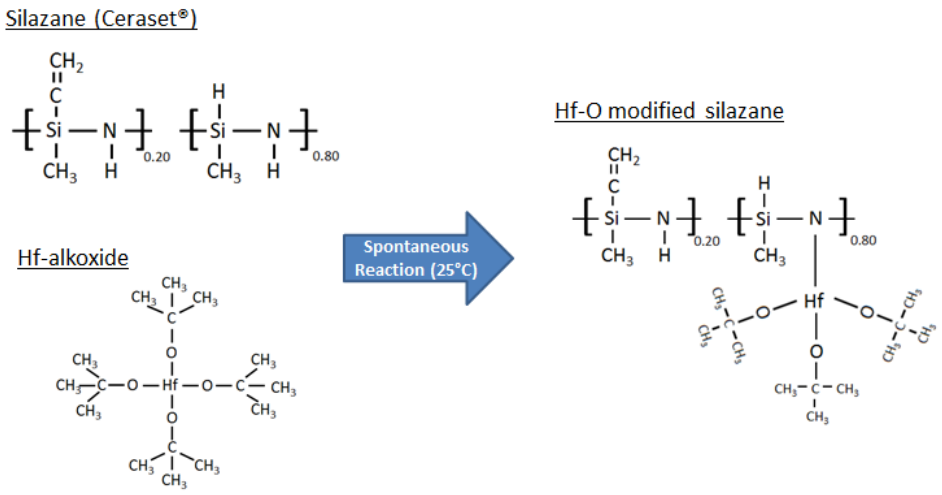

Fig. 42. Expected liquid state reaction of silazane and alkoxide

The proposed liquid state reaction for the formation of Hf-N bonds is shown above in Fig. 42. The faster than ROM decrease in N-H absorbance and the emergence of a peak consistent with that which is predicted for Hf-N strongly suggest the formation of Hf-N bonds between the alkoxide and silazane molecules. The FTIR evidence suggests this is likely the only significant spontaneous reaction which occurs in the liquid state.

3.4.4 The HfSiCNO-H Polymer State

The liquid precursor mixtures were thermally cross-linked into a rigid polymer at 300°C under flowing argon for 4 hours. The solid polymer was crushed with mortar and pestle and analyzed using XRD, FTIR, and Raman.

The resulting epoxy was milled into powder before collecting FTIR to increase the measurable HfSiCNO-H surface area. The FTIR spectra for the crosslinked polymer are given in Fig. 43. They show distinct reactions upon thermal cross-linking. Several

peaks present in the nominal polysilazane precursor are absent in the mixtures after polymerization. These results are summarized in Table 5, and discussed below.

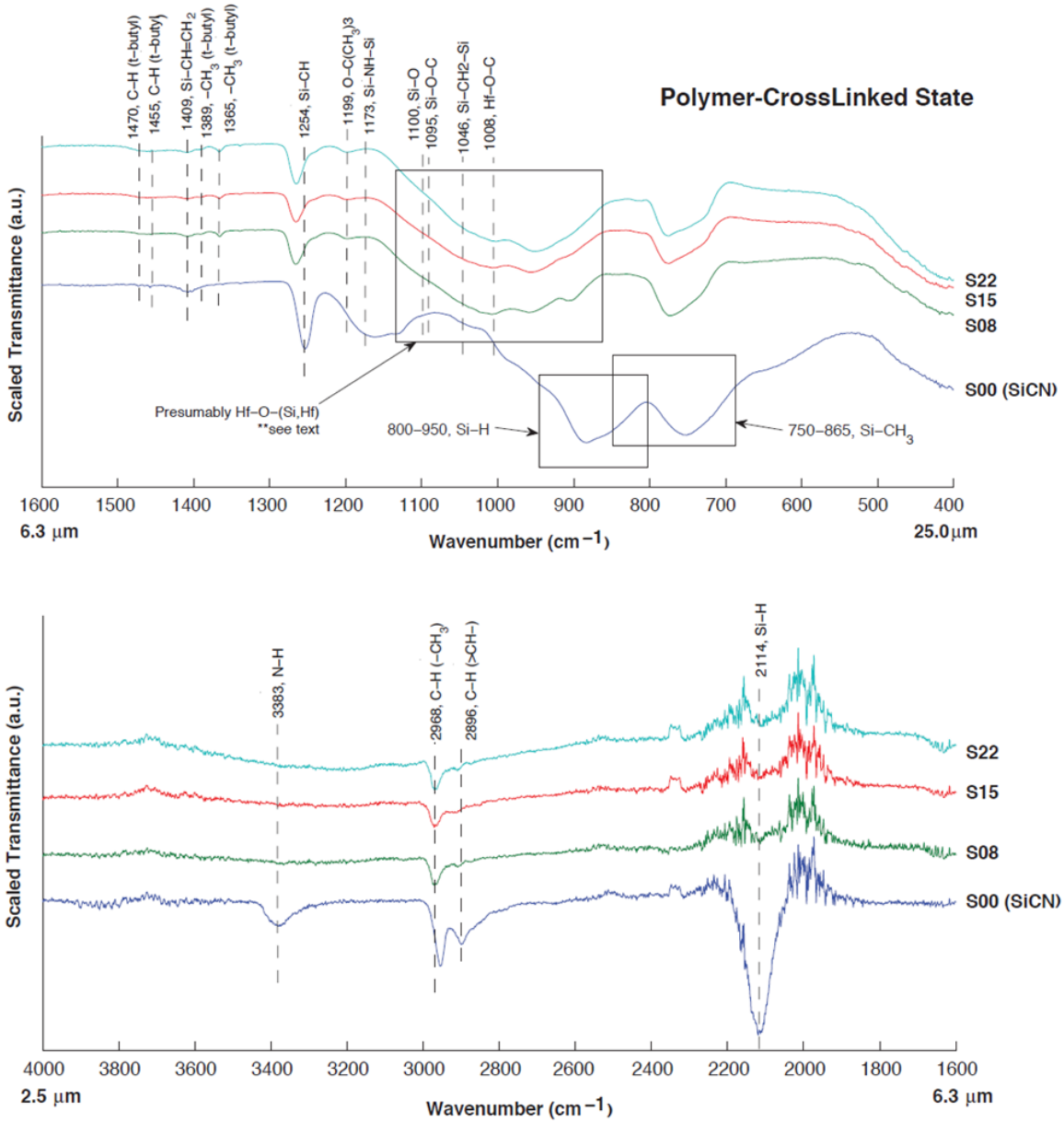

Fig. 43. Mid-IR (top) and near-IR (bottom) spectra of the cross-linked polymers

Table 5. FTIR absorbance peaks for cross-linked polymers

Wavenumber (cm^{-1})	Bond Assignment	Observation
3383 and 1173	N-H	Large absorption in S00, absent in S08-S22
2896	C-H	Large absorption in S00, absent in S08-S22
2114 and 800-950	Si-H	Large absorption in S00, absent in S08-S22
1254 and 750	$Si-CH_3$	Relatively consistent intensity, but a ~12cm^{-1} blue shift for all Hf-O modified samples.
955 and 930	Si-O-Hf	Only observed in Hf-O modified samples

Unlike the liquid state reaction, ROM analysis cannot be used for the polymer state because both precursors have differing, and unknown, amounts of volatilization upon heating. The Ceraset precursor boils off some of the small weight molecules under vacuum or upon heating. This is generally not a significant amount compared to the volatilization of Hf-butoxide. It is possible that the cross-linking reaction could be performed at an overpressure of atmospheric gas to raise the boiling point of the alkoxide above the reaction temperature. This would give a much more controlled process and would enable careful tuning of HfSiCNO-H chemistry which, in the present study, was not determined *a priori* but rather measured afterwards. A complete knowledge of the polymer chemical composition would also permit quantitative analysis of FTIR in the cross-linked state.

The Si-H and N-H peaks in the solid polymer state, which are strong in S00, are absent in the mixed samples. This is most evident in the near-IR regime (bottom) which shows large (Si, N)-H peaks in only S00. Note the liquid state Si-H absorption follows rule of mixtures behavior. The significant loss of Si-H indicates it is a primary reaction site for the cross-linking reaction. The alkoxide and silazane bond reaction

pathways have been discussed previously in a recent study [118]. The expected cross-linking reaction results in the formation of Si-O-Hf bonds.

Evidence for the formation of Si-O-Hf bonds can also be seen in the shift of Si-CH_3 peak which is absorbs at 1254cm^{-1} in the S00 sample. This peak, shown in Fig. 44 (top), has a blue shift of ~12cm^{-1} when cross-linked in the presence of the alkoxide. This shift is ascribed to the addition of O to Si. For example, Si-3(CH_3) absorbs at 1250 cm^{-1}, but the peak for 3(O-)Si-CH_3 occurs at 1270 cm^{-1} [129]. The absorption shift associated with increasing oxygen coordination to Si is shown in Fig. 44. It is also worth noting the absorption peak is Gaussian in S00 but skewed to lower wavenumbers with the alkoxide addition. This suggests the indexed Si-CH_3 peak is actually the linear combination of several Si-CH_3 peaks with various oxygen coordination around Si.

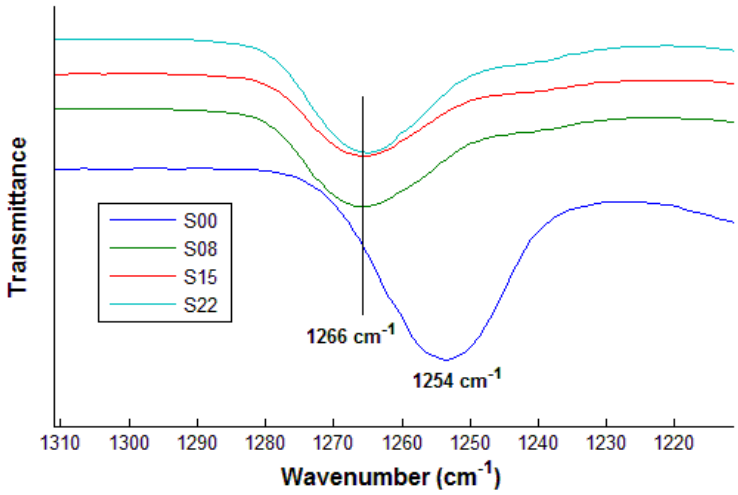

3:1 C to O	2:2 C to O	1:3 C to O
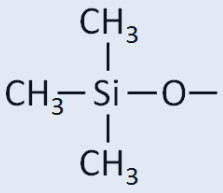	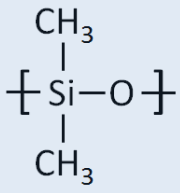	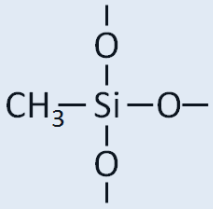
1250 cm^{-1}	1260 cm^{-1}	1270 cm^{-1}

Fig. 44. Shift in silazane Si-CH_3 peak with introduction of alkoxide (top) and tabulated shift in Si-CH_3 peak shift with increasing oxygen coordination (bottom)[129]

Further evidence for the formation Si-O-Hf bonds is found in the large absorption band which appears in the range 850-1150cm^{-1}. This absorption band is absent in undoped sample S00 with no Hf-O content. Significant peaks from M-O-Si bonds in the cross-linked polymer state are known to fall in the 900 cm^{-1} -1000 cm^{-1} range, where M=Ti[130,131], Nb[113], Ta[110], V[111], Zr[132], Hf[133-135].

The N-H peaks, which were below expected ROM amouts in the liquid state, are now completely absent in the alkoxide containing polymers. This is attributed to the

formation of Hf-N bonds as dicussed previously for the liquid state. The undoped SiCN-H samples still shows sgnificant Si-H and Ni-H bonding in the polymer state. This is an interesting result. Even the smallest introduction of Hf-alkoxide leads to the total absence of (Si, N)-H bonds observed in the undoped S00 polymer. The expected result of this is an extrememe degree of moleular cross-linking. Attempts were not made to characterize mechanical properties in the polymer state for these samples. However, it is reasonable to expect the viscoelastic behavior of doped silazane and siloxane polymers could be tuned by the incorporation of even small amounts of alkoxide.

Note that t-butyl peaks are largely reduced in mixed precursor cases meaning that the alkoxide retained in the mixture has reacted with the polysilazane network during thermal crosslinking. The only significant bonds remaining from the base silazane precursor are Si-N-Si and Si-CH_3.

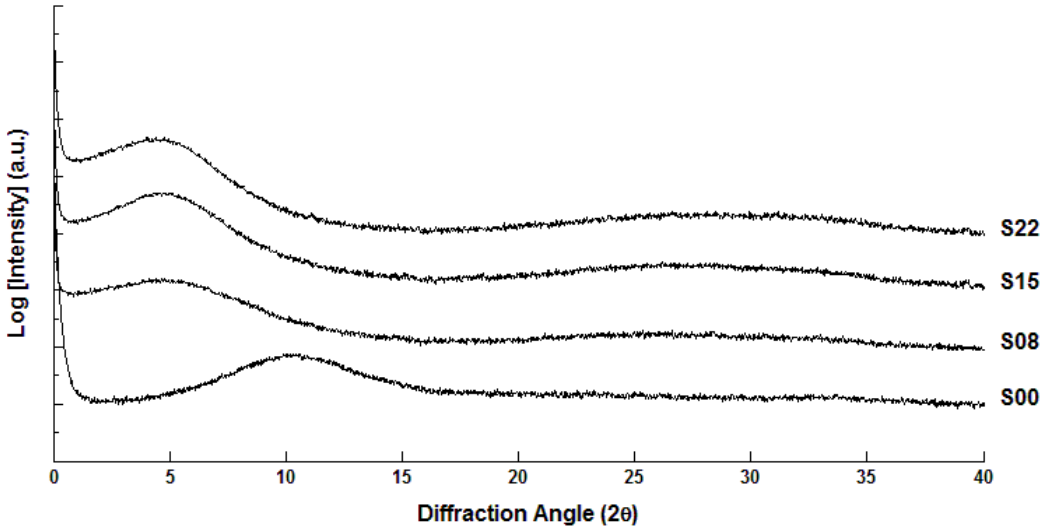

Fig. 45. Wide angle X-ray diffraction spectra of cross-linked powders

All polymer powders were x-ray amorphous after annealing at 300°C, Fig. 45. A noteworthy structural feature is observed at shallow 2θ angles. The undoped SiCN-H

sample S00 show a broad diffraction band or “halo” from 5° < 2θ < 15° which is typical of amorphous polymers. However, one interesting results is a distinct shift in the amorphous halo for alkoxide modified samples. All samples doped with Hf-alkoxide showed the halo centered at ~5° whereas the undoped case is centered at ~10°.

It is interesting that the S00 halo disappears entirely in the alkoxide modified polymers. This confirms what was suggested by FTIR that even the smallest amount of doping results in a polymer of completely different cross-linked structure. The shift to smaller scattering angles would be the result of larger spacing between repeating diffraction features. It is believed that the alkoxide modified polymer therefore has a more open polymer structure compared to SiCN-H alone. A possible culprit would be the bridging of silazane molecules by –Si-O-Hf-O-Si– bonding. FTIR results suggest significant amounts of Si-O-Hf bonding. This may also explain the shallow XRD halo from 20° < 2θ < 38° which emerges with increasing alkoxide concentration. Amorphous ceramic glasses shows a similar halo from short range order centered in the same vicinity.

Raman spectra were also collected for the cross-linked polymer samples, Fig. 46. These data confirm many of the observation made by FTIR and XRD. The Si-H and N-H peaks are found to only exist in the undoped sample. The Si-CH_3 peak remains unaltered across all doped and undoped samples. No evidence of any crystalline phase was found in the spectra.

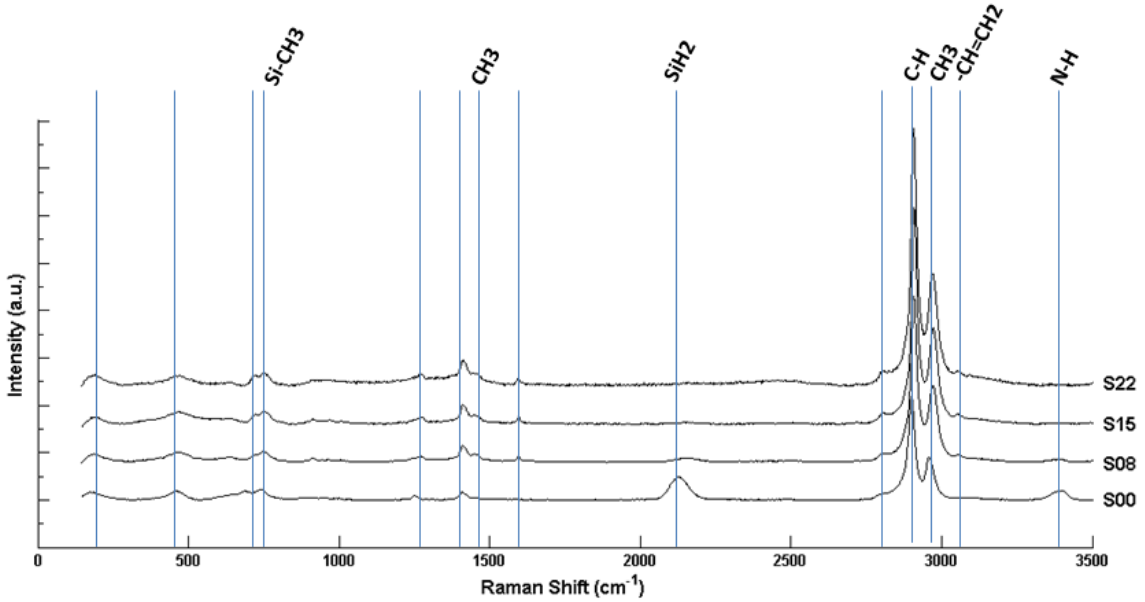

Fig. 46. Raman spectra of cross-linked polymer samples

3.4.5 The HfSiCNO Ceramic State

The HfSiCNO-H polymer powder was pyrolyzed at 1000°C in an alumina tube furnace for 2 hrs under flowing argon. The ceramic samples were analyzed using FTIR, XRD, SAXS, and Raman.

All ceramic compositions were x-ray amorphous, except for the S22 composition which showed very shallow diffraction peaks from monoclinic and tetragonal HfO_2. The crystalline hafnia peaks are broad, indicating nano-scale hafnia precipitates. High fidelity SEM micrographs do not show visible precipitates HfO_2. The minimum detectable crystallite size for XRD is ~2 nm, and the minimum detectable size for visibility via SEM is ~15 nm. Application of the Scherrer Formula predicts the HfO_2 crystal size in sample S22 to be 9.8 nm based on diffraction peak geometry. This value is consistent with XRD and SEM observations.

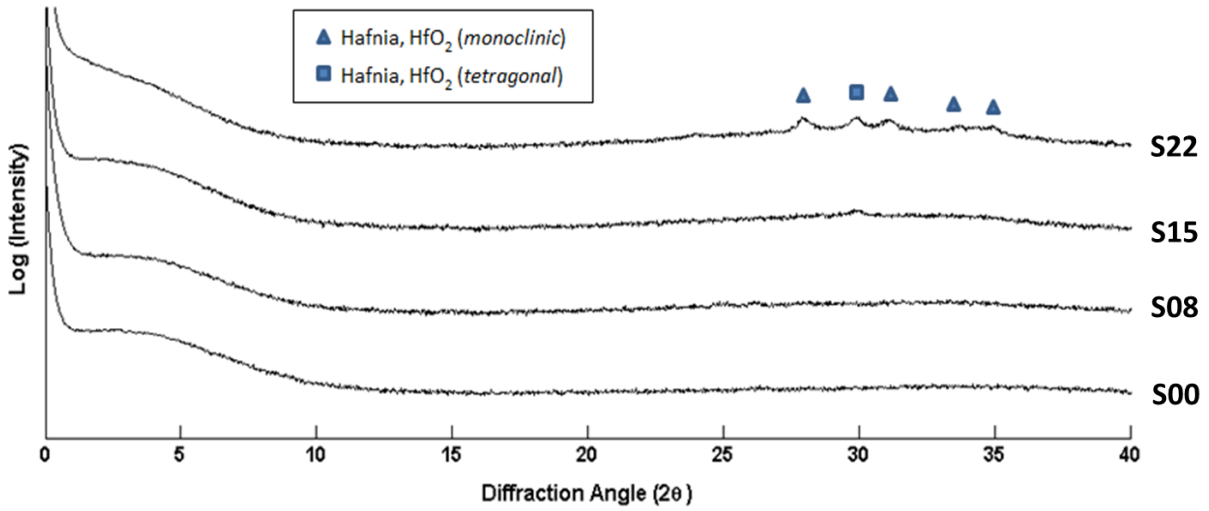

Fig. 47. X-ray diffraction patterns of pyrolyzed HfSiCNO powders

Further evidence for nano-size crystals of HfO_2 is found by the existence of both m-HfO_2 and t-HfO_2 phases. Bulk hafnia is nominally monoclinic phase at room temperature and converts to tetragonal upon heating to ~1700°C. However, at nano length scales the crystal structure becomes dominated by surface energy effects resulting in a different phase. Reports in literature shows size dependent phase conversion from tetragonal (and/or cubic) to monoclinic at sizes of ~6 nm [136, 137]. Note that it is difficult to distinguish the difference between cubic and tetragonal phases when the diffractions peaks are small since the primary diffractions peaks fall atop one another. The peak patterns in these samples appeared most consistent with tetragonal phase. The size dependent phase transformation is expected to be on the order of ~10nm.

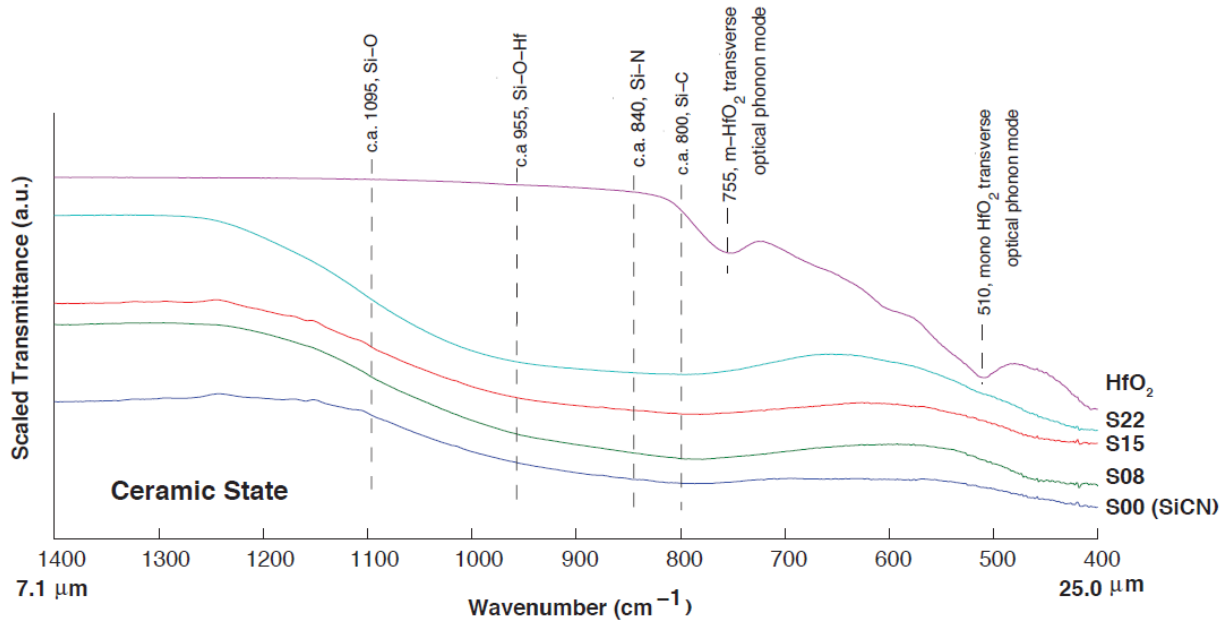

Fig. 48. Mid-IR spectra of the HfSiCNO ceramic state. Undoped SICN and commercial HfO_2 are included for reference

FTIR analysis showed distinct bonding schemes and reaction pathways in the liquid and epoxy state. The ceramic state FTIR spectra of Fig. 48, however, are far less revealing. The near-IR spectra were featureless confirming the absence of hydrogen in the system after pyrolysis. Absorption frequencies depend on both the bond stiffness and relative masses of the constituent atoms. For these HfSiCNO-H systems, only H-bonds are seen in the near-IR due to the extremely low atomic mass of hydrogen. The mid-IR showed broad absorbance bands, spanning several hundred wavenumbers, confirming a wide dispersion of vibration states in the amorphous ceramic. The S22 sample shows a shallow peak at 510 cm^{-1} that is assigned to the transverse optic phonon mode of monoclinic HfO_2 [134, 135]; this peak is absent in S08 and S15. These results are consistent with X-ray diffraction spectra which show broad X-ray diffraction peaks of HfO_2 for S22 but not for the lower Hf compositions [75].

The mid-IR regime shows two distinct bands. The most prominent band spans from approximately 700 cm^{-1}-1200 cm^{-1} and includes Si-C, Si-O, Si-N, and Si-O-Hf bonds. A low frequency band is also evident < 550 cm^{-1}. However, experimental limits prevented measuring this band in its entirety with the lowest experimental frequency cutoff being 400 cm^{-1}.

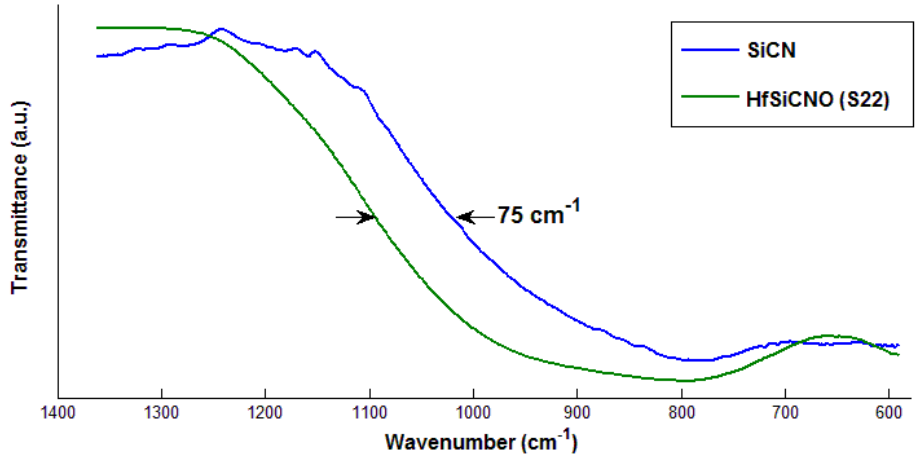

Fig. 49. Blue shift of ~75cm^{-1} in sample S22 IR absorption band edge compared to S00

Both absorption bands show a widening of the high frequency edge with increasing amounts of doping. In S00 the primary band spans from 700 cm^{-1} to 1100 cm^{-1}. With increasing Hf-O content the absorption intensity increases and (in case of S22) extends to 1250 cm^{-1}, Fig. 49. This shift is attributed to the increase in Si-O bonding in the doped materials.

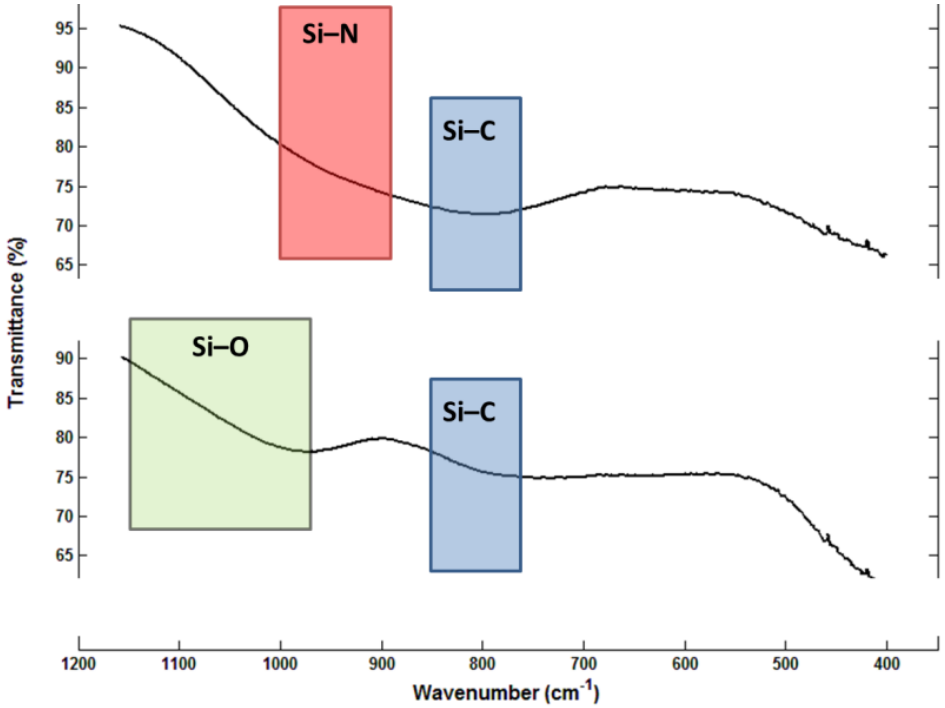

Fig. 50. Comparison of SiCN (top) and SiCO (bottom) ceramic state IR spectra.

This point is demonstrated nicely in Fig. 50 which shows a comparison of the IR bands for polymer derived SiCO and SiCN ceramics pyrolyzed at 1000°C. Both materials show a broad Si-C absorption centered at 800 cm^{-1}. In the case of SiCN (S00 sample), the Si-C and Si-N peak centers are close enough in frequency that they merge to form one broad absorption. The Si-C and Si-O bonds, on the other hand, can be identified as independent absorptions with the Si-O peaks extending to higher frequencies. Mixtures of SiCNO show an extension of the high frequency edge due to an increased presence of Si-O bonding.

The lower frequency band, which terminates at ~500 cm^{-1} in S00, also shows a widening with increasing Hf-O concentration. This edge extends to ~600 cm^{-1} in the S22 sample with highest hafnium and oxygen concentration. This band is harder to deconvolute due to the relatively tight overlap of peaks within this range. Simple

harmonic oscillator calculations given in Appendix B find Hf-(O,C,N) stretch modes to be within this range. The Hf-O bond, with absorption from 520-620 cm^{-1} depending on Hf coordination, is expected to the most responsible for the edge widening of the low frequency band. Hf-N (436-534 cm^{-1}) and Hf-C (476-583 cm^{-1}) would contribute as well, though their band centers are more closely aligned with that observed in S00. This would likely add more to absorption intensity rather than a significant widening of the band.

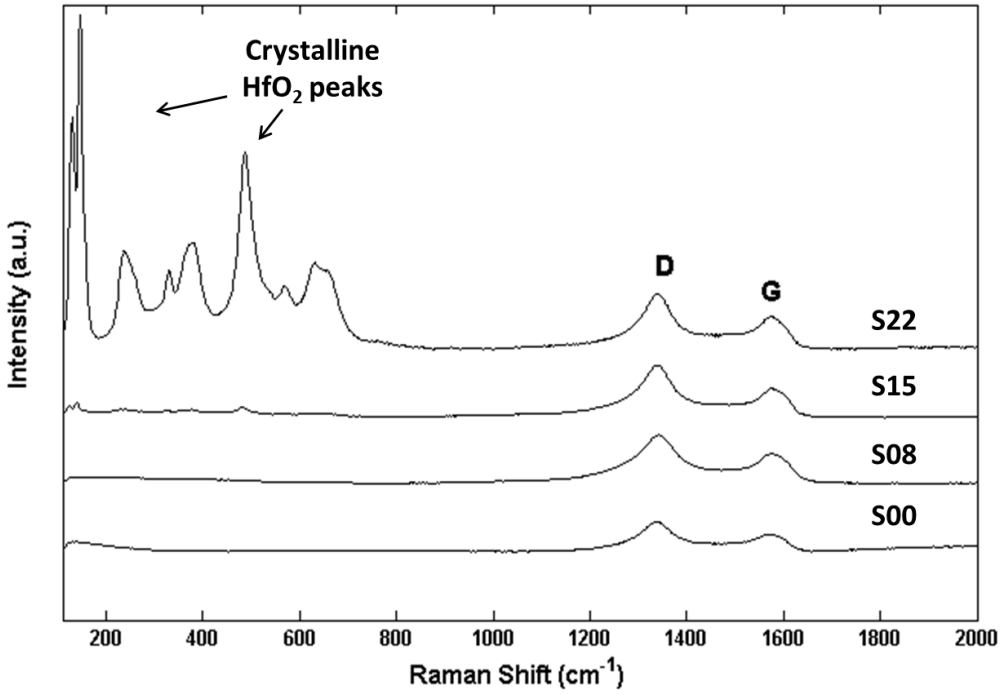

Fig. 51. Raman spectra of ceramic HfSiCNO compositions

Raman spectra were collected on all ceramic powder samples, Fig.51. They too show a complete absence of H- bonding. Samples appeared amorphous except for S22 which shows a distinct fingerprint of peaks for crystalline HfO_2 in the 100 cm^{-1} to 800 cm^{-1} range. These results confirm XRD and FTIR results which show no long range order of

HfO_2 up to a Hf:Si ratio of 0.22. The crystalline peaks in the Raman spectra are quite striking compared to those from XRD and FTIR. It is unknown what the experimental detection limits are for crystallite size, but it is worth noting for future studies that the Raman spectrometer (chosen to observe carbon structure) appears to be an ideal detection tool for nano-scale crystalline precipitates. Quantitative Raman was not attempted in this work; however, it could be performed with the inclusion of a reference intensity standard in similar fashion to the X-ray diffraction RIR method for quantitative analysis [139].

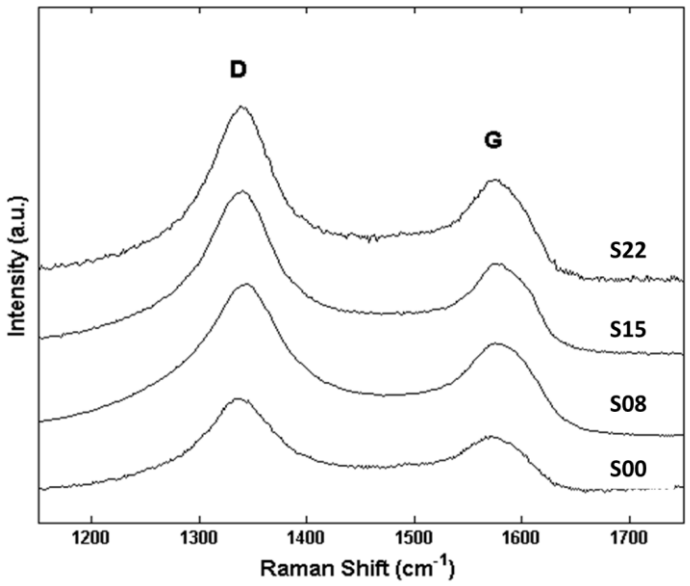

Fig. 52. Raman spectra of sp^2 carbon D and G peaks

The primary focus of the Raman spectra was to observe the materials' carbon structure which is only visible by XRD if the carbon is crystalline and by FTIR in unique cases [140]. Distinct D and G sp^2 carbon peaks are observed in all samples at 1340 cm^{-1} and 1580 cm^{-1}, respectively, Fig. 52. As discussed in Section 1.4.2, Raman sp^2 D and G carbon peaks are a signature of nanostructured PDCs. It is interesting that the carbon structure remains intact even with the significantly lower carbon content. It

can be seen from Fig. 53 that the relative carbon content decreases considerably with higher Hf-O doping, only 10% mol in S22. It is expected that the "free carbon" content present in PDCs stabilizes the amorphous structure and is directly responsible for their lack of crystallization at high temperature. The nano-scale precipitates of HfO_2 in S22 may be an indicator of the minimum carbon content necessary to maintain the amorphous nanodomain structure of SiC(N,O) materials.

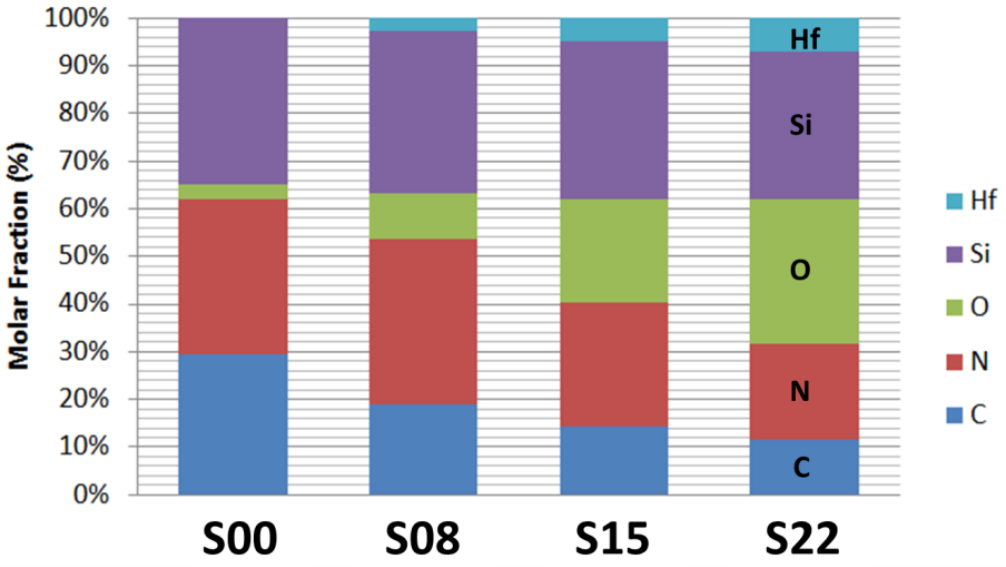

Fig. 53. Chemical composition diagram of prepared HfSiCNO ceramic powders. Note the decrease in carbon content with increasing Hf-O doping

A qualitative assessment of carbon order can be determined from the relative D and G Raman peak ratio. The G peaks corresponds to the stretching of sp^2 carbon rings [141]. In an idealized sp^2 state, such as pristine graphite or graphene, only the G peak would be evident. The D peak arises from defects in the carbon structure and has been attributed to double resonant Raman scattering [142, 143]. Corresponding overtones of the D and G peaks (not shown) were also observed in these materials centered at ~2775cm^{-1}.

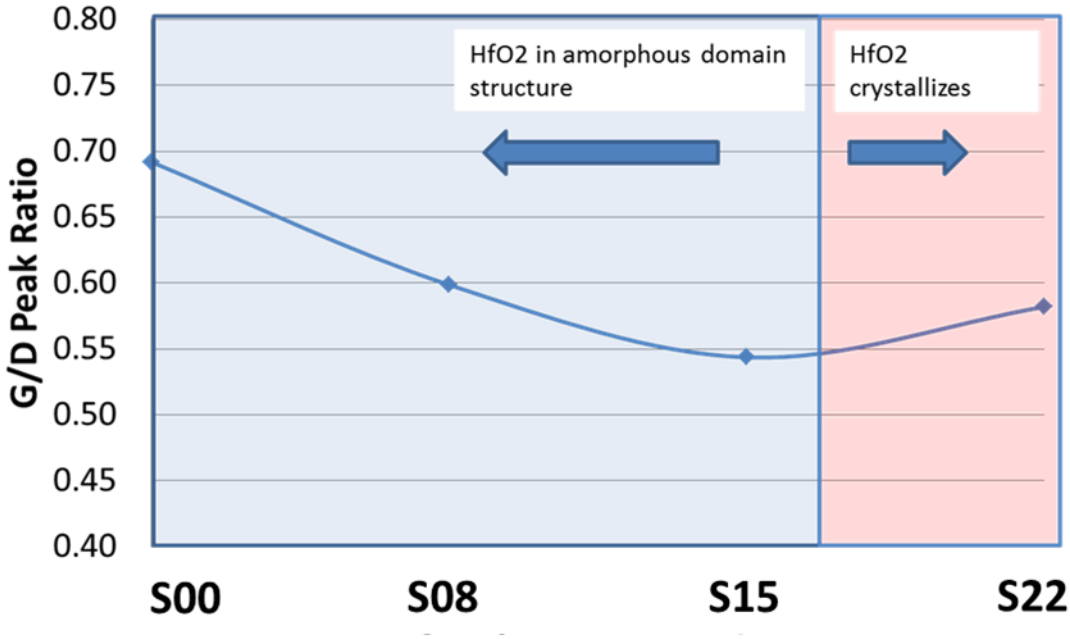

Fig. 54. Carbon G/D Raman peak ratio showing increased disorder with Hf content

The intensity of the carbon D and G peak ratio after baseline correction are plotted in Fig. 54 as I(G)/I(D). This shows decrease in sp^2 graphitic order with an increase Hf doping. This trend is qualitatively consistent with the decrease in carbon content up to a Hf:Si ratio of 0.15. With further Hf-O doping the I(G)/I(D) ratio appears to level off. Any additional doping of Hf-O results in crystallization of HfO_2 precipitates surrounded by an HfSiCNO matrix.

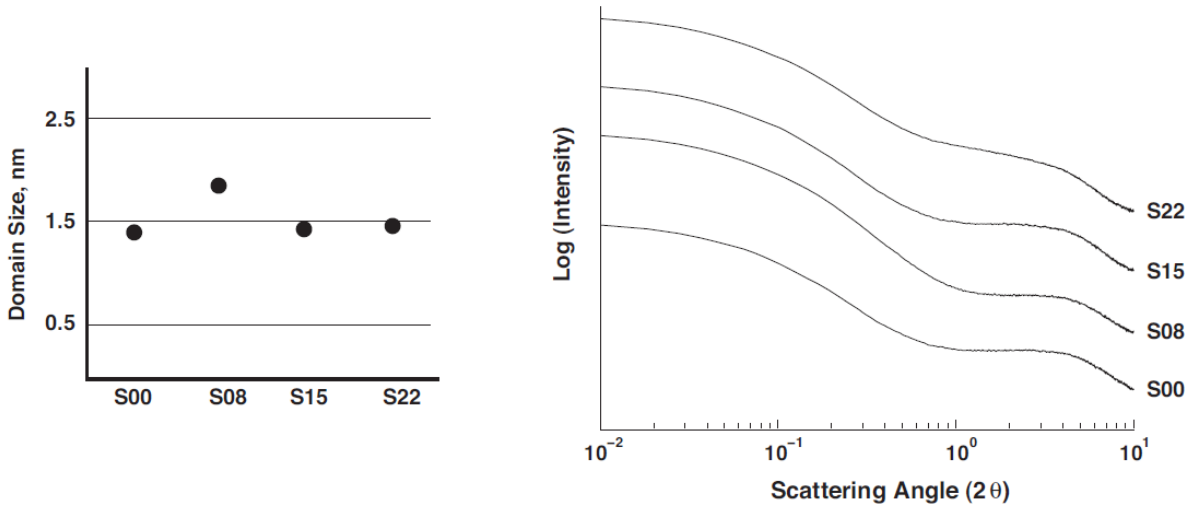

Fig. 55. Calculated nanodomain sizes (left) and corresponding SAXS profile (right)

The nanodomain structure of polymer-derived materials is difficult to analyze with tools such as TEM or XRD because of their amorphous nature. Small-angle x-ray scattering were performed on the 4 compositions to gage domain size. The domain structure of these materials, similar to SiCNO, is visualized to be amorphous Hf,Si,N,O with interspersed networks of disordered carbon. The calculated domain sizes and respective SAXS profiles are shown in Fig. 55. Details of the experimental SAXS technique and calculation of domain sizes are given in the Appendix C. These results show the domain size to remain essentially unaltered with increasing Hf-O doping.

Ab-initio molecular simulations were performed on models which parallel the experimental compositions. Each model consisted of 100 atoms. The amorphous HfSiCNO structure was created by heating to ultra-high temperature, 5000°K, and then quenching to create a melt-like state. Specific details of analysis are given in literature [144].

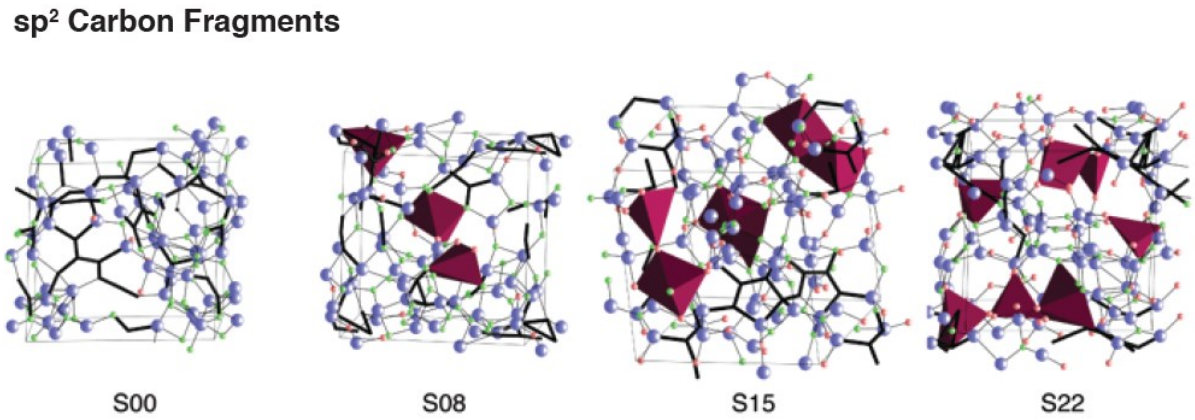

Fig. 56. HfSiCNO ab-initio models for the various experimental compositions. Shown are carbon segments (black), silicon atoms (purple), oxygen (red), nitrogen (green), and hafnium centered polyhedral (burgundy). *(Image from Peter Kroll, University of Texas at Arlington)*

Results for structure of S00, S08, S15, S22 are shown in Fig. 56. The HfSiCNO structures comprise predominantly Hf-C,N,O and Si-C,N,O bonds, as well as C-C bonds. The absence of C-O, N-N, O-O, and O-N bonds is consistent with NMR studies of polymer-derived-ceramics reported in [145-148]. Also consistent with these studies is carbon being in sp^2 coordination when bonded to itself and in the sp^3 state when bonded to Si. Note the segregation of carbon fragments. The "free carbon" is consistent with experimental Raman observations and other materials of similar structure such as SiCO [149,150].

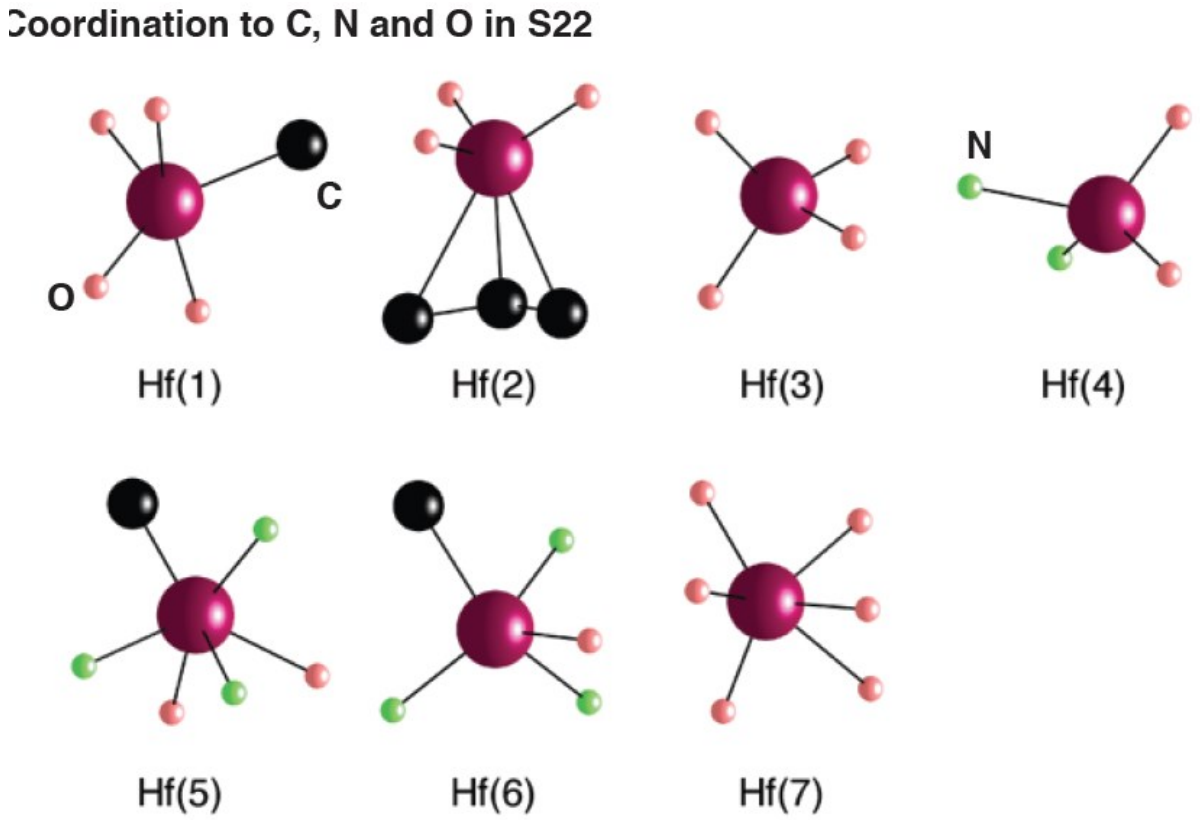

Fig. 57. Various coordination around a central Hf atom observed in S22. Shown are hafnium (red), carbon (black), oxygen (red), and nitrogen (green). *(Image from Peter Kroll, University of Texas at Arlington)*

An interesting discovery by the models is the various Hf coordinations. Only a couple known studies to date have examined the coordination structure of dopants experimentally. These models show various coordination around Hf ranging from tetrahedral to octahedral. Also observed are a variety of mixed bonding schemes which include Hf-(C, N, O) bonds, which is consistent with experimental observation. No Hf-Hf bonds were observed. Trace amounts of Hf-Si, Si-Si, and C-N bonds were observed, as well as defective sites such as 3-coordinated Si and 2-coordinated C. However, these are expected to be the result of limiting the models to such a small number of atoms.

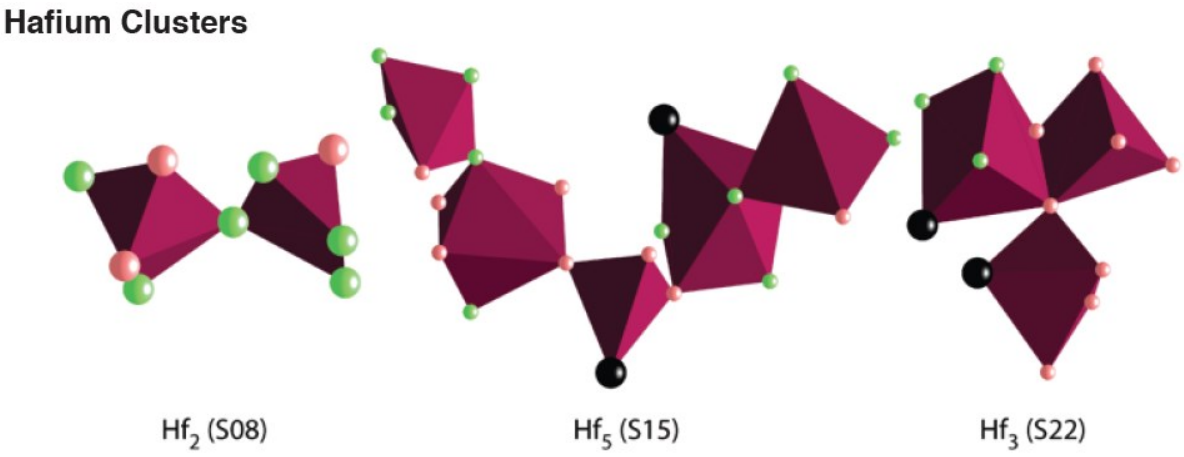

Fig. 58. Observed Hf chain-like clusters in S08, S15, and S22. *(Image from Peter Kroll, University of Texas at Arlington)*

In addition to carbon segregation, it is observed that Hf-centered polyhedral tend to form chainlike configurations, as shown in Fig. 58. The average model coordination of Hf is 5.3 and Si is 3.7. Models corresponding to the three HfSiCNO compositions were created where the Hf content was extracted as HfO_2. The energy difference between these SiCNO models and the HfSiCNO reflect the enthalpy of inserting HfO_2 into SiCNO. This energy can then be compared to crystalline HfO_2. A positive value would suggest HfO_2 favors crystallization and a negative value favors amorphous HfO_2 solubility in SiCNO. The energy of mixing was computed to be -0.71, -0.41 and +0.49 eV per HfO_2 unit. This results corresponds nicely with XRD, FTIR, and Raman measurements which shows solubility of HfO_2 up to a Hf:Si ratio approaching 0.22.

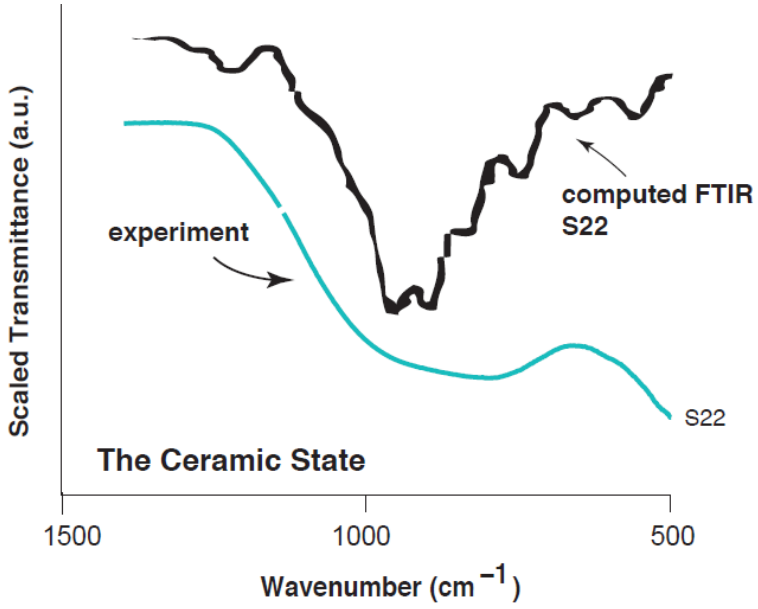

Fig. 59. Experimental IR spectra of S22 compared with simulated spectra from ab-initio model

The FTIR spectra for the amorphous ceramic state yields broad absorption bands, as has been reported in the literature [113]. Nevertheless an attempt to compare the experimental FTIR spectra with computationally calculated spectra for the case of S22 sample is considered. The results presented in Fig. 59 have the important caveat that the computed spectrum is from a small sample size which cannot determine absorption at long wavelengths. Thus, the computed spectrum does not show much absorption beyond 1000 cm^{-1}. However, the apparently close resemblance between theory and experiments in the 1000 cm^{-1} to 1400 cm^{-1} range is quite striking. The computed "sample size" consisted of mere 100 atoms, and therefore the absorption spectrum contains undulations from reflecting vibration states.

3.5 Ultra-high Temperature Behavior of HfSiCNO

The behavior of polymer derived SiCN, SiCO and HfSiCNO (S08) powders were characterized after annealing in argon atmosphere from 1300-1500°C. Specific weight change and crystallization behavior from carbothermal reduction are measured. The high-temperature transition from reducing to oxidizing regimes is given as a function of oxygen partial pressure for SiCN. It is shown that the suppression of decomposition in oxidizing environments is due to the virtual gas pressure (p_{N_2} or p_{CO}) which occur at the SiO_2-SiCN interface while the oxide layer is growing.

3.5.1 Inert Atmosphere Behavior

Powders of polymer derived SiCN, SiCO, and HfSiCNO were prepared using methods discussed previously in Section 3.41. Powders were annealed at 1300°C, 1400°C, and 1500°C for up to 25 hrs, and weight change was tracked at 5 hr interrupted intervals, Fig 60. The powders were contained in graphite crucibles. Annealing was performed in a Centorr M60 tungsten element furnace with under flowing argon at ambient pressure.

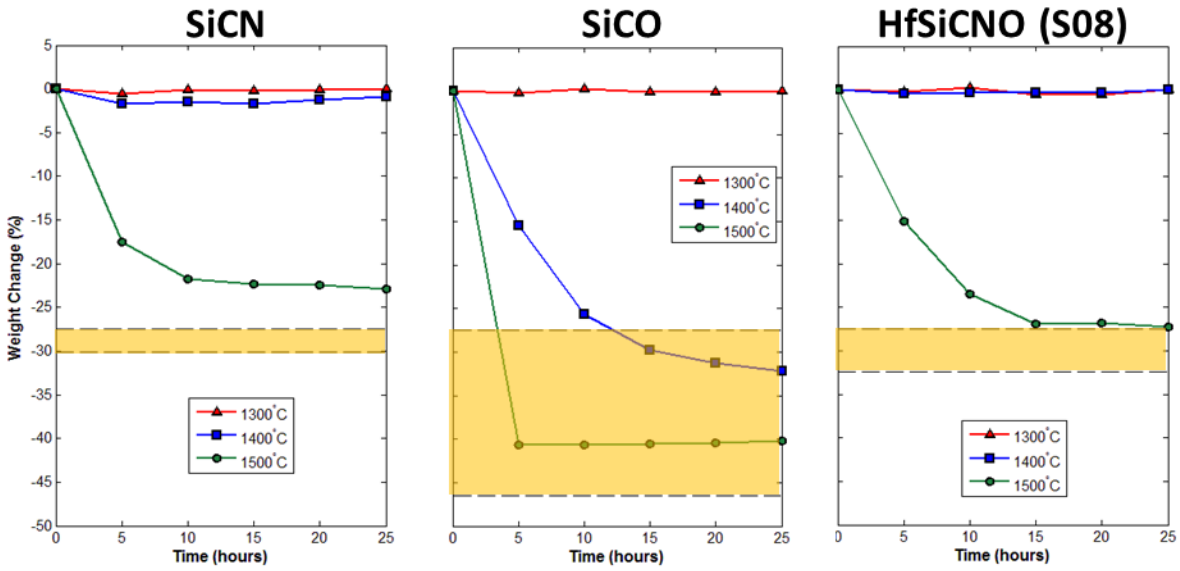

Fig. 60. Rapid weight loss from carbothermal reduction for different PDC systems in Ar

All three materials appear to be stable at 1300°C with no measurable weight loss. All show rapid decomposition at 1500°C with SiCO reducing completely within the first 5 hours. The nitrogen containing systems showed slower reduction at 1500°C, 10 hrs for SiCN and 15 hrs for HfSiCNO. At 1400°C, only the SiCO decomposed. The shaded regions in Fig. 60 represent the calculated weight loss from reduction of the powders based on their initial chemistry. The lower bound is the predicted weight loss if all N and O were removed from the powders, in the form of CO and N_2, where the graphite crucible provides any shortage of carbon to form CO and (Hf,Si)C. This is necessary since the both the crucible and powder were weighed as one. The upper bound of the shaded region assumes only the O and N leave the system without sacrificing any carbon from the crucible. In this case the PDC materials were assumed to reduce to elemental Si and Hf if there were not enough inherent carbon in the powders themselves for carbothermal reduction.

It is expected there is scalable error in the plots which was never fully quantified. A significant problem with these experiments was finding a crucible which was non-reactive with the PDC materials at these temperatures. The weight measurements were taken as powder + crucible with the crucible weight being factored out afterwards. Graphite was chosen as the crucible material with the understanding that is may react with excess oxygen in the SiCO and HfSiCNO systems and may also provide carbon to any materials which have deficiency to fully reduce the systems to HfC and SiC. It was noticed that the carbon crucible experience some surface pitting during UHT annealing. The exact reason is unknown but a likely explanation is reaction with O to form CO. A dummy crucible was run simultaneously with the 3 samples to correct for crucible weight loss. Each of the four crucibles – SiCN, SiCO, HfSiCNO, and blank – did not appear to experience the exact same degree of crucible loss despite being run simultaneously. This lead to some visible error in the data. For example, the 1400°C curve of SiCN shows 1-2% weight loss. This, in reality, is expected to be poor correction of crucible weight loss. SiC crucibles would likely be a better choice over graphite for future experiments.

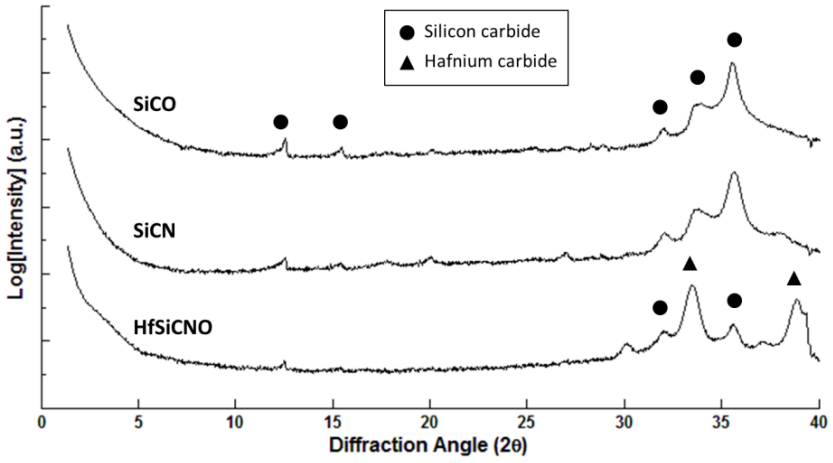

Fig. 61. X-ray diffraction patterns of SiCO, SiCN, and HfSiCNO polymer derived ceramics after annealing in inert atmosphere for 25 hrs.

X-ray diffraction patterns of samples were collected after the annealing at 1500°C for 25 hrs in argon. The only detectable peaks were Si and Hf carbide phases, shown in Fig 61. No oxide or nitride phases were observed. Similarly, there were no elemental peaks of C, Hf, Si. The lack of other peaks suggests complete carbothermal reduction at 1500°C.

The PDC powders were relatively coarse prior to annealing, ~50μm, having only been milled by mortar and pestle. After annealing the large particles were effortlessly crushed to much further refinement. The conclusion here is that the PDCs decompose rapidly within the bulk leaving behind small carbide particles. Hardly visible under the optical microscope, the carbide particles are expected to be nano-scale in size. Other evidence of nano-scale carbide is seen by the powerful small angle shoulder (<5 °2θ) and broad carbide diffraction peaks.

3.5.2 Weight loss/gain dependency on oxygen partial pressure

In the previous section it was shown that polymer derived materials of SiCN, SiCO, and HfSiCNO can rapidly decompose via carbothermal reduction at 1500°C. This carbothermal reduction is accompanied by crystallization and sharp weight loss. In oxidizing environments, however, the same materials typically show weight gain which is attributed to the formation of a passive oxide layer of SiO_2 at the exposed surfaces, Fig. 62.

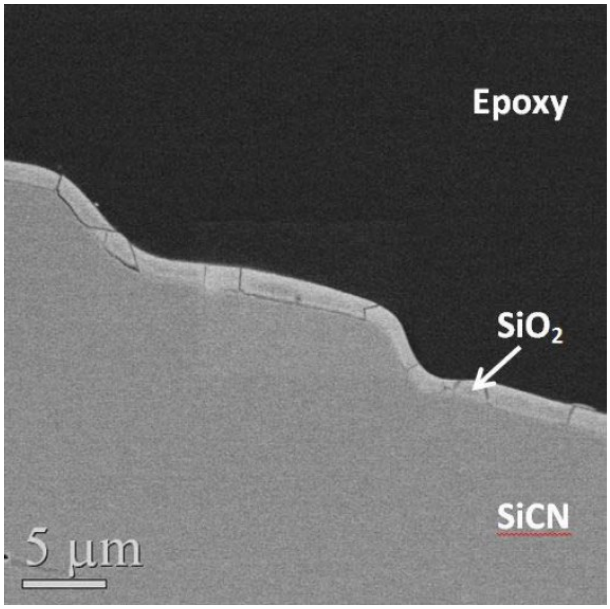

Fig. 62. Oxidized SiCN particle showing growth of passive SiO_2 layer

The carbothermal reduction of SiCN appears to be a bulk phenomenon occurring rapidly throughout, whereas the passive oxide formation is strictly a surface effect. This section details the weight/loss gain transition of SiCN as a function of the partial oxygen pressure, p_{O_2}, and demonstrates that the decomposition is tied to the virtual CO or N_2 pressure at the SiCN-SiO_2 interface. Sufficiently high interface pressure, which encapsulates the SiCN particle bulk, can prevent crystallization and decomposition of the SiCN while (and only while) the passive oxide layer is growing.

The $Si_{0.35}C_{0.29}N_{0.32}O_{0.03}$ powder was prepared as detailed in Section 3.4.1. Weight change of the particles were carried out in a Netzsch TGA (Model STA409, Netzsch-Geratebau GmbH, Selb, Germany) were recorded in various oxygen pressure atmospheres. The four different atmospheres were ambient air (p_{O_2} = 0.21), 10%O_2 in Ar (p_{O_2}= 0.1), 1%O_2 in Ar (p_{O_2}= 0.01), and ultra-pure Ar containing ~5ppm O_2 (p_{O_2}= $5x10^{-6}$). Oxygen concentration was measured by a trace oxygen analyzer (Model 2001RS, Advanced Micro Instruments, Inc. Huntington Beach, CA). Specific surface

area of the powder was measured to be 1.55 m^2g^{-1} by nitrogen adsorption BET (Model ASAP 2010, Micrometrics Instrument Corp. Norcross, GA). Powders were contained within SiC crucibles. Blank crucible baselines were run for each study to account for SiC crucible oxidation in high p_{O_2} and some degree of reaction between the SiC crucible and Al_2O_3 platform of the TGA in low p_{O_2}.

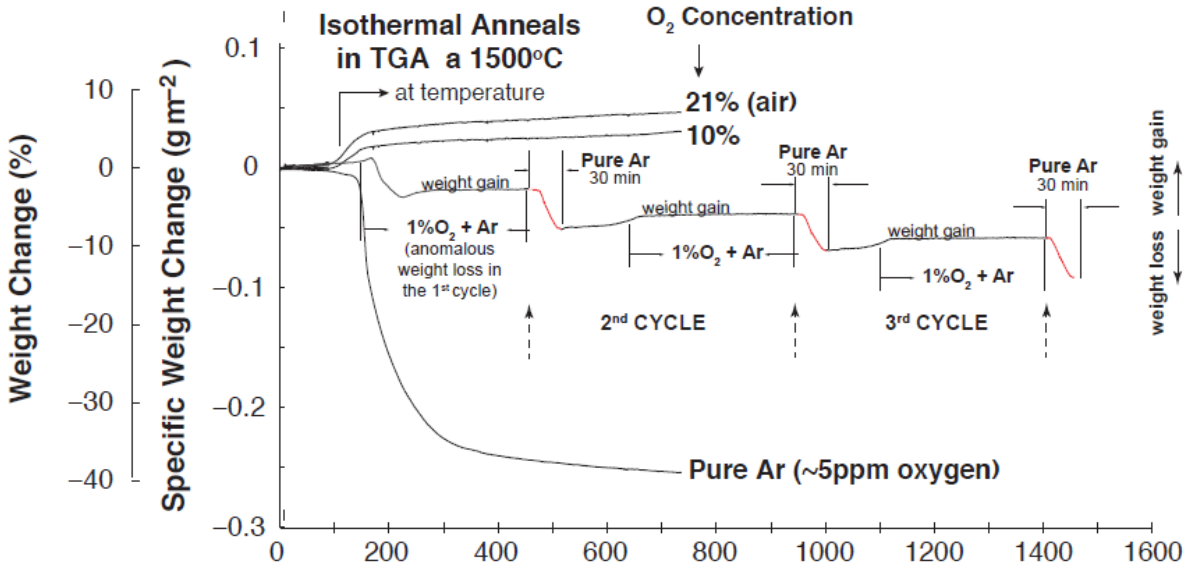

Fig. 63. Weight loss and weight gain in SiCN(O) when exposed to different oxygen atmospheres at 1500°C

The SiCN weight gain/loss behavior at 1500°C are shown in Fig. 63 as time and p_{O_2}. These data include the thermal ramp up which takes 145 minutes. The 10%O_2 and 21%O_2 samples begin to show weight gain during the ramp and continue at temperature. This measured weight gain is due to the formation of silica by the following:

$$Si_1C_{0.83}N_{0.91}O_{0.09}(s) + 1.37O_2^*(g) = SiO_2(s) + 0.83CO^*(g) + 0.46N_2^*(g)$$

The base material is oxidized by environmental O_2 to form SiO_2. Carbon monoxide and diatomic nitrogen are the gaseous products of the reaction. Literature has shown that

the oxidation of SiCN materials under these conditions show quadratic growth behavior, like the oxidation of Si and SiC. It can be concluded from the quadratic growth rate that the rate limiting step is the diffusion of some species through the passive oxide scale, illustrated in Fig. 64. Thermal oxidation of pure Si is known to be rate limited by O_2 diffusion through the oxide scale (except for the early stages of oxidation where there is a reaction limited initial transient). The thermal oxidation of SiC at high temperatures are an order of magnitude lower than Si, though still exhibiting quadratic growth, lending to the belief that SiC oxidation is rate limited by CO diffusion through the oxide scale. SiCN oxidization rates are comparable to SiC and therefore is expected to be rate limited by the same means.

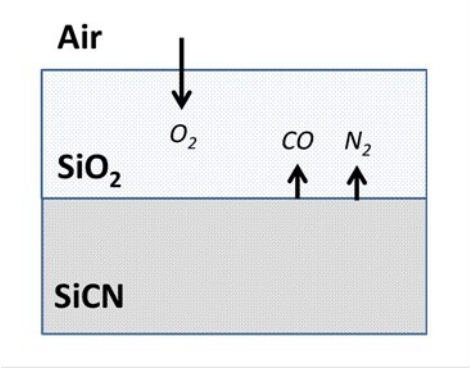

Fig. 64. Oxidation schematic of SiCN showing inward diffusion of O_2 and outward diffusion of CO and N_2

The SiCN powder in pure Ar (5 ppm O_2) shows rapid decomposition upon reaching 1500°C. This is due to the crystallization of SiCN into SiC. Significant weight loss accompanies this by the release of gaseous CO and N_2.

The 1%O_2 cycle showed a three stage behavior. (1) The first stage shows a small amount of weight gain from passive oxidation during the furnace ramp when below ~1450°C. In the previous section it was shown that SiCN begins to decompose via carbothermal reduction between 1400°C and 1500°C in oxygen free environments. (2)

The second stage shows a sharp weight loss from carbothermal reduction followed by (3) a slow growth from continued passive oxidation.

Various SiCN trials were performed at 1%O_2 and consistently showed this anomalous loss of weight upon reaching 1500°C. Further experiments were carried out cycling between 1%O_2 and pure Ar, shown in Fig. 63. Only the first cycle showed this anomalous behavior. It is not fully understood why this singular decomposition exists. It may be attributed to surface chemistry which is dissimilar to the bulk SiCN. STEM elemental mappings have shown that ceramic fibers created from the polymer route can have differing surface chemistries up to 150 nm in thickness [151]. The anomalous weight loss may also be tied to a low interfacial CO pressure when the oxide layer is very thin and the supply p_{O_2} for oxidation is low. After the first cycle the 1%O_2 sample showed consistent cycling behavior. The first step of the cycle is 1%O_2 where the material shows a small weight gain from passive oxidation. This is followed by a sharp weight loss from carbothermal reduction when the environment is switched to pure Ar.

The varying p_{O_2} experiments demonstrate that bulk carbothermal reduction of SiCN is suppressed while the particle is oxidizing. Subsequent analysis shows that the unoxidized core of an SiCN particle remains unaltered while the surface oxidizes. The cycling experiments demonstrate that the SiO_2 layer only protect the particle from decomposition while the passive SiO_2 is growing. The explanation for this is due to high interfacial pressures (or virtual pressures) of either outward diffusing CO or N_2. If the passive SiO_2 layer itself was responsible for the lack of decomposition, then the material would not show weight loss when cycled to Ar.

If the oxidation of SiCN is rate limited by CO diffusion outward (or N_2), then it is expected that significant pressures of CO can build at the interface. It has been shown that crystallization behavior of similar SiCN material at 1600°C can be controlled by

artificially imposing varying degrees N_2 overpressure [152]. When the p_{N_2} is less than ~4 bar, the SiCN decomposed to SiC. High p_{N_2} (>11 bar) crystallizes the SiCN in to Si_3N_4 and carbon. Between these two regimes the material shows no weight change and remains amorphous.

This study shows a similar effect, only that the decomposition here is restricted intrinsically during oxidation by interfacial gas pressure resulting from the oxidation reaction. The reaction for carbothermal reduction to SiC is

$$Si_1C_{0.83}N_{0.91}O_{0.09}(s) \;=\; 0.74SiC(s) + \;0.26Si(s) + 0.09CO(g) + 0.46N_2(g) \qquad (13)$$

It is assumed here that complete reduction takes place and any excess silicon, which cannot react to form SiC, reduces to elemental Si. The gaseous byproducts are carbon monoxide and diatomic nitrogen. The equilibrium condition for carbothermal reduction is,

$$\Delta G_{SiCNO} = 0.74\Delta G_{SiC} \;+\; 0.09\Delta G_{CO} - RT\ln\left(p_{CO}^{-0.09}p_{N_2}^{-0.46}\right) \qquad (14)$$

where $p_{N_2}$and p_{CO} are the atmospheric pressures of nitrogen and carbon monoxide. ΔG_{SiCNO}, ΔG_{SiC}, and ΔG_{CO} are the free energies of formation of SiCNO, SiC, and CO from the standard state of their constituents. The latter two values can be obtained from thermochemical tables [123]. However, the free energy of formation for SiCN remains unknown. The condensed Si phase has an activity of 1.

The same can be carried out for the oxidation reaction,

$$Si_1C_{0.83}N_{0.91}O_{0.09}(s) + 1.37O_2^*(g) \;=\; SiO_2(s) + 0.83CO^*(g) + 0.46N_2^*(g) \qquad (15)$$

where the base SiCN material reacts with atmospheric oxygen to form a passive oxide layer of SiO_2. As seen in Fig. 65 the governing pressures for the oxidation reaction are determined by the gas pressure at the SiO_2-SiCN interface where the reaction takes

place. The pressures here exist from gases which are in solution at the interface and are therefore referred to as virtual pressures. The virtual pressures for O_2, N_2, and CO at the interface are denoted as $p^*_{N_2}$, $p^*_{O_2}$, and p^*_{CO}. The equilibrium condition for Eq.15 is

$$\Delta G_{SiCNO} = \Delta G_{SiO_2} + 0.83\Delta G_{CO^*} - RT\ln\left(p_{O_2^*}^{1.37} p_{N_2^*}^{-0.46} p_{CO^*}^{-0.83}\right) \quad (16)$$

Equating (13) and (16) gives,

$$-\Delta G_{SiO_2} - 0.83\Delta G_{CO^*} + 0.74\Delta G_{SiC} + 0.09\Delta G_{CO} = -RT\ln\left(\frac{p_{O_2^*}^{1.37} p_{N_2^*}^{-0.46} p_{CO^*}^{-0.83}}{p_{CO}^{-0.09} p_{N_2}^{-0.46}}\right) \quad (17)$$

which can be reduced to,

$$\Delta G_{SiO_2} + 0.74[\Delta G_{CO} - \Delta G_{SiC}] = RT\ln\left(p_{O_2^*}^{1.37} \cdot \frac{p_{CO}^{0.09}}{p_{CO^*}^{0.83}} \cdot \frac{p_{N_2}^{0.46}}{p_{N_2^*}^{0.46}}\right) \quad (18)$$

Note that $\Delta G_{CO^*} = \Delta G_{CO}$ since the free energy of formation of a species will be the same irrespective of whether it is at the interface or elsewhere. To prevent decomposition the ambient pressures of CO and N_2 must be greater than those specified by the equilibrium condition of Eq (14). Similarly during oxidation, decomposition of SiCNO will be suppressed when $p_{CO^*} \geq p_{CO}$ and $p_{N_2^*} \geq p_{N_2}$ in Eq (18).

The interfacial pressures of each gas species during oxidation are dependent on the respective diffusivity of the species through SiO_2. No measurements of CO or N_2 diffusivity through SiO_2 could be found in literature. Nitrogen has been shown to have high solubility in SiO_2 [153]. Silica is also used as a successful sintering aid for Si_3N_4 demonstrating that SiO_2 permits transport of Si and N through the glass by solution precipitation [154]. Therefore, nitrogen is expected to have a relatively high diffusion rate through SiO_2 resulting in a low interfacial $p_{N_2^*}$. Diffusion of O_2 is not expected to be rate limiting or the oxidation kinetics of SiC and SiCN should be roughly the same as Si, which is not the case. There is a significant body of evidence (see Section 1.3) to

suggest that CO diffusion through silica is the rate limiting mechanism for the oxidation of SiC and SiCN materials under the experimental conditions applied in this study. Thus, the interfacial pressure is dependent on the rate of CO production at the interface and the diffusivity of CO through the SiO_2 scale. Further evidence of this was shown in Section 2.4 by the formation of CO bubbles at the oxide growth interface.

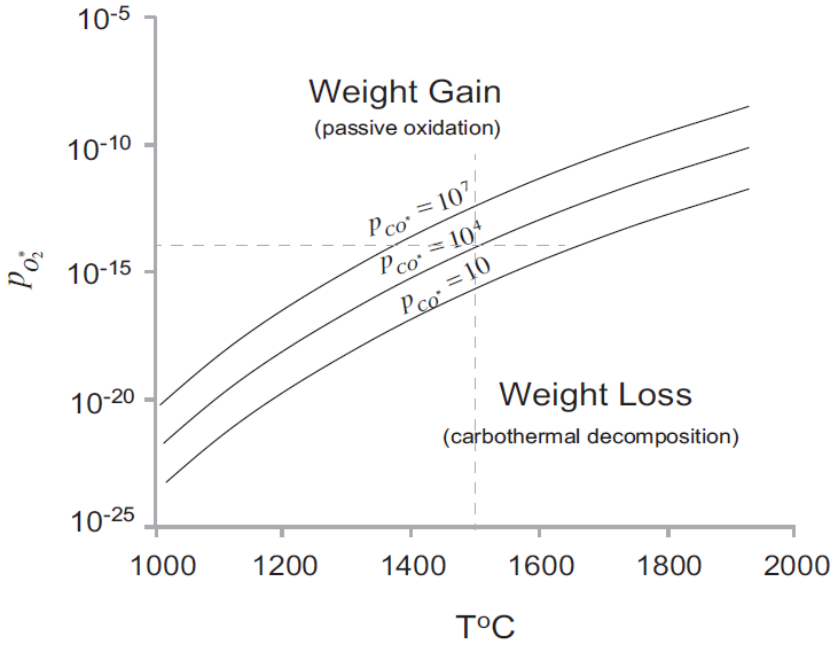

Fig. 65. SiCN decomposition condition

It is to be noted from Eq (6) that the equilibrium condition for decomposition also depends on the interfacial oxygen pressure, $p_{O_2^*}$, which is an unknown quantity and a function of p_{O_2}. The interfacial p_{CO^*} is also unknown and is estimated from the oxidation of SiC to be in the range 10-10^5 atm in the 1400°C-1800°C range. Substituting values for free energy of formation into Eq (18) and plotting for $p_{O_2^*}$ gives Fig. 65. The current experiments, done at 1500°C, show the $p_{O_2^*}$ transition to be in the 10^{-10} to 10^{-15} atm over the range of expected p_{CO^*}. These interfacial pressures of O_2 are within the range predicted from a recent study which estimated them from oxidation $p_{O_2^*}$ [155].

3.6 Oxidation Behavior of HfSiCNO

This section gives a detailed study on the oxidation behavior of HfSiCNO ceramics up to 1600°C in ambient air.

3.6.1 Sample Preparation

Multiple oxidation studies were performed to access the oxidation behavior of HfSiCNO. S08, S15, and S22 composition powders were used in early experiments. These powders were used to develop a basic understanding of the oxidation mechanism and reactions. Quantitative x-ray analysis was performed on S08 powders, and a model was created to relate measured weight gain to oxide scale overgrowth. Nominally S08 composition thin films were also deposited on SiC-SiC minicomposites and measured for oxidation protection. Latter experimental powders used for cross-section analysis were of S14, S26, and S39 compositions. The “S - -”nomenclature is again to denote the Hf:Si ratio. For example, S14 means a Hf:Si ratio of 0.14 in the pyrolyzed ceramic state. The HfSiCNO powders were prepared as detailed in the preceding section.

SiC–SiC minicomposites, in the form of cylindrical rods with a diameter of about 1 mm, were fabricated from a single tow of SiC fibers (Sylramic fibers, 500 fibers/tow, fiber diameter 10 μm). The individual fibers were surrounded by a thin weak boron nitride interphase of thickness 0.5–2 μm. The fiber bundle was within a matrix of SiC formed by chemical vapor infiltration. The outer layer of the matrix surrounding the fiber bundle was about 40 μm thick. These minicomposites were coated with a layer of SiCN and HfSiCNO by dip-coating in a solution of 0.5% precursor in 99.5% tetrahydrofuran. A dipping feed rate of ~1 cm/s was used. The polymer films deposited by dip-coating were

immediately cross-linked at 300°C by heating on a hot plate. The dip-coating and cross-linking was carried out within a glove box. Ten dip cycles were followed by pyrolysis for 2 hrs at 1000°C. The final coating having a thickness of ~1 μm was achieved by 40 dip cycles, which included four pyrolysis steps.

All oxidation experiments were carried out in ambient air. Two sets of studies were performed. In one case, a molybdenum silicide element box furnace, which could accommodate large sample quantities for chemical and X-ray analysis, was used. In the second set of experiments, the weight gain during oxidation was measured in a silicon carbide element thermogravimetric analysis tube furnace (Netsch). All samples were placed in alumina crucibles during oxidation. Samples were oxidized for 1 hr at 1400°C, 1500°C, and 1600°C with heating and cooling rates of 5°C/min. Extended oxidation on HfSiCNO powders up to 50 hrs was performed at 1500°C; weight gain was measured and translated into estimates of oxide scale thickness with a simple model. In addition, extended oxidation of single crystals of 6H–SiC (Cree, Inc.) was performed at 1500°C for side-by-side material comparison.

The SiC–SiC minicomposites were oxidized in a molybdenum disilicide element furnace with a hot zone of 25 mm. The samples were made to extend significantly outside the furnace hot zone to prevent silica formation at the exposed ends which can lead to wicking of the silica along porosity and interfaces into the interior of the composite. The oxidation was carried out in ambient air at 1600°C for up to 1000 hours. The fiber tow minicomposites resulted in unique oxidation behavior and required different analysis than offered in the remainder of this section. Tow oxidation results are given in Appendix F.

3.6.2 Chemistry and Phase Evolution in Oxidized HfSiCNO

S00, S08, S15, and S22 powder were oxidized in air and for 1 hr at 1400°C, 1500°C, and 1600°C. All samples were x-ray amorphous after pyrolysis at 1000°C except for S22 which showed precipitates of monoclinic and tetragonal HfO_2 on the order of ~10nm. Their x-ray diffraction patterns after oxidation are shown in Fig. 66. Each spectra shows a strong Nb peak at 38.5°, which was introduced in the form of Nb powder to serve as a reference intensity standard for quantitative x-ray analysis using the reference intensity ratio (RIR) method.

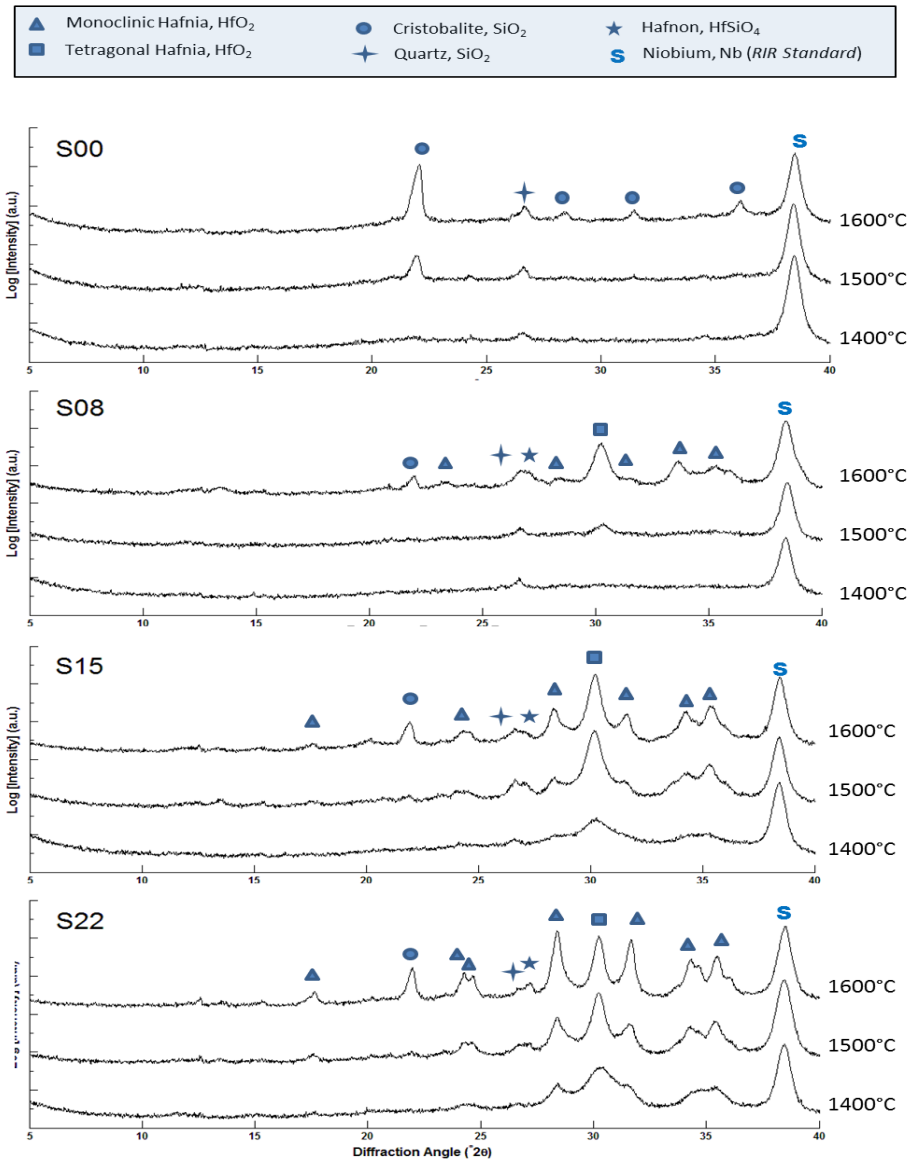

Fig. 66. Phase evolution in HfSiCNO powders after oxidation for 1 hour in air

X-ray results of S00 show the evolution of cristobalite and a trace amount of quartz, both polymorphs of SiO_2, after oxidation. The quartz peak arises after oxidation at 1400°C and the cristobalite at 1500°C. There is expected to be significant amounts of amorphous SiO_2 as well which will not show distinct diffraction peaks.

Additionally, the Hf containing materials showed peaks of monoclinic hafnia (m-HfO_2), tetragonal hafnia (t-HfO_2), and hafnium silicate ($HfSiO_4$). At low concentrations and temperatures the tetragonal hafnia is the dominant phase. Monoclinic hafnia becomes more prevalent with greater temperature and Hf concentration due to a greater crystal size of HfO_2. Hafnia shows size dependent phase transitions in the nano-scale regime from surface energy effects. This phenomenon was also observed in the S22 sample after pyrolysis. Relatively small quantities of $HfSiO_4$ are also evident. However, it is difficult to interpret qualitatively since the primary $HfSiO_4$ and SiO_2 (quartz) peaks have significant overlap.

Note the complete absence of crystalline graphite, carbide phases, and nitride phases. It was shown previously that these PDC materials can self-decompose at 1500°C in inert environment by carbothermal reduction. The formation of oxide suppress decomposition in HfSiCNO, presumably by the same means as pure SiCN (Section 3.5.2) where CO pressure at the oxidation front encapsulates the particle and prevents decomposition.

These results show that HfSiCNO oxidized to form binary oxides of (Hf, Si)O_2 and $HfSiO_4$. The expected oxidation reaction is

$$HfSiCNO(s) + O_2(g) \rightarrow HfO_2(s) + SiO_2(s) + CO(g) + N_2(g)$$

where SiO_2 and HfO_2 are the remaining solid state oxide phases and CO and N_2 are gaseous byproducts of the reaction.

3.6.3 Oxide Scale Morphology

Scanning electron microscope (SEM) images and energy dispersive X-ray spectra (EDS) were used to characterize the morphology of the HfSiCNO powder after oxidation. The results show the formation of a SiO_2 + $Hf_{1-x}Si_xO_2$ composite oxide scale and precipitation of HfO_2 nano-crystals in the unoxidized regions of the HfSiCNO particles.

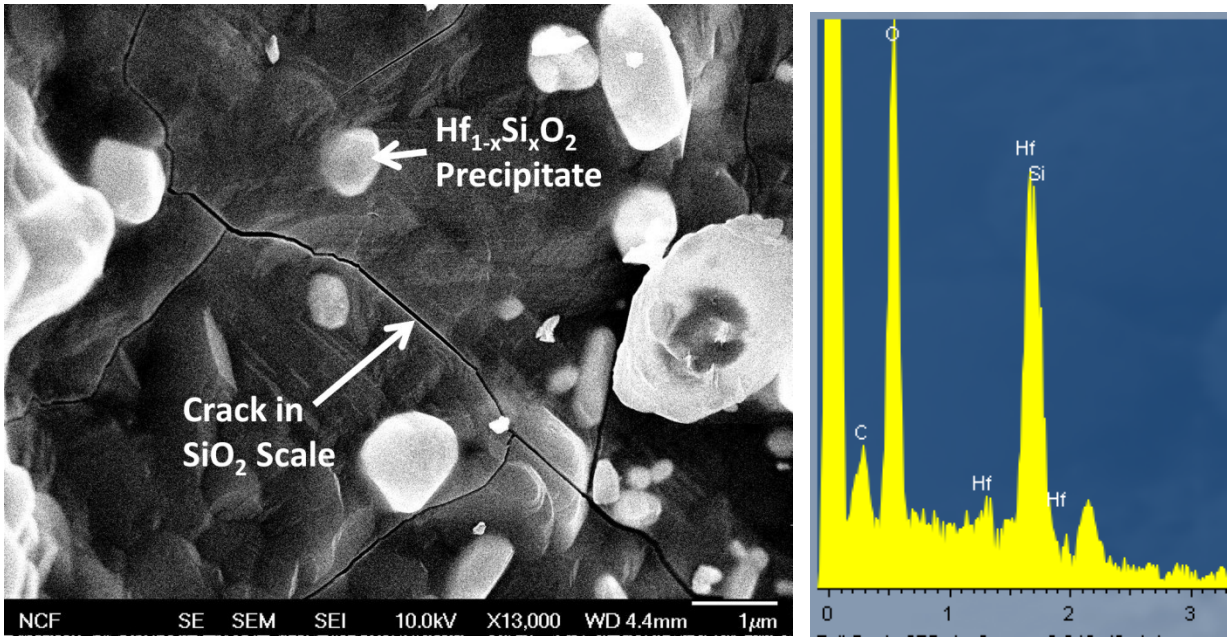

Fig. 67. Surface SEM micrograph of HfSiCNO (S08) particle oxidized for 50hrs at 1500°C, and EDS spectra of precipitates showing Hf-Si-O chemistry

The surface SEM micrograph shows spherical Hf based precipitates (bright contrast) in a SiO_2 matrix. The spots size for EDS is ~500 nm making it difficult to conclusively identify the precipitate chemistry from EDS alone. However, an EDS spectra consistent with that of $HfSiO_4$ was identified on some particles large enough to cover the spot size. Combining the XRD patterns, EDS spectra, and observations from the multilayer experiments of Ch.2, it can be concluded that the precipitates found in the oxide overgrowth emerge as HfO_2 and then react with the surrounding SiO_2 to form $HfSiO_4$.

Cracks in the SiO_2 matrix are also evident and are believed to form upon furnace cooling due to thermal expansion mismatch between the oxide scale and underlying HfSiCNO.

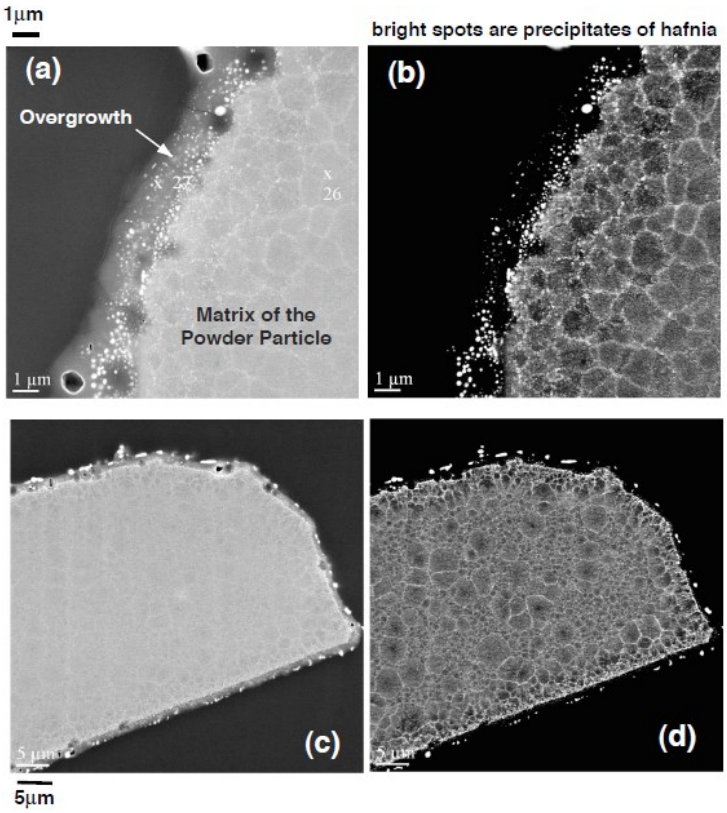

Fig. 68. Cross-section SEM micrograph of HfSiCNO (S08) particle oxidized for 50hrs at 1500°C. The left are secondary electron images, and the right are backscatter electron images. *(Images from David Marshall, Teledyne Scientific Company, Thousand Oaks, CA)*

S08 powders oxidized for 50 hrs at 1500°C were cross-sectioned with a large area ion mill and viewed under the SEM, Fig. 68. The left images were viewed with secondary electrons. They show a developed oxide scale thickness of ~2 μm at the particle surface. Bright hafnium-containing precipitates are evident at three size scales and spatial distributions: (i) relatively large precipitates (~0.2–1 μm diameter) located near the outer surface of the silica overgrowth; (ii) smaller precipitates (~50–100 nm diameter) within the silica layer and aggregated near the base of the layer; and (iii) fine

precipitates (~20 nm diameter) in the interior of the particles, partially segregated into necklace-like patterns that bound domains of diameter ~1–3 μm. These domains are consistently smaller near the surfaces of the particles (within about 5 μm of the surface) than in the interior.

The images on the right were taken with backscatter electrons which show better sensitivity to elemental contrast. These images show a granular-like structure in the particle's unoxidized core. The oxide overgrowth in the secondary electron image in Fig. 68 is darker than regions within the necklace domains in the interior of the particle. This difference is attributed to the length scale of the hafnia precipitates in the oxide overgrowth and the interior. The hafnia precipitates in the oxide overlayer are large and well separated by darker regions that are depleted in hafnium. Within the particle, the hafnia particles are much smaller. In fact, in addition to the ~20 nm size hafnia crystals in the necklace arrangement, there are even smaller precipitates within the necklace domains, as seen in Fig. 69. This fine distribution of hafnia grains within the particle interior is the reason for the brighter contrast.

Note the presence of bubbles, presumably CO, within the oxide scale. If CO diffusion is the rate limiting factor, then one would expect bubbling in silica from p_{CO} buildup along the oxidation front. Bubbling during oxidation was very apparent in the SiCN-HfO_2 multilayer experiments (Ch. 2) because they would become trapped beneath the dense HfO_2 layer. SiO_2 glass, on the other hand, has low viscosity at high temperature which enables CO to bubble cleanly though. This makes it much more difficult to find bubbles trapped in the SiO_2 layer in systems such as the SiCN, SiC, or HfSiCNO. Furthermore, traditional polishing techniques tend to fill in these small voids with polishing debris rendering them invisible.

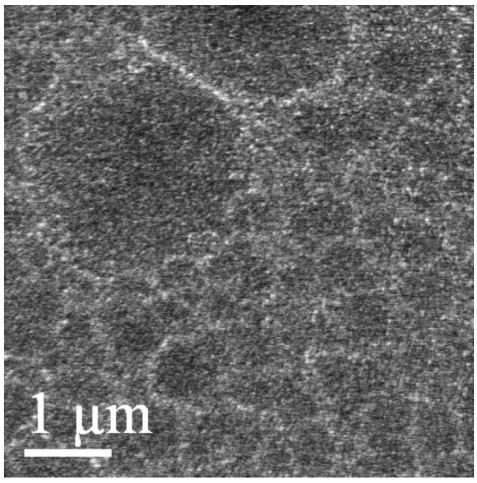

Fig. 69. Higher mag backscattered electron image from interior of oxidized HfSiCNO showing distribution of fine hafnia precipitates in the walls and interior of necklace pattern domains. *(Image from David Marshall, Teledyne Scientific Company, Thousand Oaks, CA)*

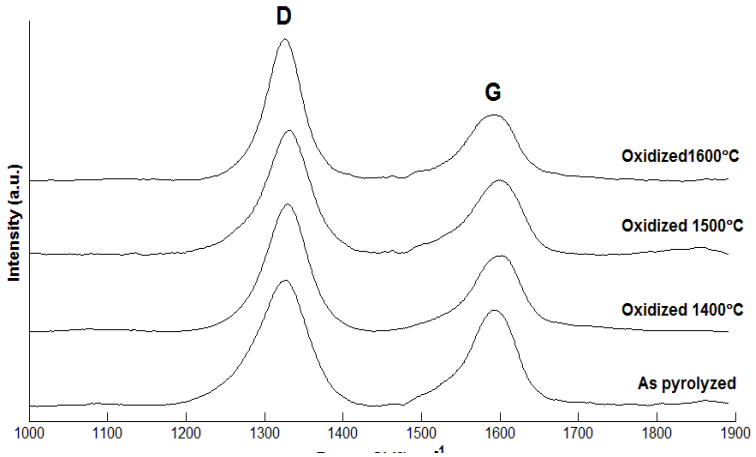

Fig. 70. Raman spectra of HfSiCNO carbon peaks after oxidation for 1 hour at 1400°C, 1500°C, and 1600°C

Despite the HfO_2 precipitation within the HfSiCNO matrix during oxidation, the internal carbon structure appears to remain unaltered, seen in Fig 70. X-ray diffraction shows no other evidence of crystallization within the unoxidzed regions, only HfO_2. The sharp boundary between the oxide overgrowth and the interior domains suggests that the oxidation of the material occurs by a different mechanism than the precipitation of hafnia within it. No “dendritic” penetration of the viscous silica overgrowth into the matrix is

observed, meaning that the necklace network does not facilitate rapid diffusion of oxygen into the matrix. Similar studies of PDC compounds doped with Zr and Hr have shown this nano-scale $(Zr,Hf)O_2$ precipitates as well. The reason for the grain-like necklace pattern of HfO_2 precipitates remains an open question. The typical size of the crystals in the necklace configurations are a few tens of nm while the evenly dispersed crystals are less than 10 nm. One possible explanation is that the pyrolysis step produces internal stresses that are distributed on the length scale that is reflected in the necklace pattern.

3.6.4 Quantitative X-ray Analysis

Quantitative x-ray diffraction analysis was performed on oxidized SiCN and HfSiCNO particles using the reference intensity ratio (RIR) method. Details of the analysis and methods used are given in Appendix D.

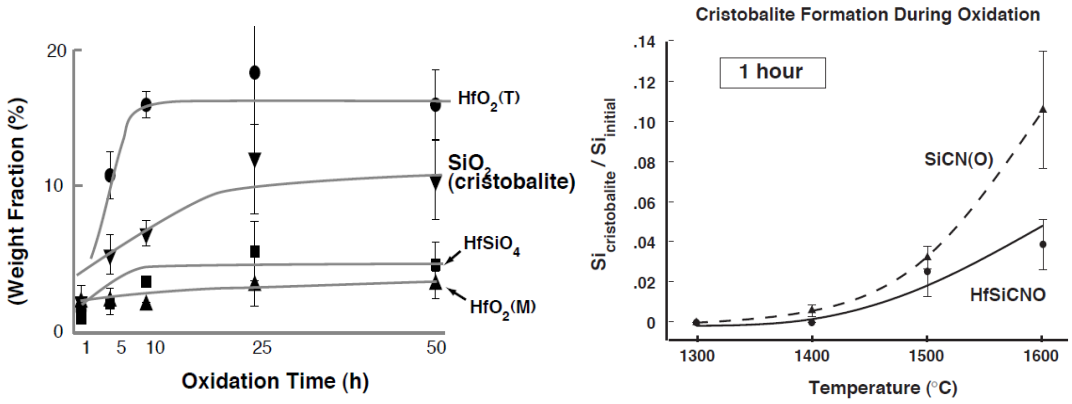

Fig. 71. Phase content of S08 oxidized at 1500°C (left), and evolution of cristobalite from SiCN and HfSiCNO after oxidation for1 hour 1400-1600°C.

The results from the quantitative X-ray analysis are given in Fig. 71. The interesting point to note is the saturation of the crystalline oxides (cristobalite, hafnia, and hafnium silicate) after 10–20 hours. Quantitative X-ray analysis requires an understanding of the

penetration depth of the X-rays into the surface of the particle. The chemical constitution of HfSiCNO was $Hf_{0.03}Si_{0.34}C_{0.19}N_{0.35}O_{0.09}$ which gives a mass absorption factor of 62.88 cm^2/g for CuKα1 radiation.[156] Multiplying the density of the powder by the mass absorption factor gives the linear absorption coefficient of 184.6 cm^{-1}. Density of the HfSiCNO powder was measured experimentally to be 2.936 g/cm^3 by Archimedes principle. It is calculated that the incident X-rays would have lost 90% intensity within the range of 0.75–2.0 μm, depending on the diffraction angle. The thickness of the overgrowths in 10–20 hrs at 1500°C was ~1 μm, and at 50 hrs in the 1.8–2.0 μm range. Therefore, the majority of the x-ray peak intensity is coming from the oxide scale.

The cristobalite peak was further investigated by quantitative X-ray analysis. The results given on the right in Fig. 71 show that the addition of hafnium into SiCN significantly suppresses the formation of cristobalite. The result is presented as the ratio of Si in cristobalite to the Si in the original constitution of the powders. The exact mechanism for the suppression of cristobalite formation is unknown. One possibility is that Hf-O in solution with the glass prevents crystallization. It may also be due to the length scale of dispersed $HfSiO_4$ precipitates in the oxide. Literature has shown for the oxidation of SiC that the cristobalite can form large crystals at distant nucleation spacing of tens of microns or greater [157]. The sub-micron spacing of $HfSiO_4$ precipitates may prevent cristobalite crystals from achieving such large sizes.

3.6.5 Calculation of Oxide Thickness from Measured Weight Gain

HfSiCNO was shown to oxidize by the formation of passive SiO_2 overlayer containing HfO_2 and/or $HfSiO_4$ precipitates. Despite the volatilization of C and N species, the material shows a net weight gain during oxidation from the addition of environmental

oxygen. This section derives a model to relate the measured weight change during particle oxidation to the oxide scale thickness. The model assumes spherical geometry of a fixed particle size. Fig. 72 shows a schematic of the HfSiCNO particle during oxidation.

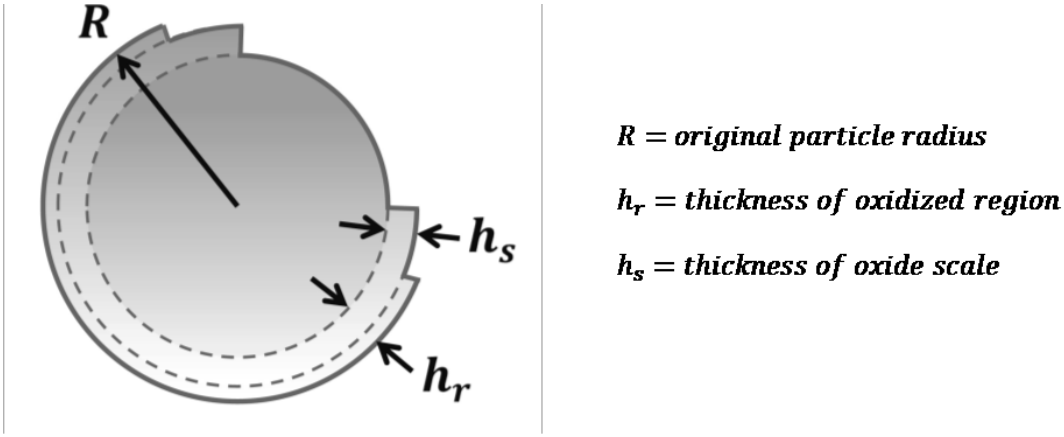

Fig. 72. Schematic representation of HfSiCNO particle during oxidation

For an initial material composition of $Hf_vSi_wC_xN_yO_z$ (where v + w + x + y + z = 1), the initial mass of one molar unit volume can be defined by,

$$M_1 = 178v + 28w + 12x + 14y + 16z \tag{19}$$

After the unit volume has been oxidized the resulting mass is

$$M_2 = v(178 + 32) + w(28 + 32) \tag{20}$$

Note that V_1 and V_2 are not equal.

The particle weights before and after oxidation are

$$W_1 = \frac{4\pi}{3} R^3 * \rho_1 \tag{21}$$

$$W_2 = \left[\left(\frac{4\pi}{3}(R - h_r)^3\right) * \rho_1\right]_{unoxidized\ core} + \left[\left(\frac{4\pi}{3}(R^3 - (R - h_r)^3)\right) * \rho_1 * \frac{M_2}{M_1}\right]_{oxidized\ region} \tag{22}$$

Since $h_r \gg R$, an approximation can be made that $(R - h_r)^3 \approx R^3\left(1 - \frac{3h}{R}\right)$.

Substituting this approximation into the weight ratio W_2/W_1 gives,

$$\frac{W_2}{W_1} = 1 + \frac{3h_r}{R} * \left(\frac{M_2}{M_1} - 1\right) \tag{23}$$

And solving for the thickness of the oxidized region, h_r,

$$h_r = \frac{R*\left(\frac{\Delta W}{W_1}\right)}{3*\left(\frac{\Delta M}{M_1}\right)} \tag{24}$$

This equation gives the total oxidized thickness, h_r, of the original particle as a function of the chemistry, measured weight gain, and particle size. Oxidation rate constants are usually reported in terms of oxide thickness, which in this case is defined as h_s. We can scale h_r into h_s by accounting for the respective densities of the raw material and its formed oxide.

The initial mass of the oxidized region be defined by the consumed volume and initial density as

$$M_{h_r} = \left(\frac{4\pi}{3}(R^3 - (R - h_r)^3)\right) * \rho_1 \tag{25}$$

This can then be converted to oxide scale mass by the scaling factor M_2/M_1 and then to volume by dividing the oxide density, resulting in a final oxide volume of

$$V_{h_s} = \left(\frac{4\pi}{3}(R^3 - (R - h_r)^3)\right) * \frac{M_2}{M_1} * \frac{\rho_1}{\rho_2} \tag{26}$$

The oxide scale volume can also be expressed geometrically as

$$V_{h_s} = \frac{4\pi}{3}((R - h_r + h_s)^3 - (R - h_r)^3) \tag{27}$$

Equating these two expressions for volume gives

$$\frac{4\pi}{3}((R - h_r + h_s)^3 - (R - h_r)^3) \;=\; \frac{4\pi}{3}(R^3 - (R - h_r)^3) * \rho_1 * \frac{M_2}{M_1} * \frac{1}{\rho_2} \tag{28}$$

Since $h_s \ll R$, then let $(R - h_r + h_s)^3 \approx R^3\left(1 - \frac{3(h_r - h_s)}{R}\right)$. Substituting this approximation and solving for h_s, Eq (28) reduces to

$$h_s = h_r * \frac{\rho_1}{\rho_2} * \frac{M_2}{M_1} \tag{29}$$

And finally substituting for h_r gives the oxide scale thickness

$$h_s = \frac{R}{3}\frac{\Delta W}{W_1}\frac{M_2}{\Delta M}\frac{\rho_1}{\rho_2} \tag{30}$$

This Eq (30) provides a simple approximation for scale thickness as a function of measured weight from oxidation.

3.6.6 Parabolic Rate Constant from Weight Gain Measurements

The weight changes for oxidized S08 composition powders were measured in interrupted tests at 1500°C at various times up to 50 hrs. These data were converted into the thickness of the overlayer using Eq (18). A plot of the square of the thickness versus time is given in Fig. 73. Note the slight increase in weight, relative to the weight of the pristine powder, at the start of the oxidation time. The step increase corresponds to an overgrowth thickness of 300–400 nm. Initial overgrowths of similar thicknesses have been reported in oxidation studies of SiBCN[151] and SiAlCN[158].

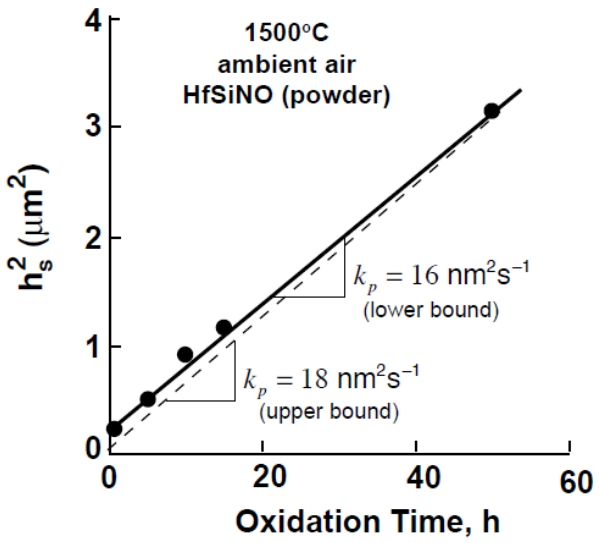

Fig. 73. Plot of the oxidation data for HfSiCNO powders at 1500°C.

The underlying mechanism for the rapid oxidation in the early stage is not understood. It may not be attributed to the ramp-up of the furnace up to the oxidation temperature; integration of the time-temperature with reasonable values of the activation energy [24] cannot account for an oxide overlayer of 300 nm. It is likely that the near-surface region of the particle develops a different chemistry which oxidizes more rapidly than the particle interior. The polymer to ceramic conversion of the particles requires the outward diffusion of hydrogen, which may affect the carbon and nitrogen concentration near the surface

The range of the values for the parabolic rate constant are obtained by measuring two slopes in plots of h_s^2 vs. time, one starting from the zero point, which gives an upper-bound value for the parabolic rate constant, and the other from the height of the initial step. These two values give a range for parabolic rate constant of 16-18 nm^{2}s^{-1}. The rate constant, k_p, is defined as:

$$h_s^2 = k_p \cdot t \tag{31}$$

where t is the oxidation time. The experiments with HfSiCNO powder were compared, for reference, with measurements of oxide scale growth of single crystal SiC by SEM cross-sections. The SiC single crystal gives a value for k_p in the range 15-21 nm^2s^{-1}.

3.6.7 Parabolic Rate Constant from Particle Cross-sections

HfSiCNO powders of composition S00, S14, S26, and S39 were prepared and oxidized in a $MoSi_2$ element box furnace at 1500°C. The chemical compositions of the powders are given in the table below. The powders were potted in epoxy after oxidation and cross-sectioned with a large area ion-miller for high-fidelity SEM images. Oxide scale thicknesses were taken directly from the images and quantified for oxidation rates.

Table 6. Molar compositions of HfSiCNO ceramic powders

	Hf	Si	C	N	O
S00	0.000	0.348	0.294	0.325	0.033
S14	0.048	0.333	0.146	0.267	0.206
S26	0.077	0.298	0.106	0.181	0.338
S39	0.099	0.257	0.077	0.117	0.450

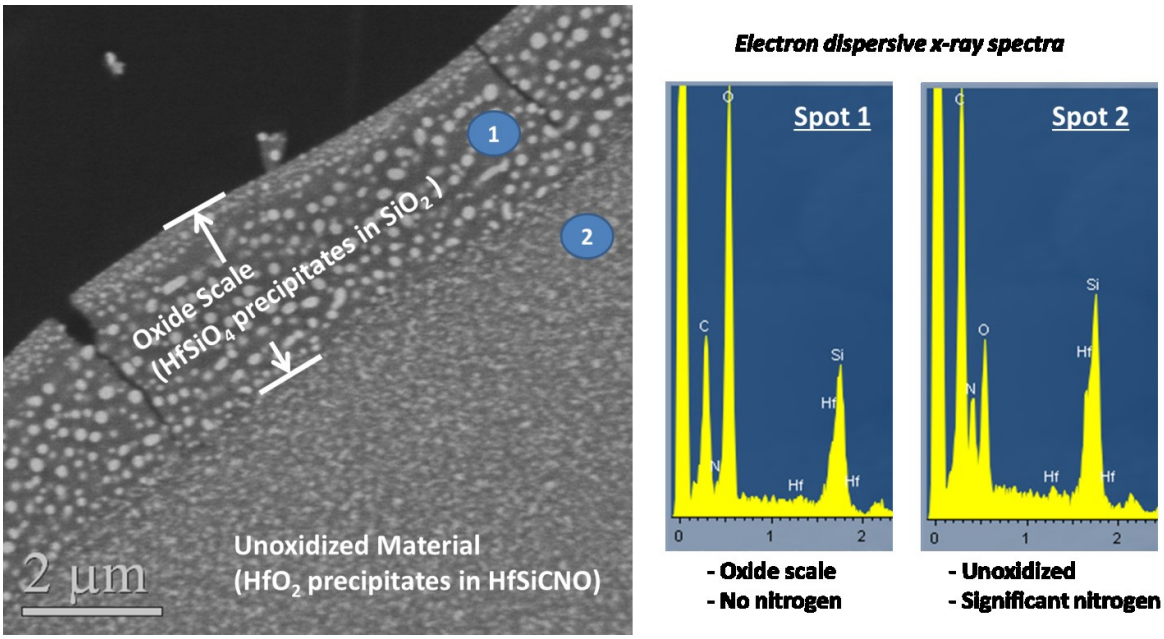

Fig. 74. Morphology of oxidized HfSiCNO (S39, 100 hrs) with corresponding EDS spectra

Fig. 74 shows a typical oxide scale for any of the given Hf containing samples. The material shows HfO_2 precipitates in the unoxidized material which are not due to inward diffusing O_2 but rather Hf-O content which is inherent to the native material. The material oxidizes, losing C and N, forming SiO_2 with precipitates of $HfSiO_4$. Note that the apparent carbon peak in both EDS spectra, Fig 74 (right), is an artifact of the measurement technique. The focused electron beam for spot chemistry analysis deposits small amounts of environmental carbon on the sample surface which is then detected by EDS.

There is a noticeable initial transient in oxidation which was common in all Hf-containing samples. This can be identified by the outer surface of the oxide layer which contains smaller precipitates (50 nm) than the remainder of the oxide layer (200 nm). This initial transient accounts for the first ~700nm of oxide thickness in the higher Hf concentration S26 and S39 samples. The S14 sample shows a significantly smaller transient layer which averages ~350 nm. This length scale is consistent with the initial step in

oxidation observed by weight measurements of S08 powder in the preceding section where an initial step of 300–400 nm was observed. The mechanism by which this layer forms is currently unknown.

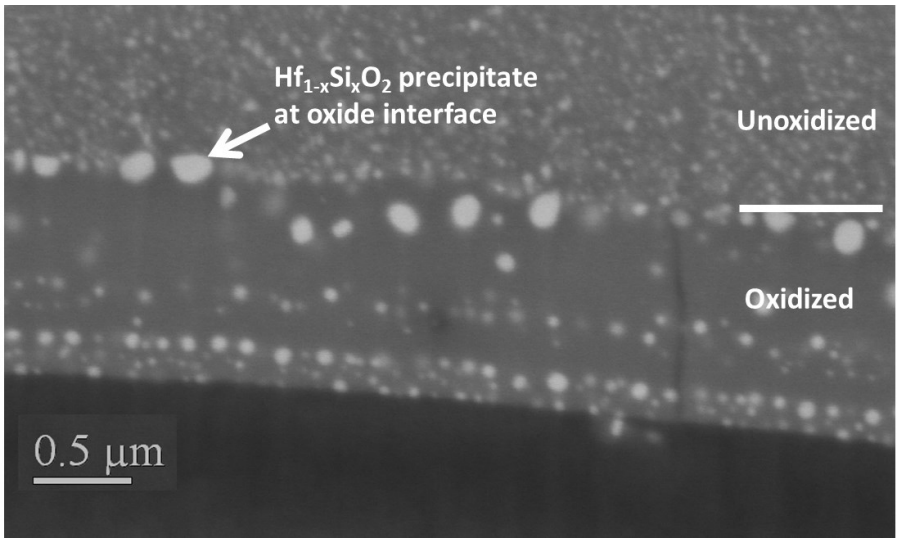

Fig. 75. Oxidized HfSiCNO (S08, 50 hrs) showing precipitates being carried with the oxidation front

The larger precipitates appear to cling to the oxidation front until they reach a critical size for detachment, shown at higher magnification in Fig. 75. This is more evident in the low Hf content samples where the precipitate distribution spacing is father apart. This detachment appears to be a size related phenomena, limiting size being ~200 nm, except for the initial transient stage of oxidation where the particles apparently detach by a different mechanism. It is unknown whether the precipitates are in the form HfO_2 and $HfSiO_4$ when they detach from the interface. TEM of the interface would be required to determine the specific phase.

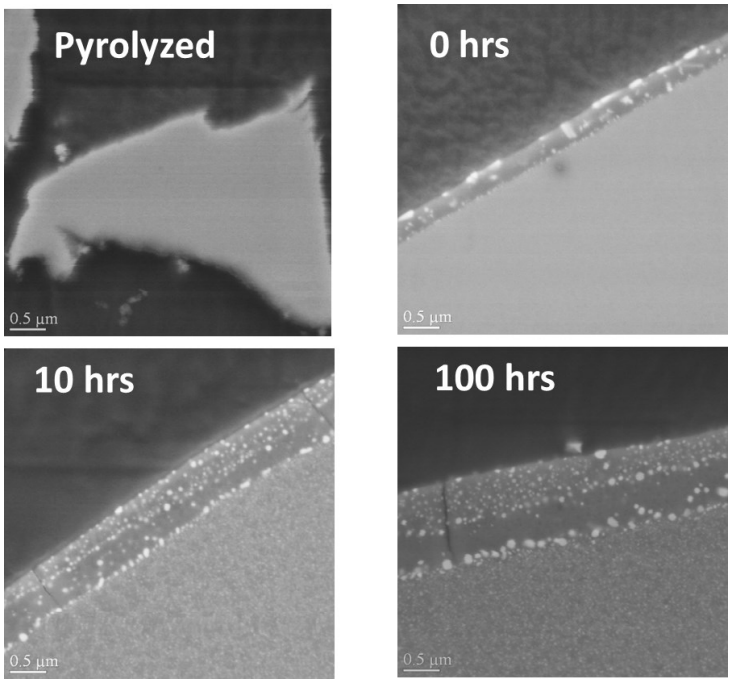

Fig. 76. Cross-section SEM images of oxide scale growth on S14 powders

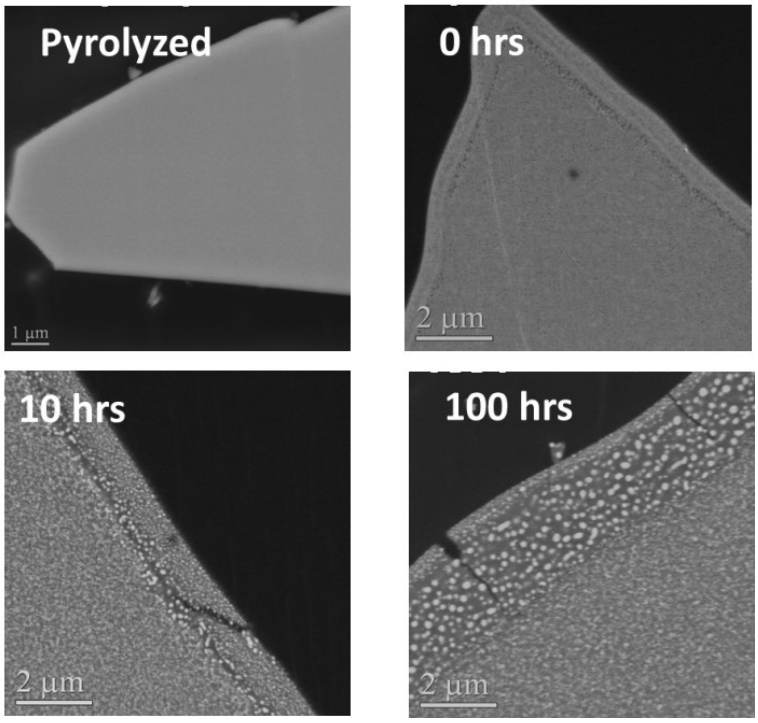

Fig. 77. Cross-section SEM images of oxide scale growth on S39 powders

Figs. 76 and 77 show oxide scale growth cross-sections of S14 and S39 HfSiCNO powders as a function of time. Similar measurements were taken for S00 and S26 compositions. Oxide scales were measured directly from these images and plotted below in Fig. 78 as the square of the oxide scale thickness vs time. These powders appear to show quadratic growth after 10 hrs for S00 and S14 and approximately 20 hours for S26 and S39. The oxidation rate in every case is faster before approaching the quadratic growth regime. This length scale of this non-quadratic growth is consistent with the initial transient layers observed by SEM cross-sections. The quadratic rate constants (after the initial transient) are also given in Fig. 78 for each composition.

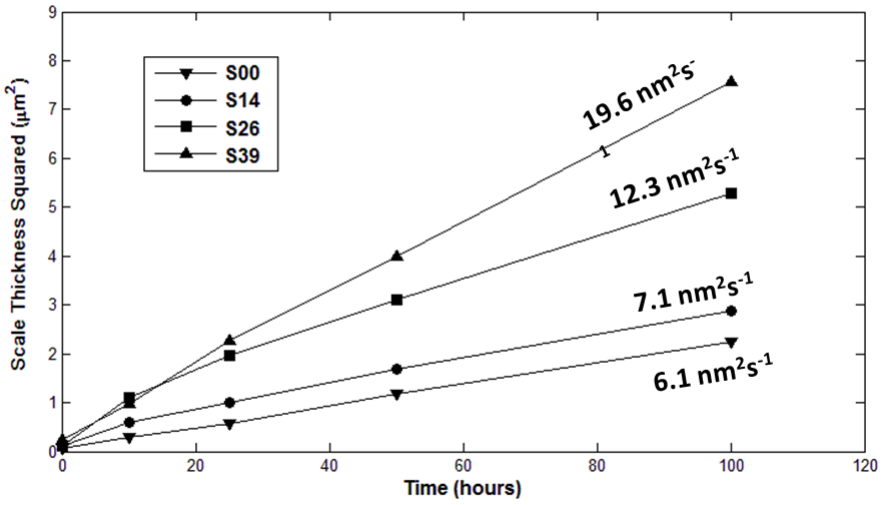

Fig. 78. Cross-section SEM images of oxide scale growth on S39 powders

The increase in oxidation rate for the Hf-containing materials can likely be attributed to one of two factors (I) the Hf doped materials already possess a significant amount of native oxygen, or (II) the Hf-materials contain less carbon. If the rate limiting mechanism for oxidation were diffusion of oxygen through the oxide scale, then Case I would influence the rate. If the rate limiting mechanism were CO diffusion through the oxide scale, then Case II would have the influence over the rate.

Table 7. Predicted oxidation rates of HfSiCNO materials compared to experimental results. Case I is if the rate is inward oxygen diffusion controlled, and Case II is if the rate is outward CO diffusion controlled.

	Oxidation Rates (nm^2s^{-1})		
	Case I	**Case II**	**Measured**
S14	7.27	12.28	7.10
S26	9.77	16.95	12.30
S39	15.48	23.39	19.60

Using the measured SiCN rate as a baseline, one can make a first order approximation of what the expected rates would be of similar compounds base solely from their respective O and C content. For example, if the oxidation were controlled by the outward diffusion of CO (Case II), then a $Si_xC_yN_z$ material with twice as much carbon content would be expected to oxidize at half the rate. Similarly for Case I, any inherent oxygen in the material would require less inward oxygen diffusion and the rate would scale accordingly. These results are presented in Table 7 along with the measured rate from powder cross-sections. All data are scaled with the measured C content, O content, and oxidation rate of undoped sample S00 which is used as the reference. Neither scenario stands out as being the evident rate controlling mechanism. The measured oxidation rate values appear to fall in between what was calculated for the two cases. Other factors, such as the influence of glass chemistry, $HfSiO_4$ precipitates, CO bubbles, etc., would likely have to be taken into account to determine which mechanism is truly dominant. All these factors would influence rates of O_2 and CO diffusion. Nevertheless, this study does confirm that the difference in oxidation rates between HfSiCNO compounds is likely explained by the base materials' C or O content.

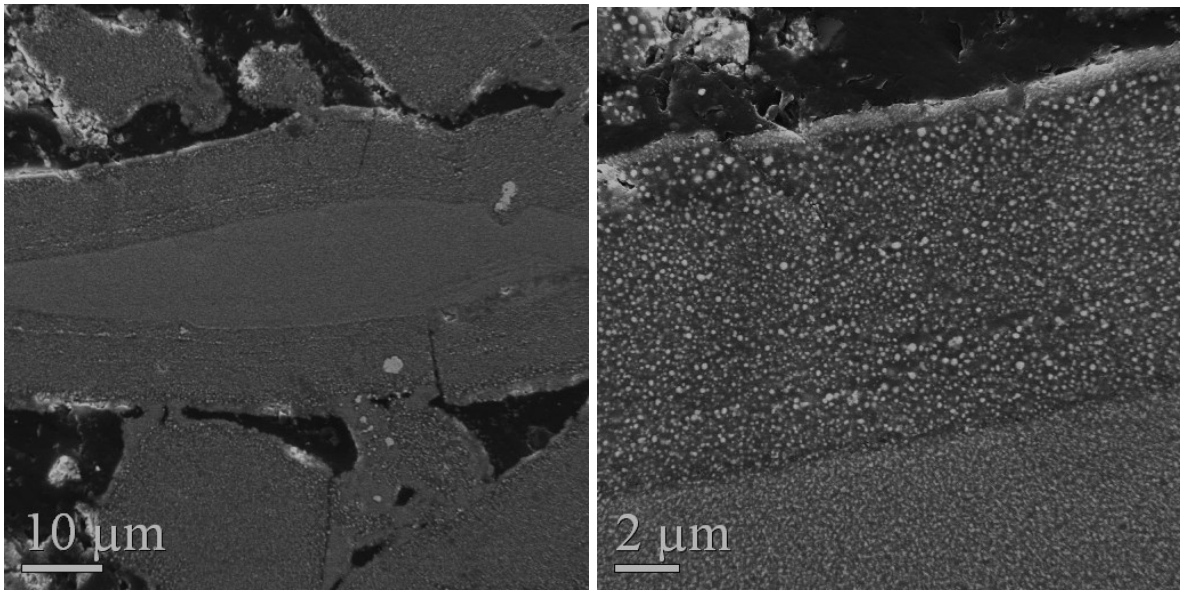

Fig. 79. Oxidation scale growth on S39 powder after 1000 hrs at 1500°C in air (left); higher magnification of the oxide scale (right)

The oxide scale on S39 composition powder was approximately 10.25 µm after oxidation in air at 1500°C for 1000 hrs. This is somewhat higher than predicted by the quadratic rate constant derived above, which would give a thickness of 8.42 µm if the data were extrapolated out. This is likely due to nonlinear effects which occur when the oxide scale approaches the radius of the particle. A planar growth rate can only be expected when the scale thickness is considerably greater than the particle radius. In these very long oxidation exposures, this assumption breaks down since the scale thickness is approaching the effective particle radius as seen in Fig. 79 (left).

Another interesting observation from the 1000 hour particle cross-section is the size of the $HfSiO_4$ precipitates in oxide scale. The precipitate sizes are in the range 50-200nm after 1000 hrs which are the same scale as found in the 10 to 100 hr regime. Furthermore, there is no measurable change in precipitate size across thickness of the scale (other than the initial transient). One can conclude from this that there is

effectively no solubility of $HfSiO_4$ in the surrounding SiO_2. Were some migration of $HfSiO_4$ permissible, then one would expect coarsening of the precipitates which formed at earlier times, particularly at such high temperatures and long exposure times.

3.7 Chapter Summary and Conclusions

A theoretical basis for doping SiCN and SiCO with transition metals was given from the standpoint of atomic substitution of Si-centered tetrahedra. Group IV elements of Ti, Zr, and Hf were found to have favorable enthalpy of substitution in both PDC material in addition to the Group V elements of Nb and Ta.

HfSiCNO ceramic powders were prepared from the polymer route by chemically modifying a polysilazane with hafnium alkoxide. The chemistry and structure of these polymer derived compounds were tracked in the liquid precursor, cross-linked polymer, and ceramic states.

FTIR analysis of the liquid state mixtures showed mostly rule-of-mixtures behavior. An absorption peak at 520 cm^{-1} was determined to be from the formation of Hf-N bonds in the liquid. Quantitative analysis reinforces the formation of Hf-N bonding by measurable consumption of N-H sites in the liquid state. Evidence for this is seen experimentally by the spontaneous effervescence upon mixing of the two precursors.

The polymer state shows strong evidence for the formation of Si-O-Hf bonds upon cross-linking. Broad absorption for Hf-doped samples is observed in the range consistent with 'M'-O-Si bonding. The absence of Si-H bonds in the polymer state and shift in the $Si-CH_3$ peak due to greater oxygen coordination also offers evidence for the formation of Si-O-Hf in mixed cases. The Hf-doped polymers show a distinctly different cross-linked structure as seen by XRD.

The ceramic state analysis revealed that the amorphous nanodomain structure of polymer-derived SiCN remains essentially unaltered up to a Hf to Si ratio of 0.22. FTIR showed broad absorption bands and gave some evidence for the existence of Hf-(C,N,O) in the ceramic state. Raman showed the same segregated carbon structure as undoped SiCN and SiCO materials, though there was measurably greater C disorder. This is disorder is qualitatively consistent with the decrease in carbon content for the Hf-doped materials. Small-angle x-ray scattering shows the amorphous nanodomains to remain consistent with Hf doping. These results show that Hf (and O) can be incorporated into the amorphous PDC structure upon thermal pyrolysis at 1000°C up to an HfSiCNO composition of S22.

Raman, XRD, and FTIR show the emergence of HfO_2 nano-crystals for an Hf to Si ratio >0.22. This was confirmed ab-initio molecular modeling calculations which show Hf-O enters an energetically favorable solution with SiCN up to S22 composition. The molecular models also predict a variety of Hf-(C,N,O) bonds in various atomic coordination ranging for 4 to 8.

The HfSiCNO material was found to carbothermally reduce at 1500°C in inert atmosphere. Carbothermal decomposition was found to be suppressed in oxidizing environment due to a virtual CO pressure which exists at the oxidation front. The transition oxygen pressure for a similar PDC material (without Hf) was found to be ~1%O_2.

HfSiCNO powders were oxidized in air at 1500°C and 1600°C. The materials were found to oxidize by the passive formation of a SiO_2 +$HfSiO_4$ scale. The unoxidized core material was found to precipitate nano-crystals of HfO_2. These hafnia precipitates coarsen at the oxidation front and release after achieving roughly 200 nm in size. A simple model was developed to quantify oxide scale thickness as a function of

measured powder weight gain during oxidation. Oxidation rates were found to be quadratic. Early experiments showed a rate constant of 16-18 nm^2s^{-1} for S08 composition which was effectively the same as the measured for SiC crystals of 15-21 nm^2s^{-1}. Latter oxidation studies showed lower rate constants for SiCN and HfSiCNO materials. These values were obtained from particle cross-sections and found the quadratic rate constant to be 7.1 nm^2s^{-1} for the lowest Hf concentration and 19.6 nm^2s^{-1} for the highest Hf concentration. (The oxidation rates from latter experiments were found to be somewhat slower. The reason for this is unknown; however, there is evidence to suggest this is due to furnace contaminants in oxide scale. EDS from early experiments showed some Al, Mg, and Na contamination in the oxide scale which lowers the glass viscosity and increases diffusion rates [30]. The source of the contamination was discovered to be from low-purity alumina cement annealed in the $MoSi_2$ element box furnace.) It is expected that the oxidation rates of HfSiCNO is controlled by the outward diffusion of CO. The difference in oxidation rates for the various $Hf_vSi_wC_xN_yO_z$ compositions is consistent with the materials' initial carbon content.

4 HfO_2-SiCN Infiltrated SiC/SiC Preforms

4.1 Introduction

SiC fiber based CMCs are of interest for high-temperature applications due to their favorable toughness, oxidation resistance and thermal conductivity. A significant problem facing SiC/SiC composite CMC design for hypersonic applications is recession of the SiO_2 oxide scale. Table 1 of Section 1.3 highlighted the various means by which silica can recess in streaming flow or active oxidation regimes. This forces the use of EBC materials in recessive environments to prevent CMC structural degradation.

All previous oxidation experiments presented in this thesis were conductive in static air under conditions where Si-based materials form passive oxide layers. Compared to most oxides, silica is ideal in these non-recessive conditions due to its high resistance to CO and O_2 diffusion. This chapter focuses on active oxidation regimes by the use of streaming water vapor at 1500°C where SiO_2 volatilizes into $Si(OH)_4$.

Silicon carbide preform CMCs were chosen to be infiltrated with a protective matrix and oxidized in recessive environments. Whereas the previous two chapters dealt with scientific understanding of the oxidation science, this chapter is focused toward application. The CMC preforms used in this study are currently leading candidates for hypersonic UHT structures. This chapter draws upon the experiments from Chapters 2

and 3 where the key result was the formation of a stable $HfSiO_4$ product upon oxidation of SiCN-HfO_2 systems. The multiple infiltration types considered are outlined in Table 8.

Table 8. Infiltration types for SiC fiber based preforms

Infiltration Material	**SiC/SiC**	**SiC**	**HfSiCNO**	**HfO_2/SiCN**
Infiltration Methods	Slurry	Chemical Vapor	Slurry	Slurry
Favorable	Dense infiltration	Dense infiltration	Oxidation resistance Stable silicate phase	High HfO_2 content Stable silicate phase
Unfavorable	Volatile oxide scale	Processing viability Volatile oxide scale	Porous infiltration Low HfO_2 content	???

The ceramic preforms are woven SiC fiber structures coated with a dense SiC layer to result in a rigid textile. The use of a SiC based CMC matrix has been shown effective in passive oxidation environments. However, recession of the formed SiO_2 oxidation scale removes these as viable options in streaming H_2O conditions. Polymer-derived HfSiCNO was selected as the primary candidate for the CMC matrix material. It was shown in Ch. 3 that these materials have good oxidation resistance resulting in an oxide scale consisting of 200 nm precipitates of $HfSiO_4$ in SiO_2. Most importantly, their ability to be processed from the polymer route ensured good bonding to the preform structure and the ability to be infiltrated as a liquid precursor. The prevailing idea was that a dense $HfSiO_4$ layer could be formed *in situ* as the SiO_2 content in the oxide scale recedes, leaving behind only $HfSiO_4$. This would effectively create a self-healing CMC matrix which would form an $HfSiO_4$ film across any receding surface. Infiltrations were attempted, but the inability to achieve a dense matrix drove the need for a new design. A similar concept to HfSiCNO was envisioned using HfO_2 powders dispersed in SiCN. Systems of this kind could also be processed from the polymer route by infiltrating the

CMC preform with a slurry of HfO_2 and liquid silazane. Nominally, the same $HfSiO_4$ in SiO_2 oxide scale was the expect result, offering a CMC matrix which would form a protective layer of dense $HfSiO_4$ upon active oxidation.

This chapter details the oxidation of such SiCN-HfO_2 ceramic composites infiltrated into SiC fiber based preforms. The composite layer was fabricated from the polymer route using vacuum infiltration of a silazane-HfO_2 powder slurry. The infiltrated preforms were oxidized in concentrated streaming water vapor at 1500°C. Analogous infiltrations, consisting purely of silicon carbide, were measured for comparison.

4.2 Preform Structure

The silicon carbide “preform” consists of woven fiber bundles which are then infiltrated further with SiC to form a rigid textile. Each fiber bundle, also called a tow, is ~1 mm in diameter and contains a series of individual SiC fibers each 10 μm in diameter. Each SiC fiber is coated by a thin layer of boron nitride (BN) around 2-4 μm thick. The BN acts a weak interface between the fibers and surrounding matrix. Creating a yielding interface gives the composite preform much higher fracture toughness than if it was SiC alone [159].

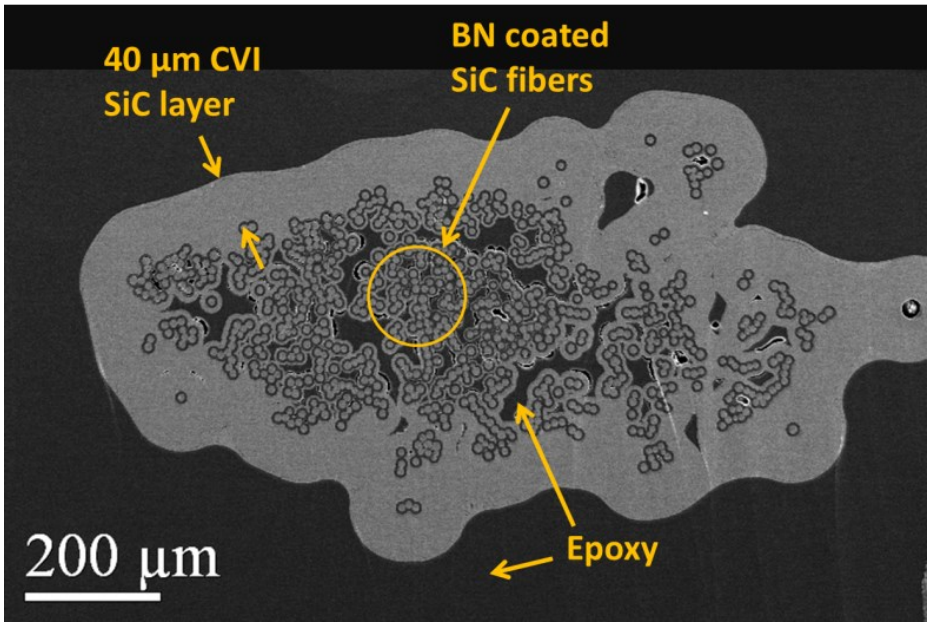

Fig. 80. Cross-section of SiC-SiC fiber tow

The fibers are bundled together into fiber tows and then interwoven together into a fabric-like sheet. The pliable fabric consisting of SiC fiber bundles is then infiltrated with a dense SiC layer by chemical vapor infiltration (CVI). The CVI SiC infiltrates the spaces between the individual fibers and ultimately leaves a 40 µm layer of dense SiC encasing the tow. The structure of an individual tow cross-section is shown in Fig. 80. The SiC fibers are clustered in the middle of the tow with a layer of CVI SiC around the bundle. The dark areas of the image are potting epoxy which is necessary for cross-sectional polishing. Note that some areas of the tow interior are porous (seen as epoxy in the section), which is due to the choking of open pores between the fibers as the CVI layer thickens.

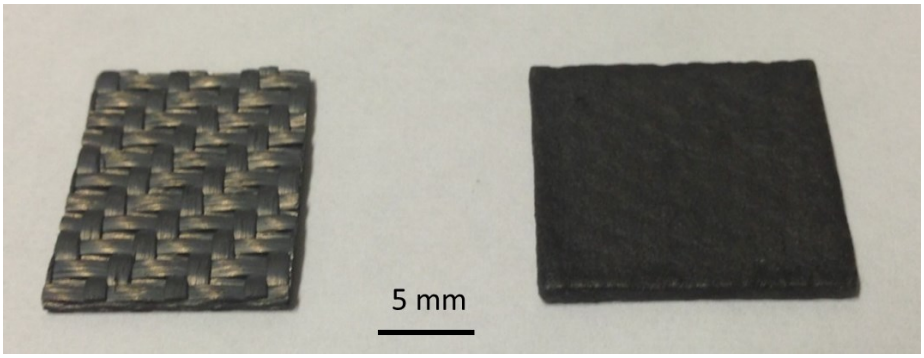

Fig. 81. SiC-SiC preform before (left) and after infiltration (right)

The CVI SiC layer serves to fill in the spaces between the individual SiC fibers and adds a dense protective layer surrounding the entire fiber tow. A further infiltration step can be performed to fill in the spaces between the tows themselves. This secondary infiltration encases the entire preform and fills in the macro-scale porosity between the SiC fiber tows. An example of this final infiltration step is shown in Fig. 81 where the left image is the uninfiltrated SiC preform, and the right image is the preform after being infiltrated with a SiCN-HfO_2 composite.

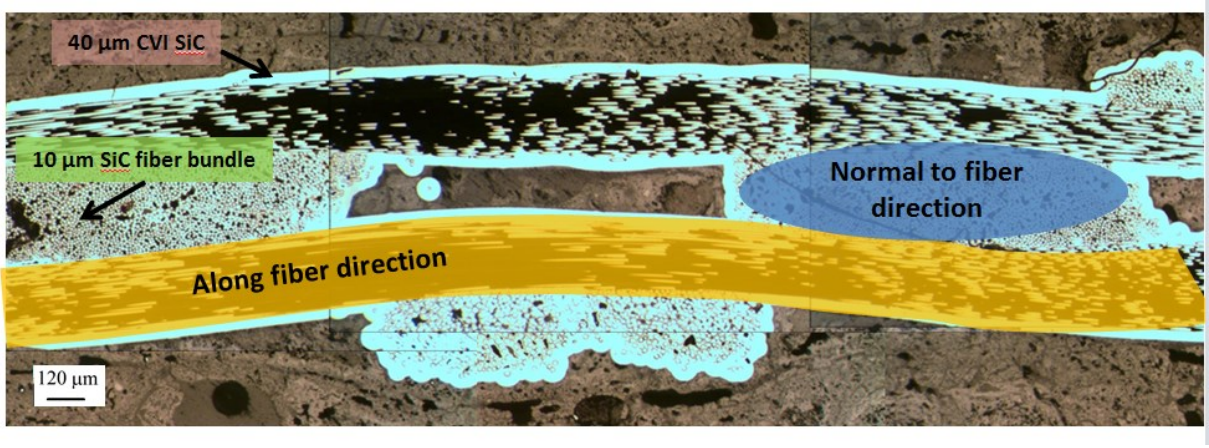

Fig. 82. Cross-section of infiltrated SiC-SiC preform

Fig. 82 shows the cross-sectional structure of a SiC-SiC preform which has been infiltrated by a SiCN-HfO_2 ceramic composite. Fiber bundles in-plane and out-of-plane are observed as well as the 40 µm thick CVI SiC layer. The surrounding area between

the fiber tows, shown as a textured brown color in the above figure, is the infiltrated layer of SiCN-HfO_2.

The remaining chapter focuses on the processing and oxidation behavior of this SiCN-HfO_2 infiltrated layer. In some cases an additional infiltration type, consisting of pure SiC, was measured for comparison to the SiCN-HfO_2.

4.3 Infiltration Processing

The structure of the SiC preform requires unique processing for infiltration. Since the preform has interior voids, vapor phase techniques would seal these spaces in the form of closed pores. Vapor phase techniques would also be expensive and time consuming to produce infiltrations on the length scale of the preform thickness, which is about 1mm. Powder infiltration of the preforms would be difficult since the materials of interest as the infiltrated layer, like SiC, are extremely difficult to sinter. Furthermore, in the case of SiCN-HfO_2, the system completely lacks the ability to be sintered by conventional means. The temperature necessary to provide diffusion migration in both materials exceeds the carbothermal reduction temperature. This renders typical free sintering or hot pressing in inert atmosphere impossible. Inert atmosphere sintering may be possible in high overpressures of CO by using a system such as a hot isostatic press (HIP) to prevent carbothermal reduction. In an air environment, the SiCN is found to largely oxidize to SiO_2 upon sintering.

The solution is to infiltrate the preforms from the polymer route. The polymer can be infiltrated into the sample (of any shape) and pyrolyzed into the desired ceramic. The only major drawback to this technique is the significant degree of volume shrinkage from the polymer during its ceramic conversion. This leaves large scale damage

throughout the sample and requires several subsequent infiltration steps, each serving the purpose of filling in the cracks from the previous cycle. As the number of infiltrations increase, the crack sizes become progressively smaller until they become completely filled.

The SiC preforms described above were infiltrated with a SiCN-HfO_2 composite. The composite layer was deposited by vacuum infiltration of a polymer/ceramic slurry into the preform. The slurry consisted of liquid Ceraset® silazane (precursor for SiCN) and 100 nm HfO_2 powder. The infiltration steps were performed in an argon glovebox containing less than 1 ppm H_2O and O_2. The slurry was made by mixing HfO_2 powder (American Elements) and Ceraset (KiON Defense Technologies) directly. The two were mixed with mortar and pestles for ~10 minutes with intermittent exposures to a gage vacuum of -25” Hg. The vacuuming of the slurry during mixing expands any trapped gas bubbles within the mixture and allows them to escape. This helps the silazane to completely wet the HfO_2 particles as well as aids in the mixing process and break-up of particle agglomerates.

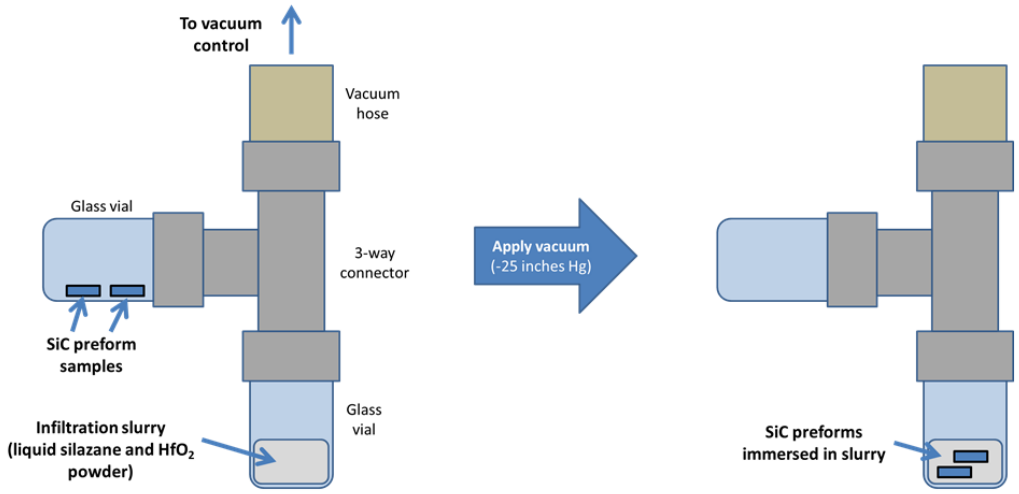

Fig. 83. Schematic of slurry infiltration setup

A simple setup was built for the vacuum infiltration of slurry into the preform. Two glass vials and a vacuum line were connected to a three-way junction, illustrated in Fig. 83. One vial contained the un-infiltrated preforms and the other contained the slurry. The system was pumped down to a vacuum and the preform samples were tipped into the slurry containing vial. The slurry containing vial was kept on a hot plate at 70°C to reduce the viscosity of the mixture. The vacuum was released once the preforms were fully immersed by backfilling with argon. Releasing the vacuum after the sample is immersed serves to push slurry into any sample gas pockets which would be at vacuum pressure. The gas pore volume shrinkage from a gage pressure of -25" Hg to ambient is approximately 6x. It should be noted though that viscosity plays a significant role in the final volume of pore size in addition to just volume shrinkage alone. Thin slurries will result in smaller pores due to capillary action from surface tension, and thick slurries will result in larger pores from viscosity restricted flow.

An alternative vacuum infiltration process would be to immerse the sample in the slurry first and then pump down to a vacuum. Open gas pores within the sample would expand under vacuum, escape, and then be filled with slurry when the vacuum is released. The drawback to this route is that the tradeoff between slurry viscosity and bubble surface tension prevents smaller bubbles from escaping, and therefore the final ceramic has a greater porosity. Wetting the sample with slurry while it is immersed in a vacuum atmosphere allows for an enhanced infiltration into smaller pores once the vacuum is released.

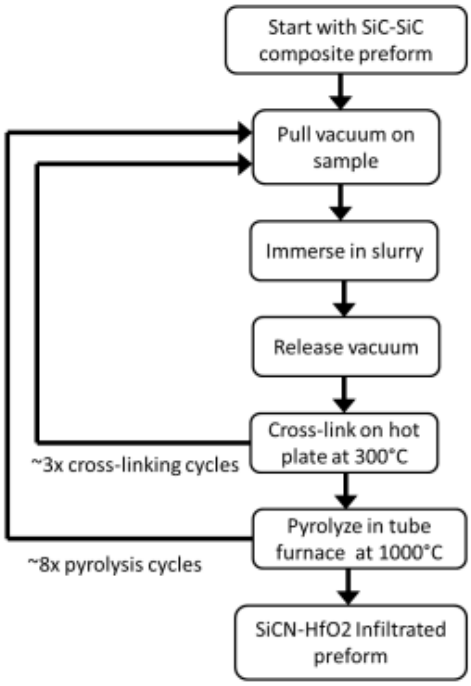

Fig. 84. Infiltration processing flow diagram

A processing flow chart of the infiltration procedure is shown in Fig. 84. Each infiltration was completed in a series of cross-linking and pyrolysis cycles. The pyrolysis shrinkage of the silazane during ceramic conversion, as detailed in Section 3.4.1, is very significant and approximately 63% by volume. Small amounts of cracking from gas

escape can occur during polymer cross-linking as well; however this is considerably less significant and a non-factor after the initial infiltration cycles.

The very first infiltration cycle is an exception to this process. The first infiltration cycle was a mixture of composite slurry and composite powder. This was achieved by pyrolyzing the slurry mixture, by itself, in an alumina boat at 1000°C. The ceramic SiCN-HfO_2 composite was crushed into a coarse <50 μm powder by milling with mortar and pestle. The pyrolyzed powder was then dispersed in the liquid slurry creating a paste of SiCN-H/HfO_2 (slurry) + SiCN/HfO_2 (powder). This paste was mechanically worked into the preform and pyrolyzed at 1000°C. The reason for this anomalous first cycle is multifold. The primary reason is that it reduces the number of subsequent cycles to create a dense infiltration and prevents first cycle spalling of the infiltrated layer. The powder inclusions reduce the total volume shrinkage and decrease the initial crack size. Undoubtedly, the paste results in greater initial pore size, but it was found these pores could be filled in by latter cycles using the normal slurry infiltration technique. Furthermore, the void sizes in the as-received SiC preforms were large enough to allow pure slurry to flow out of the preform upon heating. The powder filler of the first cycle raises the viscosity and prevents slurry seepage out of the preform. Since both the ceramic powder and slurry are composed of the same material, the resulting infiltration layer is homogenous. Following the first cycle all others used only the slurry mixture with no additional filler.

One processing related observation was that the silazane/HfO_2 slurry would slowly thicken after each vacuum infiltration cycle. This was discovered to be from the preferential volatilization small, low-viscosity silazane molecules. The small molecular weight silazane molecules would vaporize under vacuum, slowly thickening the slurry

with use. For this reason a new batch of slurry was prepared for every one pyrolysis cycle of the infiltrated layer.

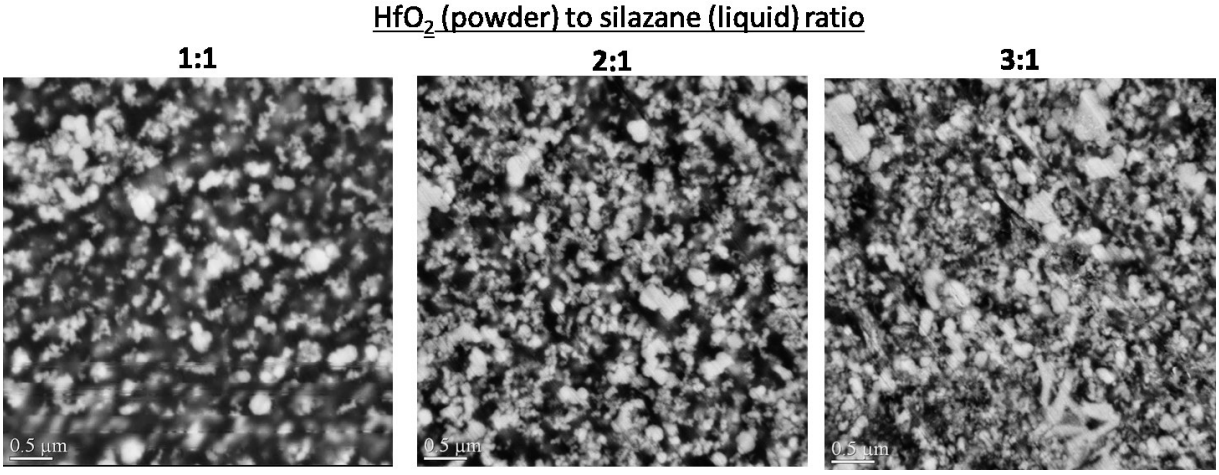

Fig. 85. HfO_2 dispersion in SiCN as a function of mixture weight

Three different slurry mixtures were attempted with HfO_2 to silazane ratios of 1:1, 2:1, and 3:1 by weight. The processing was the same for each mixture and the resulting ceramic composite for each are shown in Fig. 85. The hafnia particles were ~100 nm in size with agglomerates typically in the 200-300 nm range. All samples demonstrate a good dispersion of HfO_2 particles in an SiCN matrix

Perhaps the most significant processing variable of the various mixtures is the slurry viscosity, which should ideally be as thin as possible for greater penetration into the sample. The liquid silazane has a room temperature viscosity of 50-200 cps [59]. This viscosity is increased with added HfO_2 powder content. High viscosities prevent the slurry from flowing into tight spaces of the preform. This is particularly relevant during the latter cycles of infiltration where the shrinkage crack sizes are on the order of a couple microns. However, one processing benefit of the added HfO_2 powder is a reduction in the amount of cracking during the silazane ceramic conversion. The hafnia powder acts as filler and mitigates overall shrinkage of the SiCN-HfO_2 composite layer.

This presents a tradeoff between hafnia content and general processing requirements. If the slurry is thick (high hafnia), then fewer infiltration cycles are necessary but the final product is more porous. If the slurry is thin (low hafnia), then the porosity is reduced but at the expense of many additional infiltration cycles.

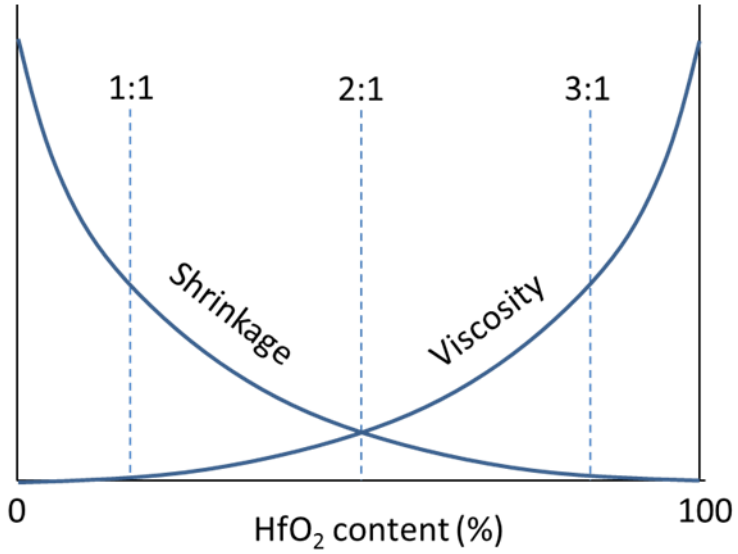

Fig. 86. Relationship between slurry viscosity and pyrolysis shrinkage

The general relationship between slurry shrinkage and viscosity are shown in Fig. 86 along with the respective positions of the attempted slurry weights. The HfO_2 to silazane ratio of 1:1 had a low slurry viscosity and was able to fill interior preform voids almost completely. However, it suffered from significant volume shrinkage with spalling after early infiltration cycles. The thickest slurry of 3:1 showed little cracking from shrinkage but did not infiltrate well due to high viscosity. A slurry weight of 2:1 was found to be a happy medium between the two competing effects. It provided the highest possible HfO_2 content while maintaining the ability to penetrate during vacuum infiltration. Samples prepared for the following oxidation experiments were done so using the 2:1 hafnia to silazane slurry.

4.4 Structure of Infiltrated Layer

The SiC preforms received 8 infiltration pyrolysis cycles to achieve a layer of HfO_2-SiCN with maximum density. All residual pores within the infiltrated layer appeared to be closed and their size increased with depth into the sample. The smaller pores near the outer surface were on the order of 1-10 μm in size whereas a few large pores of ~100 μm could be found in deep interior pockets. Examples of both can be observed in the optical micrograph of Fig. 87.

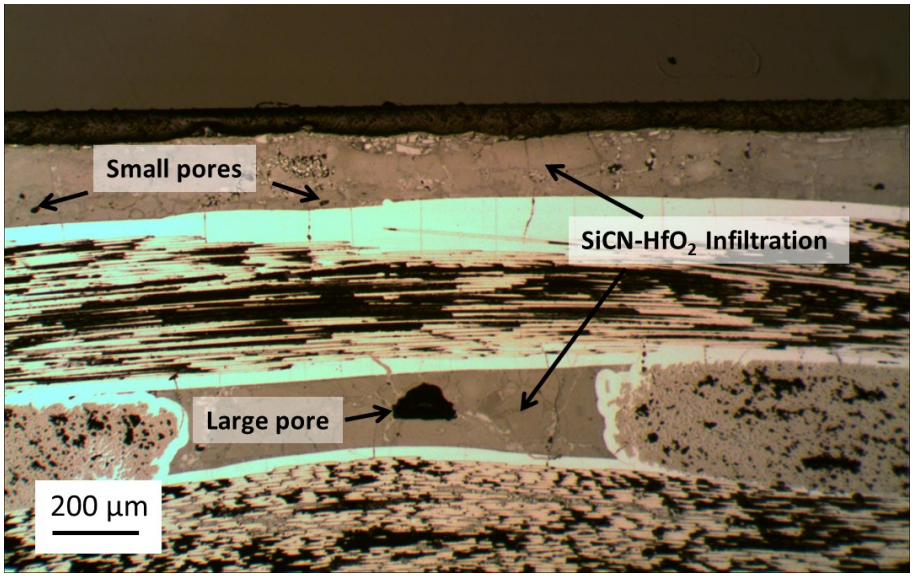

Fig. 87. Optical micrograph of SiCN-HfO_2 infiltrated preform cross-section

The infiltrated layer showed a pair of distinctly different phases. Fig. 88 shows an SEM cross-section of an interior preform void after infiltration highlighting the two phases. The first is composed of HfO_2 particles distributed in an SiCN matrix. This region looks typical of the SiCN-HfO_2 material after pyrolysis into a ceramic composite. The second phase was found by EDS analysis to be pure SiCN. This dual phase infiltrated layer is

interesting as the HfO_2 particles had not shown any preferential segregation in sub-scale testing.

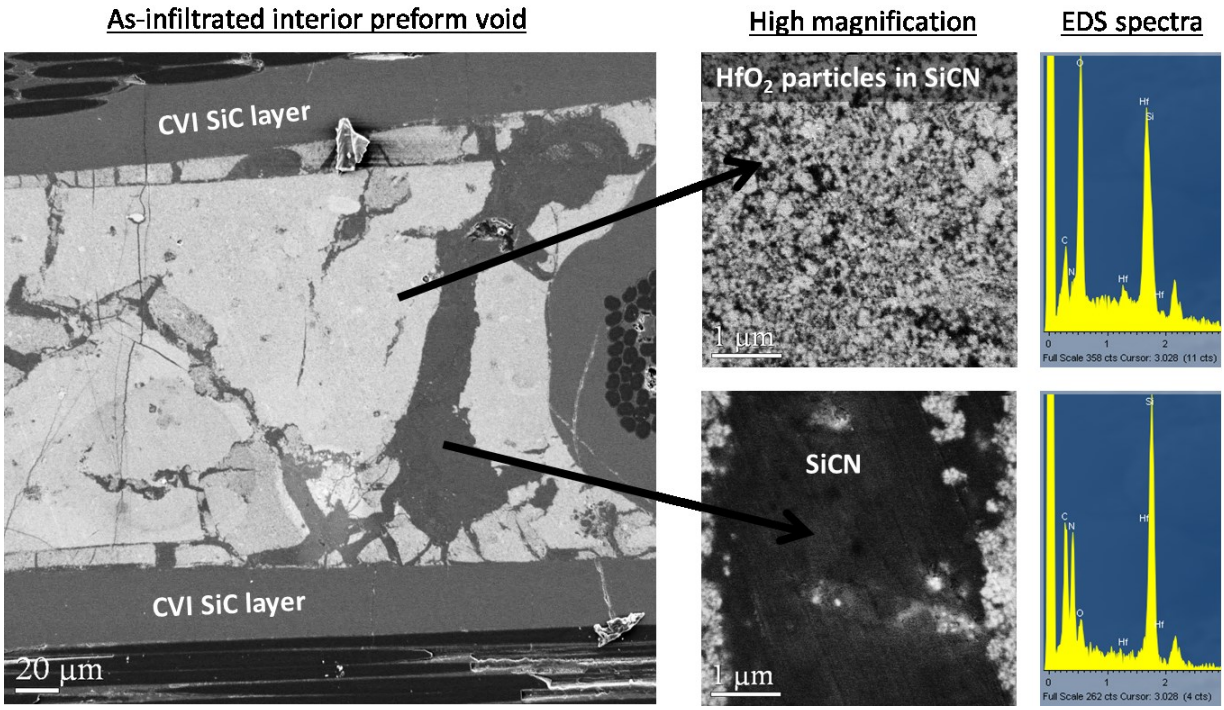

Fig. 88. SEM cross-section of infiltrated preform interior showing hafnia deficient regions

The working hypothesis for the existence of a hafnia deficient SiCN region is that the HfO_2 particles become obstructed during vacuum infiltration and only allow the silazane to seep through. Both depth into the sample and shrinkage crack width influence the ability of the slurry to fill the infiltration space. It is believed that once the slurry reaches an infiltration limit due to viscosity and/or particle clogging, only the silazane liquid is able to advance. The HfO_2 particles effectively choke the slurry from penetrating further, but the liquid component can continue permeating into voids. The voids would then be filled with only silazane which ultimately leaves pure SiCN after pyrolysis.

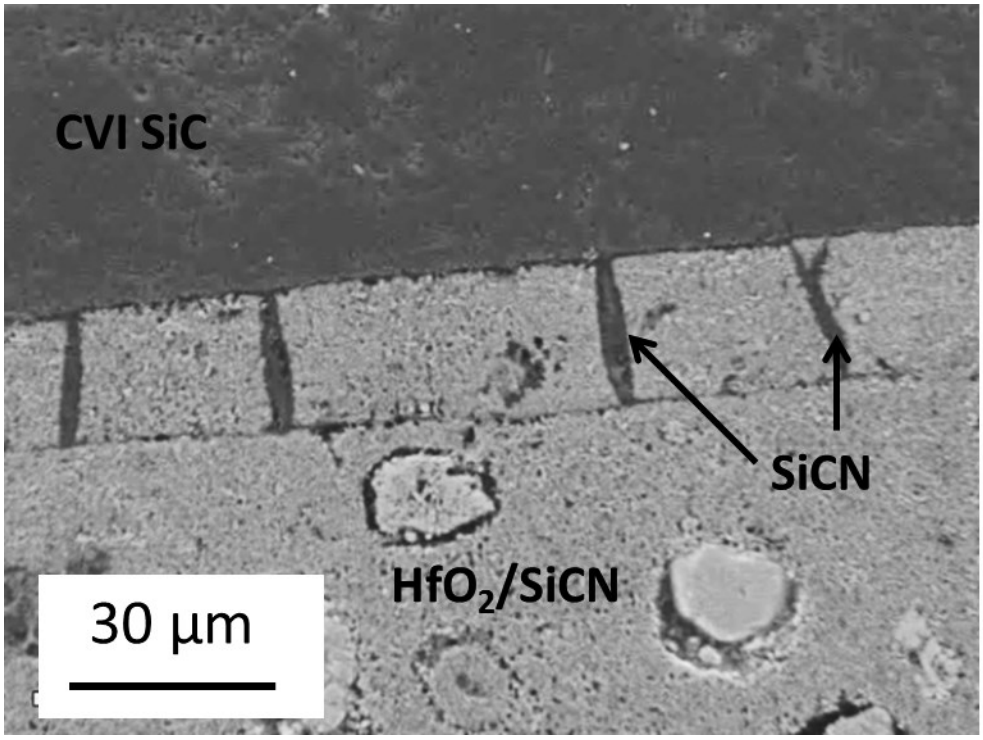

Fig. 89. Infiltration at CVI SIC interface showing shrinkage cracks

The infiltrated layer appears to have good bonding to the SiC preform. Fig. 89 shows the infiltration interface with the CVI SiC layer. This higher magnification SEM micrograph was taken from the same interior pocket of Fig. 88. Note the smaller crack spacing from shrinkage, on the order of 30 µm and highlighted by the presence of pure SiCN. The smaller spacing indicates these cracks developed during latter infiltration cycles. The larger length scale damage shown in the previous Fig. 88, hundreds of microns in size, are expected to develop from the first one or two infiltration pyrolysis cycles. The various degrees of crack size and spacing indicate the infiltration process is successful, since even the smallest observed cracks (1 µm wide) become filled with precursor.

The lack of hafnia content in some regions could be combated in future experiments by incorporating HfO_2 via the polymer route instead of using a powder slurry. Attempts were made to infiltrate the SiC preforms with polymer-derived HfSiCNO (see Ch. 3), but

volatilization of the Hf-alkoxide during vacuuming and off-gassing during pyrolysis resulted in a highly porous infiltration. A heavier Hf polymer source would have to be used to prevent volatilization, or a new infiltration method would have to be developed altogether. It was found on sub-scale testing of infiltrated pellets that the polymer-derived HfSiCNO could achieve a reasonable density if the infiltrated slurry was pyrolyzed under a hot-press. These samples were pressed in a graphite die at 50 MPa during pyrolysis at 1000°C and achieved densities in the 85-90% range depending on hafnia content.

4.5 Oxidation in Streaming H_2O

The infiltrated SiC preforms were oxidized in concentrated streaming water vapor at 1500°C. A schematic of the custom oxidation setup is shown in Fig. 90. Each preform sample was cut to have a face area of 1 cm^2 using an abrasive diamond wheel.

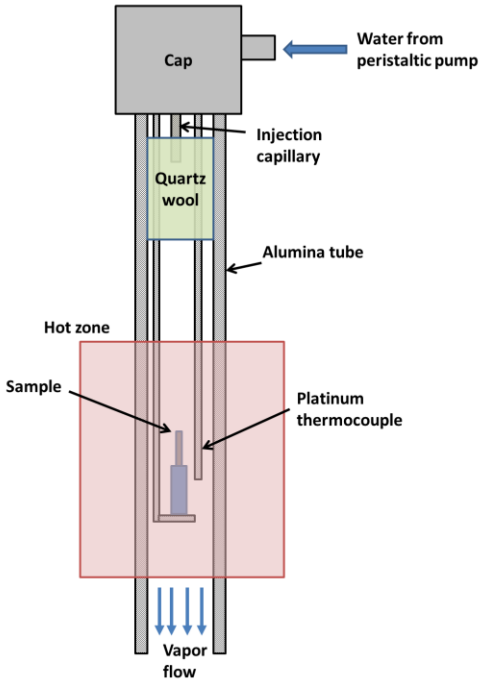

Fig. 90. Schematic of streaming H_2O oxidation setup

The streaming H_2O setup was built as a removable tube which could be inserted into a $MoSi_2$ element box furnace. The hot zone of the furnace is approximately 40 mm in length. The sample, contained in a high purity alumina tube, is centered in the hot zone and held at 1500°C. Water was pumped into the tube at 0.5 mL/min using a peristaltic pump. The water is injected into the tube through a thin capillary and onto a clog of quartz wool. The water wicks through the heated wool and vaporizes rapidly due to the high surface area to volume ratio of the quartz fibers. The stream is accelerated from volume expansion as it approaches the hot zone of 1500°C. At temperature, the stream has a flow rate of 29 cm/s. This steam flow rate was not measured experimentally but rather calculated using volume expansion from NIST superheated steam tables [160].

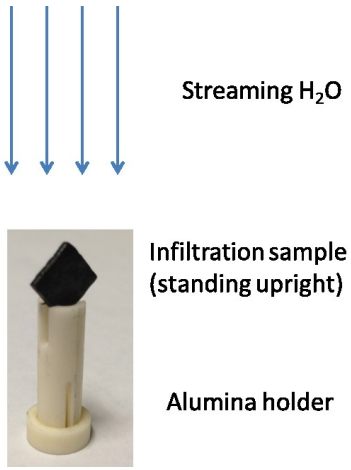

Fig. 91. Sample holder setup preform oxidation

The samples were mounted vertically in the vapor stream, Fig. 91, such that each face of the preform would receive a nominally uniform flow. The holder was constructed out of alumina tubes and alumina high-temperature cement. It was discovered that impurities within the alumina cement contaminated the infiltrated samples with trace amounts of Na, Mg, and Al content. These contaminants were found to go into solution with the SiO_2 glass oxidation product of SiC and SiCN. Subsequent experiments were conducted using only ultra-high purity Al_2O_3 powder for cement, which was applied as a slurry mixture of alumina powder, water, and nitric acid in a 15:5:1 weight ratio, respectively.

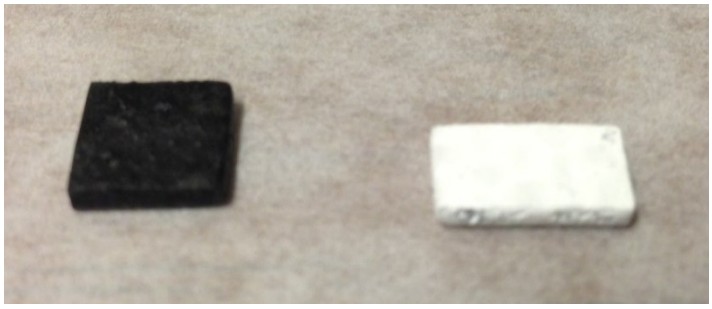

Fig. 92. SiCN-HfO_2 infiltrated SiC preform before (left) and after (right) oxidation

After oxidation the infiltrated samples turn from black to white in color, Fig. 92. This is due to the oxidation of the SiCN content, black after pyrolysis, into translucent SiO_2. The HfO_2 particles contained in the SiO_2 scatter incident light and make the oxidized sample white in appearance. The infiltration layer remained visibly intact after oxidation. A small degree of spalling was observed at free edges and corners after long oxidation exposures.

Two types of infiltrations were oxidized: (i) SiCN-HfO_2 as described, and (ii) pure SiC. Sample cross-sections were taken in the as-infiltrated state, after 10 hours oxidation exposure, and 275 hours exposure. Interrupted weight changes measurements were taken at 25 hour intervals throughout the testing. Weight change data normalized per unit surface area are given in Fig. 93 for the two samples. Both samples develop a linear rate of weight loss after an initial transient of 50 hours. After 225 hours the SiC sample showed one region, about 1mm square, where the infiltration was fully oxidized and also the CVI layer beneath it. This exposed the SiC fibers which rapidly oxidized, giving measurable weight gain. The SiCN-HfO_2 infiltration test was terminated shortly thereafter due to some noticeable spalling of the infiltrated layer, similarly convoluting the weight measurements.

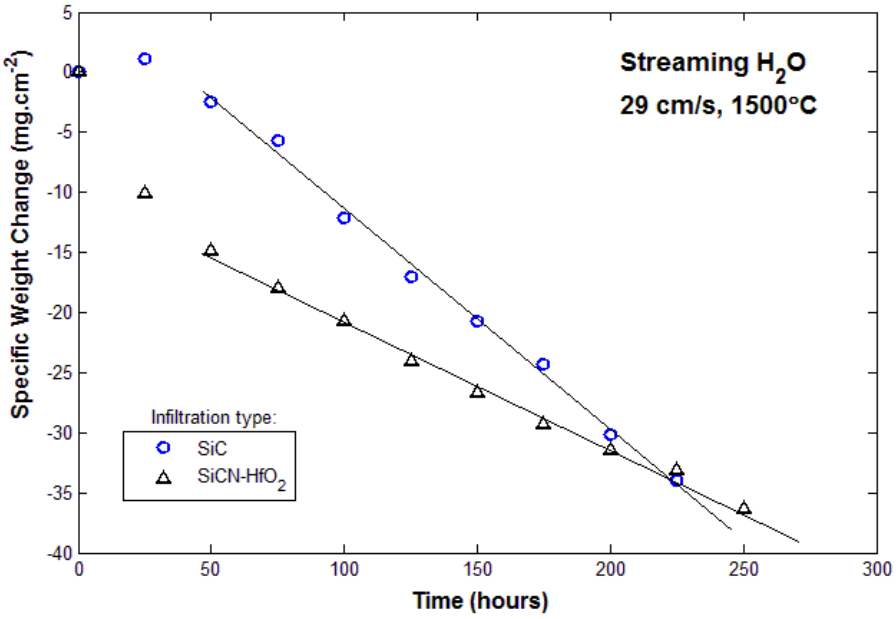

Fig. 93. Weight change of SiC and SiCN-HfO_2 infiltrated samples at 1500°C

The difference in behavior between the two samples during the first 50 hours of oxidation is noteworthy. The SiC showed and initial weight gain followed by a linear loss. This is due to a paralinear oxidation rate which has been observed in literature for SiC and Si_3N_4 under high-temperature streaming H_2O conditions [161]. The initial weight gain is from the rapid formation of silica and is followed by weight loss from recession of the oxide scale. After 50 hours, the two mechanisms reach a steady state oxide thickness and show linear weight loss behavior from SiO_2 volatilizing into gaseous $Si(OH)_4$. The SiCN-HfO_2 sample showed a rapid initial weight loss, as opposed to the gain observed in SiC.

Paralinear oxidation kinetics of the SiC can be explained by the combination of a parabolic growth from passive scale formation in combination with linear weight loss from active recession. Let the passive rate constant be defined as k_P in units of $\mu m^2.hr^{-1}$, and let the active rate constant be defined as k_A in units of $\mu m^1.hr^{-1}$. The

active recession of rate shows no dependence on scale thickness, h, and can be simply defined as

$$\frac{dh}{dt} = -k_A \tag{32}$$

Where, t, is time. Similarly, the passive scale growth rate at any positive thickness, h, can be described by

$$\frac{dh}{dt} = \frac{k_P}{2h} \tag{33}$$

Combining expressions from Eq. (32) and. Eq (33) gives the total growth rate

$$\frac{dh}{dt} = \frac{k_P}{2h} - k_A \tag{34}$$

Integrating the above equation gives

$$t = -\frac{h}{k_A} - \frac{k_P}{2{k_A}^2} \ln\left(\frac{k_P}{2} - k_A h\right) + C \tag{35}$$

Solving for the integration constant with initial condition $h = 0$ at $t = 0$, gives

$$t = \frac{k_P}{2{k_A}^2}\left[-\frac{2k_A}{k_P} h - \ln\left(1 - \frac{2k_A}{k_P} h\right)\right] \tag{36}$$

which is the time required to achieve a measured oxide scale thickness as a function of the parabolic and linear rate constants. Note the steady state oxide thickness will occur when dh/dt equals zero (Eq. 34) and therefore the steady state thickness can

be described simply by the rate constants through the relationship,

$$h_{SS} = \frac{k_P}{2k_A} \tag{37}$$

4.5.1 Microstructure of Oxidized SiCN-HfO_2 Infiltration

SEM micrographs of SiCN-HfO_2 infiltration cross-sections are shown in Fig. 94. The section taken at 10 hours is in the regime which experienced rapid initial weight loss, and the 275 hour section would be during the linear weight loss.

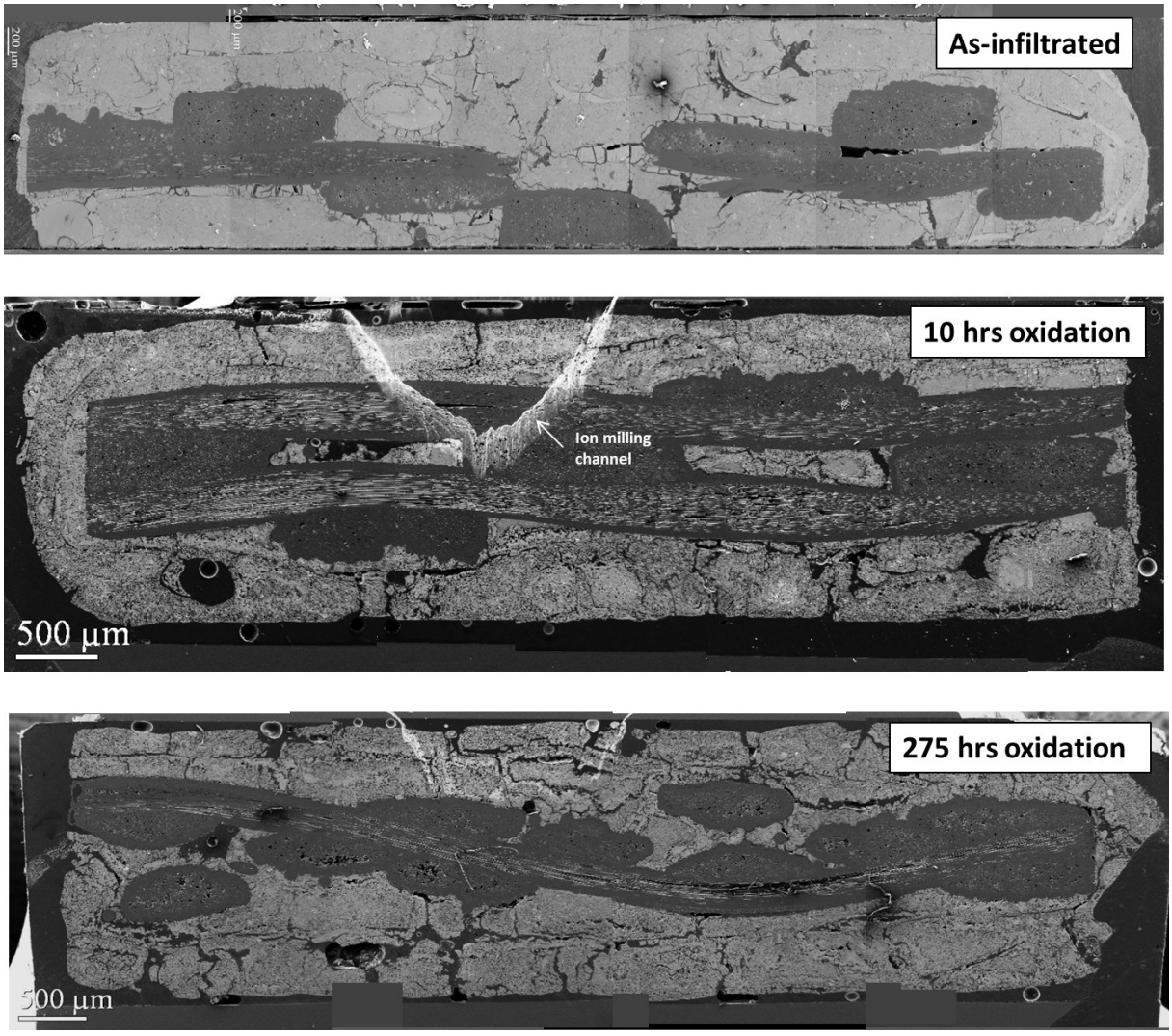

Fig. 94. As-deposited, 10 hours, 275 hours at 1500°C in streaming H_20

The infiltration layer appears mostly dense prior to oxidation. After 10 hours of oxidation exposure at 1500°C, Fig. 94 middle graphic, the infiltrated layer is found to

develop significant porosity on length scales of 1-10 μm in size. A few extremely large pores are also observed on the order of a couple hundred microns. These are shown in the micrograph as dark pockets filled by epoxy. The infiltrated layer also shows apparent surface cracking at spacing of >1 mm. Analogous experiments showed some degree SiCN-HfO_2 sintering when heated at 1450°C in air. It is possible that some of this early stage cracking is due to densification of the infiltrated layer. The cracks become significantly more prevalent after 275 hours with surface spacing of ~500 μm. The infiltration surface also develops surface roughness presumably from bloating due to pore formation. All sample surfaces were ground flat and parallel after infiltration using a diamond wheel.

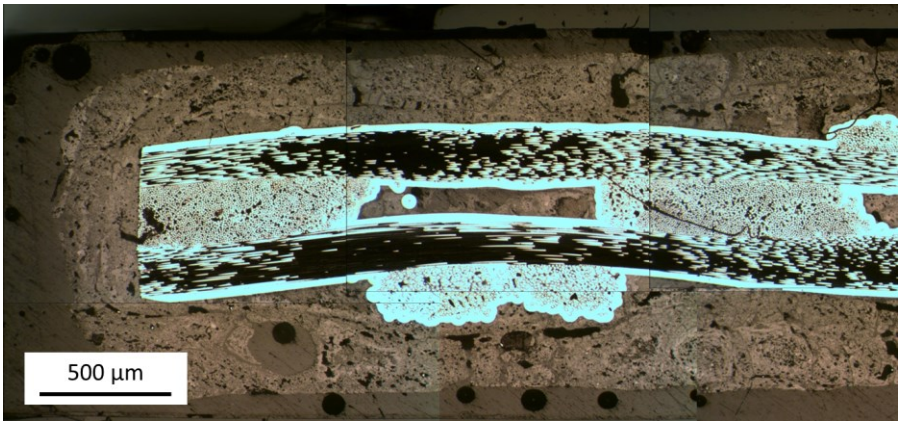

Fig. 95. Optical cross-section of SiCN-HfO_2 infiltration after 275 hours at 1500°C

Optical micrographs show similar behavior, as seen in Fig.95. The color texturing of the infiltrated layer is an indicator of the porosity found within the sample and their distribution. The areas of the infiltrated layer without peppering of dark spots were found to be unoxidized. The 10 hour sample showed a mostly unoxidized CVI SiC layer suggesting the infiltrated layer above it was unoxidized. The CVI SIC showed some oxidation only in regions where the infiltrated layer had penetrating porosity. The infiltrated layer appears to be mostly oxidized after exposure for 275 hours. Note the

significantly higher degrees of oxidation in comparison to the static air experiments of Ch.2 and 3 which showed the formation of a passive SiO_2–based layer and yielded oxidation scales typically on the order of a couple of microns. At similar exposure times, the oxidation depths of these experiments are 2 orders of magnitude higher.

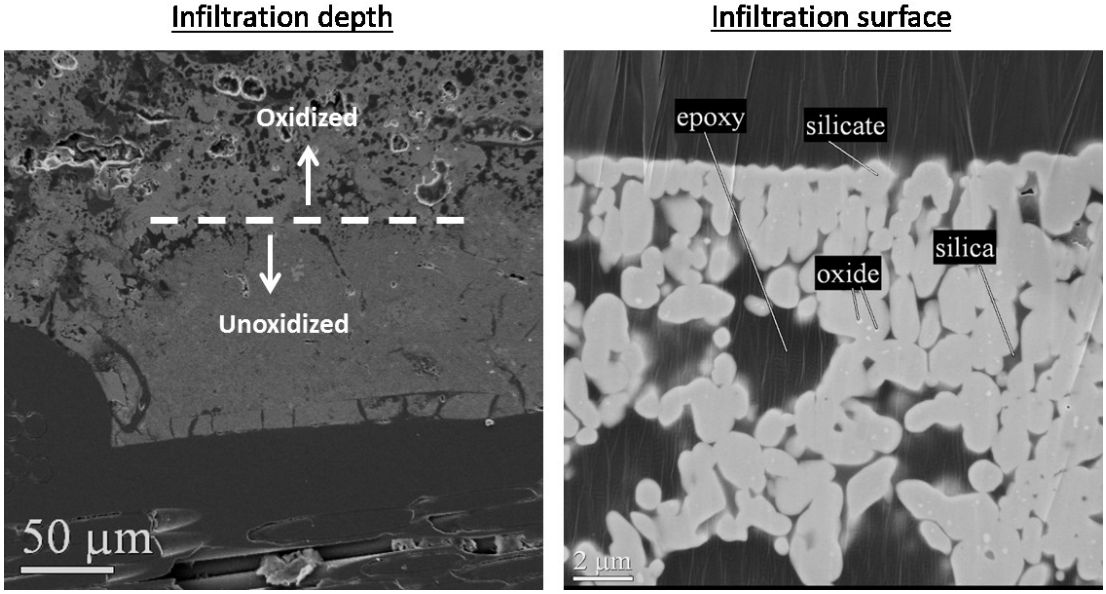

Fig. 96. SEM images of infiltration after oxidation for 10 hours. The left image shows oxidized/unoxidized morphology, and the right image shows surface structure

Fig. 96 (left) shows the difference in oxide scale morphology before and after 10 hours oxidation. The outer surface of the sample showed $HfSiO_4$ particles and open porosity in a SiO_2 matrix. A very small presence of unreacted HfO_2 was observed but the vast majority had reacted with the surrounding silica to form $HfSiO_4$. Also note the coarsening of the hafnium silicate particles at the exterior surface, Fig. 96 (right). The HfO_2 content was present in the initial infiltration as ~100 nm particles. These grains of $HfSiO_4$ are found to be 1-2 μm in size indicating significant coarsening.

This coarsening of the $HfSiO_4$ in streaming water vapor starkly contrasts the results found in Ch. 3 during the oxidation of polymer-derived HfSiCNO. In those static air

experiments, the $HfSiO_4$ was also contained in a SiO_2 oxide scale but showed no measureable coarsening even after extremely long exposures of 1000 hours at 1500°C. Coarsening of the $HfSiO_4$ particle appears to be enabled by flow of the surrounding SiO_2. Similar experiments have shown coarsening of the $HfSiO_4$ in regions where silica was noticeably wicking due to capillary forces. The static air experiments also showed similar effect were adjoining particles were in contact. The local regions of oxide would migrate by viscous flow to the contact point driven by the minimization of surface tension. Coarse $HfSiO_4$ particles were found in these regions, however none were found in the majority of the sample population where the oxide scale was static.

It is also possible that the presence of H_2O in the glass increases solubility of HfO_2 which would enable coarsening of the $HfSiO_4$ particles. Nevertheless, it can be concluded from the present results that the $HfSiO_4$ has a strong driving force for coarsening at 1500°C, but it is mostly prevented due to lack of solubility in the silica. Furthermore, careful inspection of Fig. 96 (right) shows the presence of a thin SiO_2 boundary layer between most silicate particles which is preventing direct contact. It is expected that if contact were forced between the particles, for example during SiO_2 flow, then the silicate particles would coarsen.

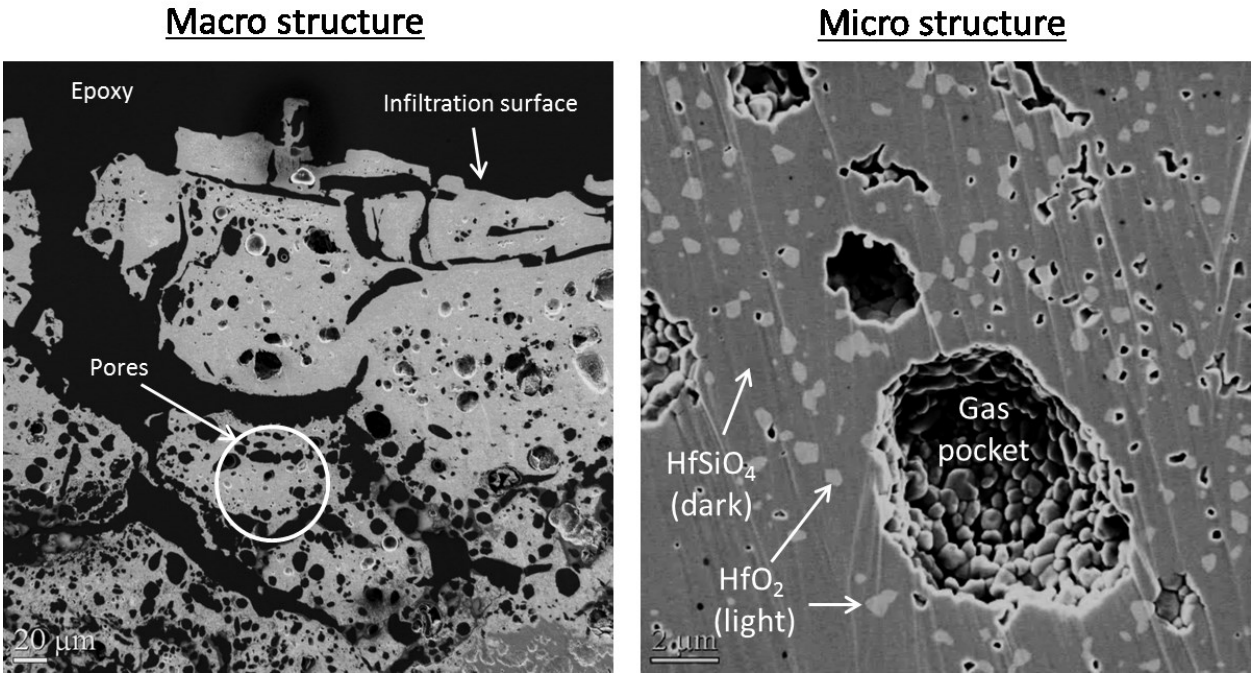

Fig. 97. Structure of oxidized SiCN-HfO_2 infiltrated layer showing gas pockets

One of the most pronounced structural features of the oxidized SiCN-HfO_2 infiltration is the presence of gas pockets. Fig. 97 (left) shows a low magnification image of the oxidized outer surface after 30 hours exposure. Significant voids can be seen throughout the infiltration thickness. The open pores appears black in color due to the back-filling with epoxy for imaging preparation, and the closed pores appear as hemispherical pits within the infiltrated layer. Several closed pores can be seen in the higher magnification right image of Fig. 97. (Note that silicate grains are not apparent due to surface preparation and would require further etching to become visible. Evidence of the silicate grains can be seen clearly inside the exposed gas pocket. Grain sizes observed here are consistent with those seen in Fig. 96 of about 1 μm. Electron charging can be seen around most of the closed pores.) The pores within the oxidized layer are the result of gaseous oxidation products from the SiCN phase. Bubbles in previous experiments of Ch.2 and 3 were determined to almost certainly be

from the nucleation of carbon monoxide. However, since the oxidation occurs so rapidly in these cases, the pores may be the results of escaping N_2 as well.

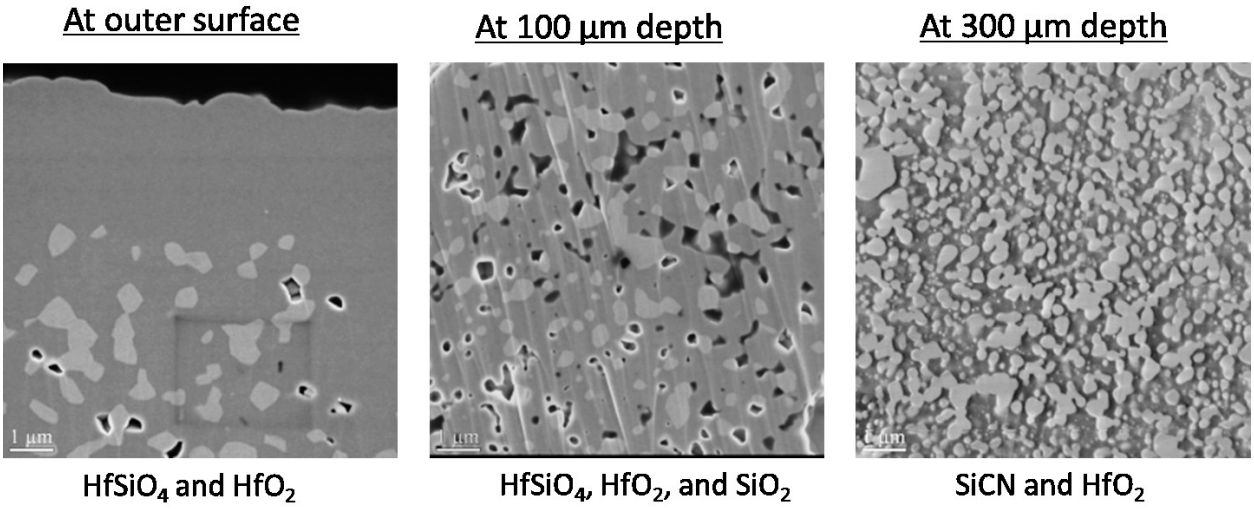

Fig. 98. Infiltration structure as a function of depth after oxidation

The oxidation depth within the infiltration varied significantly depending on the degree of local porosity within the sample. For example, areas surrounding an infiltration crack would readily oxidize down to the CVI SiC layer. However, on average, oxidization depths showed a degree of consistency across the sample and clear structural differences could be observed. The series of images in Fig. 98 shows the infiltration structure as a function of depth into the sample. These images were taken on a sample after 30 hours of 29 cm/s streaming H_2O at 1500°C. The sample revealed 3 distinct regimes from varying degrees of oxidation. The outermost layer was mostly $HfSiO_4$ with some sporadic pockets of unreacted HfO_2 which are seen as lighter color in the micrograph. The free silica content appears to have recessed away entirely. At a depth of 100 µm from the outer surface, the initial SiCN phase is oxidized entirely to SiO_2. There is still free silica observed and a greater concentration of HfO_2 grains. At 300 µm from the outer surface, the material is completely unoxidized with HfO_2 particles

suspended in a SiCN matrix. There is some coarsening of the HfO_2 into spheres of ~500 nm, but the material remains unoxidized as seen by significant nitrogen content via EDS.

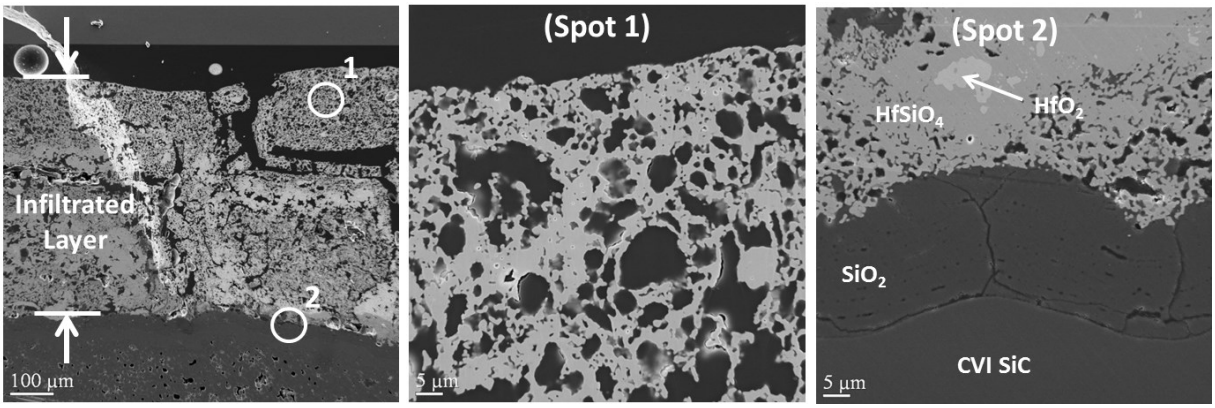

Fig. 99. SiCN-HfO_2 infiltration after oxidation exposure for 275 hours

The infiltration was completely oxidized after 275 hours at 1500°C in streaming H_2O. The left SEM image of Fig. 99 shows the complete thickness of the infiltrated layer. The middle graphic shows a higher magnification image of the oxidized pore structure. The sample was vacuum infiltrated with epoxy prior to preparation for SEM imaging. The presence of epoxy with thin pores (seen as dark pockets) indicated the majority of the porosity is open. This is also a likely explanation for the significantly higher oxidation rates of the SiCN-HfO_2 infiltration compared to the static air experiments which showed the formation of a dense oxide scales. The right image of Fig. 99 reveals oxidation of the CVI SiC layer at the infiltration interface. The oxide scale shows a layered structure which is due to the interrupted nature of the experiment. The sample was removed from the furnace every 25 hours to track measured weight change.

4.5.2 Microstructure of Oxidized SiC Infiltration

Infiltrations of pure SiC were also characterized for reference. These samples underwent the same experimental times and conditions as the SiCN-HfO_2 infiltrated samples. Fig. 100 shows optical cross-section micrographs of the SiC infiltrated preforms after streaming H_2O exposure of 1500°C for 10 hours (top) and 275 hours (bottom).

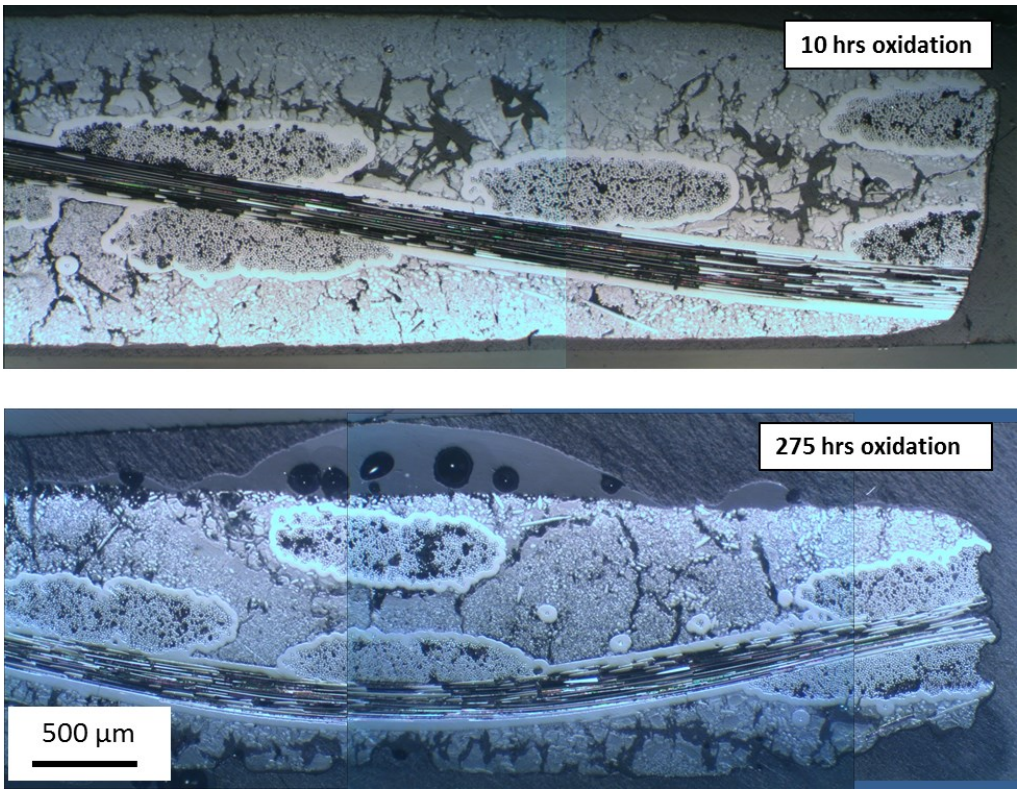

Fig. 100. Optical micrographs of SiC infiltrated sample after 10 hours and 275 hours

No significant structural changes were observed within the infiltration after 10 hours. Higher magnification SEM images of the outer SiC surface showed a SiO_2 oxide scale growth of ~10 µm. This is consistent with initial measured weight gain.

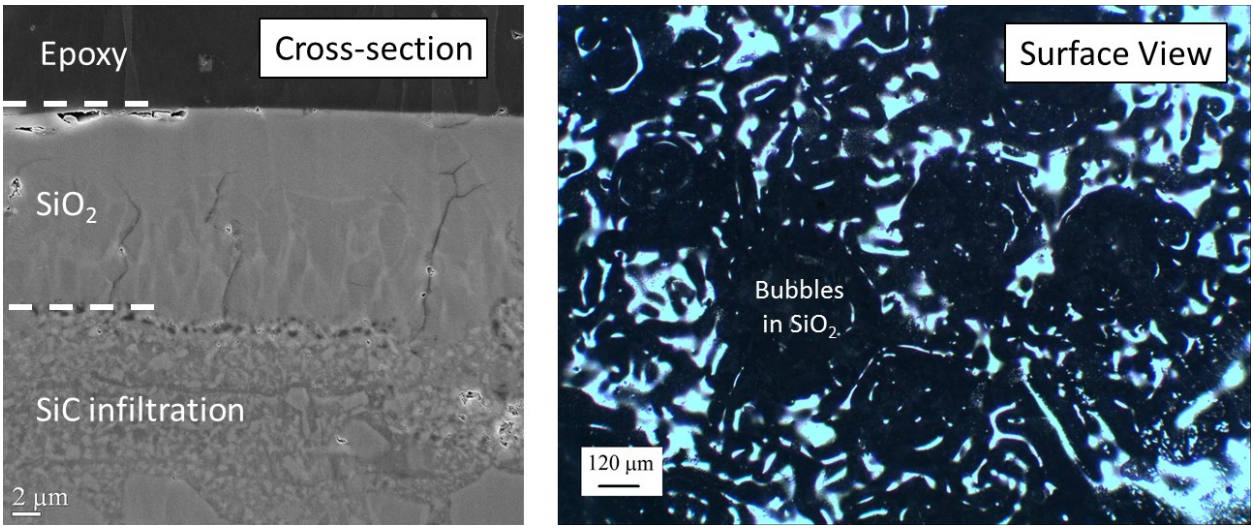

Fig. 101. Morphology of SiO_2 scale on SiC infiltration after 10 hour oxidation

Profuse amounts of silica were observed on the SiC infiltration surface after 275 hours of oxidation, mostly in the form of large pools. Fig. 101 (right) shows a top down view of the infiltration surface revealing a textured SiO_2 layer with evidence of bubbling from CO escape. The pooling of silica is evident and can be quite thick, up to 500 μm as seen in the lower image of Fig. 102. Note the significant difference in oxide scale morphology between these and the SiCN-HO_2 infiltrations. Hardly any free silica was observed in the SiCN-HfO_2 samples. The formed silica in those infiltrations reacted with the HfO_2 content to form a more stable $HfSiO_4$ phase. This could play an important role in rapidly streaming environments where the silica can not only recess by volatilization but by viscous flow as well. This contrasts the static air experiments where the oxide scales between SiC and SiCN-HfO_2 systems showed effectively equivalent behavior. It is important to note, however, that the previous experiments of Ch. 2 and 3 contained a lower HfO_2 content and therefore the oxide scales of both systems were dominated by the formation of silica.

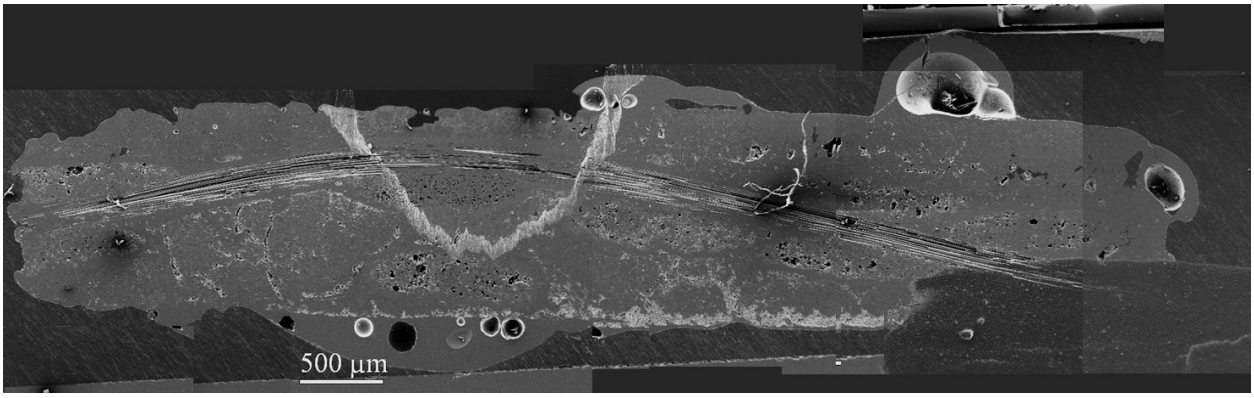

Fig. 102. SEM section of SiC infiltrated sample after 275 hours

An SEM cross-section of the SiC infiltrated sample after 275 hours is shown above. The similar contrast of the SiC and SiO_2 makes it difficult to distinguish the two with SEM. However, the image does reveal the surface pitting more clearly. This is particularly evident along the left edge of the preform in Fig. 102. The SiC infiltrated sample was ground flat and parallel after infiltration, and therefore any observed roughness in the surface is due to recession and/or flow of the SiO_2 after the SiC oxidizes. Significant pooling of SiO_2 is again evident at the infiltration surface along with bubbling from CO formation.

4.6 Discussion and Supplemental Results

The SiCN-HfO_2 infiltration resulted raised a couple questions which could not be answered by imaging alone. The first is in regards to the stability of hafnium silicate in the streaming H_2O conditions. It was assumed that the silicate phase would be stable up to ~1750°C where it is known to phase separate back into SiO_2 and HfO_2 in air. The constant rate weight loss of the SiCN-HfO_2 infiltration suggested that some product was volatilizing away. Since the outermost surface (exposed to the stream) was predominately $HfSiO_4$, it seemed plausible that the silicate phase was volatilizing to

some degree. The second question is what effect different SiCN to HfO_2 ratios would have on the oxidation rates and protective ability of the infiltration. The current experiments focused on a 2:1 liquid silazane to HfO_2 powder ratio primarily because it offered the highest HfO_2 content while maintaining processing ability. However, the results suggest this ratio is not ideal as it forms a highly porous oxide scale. Neither of these questions could be answered outright from the oxidation of the infiltrations, and separate experiments were designed in an attempt to quantify each.

The stability of $HfSiO_4$ in streaming H_2O conditions was tested by oxidizing the silicate directly in the powder form. Hafnium silicate powder was prepared by annealing a mixture of HfO_2 and SiO_2 powders in air. HfO_2 powder (100 nm, American Elements) and SiO_2 powder (30 nm, Sigma Aldrich) were mixed in a 1:1 stoichiometric ratio and dispersed in isopropanol. The liquid + powder mixture was ultrasonicated for 10 minutes to break up particle agglomerates. The mixture was heated on a hot plate to remove the solvent under constant stirring. The resulting powder mixture was annealed in air for 10 hours at 1600°C in a $MoSi_2$ element box furnace. X-ray diffraction showed the resulting powder to be crystalline $HfSiO_4$ with trace presence of unreacted cristobalite and HfO_2 content. Commercial zirconium silicate ($ZrSiO_4$) powder was also measured for reference.

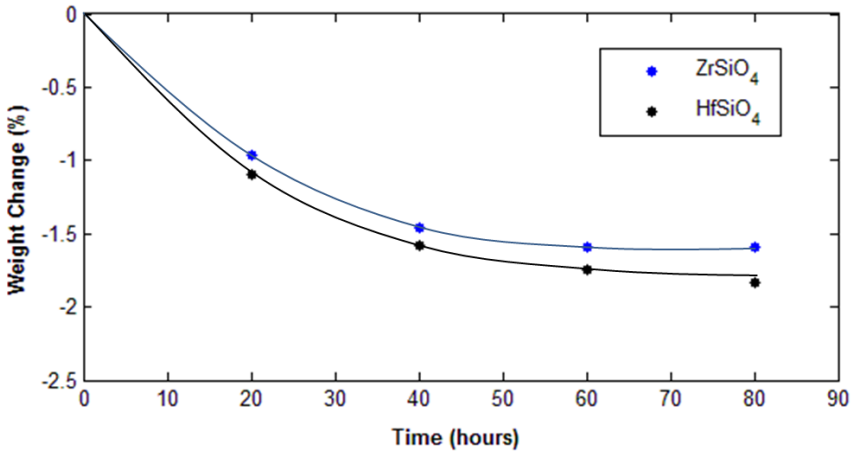

Fig. 103. Weight change of Zr and Hf silicate in streaming H_2O, 1500°C

Both samples show a small degree of initial weight loss plateauing after 60 hours as shown in Fig. 103. The loss is likely the result of unreacted SiO_2 which volatilizes to form gaseous $Si(OH)_4$. This is an important result as it shows the silicate phases themselves are stable in streaming H_2O and resistant to volatilization, unlike silica alone. This also suggests that recession in the SiCN-HfO_2 is likely due to SiO_2 recession and not the breakdown of the formed silicate phase. The stability of $HfSiO_4$ is a very favorable result since it shows that HfO_2 can be introduced into Si-based systems to react with the volatile SiO_2 and form a stable silicate phase.

An attempt was made to quantify the recession rates of various SiCN-HfO_2 ratios compared to pure SiC as a baseline. This was achieved by slotting channels in a SiC substrate and then infiltrating the channel with SiCN-HfO_2 using the aforementioned slurry vacuum infiltration technique. After the infiltration cycles, the surface of sample was polished level such that the two materials shared a common flat surface. The hypothesis was that recession could then be measured directly between the two systems. However, the results of these experiments were ambiguous mostly due to the flow of SiO_2 and swelling of the infiltrated layer from bubbling.

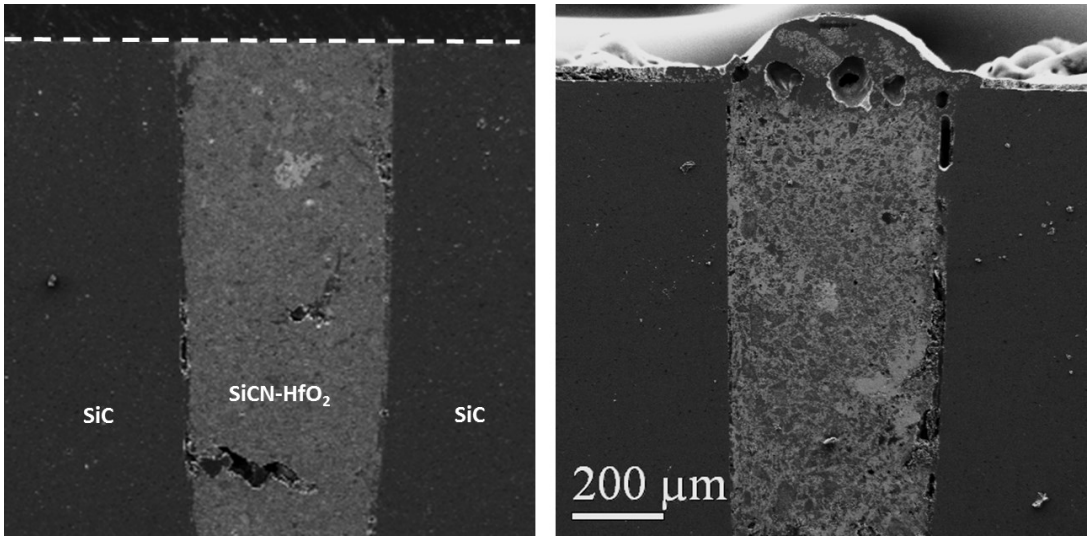

Fig. 104. Side-by-side comparisons of SiC and SiCN-HfO_2 recession surfaces

The above figure shows an example SEM cross-section of the designed recession experiments. Each image shows SiC at the left and right edges. The middle region is a channel cut by diamond saw and then backfilled with SiCN-HfO_2. The example shown above is for a silazane to HfO_2 weight ratio of 1:1. After oxidation in streaming H_2O for 10 hours (right image), noticeable bulging of the reference plane is observed above the SiCN-HfO_2 layer. The infiltrated section appeared to be wicking SiO_2 from the surrounding SiC as well as experiencing bubbling from oxidation CO or N_2 products. This shift in reference plane made the experiment impossible to quantify. However, one noteworthy observation is that the 1:1 ratio did reveal a much smaller oxidation depth than the 2:1 ratio preform infiltrations.

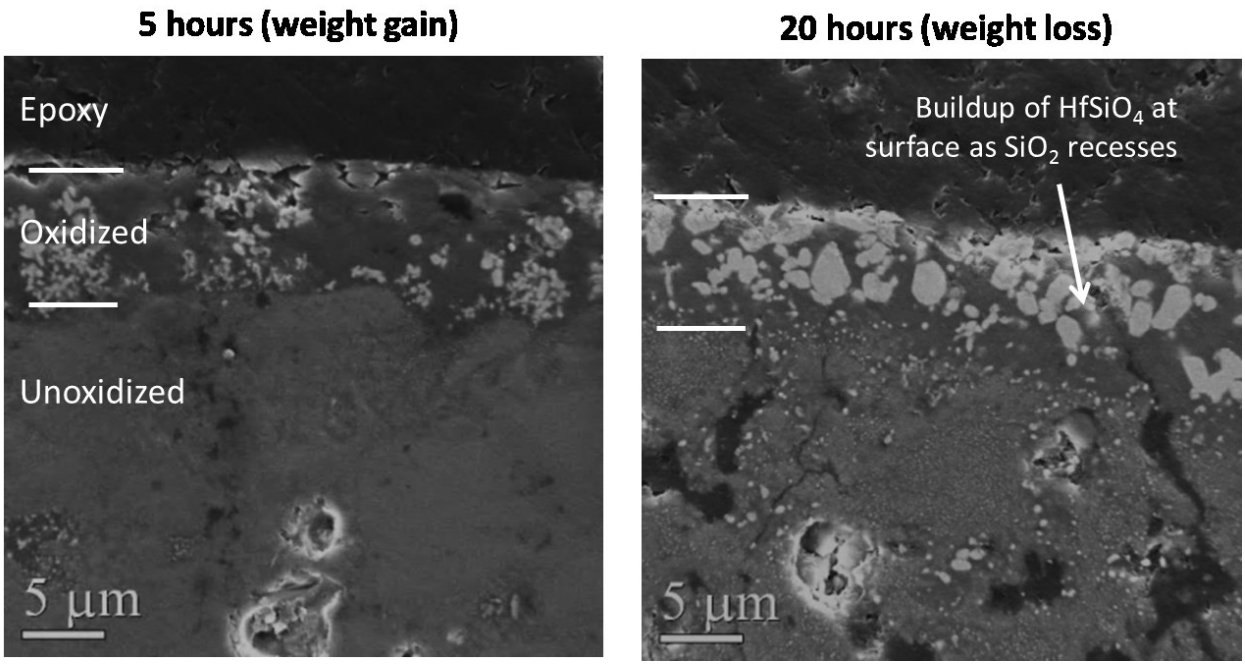

Fig. 105. Increase in $HfSiO_4$ concentration as SiO_2 recesses away

Similar observation was made in the preliminary testing of polymer-derived HfSiCNO materials in streaming water vapor. These samples were composed of S14 composition HfSiCNO (see Ch. 3) and were made using effectively the same vacuum infiltration techniques as used with SiC preforms. The primary difference was the addition of hot-pressing to lessen the formation of porosity during pyrolysis. After oxidizing in recessive H_2O conditions (1500°C, 29 cm/s) they showed behavior which was more akin to the oxidation of pure SiC or SiCN. This can be seen in Fig. 105 where the material shows a dense and continuous oxide scale, as opposed to the porous scale formed by high HfO_2 content. The steady state oxide scale thickness is ~10 μm, same as what was observed for the streaming oxidation of pure SiC. Note how the concentration of $HfSiO_4$ builds up at the outer surface due to SiO_2 volatilization. As the SiO_2 recesses, the $HfSiO_4$ content remains behind and results in a higher concentration. This further validates the conclusion that $HfSiO_4$ is stable in these streaming H_2O

conditions at 1500°C and could be as the basis for a self-healing design in streaming environments.

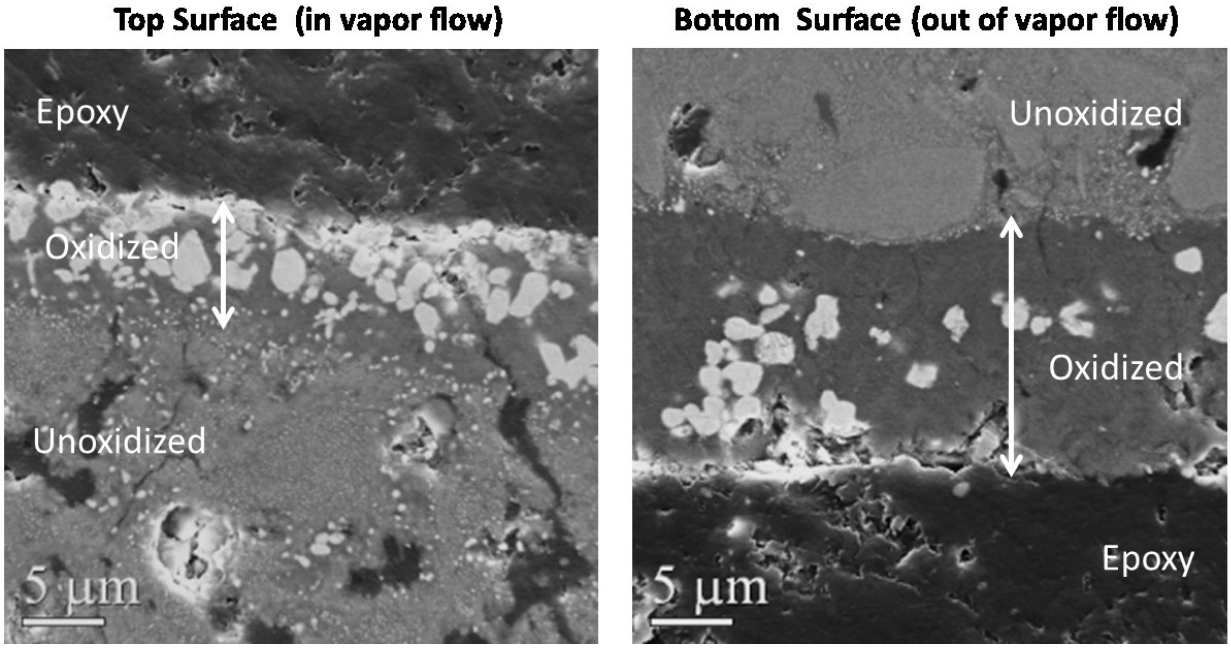

Fig. 106. Recession dependence on H_2O flow rate

The effect of $HfSiO_4$ buildup of is further highlighted by examining regions of the sample which were out of the H_2O flow. Fig. 106 shows the top and bottom faces of the same S14 HfSiCNO sample where the top face was in the H_2O flow path and the bottom was shielded. The top face shows a steady state oxide scale of 10 μm as before, and the bottom face shows a growing scale thickness of 15+ μm due to the lack of SiO_2 recession. The difference in $HfSiO_4$ concentration between the two scenarios is evident. The top face has developed a near continuous layer of $HfSiO_4$ whereas the bottom only shows intermittent $HfSiO_4$ precipitates. The question remains as to how these would behave after longer exposures in recessive environments. As the surface $HfSiO_4$ concentration increases, does it form a continuous layer and prevent the H_2O recessive flow from volatilizing the underlying SiO_2 layer, or does it leave a porous oxide layer behind as seen in the infiltration experiments? There is evidence to suggest either

case. The channeling experiments were an attempt to quantify this but were unsuccessful and require further exploration.

4.7 Chapter Summary and Interpretation

SiC-SiC structural "preforms" were infiltrated with a ceramic composite of SICN-HfO_2 via polymer slurry infiltration. The slurry was composed of liquid silazane (precursor for SiCN) and hafnia powder. Samples were infiltrated using a vacuum infiltration technique which required multiple infiltration cycles due to shrinkage of the silazane during pyrolysis. The infiltrated samples were oxidized in streaming H_2O at 1500°C and a flow rate of 29 cm/s. Infiltrations consisting only of SiC were also compared for reference.

Specific weight loss of the samples normalized per unit surface area showed similar constant rate loss from SiO_2 recession into gaseous $Si(OH)_4$ after a 50 hour initial transient. The SiCN-HfO_2 sample showed a sharp weight loss during the first 50 hours, whereas the SiC sample showed a brief initial weight gain. The immediate weight gain of the SiC followed by linear loss is consistent with paralinear kinetics involving both passive/active mechanisms concurrently. This was described mathematically in the text; however, due to highly irregular silica formation, no active or passive kinetic rates could be determined for the SiC. For future experiments, streaming H_2O oxidation on SiC crystals would offer the uniform surface oxide formation needed to quantify rates. A possible explanation for the relative rate difference between the linear weight loss of the SiC infiltration and SiCN-HfO_2 could be explained by the specific SiO_2 content between the two infiltrations. The measured linear weight loss rate of the HfO_2-SiCN infiltration was 65% that of the SiC loss rate. If all SiCN were oxidized and HfO_2 were saturated to

$HfSiO_4$, then 30% of the remaining silica would be free to volatilize. This is a factor of 2 lower than the expected. This discrepancy is likely explained by two factors (i) the theoretical SiCN content is significantly under predicted due to the hafnia deficient regions as shown in Figs. 88-89, and (ii) not all HfO_2 is reacted to $HfSiO_4$ prior to volatilization as seen by the presence of unreacted HfO_2 particles in Figs. 97 (right) and 98 (left). Follow-up experiments may try to involve annealing of the sample in static air prior to recessive environment exposure. In this way, $HfSiO_4$ could be given sufficient time to form before the silica is volatilized away.

The rapid weight loss of the SiCN-HfO_2 containing sample could not be explicitly determined from micrographs, but it seems likely due to the rapid oxidation and volatilization of the infiltration SiCN content. This is an interesting phenomenon since one expects a 13.8% net weight gain from the oxidation reaction of SiCN to form SiO_2. The open porosity formed in the SiCN-HfO_2 sample is expected to play a role it this rapid loss behavior. Since the formation of $Si(OH)_4$ is a surface effect, it stands to reason that the open porosity creates a high specific surface area in the oxide scale permitting rapid volatilization of SiO_2. Once the free SiO_2 content near the surface has either recessed or reacted with HfO_2 to form $HfSiO_4$, then active kinetics control the rate and linear weight loss is observed.

The two types of preforms show distinctly different oxide scale morphologies. The SiC infiltrated sample showed formation of SiO_2 with a significant degree of CO bubbling at the infiltration surface. The sample showed surface pitting from recession of the SiO_2 layer and viscous flow into pools. The SiCN-HfO_2 developed porosity within the infiltrated layer during oxidation, where both open and closed pores were observed. The SiCN content reacts with the ambient H_2O to form SiO_2 and trapped gas pockets of CO and possibly N_2. The rates of oxidation were observed to be 2 orders of magnitude

higher than experiments of Ch. 2 and 3 conducted in static air primarily due to the lack of a continuous passive oxide layer. The formed silica reacts with the initial HfO_2 content to form hafnium silicate which is found to be stable in streaming conditions at 1500°C.

Experimental evidence suggests that a lower initial HfO_2 content may be beneficial as it would permit the formation of a continuous oxide layer. This would force H_2O to go into solution with the oxide scale and diffuse through it to further oxidize the underlying infiltration. It is also possible that an increased initial HfO_2 content could provide a similar effect if it were sufficiently high enough to provide a dense outer scale. However, the slurry viscosity in this case would prohibit the use of the current vacuum infiltration technique.

5 Summary of Results Presented and Future Experiments

5.1 Summary of Key Results

Composite material systems based on HfO_2 and SiCN were evaluated in high-temperature oxidizing conditions for their protective ability on silicon carbide based CMCs. HfO_2 was selected as the environmental barrier layer due to its high melting temperature, chemical inertness, low vapor pressure, and phase stability. Polymer-derived SiCN was selected as a bonding layer for its high temperature stability, oxidation resistance, and chemical compatibility. Due to its inherent amorphous nature, SiCN is an exceptionally good bonding medium to oxide and non-oxide materials alike. Multiple designs of the SiCN-HfO_2 system were experimented, revealing potential for application at all levels of the CMC structure.

Multilayer films of a tiered SiCN-HfO_2 architecture were deposited on SiC single crystals and characterized for structure and oxidation rates. A hybrid PP-MOCVD system was developed to accommodate processing of the various thin films, including a new technique for conformal nanometer scale deposition of polymer-derived SiCN. High resolution TEM of the films reveal excellent bonding of the SiCN layer to both HfO_2 and SiC materials. Oxidation experiments were carried out in ambient air at 1500-1600°C in ambient air which show the formation of hafnium silicate. This $HfSiO_4$ layer was found

to be stable at the tested UHT conditions in air and streaming water vapor with no evidence of volatilization. Literature suggests this silicate phase is stable up to 1750°C making it a favorable reaction product for EBC systems particularly in streaming environments where SiO_2 is known to recess. The oxidation of the multilayer structure appeared to be rate limited by the outward diffusion of carbon monoxide through SiO_2. Upon oxidation, the SiCN/HfO_2 films result in a multilayer oxide structure consisting of an environmentally stable $HfSiO_4$ outer layer and a sub-layer of SiO_2 which acts as strong diffusion barrier to continued oxidation. The thin $HfSiO_4$ top layer was found to coarsen at prolonged exposure to 1600°C, a problem which could be mitigated by the initial deposition of thicker HfO_2.

Exploratory thin films of amorphous HfSiCNO and HfSiCO were also deposited on SiC crystal substrates and oxidized at 1600°C. Difficulties segregating film/substrate oxidation behavior led to an independent study of Hf-O doped SiCN. These materials were processed in bulk by chemically modifying a commercially available silazane with Hf-butoxide in the liquid state. Detailed FTIR studies showed the two precursors to react spontaneously in the liquid state by the formation of Hf-N-Si bonds, anchoring the alkoxide molecule to the silazane. Upon thermal cross-linking, the polymer network was found to retain Hf content and significant formation of Hf-O-Si bonds were observed.

The Hf-containing polymer was found to show amorphous solubility of Hf-O in SiCN up to a Hf/Si ratio of 0.22 upon pyrolysis at 1000°C. This solubility limit was corroborated by *ab initio* atomistic simulations which, in addition, predicted mixed coordination around Hf and mixed bonding with C, N, O consistent with that observed for Si in the amorphous network. Simulated FTIR spectra match experimental results to a significant degree suggesting the formation of Hf-(C,N,O) bonds in the pyrolyzed HfSiCNO. Above the amorphous solubility limit the material results in composite

structure consisting of ~10 nm HfO_2 crystals in an HfSiCNO matrix. Interestingly, the amorphous nanodomain structure of SiCN remains essentially unaltered after significant doping with Hf-O as revealed by SAXS, Raman, FTIR, and XRD. Theoretical enthalpy calculations for Hf atomic substitution with Si support this result.

The polymer-derived HfSiCNO was oxidized in ambient air at 1600°C. A model was developed to relate the oxide scale growth of HfSiCNO to measured weight gain. Quadratic oxidation rates were found to be in the 5-25 nm^2/s range and are expected to be limited by the outward diffusion of CO. The difference in oxidation rates between the tested HfSiCNO compositions is likely explained by the relative carbon content of the base materials. The oxidation scales were found to consist of 200 nm $HfSiO_4$ precipitates in a SiO_2 matrix. Carbothermal reduction, which occurs rapidly in inert atmosphere, was found to be suppressed during passive scale growth by CO pressure buildup which develops at the oxide interface for p_{O_2} levels >0.01.

SiC based CMCs were infiltrated using a composite of HfO_2 particles in a SiCN matrix. A process was developed for vacuum infiltration of CMC preforms using a silazane-HfO_2 slurry. Infiltrated preforms were oxidized in a recessive streaming water vapor environment at 1500°C and compared to SiC. Both infiltration types showed linear weight loss after 50 hours of exposure due to SiO_2 volatilization into $Si(OH)_4$. Despite similar rates of weight loss, the two sets of infiltrations showed distinctly different oxide morphologies. The SiC infiltrations showed heavy amount of silica growth at the infiltration surface and local areas of pitting. The SiCN-HfO_2 infiltration showed the formation of a porous $HfSiO_4$ scale which was enabled oxygen permeation. The weight loss in the SiCN-HfO_2 infiltrations appeared to be from the recession of free silica surrounding micron sized grains of $HfSiO_4$. The immediate formation of a porous

$HfSiO_4$ structure prevented the formation of a passive SiO_2 layer and led to significantly greater oxidation depths.

5.2 Design of Future Experiments

The experiments presented in this thesis offer a number of new insights into the use of oxide / non-oxide composite systems as means to protect CMCs in high-temperature applications. Several future experiments can be envisioned combining these results for various protection pathways, in addition to those already posed in the text. The body of work presented here covers fundamental materials selection, processing techniques, and performance in oxidizing environments. Future experiments and applications can pull from each of these aspects in a cohesive way to drive progressive research.

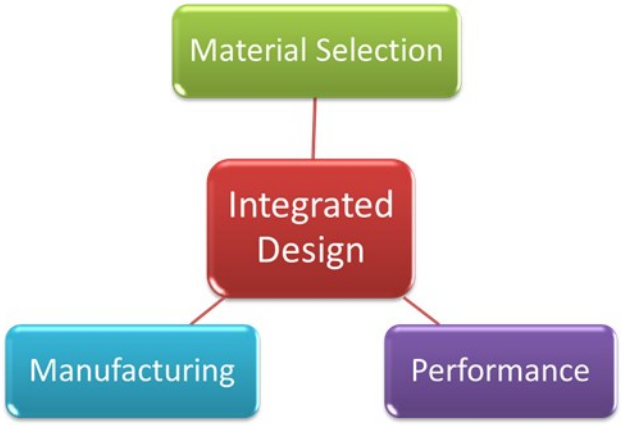

Fig. 107. Integrated approach for design of future experiments

Material Selection – This thesis work showed basic feasibility for the design of EBCs constituted from oxide and non-oxide materials. The design concept was centered around an outer EBC layer of HfO_2 adhered to structural SiC components using polymer-derived SiCN. The hafnia was shown to react with SiO_2 reaction products

to form $HfSiO_4$, which was found to be stable in air and recessive water vapor conditions at 1500°C.

Manufacturing – Novel techniques were developed for the deposition of SiCN thin films, processing of polymer-derived HfSiCNO, and infiltration of CMC preforms. The production of HfSiCNO from the polymer route is particularly interesting because it adds an entirely new dimension of flexibility for EBC/CMC design. A basic understanding of manufacturing limitations was gained from these experiments as well as insights into improved methodologies.

Performance - The performance of the SiCN-HfO_2 was accessed in both passive and active oxidizing conditions. Oxidation reactions and rate limiting mechanisms were identified for multiple design architectures.

Drawing from these three considerations, several future experiments can be envisioned in a manner which ties them all together. Principally, this research shows design concept viability; however, the key question to address moving forward is - *How does one achieve/maintain a dense $HfSiO_4$ barrier layer?* The following are several possibilities which utilize the lessons learned from all facets of this effort.

Deposit directly - One simple option would be to deposit a thick outer barrier layer of HfO_2 and/or $HfSiO_4$ rather than trying to develop the layer *in situ*. This concept has been applied in one recent study using radiation frequency magnetron sputtering to deposit HfO_2 as an EBC material on SiC [162]. The problem with this method is cost and processing limitations. Developing these EBC material structures from the polymer-route is the attractive alternative because of its inherent manufacturing flexibility. It is for this reason that state-of-the-art CMCs are already using the polymer route to manufacture both ceramic fiber and matrix materials. The development of a

dense $HfSiO_4$ layer *in situ* is particularly appealing in the case of matrix materials because it would offer a self-healing benefit in the event of spalling, fracture, etc. Nevertheless, one viable option would be to deposit a thick layer of HfO_2 or $HfSiO_4$ prior to any environmental exposure. The most useful presentation of this would be to have a thick initial layer deposited on a HfSiCNO matrix. In this way, one could have the benefit of robust outer EBC with the secondary protection of a self-healing sub-layer.

Alter HfO_2-SiCN ratio - The infiltration experiments presented here used a 2:1 liquid to powder slurry which was selected (in somewhat arbitrary fashion) due to its processing ease. The effects of varying ratios were unknown, and therefore the highest HfO_2 content which could be easily infiltrated was used. Subsequent streaming experiments give evidence to suggest this ratio should be increased significantly or decreased significantly to achieve a dense $HfSiO_4$ layer during oxidation. The presented results show that the 2:1 ratio oxidizes rapidly to significant depth due to the formation of a porous silicate scale. Higher HfO_2-SiCN ratios would form a dense $HfSiO_4$ based scale, and lower ratios would form a dense SiO_2 based scale. Either case could be employed. A higher initial HfO_2 content would be expected to densify more readily, or, even if it does not, it would offer a less porous outer EBC layer since the pores result from oxidation of the SiCN content. A significantly lower initial HfO_2 content in SiCN should also be favorable. It was shown on oxidized HfSiCNO pellets (low Hf-O) that this enables the formation of a thin, dense, passive oxide layer. During the SiO_2 recession of this passive layer, $HfSiO_4$ precipitates were observed to progressively build up towards continuous coverage without any observed porosity. Current experiments did not reveal how far this concept can be extended, but it appears feasible and is worth further investigation.

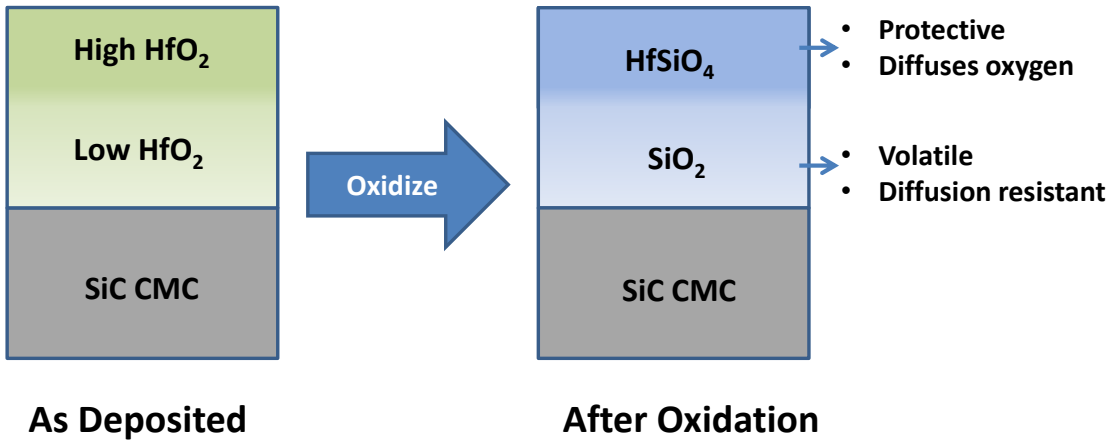

Fig. 108. Proposed graded structure to form a dense, protective, diffusion resistant EBC *in situ*

In a related manner, one can also envision creating a graded structure of differing HfO_2-SiCN ratios with each level serving a unique purpose. For example, a structure could be designed such that, upon oxidation, a protective $HfSiO_4$ layer floats above a diffusion resistant SiO_2 layer as illustrated in Fig. 108.

Increase environmental temperature - Oxidation studies on the material hafnium carbide (HfC), which has poor oxidation resistance at temperatures <1800°C, have shown that higher temperature oxidation permits the densification of the formed oxide scale. This densification in turn offers superior oxidation resistance. This is an interesting concept and is particularly relevant in to the present infiltration experiments in which SiCN-HfO_2 was shown to oxidize into a porous layer of hafnium silicate. The pressureless sintering kinetics of $HfSiO_4$ are unknown; however, current infiltration results show that the micron sized grains of $HfSiO_4$ do sinter at prolonged exposure to 1500°C. It is reasonable to suggest that higher temperature oxidation may lead to densification of the silicate layer and offer superior protection.

Pre-annealing of infiltrated layer - Another alternative to create a dense $HfSiO_4$ layer would be to pre-treat the infiltrated layer in an oxidizing environment which is non-

recessive. The intent would be to form passive SiO_2 which could then react with native HfO_2 to form $HfSiO_4$ before recession of the SiO_2 occurs. The favorable design would be to use a SiCN-HfO_2 ratio which oxidizes to form a SiO_2-HfO_2 ratio of unity. Or, perhaps, a system could be designed such that a small excess of SiO_2 promotes liquid phase sintering of the $HfSiO_4$ layer.

The current thesis work gives a foundation for the development of SiCN-HfO_2 based EBCs with regards to materials selection, processing, and oxidation performance. These experiments were mostly exploratory in nature to understand the scientific underpinnings of such EBC systems. Current results demonstrate concept feasibility, and the proposed experiments detailed above can be considered a more focused application of the learned results. A final tier of experimentation would be to quantify ultimate limits such as maximum temperature capability, performance in Mach streaming conditions, and thermal/mechanical properties. Hopefully, the results of this thesis can serve as framework for future research and development towards real-world application of oxide/non-oxide environmental barrier coatings.

6 Appendix

6.1 Appendix A – Density of SiCN and HfSiCNO Ceramics

Density measurements are reported for HfSiCNO powders with a Hf:Si ratio of 0.0 to 0.38. Measurements were taken using Archimedes method. The pyrolyzed particles were weighed and added to a very thin glass measurement pipet partially filled with water. The heavy powder sinks leaving a measurably higher water line. The pipet has sensitivity of 0.001 mL and the mass balance a sensitivity of 0.1 mg.

The powders were processed as described as in Section 3.4.1. The only difference in processing procedure was the absence of any automated powder milling. Powders here were only lightly milled using a mortar and pestle to keep the particle size as large as possible. This negates surface tension problems associates with particle wetting. After milling, the coarse powders were separated out using a wire mesh sieve.

Small quantities of powder were measured for mass and then poured into a 2mL precision fluid measuring pipet which contained an arbitrary amount of measurable water. The volume of the liquid was measured before and after adding HfSiCNO particles to determine total volume added.

Table A1. Density measurement reference standards

Material	Density (gcm^{-3})		Deviation (%)
	Measured	Theoretical	
α-SiC	3.14	3.21	-2.09
HfO_2	9.37	9.68	-3.21

Table A1 shows the accuracy of the measurement technique for known powders compared to their theoretical values. The simple technique proved accurate to within 3% of theoretical values for known powder densities. Both values are lower than predicted. This is an expect result as the powders undoubtedly carried some degree of air with them. Powders were not purged of any micro-pockets of air after being immersed in the water.

Table A2. Densities of HfSiCNO powders as a function of Hf:Si ratio

Sample	Hf:Si Ratio	Density (gcm^{-3})
SiCN	0	2.24
S08	0.08	2.94
S14	0.14	3.42
S26	0.26	3.78
S38	0.38	3.89

HfSiCNO powder densities are given in Table A2. Particulate SiCN pyrolyzed at 1000°C was measured to have a density of 2.24 $g.cm^{-3}$. This is somewhat low compared to those values reported from 2.3 to 2.7 $g.cm^{-3}$ for SiCN materials [174]. However, is it important to note that SiCN using different molecular precursors can yield markedly different properties, and therefore a broad range of densities for various $Si_xC_yN_z$ is not unexpected. XRR thin film measurements of pyrolyzed SiCN gave a density approximation of 2.27 gcm^{-3} with a standard deviation of 0.03 $g.cm^{-3}$. These thin films were on Si substrates and were made using the same Ceraset precursor as used for the powder samples. They are presumably fully dense, and a description of

their processing is in Section 2.3. This offers strong confirmation for the accuracy of the 2.24 g.cm^{-3} measurement made here for Ceraset derived SiCN.

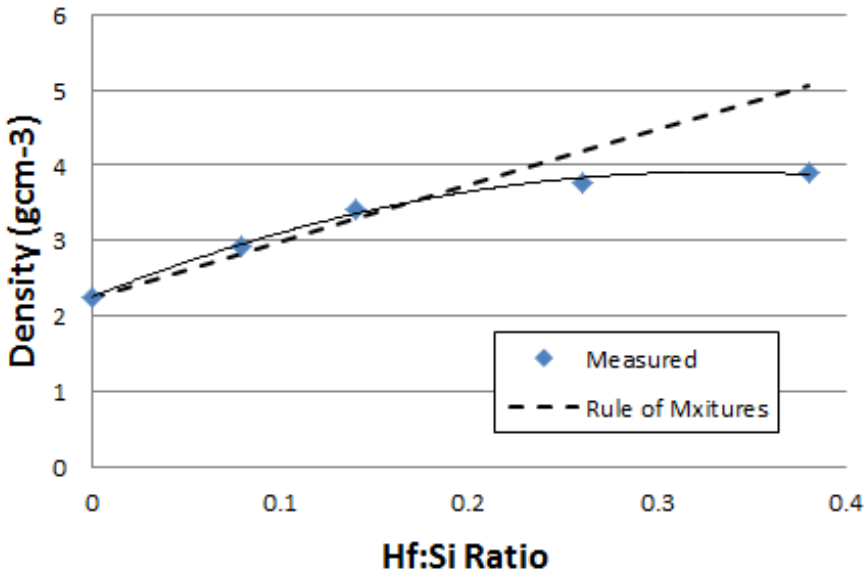

Fig. 109. Measured and theoretical densities of HfSiCNO Powder

As expected the HfSiCNO density was found to increases with an increasing Hf-O content due to the extremely high atomic weight of Hf. The measured densities appear to follow the rule of mixtures (SiCN and HfO_2) up to a Hf:Si ratio of ~0.2. At higher Hf concentrations, however, the measured densities deviate towards lower values. A likely explanation for this is the presence of particle voids. The higher Hf concentrations experience significant off-gassing during thermal cross-linking from the loss of alkoxide t-Butyl groups. Typical HfSiCNO-H mixtures were “foam” like after cross-linking. It is anticipated that similar off-gassing during the ceramic conversion leads to the formation of micron or nanometer size voids in the material as well. This is particularly true in the ceramic state where the material densifies and has dramatic increases in viscosity. The higher viscosity would be less permeable to pyrolysis volatiles which have to diffuse to a free surface to escape. If the pressure of gaseous species present in the materials

significantly exceeds the ambient pressure, then bubbles can nucleate. Complete burn off of organics is not achieved until the materials reach ~700°C.

6.2 Appendix B – Prediction for Hf-C, Hf-N, and Hf-O infrared absorption peaks

IR absorption from stretching oscillations of bonds between Hf and C, N and O are likely to be clustered at low frequencies because these elements have similar atomic weights, and the bond energies are also similar. This section theoretically calculates these absorption frequencies using the harmonic oscillator model using the known peak for Zr-N at 548 cm^{-1} as the reference.

For a simple harmonic oscillator, the frequency of oscillation is given by

$$\nu = \frac{1}{2\pi}\sqrt{\frac{k}{\mu}} \tag{B1}$$

where k is the spring constant and μ is the reduced mass which is written as $\frac{m_1 m_2}{m_1+m_2}$. It is assumed that the effective masses are proportional to the elemental AMU and that spring stiffness is proportional to bond energy. Thus, it can be written that,

$$\nu_{Zr-N} = C \cdot \sqrt{E_{Zr-N}\frac{M_{Zr}+M_N}{M_{Zr}M_N}} = 548cm^{-1}(experimental) \tag{B2}$$

where the spring stiffness is now represented by the bond energy, E_{Zr-N}, in kJ.mol^{-1} and C is a constant with appropriate units; it is related to the stretching displacement that leads to bond rupture, assuming linear elastic behavior. Substituting in values for the Zr-N system the proportionality constant is calculated to be

$$C = 548cm^{-1} \cdot \left(345\ kJ.mol^{-1} \cdot \frac{91\ amu + 14\ amu}{91\ amu \cdot 14\ amu}\right)^{-1/2} = 102.77\left(\frac{cm^2.mol.amu}{kJ}\right)^{1/2} \tag{B3}$$

The various Hf bond frequencies can now be approximated by substituting in the known masses and bond energies into Eq. B2 for the various Hf bonds. For example, in the case of four-coordinated Hf-C, the predicted peak location is found to be

$$\nu_{Hf-C} = 102.77\left(\frac{cm^2.mol.amu}{kJ}\right)^{1/2} \cdot \sqrt{362\ kJ.mol^{-1} \cdot \frac{178\ amu + 12\ amu}{178\ amu \cdot 12\ amu}} = 583 cm^{-1} \qquad \text{(B4)}$$

The bond frequency approximations and the values used to calculate them are listed in Table B1.

The bond energies given in Table B1 are given a range, with lower values corresponding to the assumption of five-coordinated bonding, and the higher values to tetrahedral coordination around the central Hf atom. One literature source assigns the four-coordinated Hf-N absorbance peak to be at 527 cm^{-1} for a HfN CVD precursor [128]. The calculated value for four-coordinated Hf-N bond is 534 cm^{-1} is in good agreement with the experimental value.

Table B1. Estimated absorption peaks for Hf bonds with N, C and O.

	Zr – N	**Hf-N**	**Hf-C**	**Hf-O**
M_1 (AMU)	91	178	178	178
M_2 (AMU)	14	14	12	16
Bond Energy ($kJ.mol^{-1}$)	345	233-350	241-362	356-534
Wavenumber (cm^{-1})	548 (*experimental)*	436-534	476-583	506-620

6.3 Appendix C – SAXS Nanodomain Analysis of HfSiCNO Compounds

Small angle X-ray scattering is a non-destructive analysis technique for the determination of material structure on the nanometer length scale. This appendix details the methods used to analyze the SAXS profiles for amorphous HfSiCNO compounds for their atomic nanodomain structure.

6.3.1 Principles of Small-Angle X-ray Scattering (SAXS)

Small angle x-ray scattering (SAXS) is a method by which particles or structures can be resolved having sizes within the range of 1-50nm. X-ray analysis techniques in materials science are typically separated into two broad categories- scattering and diffraction. Scattering is used at small incident beam (Bragg) angles to determine size and structure of individual features, whereas diffraction is used at large Bragg angles to determine long range order of atomic structure.

Table C1. X-ray scattering regimes for material analysis

2Θ angle (°)	Structure Scale (nm)	Analysis Type
0-1	10 - 50	Ultra small-angle x-ray scattering
1-10	1 - 10	Small angle x-ray scattering
10-100	< 1	Wide angle x-ray scattering (diffraction)

Like all forms of electromagnetic radiation, x-rays interact with matter by absorption, transmission, and reflectance. The relative scattered intensity depends on material density, mass-aborption coefficient, and scattering cross-section. Atoms and clusters of atoms (particles) both contribute to x-ray scattering with unique signatures. Scattering of x-rays by materials occurs in two forms (i) Compton scattering [163] and (ii) Raleigh

scattering [164]. Both forms scattering are predominately the results of x-ray interaction with electrons.

Compton scattering is visualized easily by considering both the incident x-ray and interacting electron as particles. When X-ray photons strike loosely bound electrons they are deflected away. Some part of the photon's momentum is transferred during the collision, and therefore the scattered radiation wavelength is longer (redshift) than the incident beam. Compton scatter is random, incoherent, and shows no dependence on incident radiation angle. Since the scattered photon frequencies vary randomly, Compton scatter shows no interference effects. Experimentally this produces a near uniform background intensity, and no structural information can be derived from it.

Raleigh scatter is the type exploited in materials science and is best described by visualizing the incident x-ray as a wave. X-rays are electromagnetic waves and thus have electric and magnetic fields whose strengths vary sinusoidally with time. The varying electronic field will interact locally with any charged particles. This includes both electrons and protons; however, protons generally have too much mass to be excited by x-rays. The fields from radiation cause tightly bound electrons to oscillate at the same frequency as the incident beam. These electrons are bound too strongly for the x-ray to impart any momentum to it, as with Compton scattering. When the oscillating electron (higher energy) decelerates it emits a photon of equal wavelength as the one absorbed following energy conservation. This ejected photon has phase dependency on the incident beam and is called "coherent scattering". This coherent scattering produces constructive and destructive interference patterns when the atomic structure is regular, such as in crystals, giving rise to the commonly used x-ray diffraction technique for determination of crystal structure.

Unlike diffraction from regular interference, structure determination from SAXS relies on "contrast" between electron densities of adjacent regions. That is, determination of domain size requires that the domains have a different electron density than their surroundings. Inclusions and voids will both contribute to the SAXS spectra of materials like HfSiCNO or SiCN. The difference in scattering intensity is not sign dependent and therefore a void in a solid matrix would give the same intensity as solid particle in a void matrix. This phenomenon is known as Babinet's Principle [165] where two complimentary structures produce the same scattering, Fig. 110.

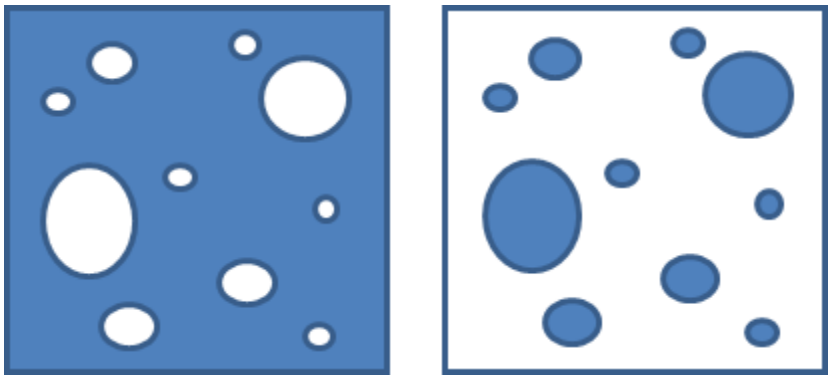

Fig. 110. Voids in a solid matrix (left) and corresponding solid particles in void matrix (right). Both have equivalent SAXS profiles.

6.3.2 Methods of Analysis

X-ray scattering intensity profile can be represented mathematically by two main parameters- the structure factor, S(q), and form factor, F(q), where q is the spatial scattering vector. The form factor accounts intra-particle interactions of x-rays and contains information about particle size and shape. The structure factor includes inter-particle scattering effects and accounts for long range and local order and particle-particle interactions.

SAXS patterns were used to determine nanodomain size by fitting the experimental pattern with a distributed sum of form factors for spherical nanoparticles. Fig. 110 shows a typical intensity profile (form factor) for the x-ray scattering by a nanoparticle.

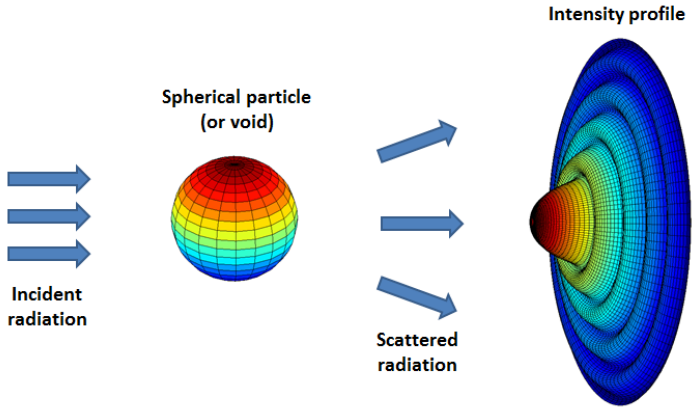

Fig. 111. Illustration example of form factor. A spherical domain and resulting SAXS intensity profile.

The total experimental small angle intensity, I(q) , varies with scattering angle and can be written in terms of 3 factors:

$$I(q) = I_L(q) + I_N(q) + I_D \qquad \text{(C1)}$$

I_D represents the diffuse scattering, showing no dependence on q, and experimentally is observed as constant background intensity. I_L and I_N represent the scattering intensity from large and nano-scale features, respectively. Large features, greater than ~50nm, do not contribute much to the normal small angle regime occurring only at the ultra-small angles. These would typically be found at < 1 °2Θ and are largely irrelevant for typically small angle experiments. Only the tail of I_L can be seen experimentally with typical radiation sources. I_L follows power law type behavior where the power S is dependent on beam geometry [166]. These experiments use S = -3 for a line beam (S = -4 for point beam).

$$I_L(q) = A \cdot q^S \quad \text{(C2)}$$

$I_N(q)$ is of primary interest and represents the intensity from nanostructured features from about 1nm to 50nm. This scattering intensity for a single particle can be described by

$$I_N(q) = Cv^2(n_p + n_m)^2 P(q)^2 \quad \text{(C3)}$$

where C is a constant, *v* is the particle volume, n_p and n_m are the respective electron densities of the particle and surrounding matrix, and P(q) is the form factor of the particle. The form factor is most important regarding the shape of intensity profile. Fig. 112 shows how form factor varies for three different size nanoparticles.

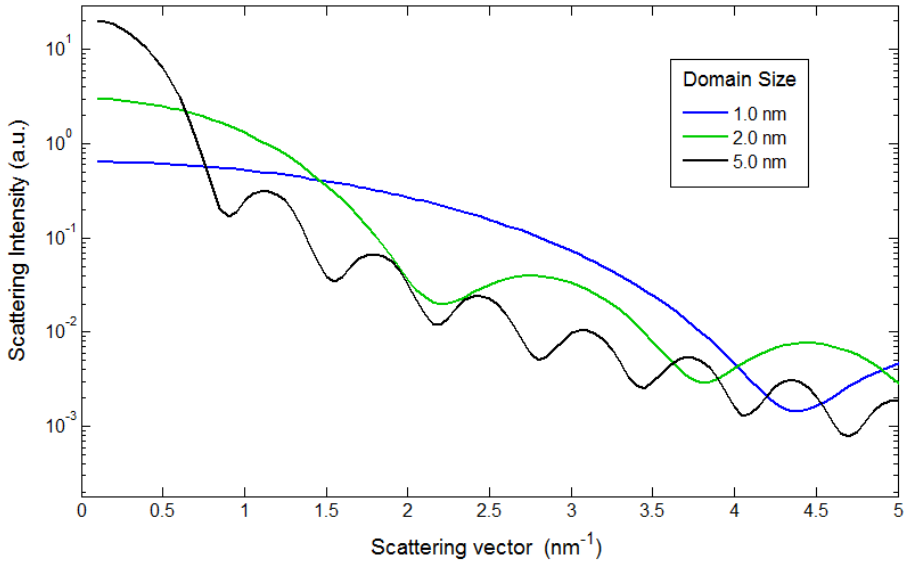

Fig. 112. Form factor intensity as a function of domain size and scattering angle profiles.

The SAXS profiles were analyzed using an automated fitting MATLAB program. The program was adopted from Don Williamson's DOS-based version designed to analyze domain size in a-Si:H. Details of the original program are given in literature [167].

Curves were fit to experimental SAXS pattern by regressing the following expression for intensity against the experimental data

$$A\sum_{i=1}^{n}[P_i(q)\cdot W_i] + I_D + B/q^S \qquad \text{(C4)}$$

The summation is the most important quantity which relates the form factor for a given nanoparticle, $P_i(q)$, and it's given distribution weight, W_i, in the system. The other parameters I_D and B/q^S contribute only to the amplitude and shape of the background intensity and do not contain nano-structural information. The discrete summation is taken over domain sizes I = 0.5 nm to 25 nm, each with a unique form factor. The relative distribution of weights, W_i, defines the amount each domain size 'r_i' contributes to the overall intensity profile.

The wide-angle X-ray diffraction experiments were carried out with CuKα radiation. The SAXS measurements were made on SAXSess High-Flux Small-Angle X-ray Scattering System from Anton Paar GmBH, Graz, Austria. Acceleration volatage and current were 40kV and 50mA, respectively. Beam exposure time was 15 minutes per sample.

The resulting data in the form of scattering vector vs. intensity was loaded into the MATLAB program and fit the above equation with a series of iterative optimization loops, Fig. 113.

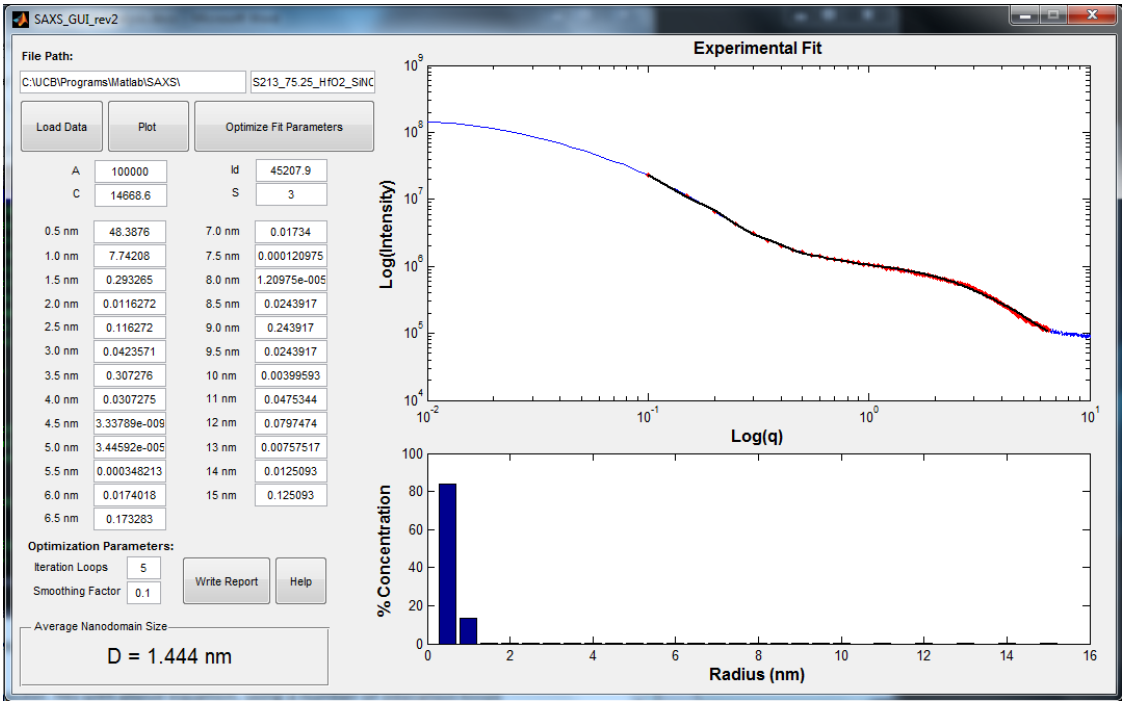

Fig. 113. Matlab GUI for SAXS profile analyzer showing example fit of HfSiCNO sample. The blue line is the experimental data, red is the fitted region, and black is the regression fit.

Due to the high number of independent variables, the canned routine used to optimize the variables may not find the absolute min right away, but rather local minima. The iteration loops allow the routine more opportunities to narrow down the absolute minimum. A smoothing function was also used to remove noise effects. The smoothing parameter, χ, limits each intensity factor to be within χ of its nearest neighbor. For example, if the smoothing parameter is 10% ($\chi=0.1$), then a domain size of 14 nm with an intensity factor of 50 would require that each neighbor (13 nm and 15 nm) have an intensity factor of at least 5. This condition greatly increases the optimizer efficiency and reduces fitting error due to experimental noise in the data, particularly at the low scattering angles where very few data points are available. However, the caveat here is that scattering intensity does not vary linearly with particle size. A more appropriate way to constrain the system would be to require that quantity of domain of size 'R_1' is some fraction of its neighbor 'R_2'. This would enforce the Gaussian-type distribution to

follow the feature size, not their scattering intensity. Constraining the intensity factors worked well for these HfSiCNO materials and therefore was not refined further. Another condition which aids the optimizer routine is that all values must be non-negative. Any constraints that can be placed on the system will help the optimizer routine, since it will significantly reduce the degrees of freedom for the optimizer to search through. Due to the amorphous nature of the system, it is expected that any HfSiCNO type system should have Gaussian-like distribution for the domain size.

6.3.3 Domain Size Results for HfSiCNO Materials

Polymer derived materials such as SiCN and HfSiCNO are amorphous and therefore do not show Bragg diffraction peaks from long range order. Their wide-angle diffraction spectra show a broad 'halo' which is typical of amorphous materials. This halo arises from short range order. The more ordered, the narrower the band. Amorphous SiO_2, for example, shows a much narrower halo than SiCO materials due to its more ordered state.

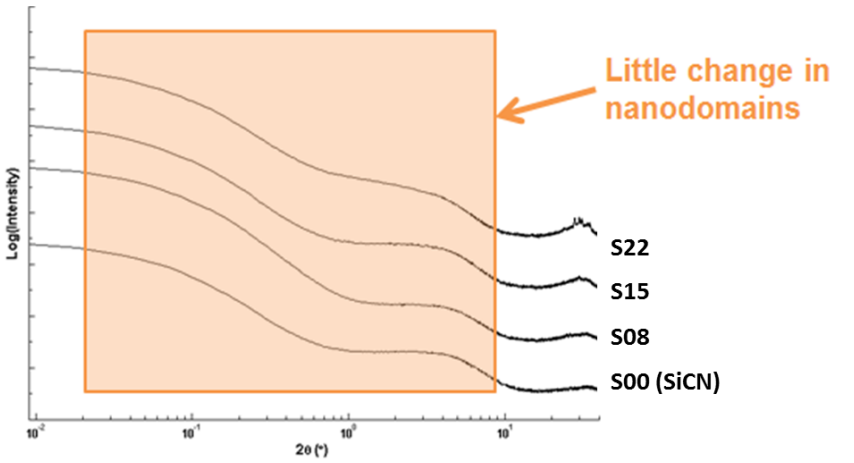

Fig. 114. SAXS profiles for as-pyrolyzed HfSiCNO compositions

All HfSiCNO compositions were x-ray amorphous after pyrolysis at 1000°C, except those with Hf:Si ratios of >0.22 which show some crystalline HfO_2. Fig. 114 highlights the SAXS regime for four HfSiCNO compositions. All materials show small angle profiles incredibly similar to that of SiCN, even after significant amounts of Hf-O doping. The calculated domain sizes of these materials were given in Fig. 55 of Ch. 3.

6.4 Appendix D – Methods for Quantitative X-ray Analysis of HfSiCNO

This section details the methods using to quantify phase information from HfSiCNO oxidized powders. The most common method for quantitative XRD is the reference intensity ratio (RIR) method. This method uses the relative peak heights of various observed phases to determine their respective concentrations within the sample. This intensity ratio between respective phases can either be found experimentally by creating samples of known concentrations, or the intensity ratio can be taken from literature databases such as the Powder Diffraction File released by the International Centre for Diffraction Data [168].

Quantitative analysis of $Hf_vSi_wC_xN_yO_z$ materials poses several significant challenges:

1. Amorphous content. Quantitative XRD on ceramics are often performed without introducing a reference standard since it can be assumed the cumulative sum of the phase fractions is unity. That is to say, the total amorphous content in the sample is low enough that it can be assumed to be zero. Since amorphous content gives a broad diffraction "halo" rather than a distinct peak, it is extremely difficult to extract quantitative phase fractions directly from the diffraction ratios. A reference standard is therefore introduced at a known weight percent to relate all other crystal phases to. A reference standard of niobium (Nb) was chosen for this system since it has no diffraction peaks within the lower 2θ angles, and the Nb primary peak did not overlap with any of the experimentally observed HfSiCNO diffraction peaks.

2. Nanometer crystal sizes. Sub-micron crystal size leads to a broadening of the Guassian shaped diffraction peaks. This size dependency of XRD peak shape is

often used to determine nanometer scale particle size by use of the Scherrer Equation. Due to this size dependent effect, integral peak areas were used for quantitative analysis as opposed to a simple measure of the ultimate peak intensity.

3. High Elemental Diversity. The quintenary HfSiCNO system has a high number of potential crystalline phases which could form its constituent element (Si_3N_4, HfN, (Hf, Si)O_2, (Hf, Si)C, HfSiO4). Within each chemical structure, there are several potential polymorphs, for example SiO_2 content could be amorphous, quartz, cristobalite, etc. or combinations thereof. The high number of potential phases and polymorphous creates a cluttered spectra with many overlapping diffraction peaks.

4. Non-homogeneity. The distribution of phases in HfSiCNO appears to be homogenous in the polymer state and after decomposition in inert atmosphere. However, during oxidation the HfSiCNO develops a passive oxide layer on any exposed surface. To properly quantify this system the surface layer must be separated from the unoxidized core of the particle.

Powder diffraction spectra were taken on a SAXSess High-Flux Small Angle X-ray Scattering system from Anton Paar GmBH, Graz, Austria with detection angles from 0-45 degrees 2θ. Each HfSiCNO sample was lightly mixed with 25% wt. niobium metal using a mortar and pestle. Niobium was used as the reference intensity standard. This sample/reference composite was dispersed in acetone and spread onto a thin Si wafer. The acetone from the slurry readily evaporates away leaving behind a ~50 μm film of HfSiCNO +Nb. The single crystal Si is x-ray transparent in the diffraction angles observed and therefore serves as an ideal substrate for the HfSiCNO particulate film.

The x-ray beam was generated with an accelerating voltage of 40kV and applied current of 50mA. Each x-ray exposure was for 15 minutes under vacuum. Diffraction intensity data were collected on a photostimulated luminescence image plate and transferred onto a computer using a Cyclone phosphor image scanner by PerkinElmer. Intensities were integrated across the plate to produce a dataset of intensity vs. scattering angle, as shown Fig. 115.

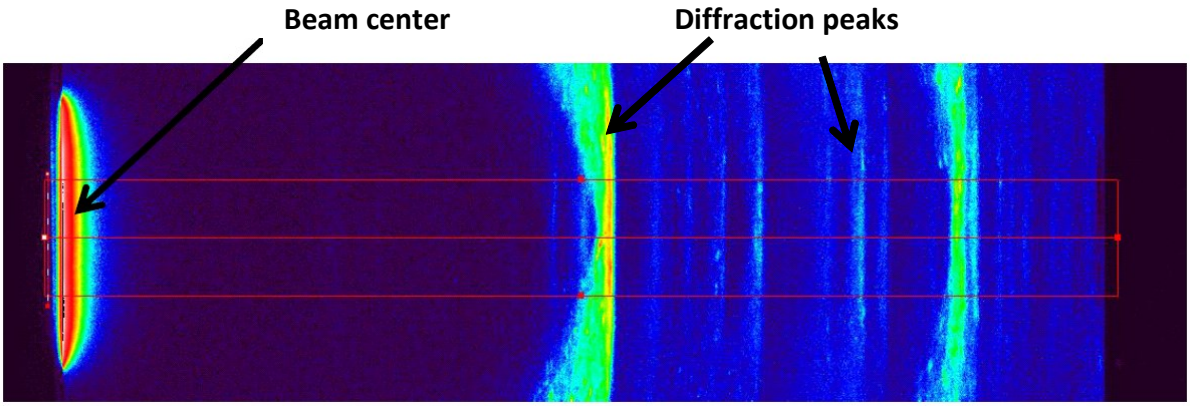

Fig. 115. Experimental diffraction spectra on image plate

Data were removed for Si background and loaded into a Matlab program to analyze peak shape, Fig 116. Peaks were manually fit with Gaussian curves. Data were collected for primary peaks, and, in cases where there was significant peak overlap, secondary peaks were fitted as well.

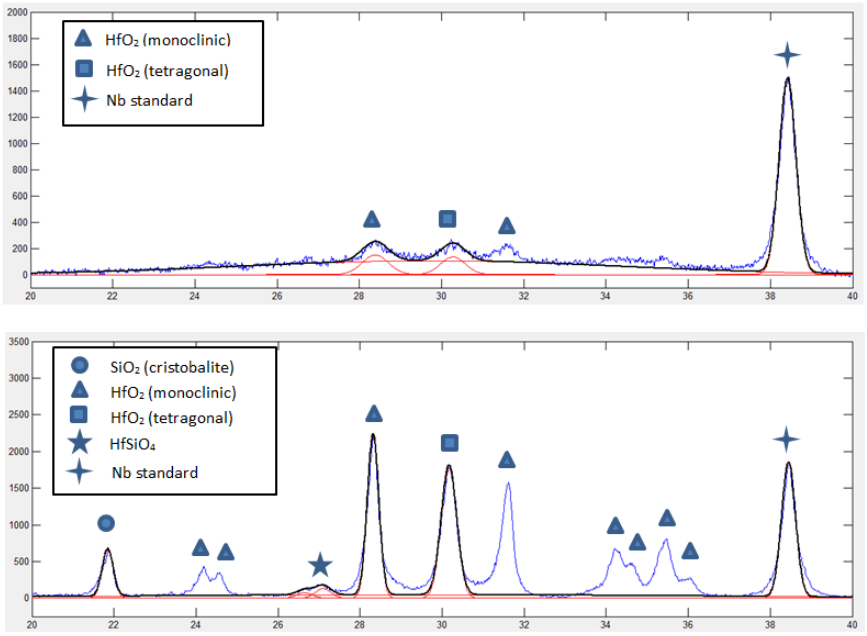

Fig. 116. Example of Gaussian peak fitting for HfSiCNO diffraction patterns

When RIR intensities are cited in literature they are almost always with respect to corundum (α-Al_2O_3). The RIR value is the ratio of the highest peak in the given phase to the highest peak of corundum. This value for a given phase is denoted as $I/I_{C.}$ For example, the I/I_C for SiO_2 (cristobalite) is 5.79. This means, in a 50/50 mixture of Al_2O_3 and SiO_2 by weight, the highest cristobalite peak will be 5.79 times higher than the highest Al_2O_3 peak. Determining the reference intensity to Nb is as simple as normalizing every RIR by I_C/I_{Nb}, which would reference every intensity to Nb instead of Al_2O_3. From the known experimental peak area, intensity area ratios, and known Nb concentration, one can directly calculate the relative quantity of any crystalline phase within the sample.

6.5 Appendix E – Effect of Particle Size Distribution on Oxidation Weight Gain

Section 3.6 proposed a simple model for determining oxide scale thickness based off the measured weight gain of particles during oxidation. For simplicity, this analysis assumed oxide overgrowths on mono-sized particles. Here this model is extended to particles of varying size distribution using discrete particle sizes and skewed log-normal fitting. The results are applied to the oxidation of S08 composition HfSiCNO powders.

6.5.1 Experimental Methods

Three particle distributions of S08 composition powder were prepared from an Hf-modified silazane polymer. The specific processes used were the same manner as described previously in Section 3.4.1. To make the three different size distributions the final ball milling step was omitted and replaced by varying degrees of milling by mortar and pestle. The three distributions are denoted D1, D2, and D3. The distribution with the largest particles, D1, received a coarse milling by mortar and pestle for approximately 1 minute, and the finest particle size distribution, D3, received 15 minutes of milling.

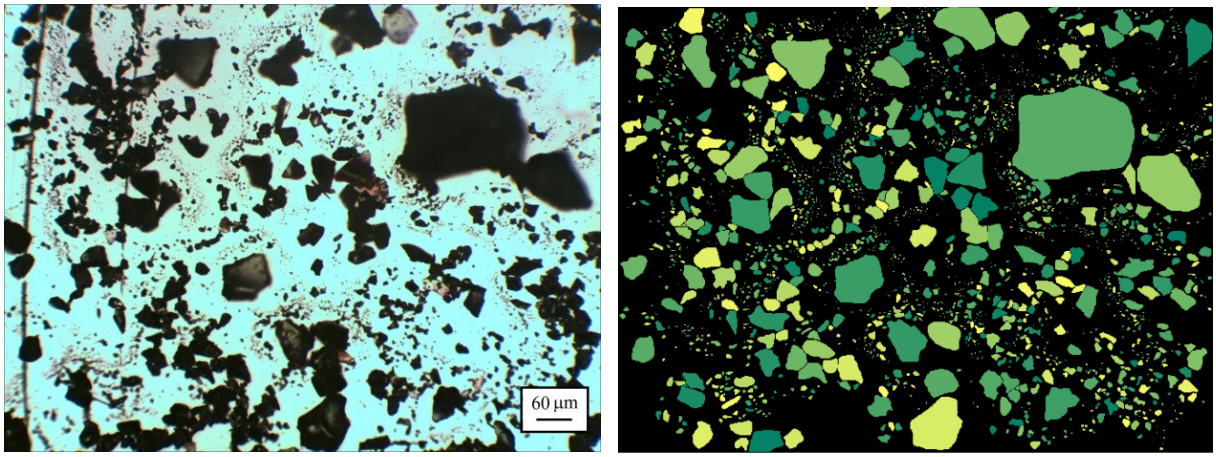

Fig. 117. Optical image of D1 particle distribution (left); and analysis trace (right)

The powders were dispersed in oil and stirred to break up agglomerates. The particle-in-oil mixtures were sandwiched between glass slides and captured using an optical microscope. The images were analyzed in Matlab to produce a distribution of particle cross-section areas, Fig. 117.

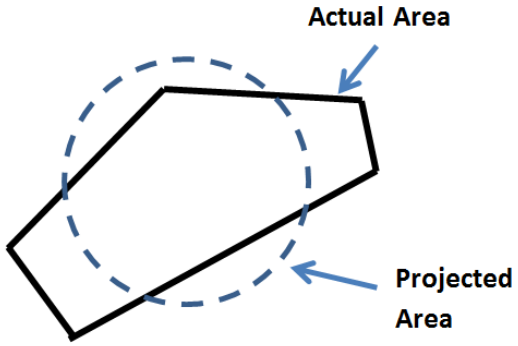

Fig. 118. Spherical particle representation

Each measured area was reduced to an effective radius by assuming all particle geometries to be spherical, Fig. 118. The image resolution of the particles was ~2 pixels per µm. Assuming a minimum particle size of 1 pixel squared, the smallest measurable particle radius is then ~250nm.

6.5.2 Distribution Concept and Hypothesis

From the reaction,

$$HfSiCNO + O_2 \rightarrow HfO_2 + SiO_2 + N_2 + CO, \qquad (E1)$$

the theoretical weight gain of S08 from oxidation is calculated to be 13.6%. This calculation is based off of initial and oxidized chemistry alone, and it is assumed that no Hf or Si is lost to the environment with the only remaining products of oxidation being $(Hf, Si)O_2$. Further reactions, the most plausible being $SiO_2 + HfO_2 \rightarrow HfSiO_4$, would not influence the measured powder weight gain. The only expected effect of size distribution is the rate at which the weight gain of each distribution approaches this theoretical limit.

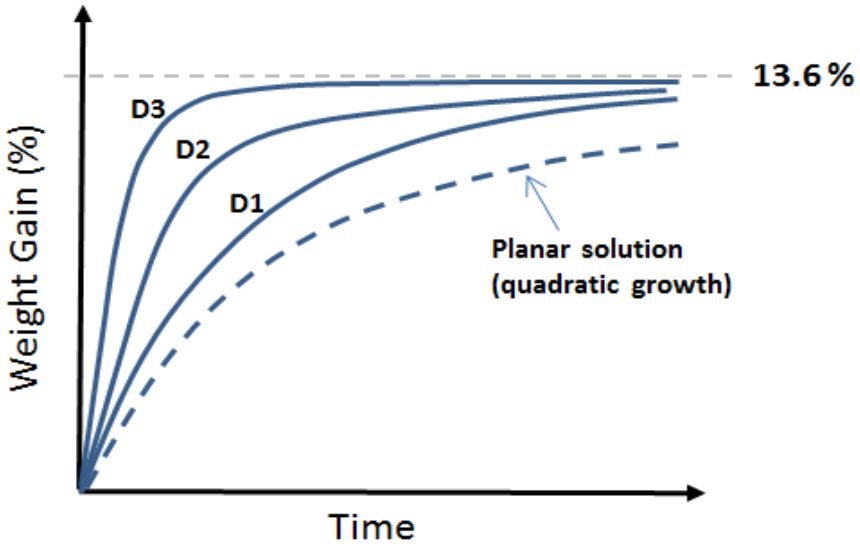

Fig. 119. Predicted effect of particle size dependency on measured weight gain

A qualitative prediction of weight gain behavior is shown in Fig. 119. Note the two limiting cases would be (1) the planar quadratic solution to a gain of 13.6% for very large particles and (2) an instantaneous jump to 13.6% for very small particles. A

distribution of particles would be expected to show a combination of both limiting cases. The presence of small particles is expected to control the initial rate of weight gain, whereas the larger particles influence the longer oxidation times and define the rate at which the weight gain approaches 13.6%.

Using the methods detailed in section 3.6.5 for fixed particle size, one could extend the analysis technique to particle distributions simply by summation of discrete particles,

$$\frac{\Delta W}{W}(total) = \frac{\sum_{i=1}^{n} {W_2}^i}{\sum_{i=1}^{n} {W_1}^i} - 1 \qquad \text{(E2)}$$

where W_1^i and W_2^i represent the particle weight gains before and after oxidation, respectively. Instead of plotting weight gain against time, one could similarly plot Kp*t using the equations (E3) and (E4) as described previously in the text.

$$h_s = \frac{R}{3}\frac{\Delta W}{W_1}\frac{M_2}{\Delta M}\frac{\rho_1}{\rho_2} \qquad \text{(E3)}$$

$$h_s^2 = k_p \cdot t \qquad \text{(E4)}$$

The scenario shows the nonlinear effects of particle distribution on weight determined rate constant at a given time, Fig. 120. At the onset of oxidation, all distributions would be expected show weight gain rates in accordance with planar oxidation since the oxidize scale, h_s, is much greater than the particle radius, R. The y-axis of this figure gives K_p*t which is essentially h_s^2 and carries units of length squared. The dotted horizontal lines in this figure represent the square of largest particle within each distribution. Once $\sqrt{k_P * t}$ (alternatively, h_s) reaches the largest possible R, then weight gain ceases and the distribution is fully oxidized.

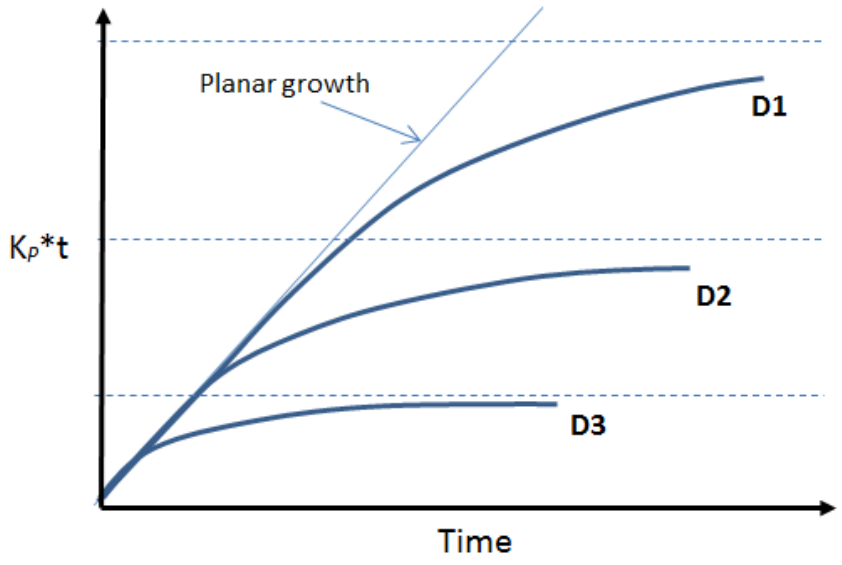

Fig. 120. Predicted effect of particle size dependency on K_p*t

6.5.3 Oxidation and Modeling of S08 Powder Distributions

Analysis of the particle distributions were carried out as described above using discrete distributions. The distributions were obtained from optical measurements of particle dispersions. The model was inconsistent with experimental results due to the significant influence of the distribution "tails". The early jumps in oxidation weight gain were controlled by extremely small particles, some of which were small enough to oxidize during thermal ramping of the furnace. Similarly, since the discrete distributions only capture a few particles of the largest sizes (see Fig. 117) the high end of the particle distributions was also misrepresented by the discrete data. There were two possible solutions to correct for this. The first would be to have much larger sampling sizes and therefore create a smoother discrete distribution. This larger distribution would decrease the tail error and would be a more accurate representation of the actual powders. However, the problem with this approach is the smallest particle would still be

unknown due to size limitations of the optical measurement method. A second solution is to use a continuous distribution based off the discrete measurements. In this way, one could properly account for the distribution tails without large discretization errors and absent values from experimental limitations.

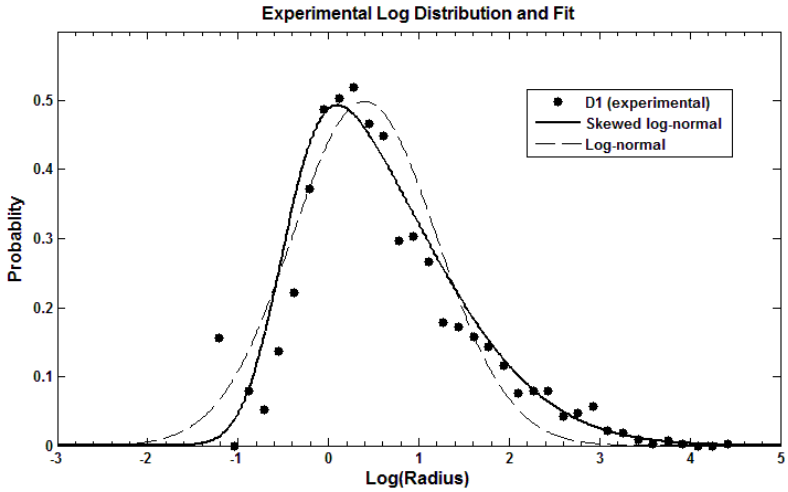

Fig. 121. Discrete experimental distribution of D1 as fit by log-normal and skewed log-normal probability density functions.

Continuous models were created analyzed for the three distributions. The first attempt was to use log-normal distributions. Literature has shown milled particulate systems to follow log-normal behavior for size dependency [169-170]. However, the distributions of HfSiCNO powders did not closely follow log-normal behavior. As seen Fig. 121, the distributions tended to have extended tails towards the larger sizes. (Note the x-axis is plotted as the log of the particle radius) This behavior can be described by a skewing factor and has been observed previously in literature for similar distributed systems [171]. This skewing was determined to be from the relatively slight degree of powder milling. As the milling increased, the distributions moved closer to log-normal shape with the D3 sample (smallest particles) matching log-normal almost exactly. The

problem with using a simpler log-normal model for the analysis was the same as the discrete model. Neither tail of the distribution is captured well, leading to significant modeling error. It is for this reason a skewed log-normal function was chosen as the model function to complete the analysis.

For a skewed normal distribution [172], the probability density function (PDF) can be described by,

$$p(x) = 2\varphi(x)\gamma(\alpha z) \tag{E5}$$

Where $\varphi(x)$ is the Gaussian distribution function and $\gamma(\alpha z)$ is the skewing function. These are defined as

$$\varphi(x) = \frac{1}{\sigma\cdot\sqrt{2\pi}} e^{-\frac{(x-\mu)^2}{2\sigma^2}} \tag{E6}$$

$$\gamma(\alpha z) = \frac{1}{2}\left[1 + erf\left(\frac{\alpha z}{\sqrt{2}}\right)\right] \tag{E7}$$

where $z = \frac{x-\mu}{\sigma}$ and erf is the Gaussian error function. The fit of the experimental distributions were performed visually for the 3 distributions. The broadening, center, and skew of the distributions were controlled by the parameters σ, μ, and α, respectively.

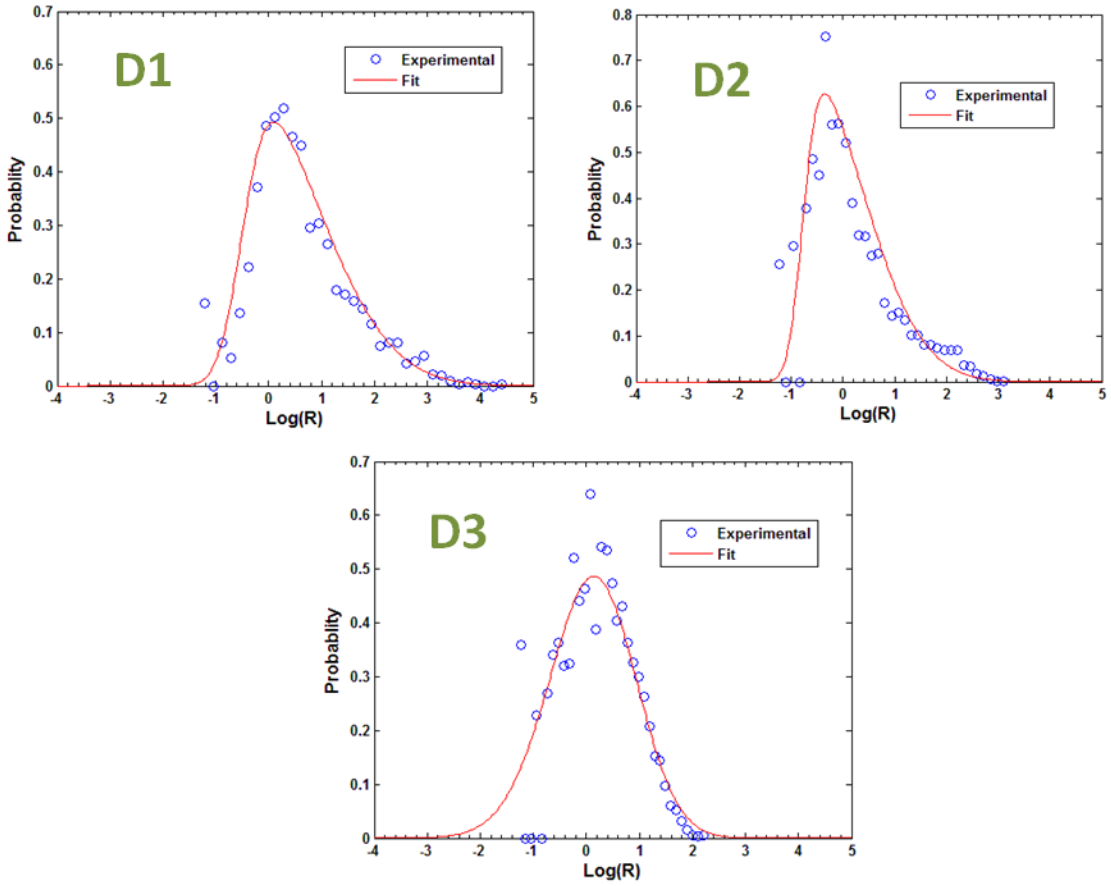

Fig. 122. Distribution of D1-D3 plotted against their skewed log-normal fit (note particle is plotted as log of radius in microns)

Fig. 122 shows the three S08 distributions with D1 being the largest and D3 being the smallest. Both samples D1 and D2 show a high degree of skew when plotted along a log-scale. Note the D3 samples appear nearly Gaussian (log-normal) after receiving the highest degree of milling. The left edge of the distribution is absent due to size limitation of the optical microscope. The smallest detectable value is a radius log of -1.3 which corresponds to ~250nm.

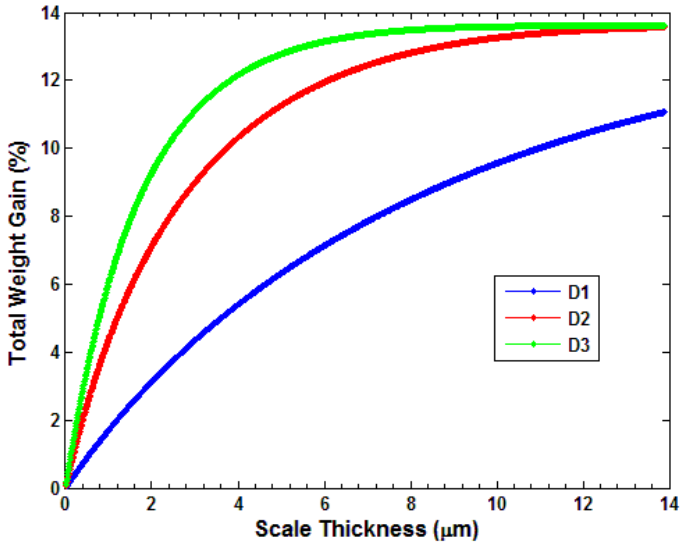

Fig. 123. Predicted effect of particle size dependency on measured weight gain

Using the continuous model for particle distribution, the weight gain for the three powder sets could be predicted as a function of developed oxide scale thickness, Fig. 123. These curves are drawn upon for the experimental weight gain measurements to obtain scale thickness of the oxidized powders.

The HfSiCNO powders were oxidized in a $MoSi_2$ element box furnace in ambient air at 1500°C for 400hrs. The weight gain was measured at various interrupted intervals throughout the test. Alumina crucibles contained each powder distribution. The weight of the crucible w/powder was recorded using a mass balance. Samples were cooled to room temperature for each measurement.

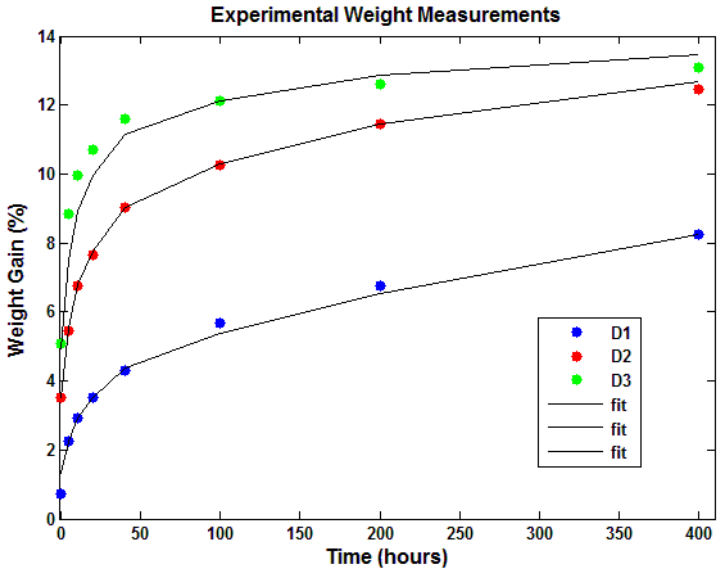

Fig. 124. Experimental weight gain plotted against model prediction for single values of scale thickness

Fig. 124 shows the experimental weight gain data for the three distributions. For each increment of time, the experimental weight gains were compared to the modeled weight gains (Fig. 123) to obtain a value of scale thickness. The only constraint to obtain a single solution was that the scale thickness, h_s, had to be equivalent for all three distributions at any given time. The model results after applying the singular h_s values to each continuous distribution are also shown in Fig. 124 as solid lines. The model was found to be excellent agreement with respect to the shape of the weight gain for the various distributions. The only significant observed error was the early shape of distribution D3. The exact reason for this slight deviation is unknown but it is expected to be from the non-linear effect of oxidizing curved surfaces [173]. For example, the scale thickness of a 5 μm radius particle oxidized for 100 hours would be slightly thicker than a similarly oxidized particle of 50 μm radius. The larger particle more closely resembles planar geometry and has significantly less non-linear influence on the development of nanometer or micron thick oxide scales. For this analysis, it was

assumed that the developed oxide scale of each distribution was equivalent for the three distributions at any given time.

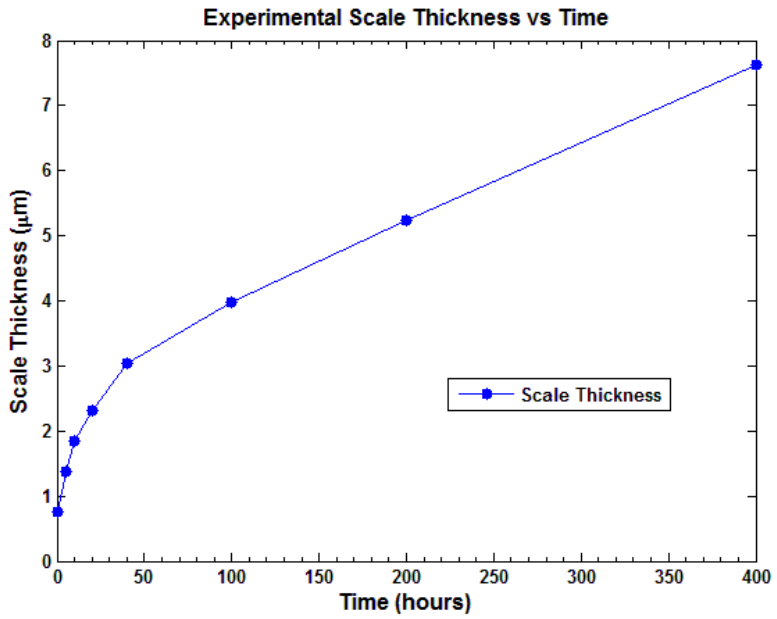

Fig. 125. Predicted effect of particle size dependency on measured weight gain

The set of scale thickness values used for the model curves of Fig. 123 are plotted alone in Fig. 125. They demonstrate near quadratic behavior with a rate constant of 38.5 nm^2s^{-1}. When the weight gain was modeled using a fixed average R value, this HfSiCNO powder was reported to have an oxidation rate constant of ~20 nm^2s^{-1}. Cross-sections of particles oxidized after 50hrs at 1500°C found this approximation to be an under prediction as cross-sections show the actual rate constant to be closer to 35 nm^2s^{-1} (~2.5µm after 50 hrs at 1500°C). The rate constant error was approximately -42% using a fixed R values whereas only 10% when accounting for the particle size distribution. The current model slightly over predicts the weight gain which is expected to be the result of the assumption that all particles are spherical. The actual particles are non-spherical implying the surface area to mass ratio is higher than model

assumes. This would result in a greater weight gain since oxidation is a surface phenomenon, but the total measured weight is a function of particle volume.

6.5.1 Summary of Oxidized Distributions

Distributions of S08 HfSiCNO were powder were measured optically and fit using a skewed log-normal distribution. Discrete and log-normal distributions were attempted but resulted is significant modeling error. The skewed function was chosen because it makes the model more accurate by permitting a careful fit of the distribution tails. The distribution tails were found to have significant influence over the shape of the measured weight gain curves.

A simultaneous model fit to the D1-D3 weight gain curves resulted in a close match with the experimental data and gave a quadratic rate constant of 38.5 nm^2s^{-1}. The model for scale thickness was found to be slightly above the actual values which are attributed to the erroneous assumption of perfectly spherical particles. The model could be further refined by including a shape scaling factor which corrects the surface area to volume ratio for non-spherical geometries. Experimentally this value could be produced from BET specific surface area measurements in conjunction with the measured particle size distributions.

6.6 Appendix F – Oxidation of SiC/SiC Coated Minicomposites

The SiC/SiC minicomposites of section 3.6.1 were difficult to analysis using traditional measn due to non-homogeneity of the developed oxide scale thicknesses. Three different tows were oxidized (i) uncoated, (ii) SiCN coated, and (iii) HfSiCNO coated. Both of the coated samples had film thicknesses of 1 μm. These fiber tow based composites were oxidized up to 1000 hours at 1600°C in air. The reason for such high temperature and long exposure times was to create an oxide layer on the uncoated sample which was considerably thicker than the deposited film thickness of the other two samples. This would result in a very simple pass-fail scenario for the EBC films. If the 1 μm films offered significant protection, then it would be plainly evident if the grow oxide layer on the uncoated sample was an order of magnitude greater.

However, the high temperature and prolonged exposure times resulted in viscous flow of the thermally grown silica scale. The silica wicked into pores and valleys of the composite surface to minimize its surface tension. This wicking created a final oxide thickness which was significantly non-uniform around the perimeter of the three composites. Visual quantification of the film thickness was found difficult to achieve without conformation bias. As a result, cross-sections of the minicomposites were analyzed across the entire perimeter to obtain an average value of oxide scale thickness. Despite gross differences in scale thicknesses around the samples, this analysis provided reasonable average values to be used for purposes of comparison.

Each minicomposite sample was cross-sectioned and imaged under the SEM. Mosaics were created of the entire minicomposite surface perimeter to highlight the complete

oxidation scale development. The oxidation scales were traced and analyzed in matlab to give the total area occupied by the oxide scale in the section. The scale was analyzed in two ways. The first was to create a distribution of the oxide scale thickness around the sample. This was done on a pixel-by-pixel basis. A line was drawn tangent to the surface for each pixel at the silica outer surface. The distance required to hit a pixel on the inner silica surface was considered to be the thickness at that point. The second method of analysis was to take the entire SiO_2 occupied area and divide by the perimeter of the minicomposite. This was proven to be the most reliable method of obtaining an average thickness. The results of this analysis for each sample are given in Figs. 126-128 for the HfSiCNO coated, and SiCN coated, uncoated sample, respectively.

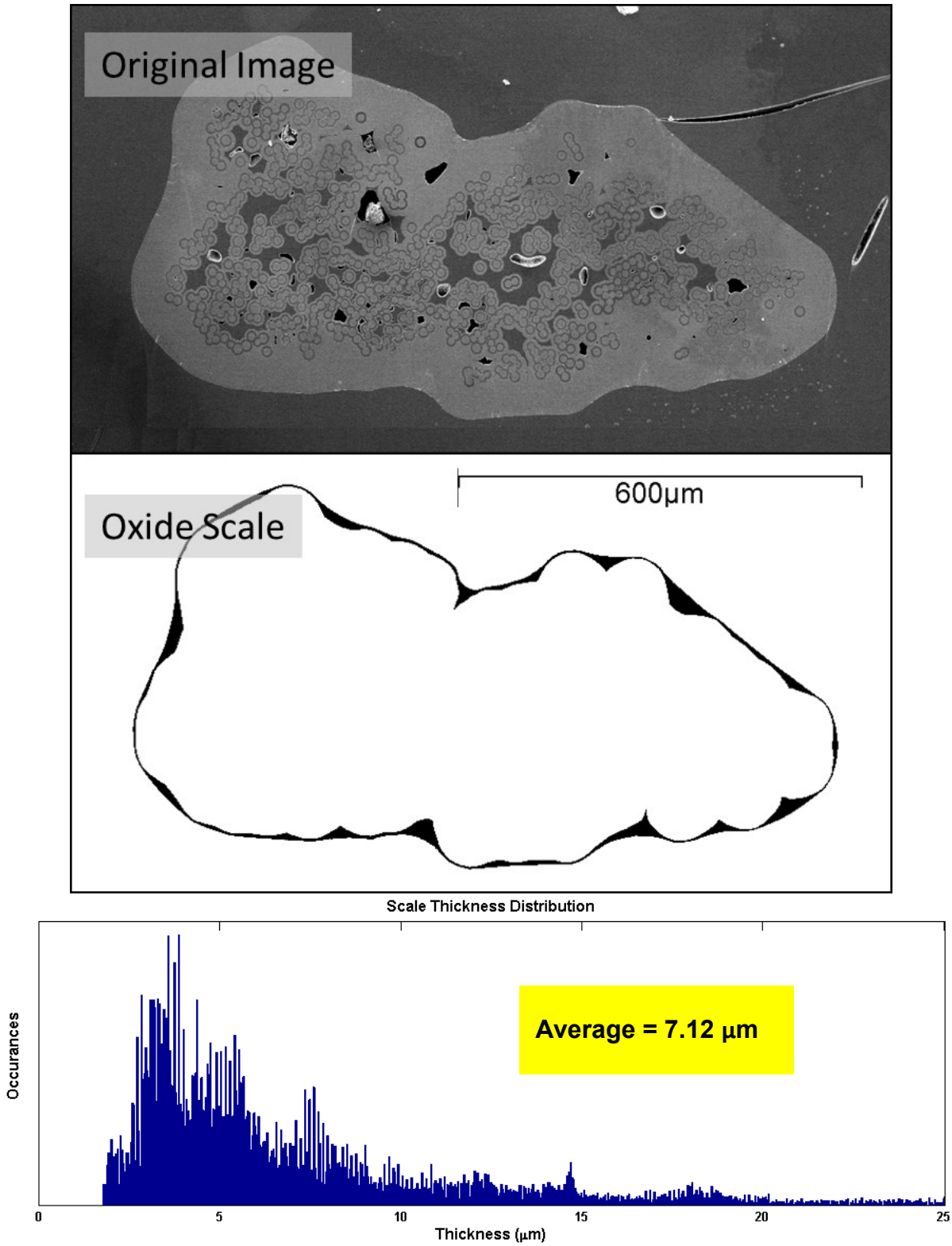

Fig. 126. HfSiCNO coated SiC/SiC minicomposite after oxidation for 1000 hours at 1600°C. SEM section (top), oxide scale area (middle), thickness distribution (bottom).

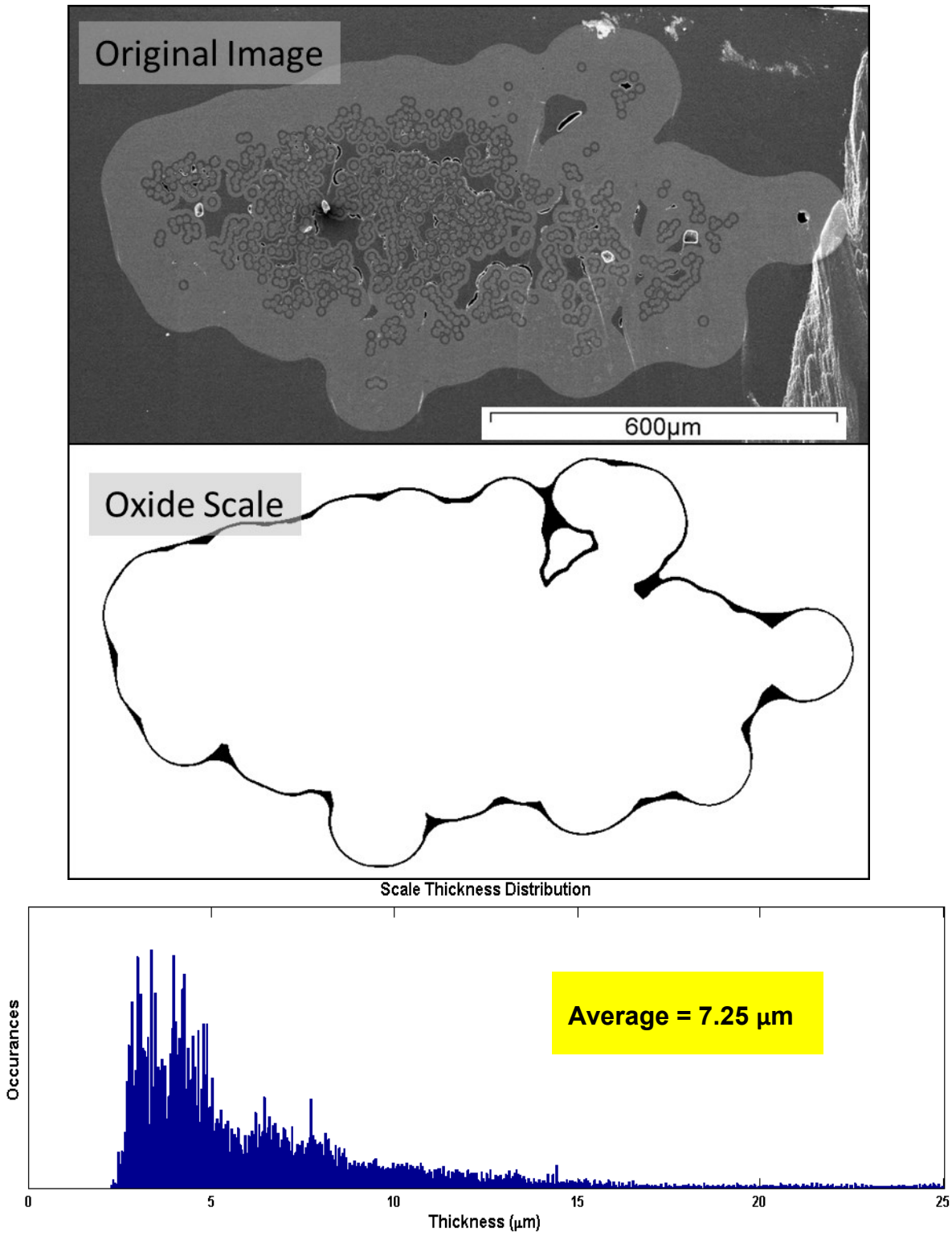

Fig. 127. SiCN coated SiC/SiC minicomposite after oxidation for 1000 hours at 1600°C. SEM section (top), oxide scale area (middle), thickness distribution (bottom)

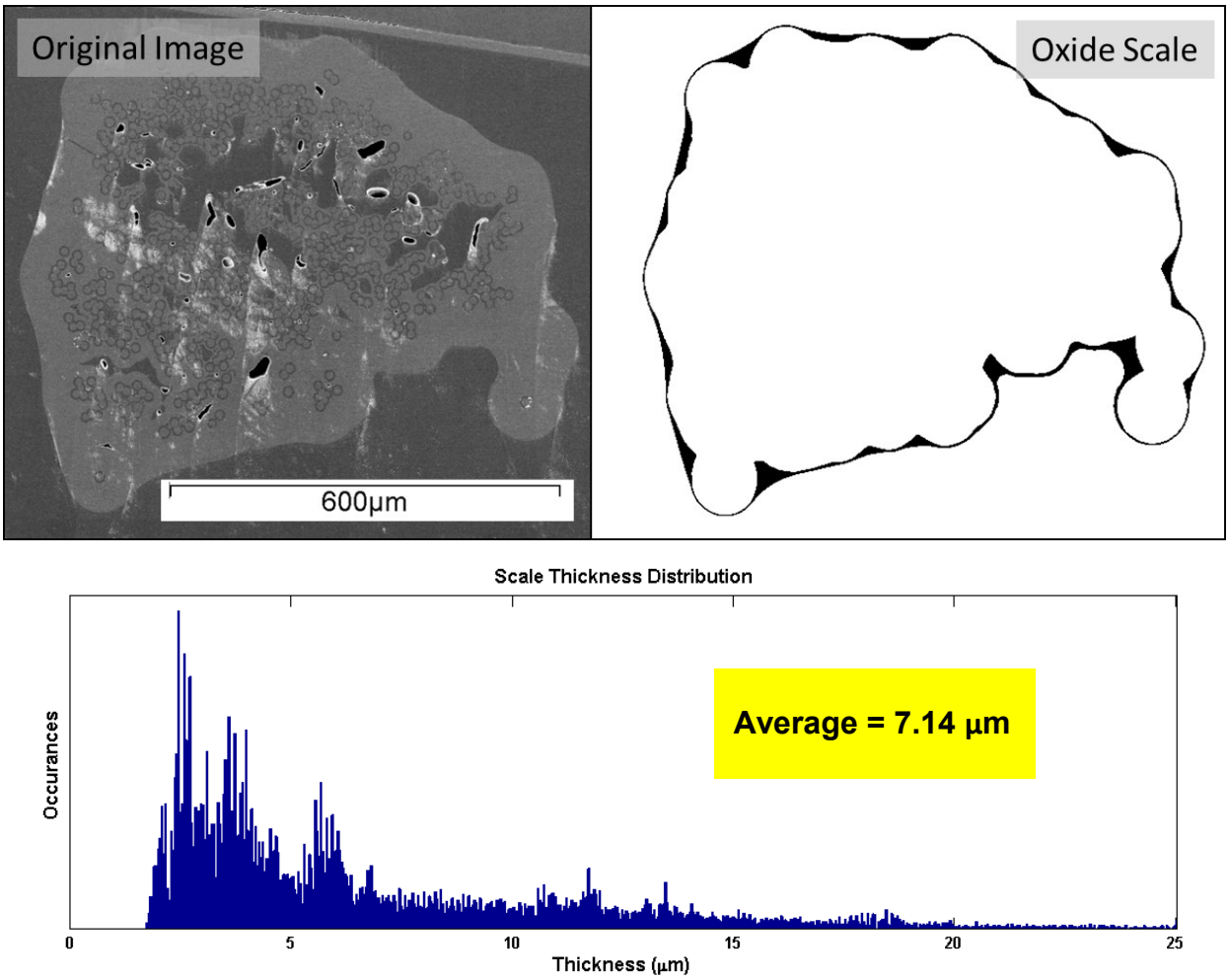

Fig. 128. Uncoated SiC/SiC minicomposite after oxidation for 1000 hours at 1600°C. SEM section (top), oxide scale area (middle), thickness distribution (bottom)

The results of the oxidation analysis show no significant difference between the 3 samples. All showed an average oxide scale thickness in the range 7.12 µm – 7.25 µm. Subsequent analysis of bulk SiCN and HfSiCNO verified this result showed similar oxidation rates to pure SiC crystals. The primary reason for the small thickness differences seen here is thought to be from variability of surface texture between samples.

Bibliography

[1] R. Tanaka, “Future of Ultra-High Temperature Materials” *Proceedings of the International Symposium on Ultra-High Temperature Materials*, Japan. pp. 2-12, 15 March, 1991

[2] E. Wuchina, E. Opila, M. Opeka, W. Fahrenholtz, and I. Talmy “UHTCs: Ultra-High Temperature Ceramic Materials for Extreme Environments” *The Electrochemical Society Interface,* vol. 16, no. 4, pp. 30-36, 2007

[3] P. Bundy, "Pressure-temperature phase diagram of elemental carbon." *Physica A: Statistical Mechanics and its Applications* , vol. 156, no. 1, pp. 169-178, 1989

[4] C. Li, T. Brown, “Carbon oxidation kinetics from evolved carbon oxide analysis during temperature-programmed oxidation”, *Applied Catalysis B: Environmental*, vol. 50, no. 3, pp. 185-194, 2004

[5] A. Noor (Ed.) *Structures Technology: Historical Perspective and Evaluation*. AIAA, 1998.

[6] X. Peng and F. Wang "High-Temperature Oxidation of Aerospace Materials." *Aerospace Materials Handbook*, 1, 237, 2012.

[7] T. Kosolapova, *Handbook of high temperature compounds: properties, production, applications*. CRC Press, 1990

[8] E. Courtright, H. Graham, A.Katz, and R. Kerans, “Ultrahigh Temperature Assessment Study: Ceramic Matrix Composites” Battelle Pacific Northwest Labs, Richland, WA, 1992.

[9] M. Gasch, S. Johnson, and J. Marschall. "Thermal Conductivity Characterization of Hafnium Diboride-Based Ultra-High-Temperature Ceramics." *Journal of the American Ceramic Society*, vol. 91, no. 5, pp. 1423-1432, 2008

[10] J. Zimmermann, G. Hilmas, W. Fahrenholtz, R. Dinwiddie, W. Porter, and H. Wang. "Thermophysical properties of ZrB_2 and ZrB_2–SiC ceramics." *Journal of the American Ceramic Society*, vol. 91, no. 5, pp.1405-1411, 2008

[11] M. Opeka, I, Talmy, E. Wuchina, J. Zaykoski, and S. Causey. "Mechanical, thermal, and oxidation properties of refractory hafnium and zirconium compounds." *Journal of the European Ceramic Society*, vol. 19, no. 13, pp. 2405-2414, 1999

[12] J. Berkowitz-Mattuck, "High-Temperature Oxidation III. Zirconium and Hafnium Diborides." *Journal of the Electrochemical Society*, vol. 113, no. 9, pp. 908-914, 1966

[13] R. Voitovich and E. Pugach. "High-temperature oxidation of ZrC and HfC." *Powder metallurgy and metal ceramics*, vol. 12, no. 11, pp. 916-921, 1973

[14] R. Savino, M. De Stefano Fumo, L. Silvestroni, and D. Sciti. "Arc-jet testing on HfB_2 and HfC-based ultra-high temperature ceramic materials." *Journal of the European Ceramic Society*, vol. 28, no. 9, pp. 1899-1907, 2008

[15] D. Fox, “Oxidation Behavior of Chemically-Vapor-Deposited Silicon Carbide and Silicon Nitride from 1200° to 1600° C.” *Journal of the American Ceramic Society,* vol. 81, no. 4, pp. 945–950, 1998

[16] G. Samsonov, (Ed.) *The Oxide Handbook*. New York: Ifi/Plenum, 1973.

[17] W. Tripp, H. Graham. "Oxidation of Si_3N_4 in the Range 1300 to 1500°C." *Journal of the American Ceramic Society,* vol. 59, no. 9-10, pp. 399-403, 1976.

[18] H. Ohnabe, S. Masaki, M. Onozuka, K. Miyahara, and T. Sasa. "Potential application of ceramic matrix composites to aero-engine components." *Composites Part A: Applied Science and Manufacturing*, vol. 30, no. 4, pp.489-496, 1999

[19] M. Opeka, I. Talmy, and J. Zaykoski. "Oxidation-based materials selection for 2000 C+ hypersonic aerosurfaces: theoretical considerations and historical experience." *Journal of materials science*, vol. 39, no. 19, pp. 5887-5904, 2004

[20] T. Osada, W. Nakao, K. Takahashi, and K. Ando. “Kinetics of Self-Crack-Healing of Alumina/Silicon Carbide Composite Including Oxygen Partial Pressure Effect.” *Journal of the American Ceramic Society*, vol. 92, no. 4, pp. 864–869, 2009

[21] J. Evans, and S. Chatterji, "Kinetics of the oxidation and nitridation of silicon at high temperatures." *The Journal of Physical Chemistry*, vol. 62, no. 9, pp. 1064-1067, 1958

[22] J. Rodriguez-Viejo, J. Sibieude, and M. Clavaguera-Mora. "High-temperature oxidation of CVD β-SiC part I. Experimental study." *Journal of the European Ceramic Society*, vol. 13, no. 2, pp. 167-175, 1994

[23] S. Singhal, "Thermodynamics and kinetics of oxidation of hot-pressed silicon nitride." *Journal of Materials Science*, vol. 11, no. 3, pp. 500-509, 1976

[24] R. Raj, L. An, S. Shah, R. Riedel, C. Fasel, and H.-J. Kleebe, “Oxidation Kinetics of an Amorphous Silicon Carbonitride Ceramic”. *Journal of the American Ceramic Society*, vol. 84, pp.1803–1810, 2001

[25] J. Costello, “Isotope Labeling Studies of the Oxidation of Silicon at 1000° and 1300°C.” *Journal of The Electrochemical Society*, vol. 131, no. 8, pp.1944-1947, 1984

[26] Ogbuji, Linus UJT, and Scott R. Bryan. "The SiO_2-Si_3N_4 Interface, Part I: Nature of the Interphase." *Journal of the American Ceramic Society*, vol. 78, no. 5, pp. 1272-1278, 1995

[27] B. Deal and A. Grove. "General relationship for the thermal oxidation of silicon." *Journal of Applied Physics*, vol. 36, no. 12, pp. 3770-3778, 1965

[28] J. Costello and R. Tressler, "Oxidation kinetics of silicon carbide crystals and ceramics: I, in dry oxygen." *Journal of the American Ceramic Society*, vol. 69, no. 9, pp. 674-681, 1986

[29] L. Ogbuji, "Effect of oxide devitrification on oxidation kinetics of SiC." *Journal of the American Ceramic Society*, vol. 80, no. 6, pp. 1544-1550, 1997

[30] O. Elizabeth. "Influence of Alumina Reaction Tube Impurities on the Oxidation of Chemically-Vapor-Deposited Silicon Carbide." *Journal of the American Ceramic Society*, vol. 78, no. 4, pp. 1107-1110, 1995

[31] R. Sickafoose and D. Readey. "Active gaseous corrosion of porous silicon carbide." *Journal of the American Ceramic Society*, vol. 76, no. 2, pp. 316-324, 1993

[32] N. Jacobson, B. Harder, and D. Myers. "Oxidation Transitions for SiC Part I. Active-to-Passive Transitions." *Journal of the American Ceramic Society*, vol. 96, no. 4, pp. 838-844, 2013

[33] B. Harder, N. Jacobson, and D. Myers. "Oxidation Transitions for SiC Part II. Passive-to-Active Transitions." *Journal of the American Ceramic Society*, vol. 96, no. 2, pp.606-612, 2013.

[34] J. Hinze and H. Graham. "The Active Oxidation of Si and SiC in the Viscous Gas-Flow Regime." *Journal of the Electrochemical Society*, vol. 123, no. 7, pp. 1066-1073, 1976

[35] S. Shah and R. Raj. "Multilayer Design and Evaluation of a High Temperature Environmental Barrier Coating for Si-Based Ceramics." *Journal of the American Ceramic Society*, vol. 90, no. 2, pp. 516-522, 2007

[36] Ruh, Robert, and Vinod A. Patel. "Proposed Phase Relations in the HfO_2-Rich Portion of the System Hf-HfO_2." *Journal of the American Ceramic Society*, vo. 56, no. 11, pp. 606-607, 1973

[37] A. Stoklosa and B. Laskowska. "The Bond Energy and the Composition of Metal Oxides." High Temperature Materials and Processes, vol. 26, no. 2, pp. 93-102, 2007

[38] R. Ruh, H. Garrett, R. Domagala, and N. Tallan. "The Svstern Zirconia-Hafnia." Journal of the American Ceramic Society, vol. 51, no. 1, pp. 23-28, 1968

[39] W. Klopp, C. Powell, D. Maykuth, and H. Ogden. “Development of Protective Coatings for Tantalum-Base Alloys” No. ASD-TR-61-676. Battelle Memorial Inst., Columbus, Ohio, 1962.

[40] P. Colombo, G. Mera, R. Riedel, and G. Soraru. "Polymer-Derived Ceramics: 40 Years of Research and Innovation in Advanced Ceramics." *Journal of the American Ceramic Society,* vol. 93, no. 7, pp.1805-1837, 2010

[41] R. Raj, R. Riedel, and G. Soraru. "Introduction to the Special Topical Issue on Ultrahigh-Temperature Polymer-Derived Ceramics." *Journal of the American Ceramic Society*, vol. 84, no. 10, pp.2158-2159, 2001

[42] A. Saha, R. Raj, and D. Williamson, “A Model for the Nanodomains in Polymer-Derived SiCO”. *Journal of the American Ceramic Society*, vol. 89, pp. 2188–2195, 2006

[43] T. Varga, A. Navrotsky, J. Moats, R. Morcos, F. Poli, K. Müller, A. Saha, and R. Raj, “Thermodynamically Stable $Si_xO_yC_z$ Polymer-Like Amorphous Ceramics.” *Journal of the American Ceramic Society*, vol. 90, pp. 3213–3219 , 2007

[44] R. Riedel, A. Kienzle, W. Dressler, L. Ruwisch, J. Bill, and F. Aldinger, “A silicoboron carbonitride ceramic stable to 2,000°C”. *Nature*, vol. 382, 6594, pp.796-798, 1996

[45] L. An, R. Riedel, C. Konetschny, H.-J. Kleebe, and R. Raj, “Newtonian Viscosity of Amorphous Silicon Carbonitride at High Temperature”. *Journal of the American Ceramic Society*, vol. 81, pp. 1349–1352, 1998

[46] J. Torrey, R. Bordia, C. Henager, Y. Blum, Y. Shin, and W. Samuels, “Composite polymer derived ceramic systems for oxidizing environments”. *Journal of Material Science*, vol. 41, pp. 4617–4622, 2006

[47] M. Günthner, S. Adelheid, U. Glatzel, K. Wang, R. Bordia, O. Greißl, W. Krenkel, and G. Motz, “High performance environmental barrier coatings, Part I: Passive filler loaded SiCN system for steel” *Journal of the European Ceramic Society*, vol. 31, pp. 3003–3010, 2011

[48] Y. Wang, and L. An, “Polymer Derived SiAlCN for Environmental Barrier Coatings”, *ASME Conference Proceedings*, 237, 2005

[49] S. Krumdieck, Susan P., and Rishi Raj. "Experimental characterization and modeling of pulsed MOCVD with ultrasonic atomization of liquid precursor." *Chemical Vapor Deposition*, vol. 7, no. 2, pp. 85-90, 2001

[50] M. Walawalkar, A. Kottantharayil, and V. Ramgopal Rao. "Chemical vapor deposition precursors for high dielectric oxides: zirconium and hafnium oxide." *Synthesis and Reactivity in Inorganic, Metal-Organic, and Nano-Metal Chemistry* vol. 39, no. 6, pp. 331-340, 2009

[51] N. Turova (Ed.) *The chemistry of metal alkoxides*. Springer, 2002.

[52] R. Matsumoto, "Crystallization of Pyrolyzed Polysilazanes," *Material Research Society Symposium Proceedings*, vol.180, pp. 797-800,1990

[53] C. Curtis, L. Doney, and J. Johnson. "Some properties of hafnium oxide, hafnium silicate, calcium hafnate, and hafnium carbide." *Journal of the American Ceramic Society*, vol. 37, no. 10, pp.458-465, 1954

[54] A. Patterson, "The Scherrer formula for X-ray particle size determination." *Physical review*, vol. 56, no. 10, 978, 1939

[55] D. Salt, and G. Hornung. "Synthesis and X-Ray Study of Hafnium Silicate." *Journal of the American Ceramic Society*, vol. 50, no. 10, pp. 549-550, 1967

[56] E. Ionescu, C. Linck, C. Fasel, M. Mahller, H.-J. Kleebe, and R. Riedel. “Polymer-Derived SiOC/ZrO_2 Ceramic Nanocomposites with Excellent High-Temperature Stability.” *Journal of the American Ceramic Society*, vol. 93, no. 1, pp. 241-250, 2010

[57] K. Terauds, Measurents of solvent-PDC surface tension (*unpublished*)

[58] E. Plueddemann, (Ed.) *Silane Coupling Agents*. Springer, 1982.

[59] KiON® Ceraset® Polyureasilazane and KioN® Ceraset® Polsilazane 20, Technical Datasheet, Kion Defense Technologies, Huntingdon Valley, PA

[60] M. Birkholz. *Thin film analysis by X-ray scattering*. Wiley, 2006.

[61] S. Brahmandam and R. Raj. "Novel Composites Constituted from Hafnia and a Polymer-Derived Ceramic as an Interface: Phase for Severe Ultrahigh Temperature Applications." *Journal of the American Ceramic Society*, vol. 90, no. 10, pp. 3171-3176, 2007

[62] K. Terauds and A. Taylor, Thin PDC films on Cu and other metals, (*unpublished)*

[63] J. Costello and R. Tressler, "Oxidation Kinetics of Hot-Pressed and Sintered α-SiC." *Journal of the American Ceramic Society*, vol. 64, no. 6, pp. 327-331, 1981.

[64] A. Heuer, L. Ogbuji, and T. Mitchell. "The microstructure of oxide scales on oxidized Si and SiC single crystals." *Journal of the American Ceramic Society*, vol. 63, no. 5-6, pp. 354-355, 1980

[65] Z. Zheng, R. Tressler, and K. Spear, "Oxidation of Single-Crystal Silicon Carbide Part I. Experimental Studies" *Journal of The Electrochemical Society*, vol. 137, no. 3, pp. 854-858, 1990

[66] R. Harris, "Oxidation of 6H-α Silicon Carbide Platelets." *Journal of the American Ceramic Society*, vol. 58, no. 1, pp. 7-89, 1975

[67] G. Schiroky, "Oxidation behavior of chemically vapor-deposited silicon carbide." *Advanced Ceramic Materials*; (USA), vol. 2, no. 2, pp.137-141, 1987

[68] C. Tedmon, "The Effect of Oxide Volatilization on the Oxidation Kinetics of Cr and Fe-Cr Alloys." *Journal of the Electrochemical Society*, vol 113, no. 8, pp. 766-768, 1966

[69] E. Opila, and R. Hann. "Paralinear oxidation of CVD SiC in water vapor." *Journal of the American Ceramic Society*, vol. 80, no. 1, pp. 197-205, 1997

[70] J. Smialek, C. Robinson, E. Opila, D. Fox, and N. Jacobson. "SiC and Si_3N_4 recession due to SiO_2 scale volatility under combustor conditions." *Advanced Composite Materials*, vol. 8, no. 1, pp. 33-45, 1999

[71] V. Parfenenkov, R. Grebenshchikov, N. Toropov; “Phase equilibriums in the hafnium dioxide-silicon dioxide system “ *Dokl. Akad. Nauk SSSR*, vol. 185, no. 4, pp. 840–842, 1969

[72] M. Lamkin, L. Riley, and R. Fordham. "Oxygen mobility in silicon dioxide and silicate glasses: a review." *Journal of the European Ceramic Society*, vol. 10, no. 5, pp. 347-367, 1992

[73] E. Williams, "Diffusion of oxygen in fused silica." *Journal of the American Ceramic Society*, vol. 48, no. 4, pp. 190-194, 1965

[74] R. Doremus "Oxidation of silicon by water and oxygen and diffusion in fused silica." *The Journal of Physical Chemistry*, vol. 80, no. 16, pp. 1773-1775, 1976

[75] K. Terauds and R. Raj "Limits to the Stability of the Amorphous Nature of Polymer-Derived HfSiCNO Compounds." *Journal of the American Ceramic Society*, vol. 96, no. 7, 2013

[76] R. Riedel, L. Ruswisch, L. An, and R. Raj. "Amorphous silicoboron carbonitride ceramic with very high viscosity at temperatures above 1500°C." *Journal of the American Ceramic Society*, vol. 81, no. 12, pp. 3341-334, 1998

[77] P. Ramakrishnan, Y. Wang, D. Balzar, L. An, C. Haluschka, R. Riedel, and A. Hermann. "Silicoboron–carbonitride ceramics: A class of high-temperature, dopable electronic materials." *Applied Physics Letters*, vol. 78, no. 20, pp. 3076-3078, 2001

[78] A. Tavakoli, R. Campostrini, C. Gervais, F. Babonneau, J. Bill, G. Sorarù, and A. Navrotsky. "Energetics and Structure of Polymer-Derived Si–(B–) O–C Glasses:

Effect of the Boron Content and Pyrolysis Temperature." Journal of the American Ceramic Society, vol. 97, no. 1, pp. 303-309, 2014

[79] V. Liebau, R. Hauser, and R. Riedel. "Amorphous SiBCO ceramics derived from novel polymeric precursors." *Comptes Rendus Chimie*, vol. 7, no. 5, pp. 463-469, 2004

[80] R. Riedel, A. Kienzle, W. Dressler, L. Ruwisch, J. Bill, and F. Aldinger. "A silicoboron carbonitride ceramic stable to 2,000 C." *Nature*, vol. 382, no. 6594, pp. 796-798, 1996

[81] A. Saha, S. Shah, R. Raj, and S. Russek. "Polymer-derived SiCN composites with magnetic properties." *Journal of materials research*, vol. 18, no. 11, pp. 2549-2551, 2003

[82] R. Hauser, A. Francis, R. Theismann, and R. Riedel. "Processing and magnetic properties of metal-containing SiCN ceramic micro-and nano-composites." *Journal of Materials Science*, vol. 43, no. 12, pp. 4042-4049, 2008

[83] L. Biasetto, A. Francis, P. Palade, G. Principi, and P. Colombo. "Polymer-derived microcellular SiOC foams with magnetic functionality." *Journal of Materials Science*, vol. 43, no. 12, pp. 4119-4126, 2008.

[84] G. Sorarù, Y. Zhang, M. Ferrari, L. Zampedri, and R. Gonçalves. "Novel Er-doped SiC/SiO_2 nanocomposites: Synthesis via polymer pyrolysis and their optical characterization." *Journal of the European Ceramic Society*, vol. 25, no. 2, pp. 277-281, 2005

[85] Y. Wang, "Polymer-derived Si-Al-C-N Ceramics: Oxidation, Hot-corrosion and structural evolution" PhD Dissertation, University of Central Florida, Orlando, FL, 2006

[86] W. Yifei, F. Chunxiang, and S. Yongcai. "Study of the Preparation and Electric Properties of Si Ti CO Fibers." *High Technology Letters*, vol. 5, 1999.

[87] F. Babonneau, and G. Soraru. "Synthesis and characterization of SiZrCO ceramics from polymer precursors." *Journal of the European Ceramic Society*, vol. 8, no. 1, pp. 29-34, 1991.

[88] R. Sujith, A. Kousaalya, and R. Kumar. "Synthesis and phase stability of precursor derived HfO2 /Si–C–N–O nanocomposites." *Ceramics International*, vol. 38, no. 2, pp. 1227-1233, 2012

[91] S. Yajima, Y. Hasegawa, J. Hayashi, and M. Iimura. "Synthesis of continuous silicon carbide fibre with high tensile strength and high Young's modulus." *Journal of Materials Science*, vol. 13, no. 12, pp. 2569-2576, 1978

[92] D. Seyferth, "Polycarbosilanes: an overview." *In ACS symposium series*, no. 360, pp. 21-42. Oxford University Press, 1988.

[93] K. Okamura, "Ceramic fibres from polymer precursors." *Composites*, vol. 18, no. 2, pp. 107-120, 1987

[94] T. Yamamura, T. Ishikawa, M. Shibuya, T. Hisayuki, and K. Okamura. "Development of a new continuous Si-Ti-CO fibre using an organometallic polymer precursor." *Journal of materials science*, vol. 23, no. 7, pp. 2589-2594, 1988

[95] T. Yamamura, T. Ishiawa, M. Shibuya, M. Tamura, T. Nagasawa, and K. Okamura. "A New Type of Ceramic Matrix Composite Using Si-Ti-C-O Fiber." In A Collection of Papers Presented at the 13th Annual Conference on Composites and Advanced Ceramic Materials, Part 1 of 2: Ceramic Engineering and Science Proceedings, vol. 10, no. 7/8, pp. 736-747. John Wiley & Sons, Inc.

[96] S. Yajima, T. Iwai, T. Yamamura, K. Okamura, and Y. Hasegawa. "Synthesis of a polytitanocarbosilane and its conversion into inorganic compounds." *Journal of Materials Science*, vol. 16, no. 5, pp. 1349-1355, 1981

[97] V. Siriwongrungson, S. Krumdieck, and M. Alkaisi. "Pulsed-Pressure MOCVD Processing Investigation for TiO2 Films on Si3N4 Substrate from TTIP." *ECS Transactions*, vol. 25, no. 8, pp.987-990, 2009

[98] P. Falaras, and A. Xagas. "Roughness and fractality of nanostructured TiO_2 films prepared via sol-gel technique." Journal of materials science, vol. 37, no. 18, pp. 3855-3860, 2002

[99] K. Okamura, M. Sato, T. Matsuzawa, T. Seguchi, and S. Kawanishi. "Silicon-based ceramic fibers." In Proceedings of the 12th Annual Conference on Composites and Advanced Ceramic Materials, Part 1 of 2: Ceramic Engineering and Science Proceedings, vol. 9, vol. 7/8, pp. 909-918. John Wiley & Sons, Inc., 1988.

[102] C. Zheng, X. Li, Y. Yu, and F. Cao. "Preparation of high temperature resistance Si-Al-C-O fibers by polymer-derived method." *Journal of Material Engineering*, vol. 12, pp. 25-28, 2004

[103] F. Cao, X. Li, P. Peng, C. Feng, J. Wang, and D. Kim. "Structural evolution and associated properties on conversion from Si-CO-Al ceramic fibers to Si-C-Al fibers by sintering." *Journal of Materials Chemistry*, vol. 12, no. 3, pp. 606-610, 2002

[104] C. Zheng, X. LI, and D. Zhao "Conversion of polyaluminocarbosilane (PACS) to Si-Al-C-(O) fibers: evolutions and effect of oxygen." *Transactions of Nonferrous Metals Society of China*, vol. 16, no. 2, pp. 254-258, 2006.

[105] T. Ishikawa, Y. Kohtoku, K. Kumagawa, T. Yamamura, and T. Nagasawa. "High-strength alkali-resistant sintered SiC fibre stable to 2,200 C." *Nature*, vol. 391, no. 6669, pp. 773-775, 1998

[106] K. Kumagawa, H. Yamaoka, M. Shibuya, and T. Yamamura. "Thermal stability and chemical corrosion resistance of newly developed continuous Si-Zr-CO Tyranno fiber." In 21st Annual Conference on Composites, Advanced Ceramics, Materials, and Structures-A: Ceramic Engineering and Science Proceedings, vol. 208, pp.113. Wiley, 2009.

[107] H. Yamaoka, T. Ishikawa, and K. Kumagawa. "Excellent heat resistance of Si-Zr-CO fibre." *Journal of materials science,* vol. 34, no. 6, pp. 1333-1339, 1999

[108] K. Suzuki, K. Kumagawa, T. Kamiyama, and M. Shibuya. "Characterization of the medium-range structure of Si-Al-CO, Si-Zr-CO and Si-Al-C Tyranno fibers by small angle X-ray scattering." *Journal of materials science*, vol. 37, no. 5, pp. 949-953, 2002

[109] T. Yamaamura, S. Masakl, T. Ishlkawa, M. Sato, M. Shibuya, and K. Kumagawa. "Improvement of Si-Ti(Zr)-C-O fiber and precursor polymers for High Temperature CMC" In 20th Annual Conference on Composites, Advanced Ceramics, Materials,

and Structures-B: Ceramic Engineering and Science Proceedings, vol. 12, no. 4, p. 184. John Wiley & Sons, 2009.

[110] N. Yamada, I. Yoshinaga, and S. Katayama. "Synthesis and dynamic mechanical behaviour ofinorganic–organic hybrids containing various inorganiccomponents." *Journal of Material Chemistry*, vol. 7, no. 8, pp. 1491-1495, 1997.

[111] B. Alonso and C. Sanchez. "Structural investigation of polydimethylsiloxane–vanadate hybrid materials." *Journal of Materials Chemistry*, vol. 10, no. 2, vol. 377-386, 2000

[112] M. Ho, Y. Wang, R. Brewer, L. Wielunski, Y. Chabal, N. Moumen, and M. Boleslawski. "In situ infrared spectroscopy of hafnium oxide growth on hydrogen-terminated silicon surfaces by atomic layer deposition." *Applied Physics Letters*, vol. 87, no. 13, pp. 133103, 2005

[113] M. Fukushima, E. Yasuda, Y. Nakamura, and Y. Tanabe. "Pyrolysis behavior of organic-inorganic hybrids with Si-O-Nb/Si-O-Ta oxygen bridged heterometallic bonds." *Journal of the Ceramic Society of Japan*, vol. 111, no. 11, pp. 857-8599, 2003

[114] A. Saha, S. Shah, and R. Raj. "Oxidation Behavior of SiCN–ZrO2 Fiber Prepared from Alkoxide-Modified Silazane." *Journal of the American Ceramic Society*, vol. 87, no. 8, pp. 1556-1558, 2004

[115] E. Ionescu, B. Papendorf, H. Kleebe, F. Poli, K. Müller, and R. Riedel. "Polymer-Derived Silicon Oxycarbide/Hafnia Ceramic Nanocomposites. Part I: Phase and Microstructure Evolution During the Ceramization Process." *Journal of the American Ceramic Society*, vol. 93, no. 6, pp. 1774-1782, 2010

[116] E. Ionescu, C. Linck, C. Fasel, M. Müller, H.-J. Kleebe, and R. Riedel. "Polymer-Derived SiOC/ZrO2 Ceramic Nanocomposites with Excellent High-Temperature Stability." *Journal of the American Ceramic Society*, vol. 93, no. 1, pp. 241-250, 2010

[117] N. Koslova, B. Viana, and C. Sanchez. "Rare-earth-doped hybrid siloxane–oxide coatings with luminescent properties." *Journal of Material Chemistry*, vol. 3, no. 1, pp.111-112, 1993

[118] B. Papendorf, K. Nonnenmacher, E. Ionescu, H.-J. Kleebe, and R. Riedel. "Strong Influence of Polymer Architecture on the Microstructural Evolution of Hafnium-Alkoxide-Modified Silazanes upon Ceramization." *Small*, vol. 7, no. 7, pp. 970-978, 2011

[119] A. Dhamne, W. Xu, B. Fookes, Y. Fan, L. Zhang, S. Burton, J. Hu, J. Ford, and L. An. "Polymer–ceramic conversion of liquid polyaluminasilazanes for SiAlCN ceramics." *Journal of the American Ceramic Society*, vol. 88, no. 9, pp. 2415-2419, 2005

[120] B. Boury and D. Seyferth. "Preparation of Si/C/Al/N ceramics by pyrolysis of polyaluminasilazanes." *Applied organometallic chemistry*, vol. 13, no. 6, pp. 431-440, 1999

[121] R. Morcos, G. Mera, A. Navrotsky, T. Varga, R. Riedel, F. Poli, and K. Müller. "Enthalpy of Formation of Carbon-Rich Polymer-Derived Amorphous SiCN Ceramics." *Journal of the American Ceramic Society*, vol. 91, no. 10, pp. 3349-3354, 2008

[122] R. Morcos, A. Navrotsky, T. Varga, D. Ahn, A. Saha, F. Poli, K. Müller, and R. Raj. "Thermodynamically Stable SiwCxNyOz Polymer-Like, Amorphous Ceramics Made from Organic Precursors." *Journal of the American Ceramic Society*, vol. 91, no. 7, pp. 2391-2393, 2008

[123] D. Stull and H. Prophet. JANAF thermochemical tables. No. NSRDS-NBS-37. National Standard Reference Data System, 1971.

[124] A. Stoklosa and B. Laskowska. "The Bond Energy and the Composition of Metal Oxides." *High Temperature Materials and Processes*, vol. 26, no. 2, pp. 93-102, 2007

[125] R. Harshe, C. Balan, and R. Riedel. "Amorphous Si (Al) OC ceramic from polysiloxanes: bulk ceramic processing, crystallization behavior and applications." *Journal of the European Ceramic Society*, vol. 24, no. 12, pp.3471-3482, 2004

[126] D. Bradley, R. Mehrotra, and W. Wardlaw. "Hafnium alkoxides." *Journal of the Chemical Society*, (Resumed), pp. 1634-1636, 1953.

[127] A. Saha, R. Raj, D. Williamson, and H-J. Kleebe. "Characterization of Nanodomains in Polymer-Derived SiCN Ceramics Employing Multiple Techniques." *Journal of the American Ceramic Society*, vol. 88, no. 1, pp/ 232-234, 2005

[128] K. Li, “Hanfium Alkylamides and Alkoxide Adsorption and Reaction on Hydrogen Terminated Silicon Surfaces in a Flow Reactor”, PhD Dissertation, University of Alabama, 2010

[129] P. Launer, “Infrared Analysis of Organosilicon Compounds: Spectra- Structure Correlations,” Silicon Compounds: Silanes and Silicones, Gelest, Inc., pp. 223-226, 2008

[130] Ren, Jun, Zhong Li, Shusen Liu, Yanling Xing, and Kechang Xie. "Silica–titania mixed oxides: Si–O–Ti connectivity, coordination of titanium, and surface acidic properties." *Catalysis Letters*, vol. 124, no. 3-4, pp. 185-194, 2008.

[131] M. Song, P. Yang, D. Xu and D. Yuan. "Structure and photoluminescence properties of sol-gel TiO2-SiO2 films" *Thin Solid Films*, vol. 413, pp.155-159, 2002

[132] S. Dire, R. Campostrini, and R. Ceccato. "Pyrolysis chemistry of sol- gel-derived poly(dimethylsiloxane)-zirconia nanocomposites. Influence of zirconium on polymer-to-ceramic conversion," *Chemistry of Materials*, vol. 10, pp. 268-278, 1998

[133] D. Neumayer and E. Cartier. "Materials characterization of ZrO2-SiO2 and HfO2-SiO2 binary oxides deposited by chemical solution deposition," *Journal of Applied Physics*, vol. 90, pp. 1801-1808, 2001

[134] M. Frank, S. Sayan, S. Dormann, T. Emge, L. Wielunski, E. Garfunkel, and Y. Chabal "Hafnium oxide gate dielectrics grown from an alkoxide precursor: structure and defects," *Materials Science and Engineering: B*, vol. 109, pp. 6-10, 2004

[135] T. Smirnova, L. Yakovkina, S. Beloshapkin, V. Kaichev, N. Alferova and S. Jeong-Hwan. "Interfaces analysis of the HfO_2/SiO_2/Si structure," *Journal of the Physical Chemistyr of Solids*, vol. 71, pp. 836-840, 2010

[136] S. Ushakov, A. Navrotsky, Y. Yang, S. Stemmer, K. Kukli, M. Ritala, M. Leskelä, P. Fejes, A. Demkov, C. Wang, B.-Y. Nguyen, D. Triyoso, and P. Tobin "Crystallization in hafnia-and zirconia-based systems." *Physica Status Solidi (b)* , vol. 241, no. 10, pp. 2268-2278, 2004

[137] C. Lu, J. Raitano, S. Khalid, L. Zhang, and S.-W. Chan "Cubic phase stabilization in nanoparticles of hafnia-zirconia oxides: Particle-size and annealing environment effects." *Journal of Applied Physics*, vol. 103, no. 12, pp. 124303, 2008

[138] K. Terauds and R. Raj "Limits to the Stability of the Amorphous Nature of Polymer-Derived HfSiCNO Compounds." Journal of the American Ceramic Society, vol. 96, no. 7, 2013

[139] S. Trassl, G. Motz, E. Rössler, and G. Ziegler. "Characterisation of the free-carbon phase in precursor-derived SiCN ceramics." *Journal of non-crystalline solids,* vol. 293, pp. 261-267, 2001

[140] R. Friedel and G. Carlson, “Infrared Spectra of Ground Graphite” *Journal of Physical Chemistry,* vol. 75, no. 8, pp. 1149-1151, 1971

[141] A. Ferrari, and J. Robertson. "Interpretation of Raman spectra of disordered and amorphous carbon." *Physical review B*, vol. 61, no. 20, pp. 14095-14107, 2000

[142] A. Ferrari, and J. Robertson. "Resonant Raman spectroscopy of disordered, amorphous, and diamondlike carbon." *Physical Review B*, vol. 64, no. 7, pp. 075414, 2001

[143] J. Maultzsch, S. Reich, and C. Thomsen. "Double-resonant Raman scattering in graphite: Interference effects, selection rules, and phonon dispersion." *Physical Review B*, vol. 70, no. 15, pp. 155403, 2004

[144] K. Terauds, P. Kroll, R. Raj, “Ab-Initio and FTIR Studies of HfSiCNO Processed from the Polymer Route,” *Journal of the American Ceramic Society*, (*submitted revision 10/2013*)

[145] G. Trimmel, R. Badheka, F. Babonneau, J. Latournerie, P. Dempsey, D. Bahloul-Houlier, J. Parmentier and G. Soraru, “Solid state NMR and TG/MS study on the transformation of methyl groups during pyrolysis of preceramic precursors to SiOC glasses,” *Journal of Sol Gel Science and Technology*, vol. 26, pp.279-283, 2003

[146] J. Seitz, J. Bill, N.Egger, and F. Aldinger, “Structural investigations of Si/C/N-ceramics from polysilazane precursors by nuclear magnetic resonance,” *Journal of the European Ceramic Society*, vol. 16, no. 8, pp. 885-891, 1996

[147] S. Trassl, D. Suttor, G. Motz, E. Rossler, and G. Ziegler, “Structural Characterisation of Silicon Carbonitride Ceramics Derived from Poymeric Precursors,” *Journal of the European Ceramic Society*, vol. 20, pp. 215-225, 2000

[148] S. Schempp, J. Durr, P. Lamparter, J. Bill, and F. Aldinger, “Study of the Atomic Structure and Phase Separation in Amorphous Si-C-N Ceramics by X-ray Neutron Diffraction,” *Zeitschrift Naturforschung A – Journal of Physical Sciences*, vol. 53, no. 3, pp. 127-133, 1995

[149] P. Kroll, "Modeling the 'free carbon' phase in amorphous silicon oxycarbide," *Journal of Non-Crystalline Solids*, vol. 351, pp. 1121-1126, 2005

[150] P. Kroll, "Searching insight into the atomistic structure of SiCO ceramics," *Journal of Materials Chemistry*, vol. 20, 10528-10534, 2010.

[151] M. Cinibulk, and T. Parthasarathy. "Characterization of Oxidized Polymer-Derived SiBCN Fibers." *Journal of the American Ceramic Society*, vol. 84, no. 10, pp. 2197-2202, 2001.

[152] M. Friess, J. Bill, J. Golczewski, A. Zimmermann, F. Aldinger, R. Riedel, and R. Raj. “Crystallization of polymer-derived silicon carbonitride at 1873 K undernitrogen overpressure” *Journal of the American Ceramic Society*, vol. 85, no. 10, pp. 2587-2589, 2002

[153] P. Becher,S. Hampshire, M. Pomeroy, J. Hoffmann, M. Lance, and R. State, “An overview of the structure and properties of silicon-based oxynitrideglasses,” *International Journal of Applied Glass Science*, vol. 2, no. 1, pp. 63-83, 2011

[154] S. Hampshire, M. Pomeroy “Grain boundary glasses in silicon nitride:a review of chemistry, properties and crystallization” *Journal of the European Ceramic Society*, vol. 32, no. 9, pp. 1925-1932, 2012

[155] R. Raj, "Chemical Potential-Based Analysis for the Oxidation Kinetics of Si and SiC Single Crystals." *Journal of the American Ceramic Society*, vol. 96, no. 9, pp. 2926-2934, 2013.

[156] B. Cullity and S. Stock. Elements of X-ray Diffraction. Vol. 3. Upper Saddle River, NJ: Prentice hall, 2001.

[157] R. Hay, G. Fair, R. Bouffioux, E. Urban, J. Morrow, A. Hart, and M. Wilson. "Hi-NicalonTM-SSiC Fiber Oxidation and Scale Crystallization Kinetics." *Journal of the American Ceramic Society*, vol. 94, no. 11, pp. 3983-3991, 2011

[158] Y. Wang, Y. Fan, L. Zhang, W. Zhang, and L. An. "Polymer-derived SiAlCN ceramics resist oxidation at 1400°C." *Scripta materialia*, vol. 55, no. 4, pp. 295-297, 2006

[159] R. Singh, and M. Brun. "Effect of Boron Nitride Coating on Fiber-Matrix." In 11th Annual Conference on Composites and Advanced Ceramic Materials: Ceramic Engineering and Science Proceedings, vol. 8, no. 7-8, p. 636. Wiley. com, 2009.

[160] A. Harvey, A. Peskin, and S. Klein. "NIST/ASME steam properties." NIST Standard Reference Database, 10, (1997).

[161] E. Opila, "Oxidation and volatilization of silica formers in water vapor." *Journal of the American Ceramic Society*, vol. 86, no. 8, pp. 1238-1248, 2003

[162] K. Mergia, V. Liedke, T. Speliotis, G. Apostolopoulos, and S. Messoloras, “Thermo-Mechanical Behaviour Of HfO2 Coatings For Aerospace Applications” *Advanced Materials Research*, vol. 59, pp. 87-91, 2009

[163] J. Hubbell, E. Veigele, E. Briggs, R. Brown, D. Cromer, and R. Howerton. "Atomic form factors, incoherent scattering functions, and photon scattering cross sections." *Journal of physical and chemical reference data*, vol. 4, 471, 1975

[164] J. Hubbell, and I. Øverbø. "Relativistic atomic form factors and photon coherent scattering cross sections." *Journal of Physical and Chemical Reference Data,* vol. 8, 69, 1979

[165] A. Babinet, "Mémoires d'optique météorologique." *Compt. Rend. Acad. Sci*., vol. 4, 638, 1837

[166] L. Feigin, and D. Svergun (1987). *Structure Analysis by Small-Angle X-ray and Neutron Scattering*. New York: Plenum Press.

[167] D. Williamson, "Nanostructure of a a-Si:H and Related Materials by Small Angle X-ray scattering," *Material Research Society Symposium Proceedings*, vol. 377, p. 251,1995

[168] File, Powder Diffraction. "International Centre for Diffraction Data." Swarthmore, PA, 19081, (2000).

[169] J. Gentry, "Estimation of parameters for a log-normal distribution with truncated measurements." *Powder Technology,* vol. 18, no. 2, pp. 225-229, 1977

[170] E. Lavernia, *Theoretical Analysis of Powder Size Distribution*. DTIC Document, California University Irvine, Department of Chemical, Biomedical Engineering, and Material Science, 1997

[171] H. Brittain, "Particle-size distribution. Part I. Representations of particle representations of partide shape, size, and distribution." *Pharmaceutical technology,* vol. 25, no. 12, pp. 38-45, 2001

[172] S. Ashour and M. Abdel-hameed. "Approximate skew normal distribution." *Journal of Advanced Research,* vol. 1, no. 4, pp. 341-350., 2010

[173] L. Wilson and R. Marcus. "Oxidation of curved silicon surfaces."*Journal of the Electrochemical Society,* vol. 134, no. 2, pp. 481-490, 1987

[174] S. Shah. *High temperature mechanical and oxidation behavior of amorphous silicon carbonitride processed via chemical nanoprecursor route.* Ph.D Thesis, University of Colorado at Boulder, 2000

[175] W. Ham, *Nickel-based superalloy operating temperature determination via analysis of gamma/gamma'microstructure and coating/base material interdiffusion*. MS Thesis, Massachusetts Institute of Technology, 2005.

[176] N. Padture, M. Gell, and E. Jordan. "Thermal barrier coatings for gas-turbine engine applications." *Science,* vol. 296, no. 5566, pp. 280-284, 2002